Microfluidics at micrometric and sub-micrometric scale : NanoPTV, droplets formation, and sub-micrometric model

Zhenzhen Li

UPMC
PARIS UNIVERSITAS

THÈSE DE DOCTORAT DE

L'UNIVERSITÉ PIERRE ET MARIE CURIE

Spécialité

Physique des liquides (ED 391)

présentée par Zhenzhen LI

Pour obtenir le grade de

DOCTEUR DE L'UNIVERSITÉ PIERRE ET MARIE CURIE

Microfluidique à L'échelle Micrometrique et Sub-micrometrique: NanoPTV, Formation des Gouttes et Modèle Sub-micrometriques

devant le jury composé de :

Mme. Valerie Cabuil	Présidente
Mme. Anne-Marie Gué	Rapporteur
M. Pierre Joseph	Examinateur
M. Philippe Renaud	Rapporteur
M. Patrick Tabeling	Directeur de thèse

Université Pierre et Marie Curie-Paris 6
Bureau d'accueil, Esc G, 2ème étage
15 rue de l'école de médecine
75270 Paris Cedex 06

Tél. Secrétariat: 01 42 34 68 35
Fax: 01 42 34 68 40
E-mail: scolarite.doctorat@upmc.fr

Acknowledgement

I would like to thank members of jury, Valerie Cabuil, Anne-Marie Gué, Pierre Joseph, and Philippe Renaud for attending my thesis defense, and thank you for your comments and suggestions.
I sincerely thank my advisor Patrick Tabeling, who worked with me constantly on my different projects. I learned a lot through our frequent discussion, not only on science, but also on philosophy and many other things. Thank you for your consistent support and inspiration, which lead my way towards a mature researcher.
A big thank to Alex Leshansky, who visited us twice during the summers and worked with us at a long distance. I am deeply impressed by his rigorous and efficient spirit.
I appreciated the collaboration with Loïc D'eramo, who contributed significantly to our project. Thank you for your outstanding numerical skills which helped us unravelling complicated problems, and his kindness.
I thank Fabrice Monti, who is always beside to solve any problems that I encountered in the lab work. I deeply appreciated the brilliant ideas he brought to me, and especially his sense of humour.
Thanks to Herve Willaime, who participated the petroleum project, and helped solved the most difficult part of the project.
Thanks to Benjamin Chollet, Bruno Bresson and Yvette Tran, who helped us constantly on chemical aspects of our projects, and offer wonderful quality of the surface treatment.
Thanks to Mathilde Reyssat, her kindness and all of her help and suggestions. Thanks to Marie-Caroline Julien, for her courses on microfluidics during my engineering education, and for her all kinds of help.
Thank Anne-Laure Vayssade, who helped me a lot and who worked on the other side of the room and on another kind of velocimetry, I believe that we shared the same happiness and confusion while we were both looking at the particles passing through a dark background.
Thank to the students who worked with me, Marc Yonger, Samuel Metais and Jeremy Foglia. I am impressed by their spirit of hard work and their vital minds, I wish them best luck for the continuation.
Many thanks to Perrine Franquet and Stephanie Le Lay, who provided me consistent help on all different issues, I wouldn't come out from all kinds of paper work without them.
Thanks to all members of the MMN, Marie, Bingqing, Anne, Laura, Marine, Vincent, Axel, Antoine and Jules. Thanks to members of the Gulliver. Thank you for your kindness, I spend a wonderful three years and a half being part of you.

Contents

Chapter 1

General introduction

Microfluidic is a science and technology related with manipulation of small amount of fluid down to $10^{-9} - 10^{-18}$ litres [142]. As a science, it involves chemical studies which serves to the material for the formation of channels with length scale from 10 μm to 100 μm. It allows a platform for many experimental studies of fluid mechanics on micro scale [125]. As a technique, it provides a large number of advantages for biological, chemical, physical applications. Its advantage relies on the characteristic of being tiny, which allows the economy of expensive reaction agents, reduced reaction time resulted from small diffusion length, limitation of exposure to hazardous chemicals. In addition, it offers precision to the analysis in molecular level, that cannot be achieved by large scale experiments. A thorough description of droplet microfluidics including channel fabrication technology, droplet production technology, manipulation methods and applications can be found in the review of Teh et al. [130]. Microfluidics has been going through a fast developing period in laboratories, and some of the conceptions have been realised into industrial products.

1.1 Device Fabrication

Since the 1990s, many efforts have been contributed to the fabrication of microfluidic devises, which are suitable for chemical and biological analysis. Polymers have been largely incorporated into these technical improvements. Bayer and Engelhardt [7] studied organic polymer capillaries for electrophoresis (CE), they tested PBTP, ethylene/vinylacetate, PMMA, and nylon for their suitability as column material in CE. Their various surface properties are applied for analysis of different chemicals. UV laser photoablation method was used to produce channels in polystyrene, polycarbonate, cellulose acetate and poly(ethylene terephthalate) [112]. The thus formed channels surfaces are demonstrated to generate electroosmotic flow in cathodic direction. The Injection-Molded plastic substrates [113] is developed and used for electrophoretic seperations of DNA with high resolution within less than 3 mins. The strategy of production consists in firstly solution-phase etching a silicon wafer, secondly electroforming a mold in nickel from the silicon mask, lastly forms acrylic substrates from the nickel mold. The X-ray lithography is performed on PMMA to fabricate microelectrophoresis devices [49]. The most widely used material is developed by Mcdonald et al. [90], which consists in PDMS molded from a silicon wafer, that with designed channel geometry realised by photolithography. The advantages of PDMS channel rely on its optical transparency which allows a number of detection schemes (UV absorbance and fluorescence emission); on its nontoxic characteristic and its compatibility with mammalian

cells implanted in vivo; its elastomeric property, which allows molding without damaging the mold; the possibility of patterning the surface by properly-controlled techniques. It is demonstrated to be applied in a wide range of chemical and biological works, such as electrophoresis, cell-sorting and DNA analysis. A substitution of PDMS channel is recently developed, by using the NOA (UV-curable polymer) [5]. This kind of material is proved to be controllable on hydrophilicity [45]. The rigidity of the NOA channel allows experiments with high pressure without deformation. However the fabrication procedure is more complicated than that of PDMS. Very recently, there emerges paper-based microfluidics, aiming to achieve simple and cheap analytical devices for diagnostics in developing world [89].

1.2 Application

1.2.1 An alternative to study fluid physics on micro and nano scale

Microfluidics has attracted the attention of fluid physicists, on the fluid boundary condition problem [78]. The classical fluid dynamics assumes no-slip of fluid on solid surface. However, since the surface patterning technology progresses, various of surface properties such as super-hydrophobic surfaces, surfaces with adsorbed surfactant molecules have emerged. Many experimental and theoretical studies put the no-slip boundary condition on interrogation. Microfluidics based on PDMS, due to its optical transparency combined with high resolution detection devices, offer a strategy to illustrate the fluid motion within $10nm$ to $1\mu m$ close to the solid surface. In addition, due to the possibility of patterning solid surface within the channels, microfluidic offers wonderful tools, from device preparation to fluid motion testing.

The first part of this thesis is contributed to the study of fluid slippage on solid surfaces, by using the Total Internal Reflection method and detection of motion of passive tracers.

1.2.2 Droplet microfluidics

Droplet microfluidics has been quickly developed as an alternative tool in chemical and biomedical applications [142]. The development of various control technology has facilitated the production of droplets with high through put and monodispersity, which provides a new platform for the paralleled procedure of chemical reaction and bioanalysis. The associated droplet manipulation technology such as sorting, fission and fusion have equally been investigated. In this section, the applications of droplet microfluidics in various fields are briefly reviewed, with an accentuation on techniques of droplet production.

1.2.2.1 Facilitated chemical and biological analysis

One of the highly developed contributions of droplet microfluidics is to the high throughput screening. In the single cell experiments [21], the micro-environment of cells are produced in the forms of droplets with different codes. Cells are encapsulated into the micro-environments via a fusion by electrodes, and subjected to incubation. Assays are carried out and coding is read afterwords. Droplets provides a comfortable compartment for the

mammalian cells and even multicellular organisms to grow [29]. Droplet based microfluidic also offers platforms for screening of protein crystallization [152], screening of drugs, such as detection of contaminants and residue analysis [67], and screening of bioactivity coupled with chromatography and mass spectrometry [36].

Another important area of application finds the cell biology. The meaning of microscale techniques for cell biology assays is reviewed in [101]. Microfluidics is capable to realise a chemical concentration gradient, which aims to detect cell behaviour in the presence or absence of specific soluble factors [72]. This technology is based on mixing of streams contain different soluble via diffusion. Microfluidic chamber also provides an ideal compartment for cell culture [73, 148, 149], stimulation substantial can be brought to cells by either diffusion or convection and controlled temporally and spatially, factors such as cell density, growth factor and migration direction can be investigated.

Microfluidcs systems contribute to precise control and detection of chemical and molecular biological reactions [41]. This ability is based on mixing technologies developed by various geometrical design, for example the diffusion between two laminar streams, the chaotic mixing in zig-zag channels at high Re [91], and the 3D mixing for intermediate Re [85]. Once mixed, chemical reactions can be performed within well controlled thermal condition, due to the reduced thermal masses and high surface-to-volume ratios [44, 95, 143]. Microfluidics provides a more efficient and fast alternative for DNA amplification via polymerase chain reaction (PCR), as small volumes can be heated or cooled within a few milliseconds. The continuous-flow PCR which offers ultra-fast DNA amplification, is based on moving continuously samples through multiple reaction zones at specific temperature [117]. Following the development of microfluidic devices such as mixer, valves and pumps and the associated temperature and electronics controlling techniques, integrated chips which serve to whole-round reactions can be envisaged [86].

Since the above mentioned applications are based on droplet microfluidics, production techniques of droplets is crucial. The chemical and bio-analysis sometimes require specific droplet size and monodispersity. In the next section, the mostly utilized techniques in droplet production are discussed.

1.2.2.2 Production of drops by microfluidic technology

The principal of droplet production consists in the realisation of an emulsion between two immiscible fluids, with dispersed phase suspended in continuous phase, and stabilised by surfactants. Conventional methods relied on the macroscopic agitation, which leads to highly polydispersed droplets. Since the study of chemical reactions and bio-sensing require accurate dosing, microfluidic which provides strict control of droplet volumes has become an overwhelming technology for droplet production. Among the most widely adapted methods, dielectrophoresis and electrowetting on dielectric are dominated by electrical force and surface tension. Whereas the T-junction, flow focusing and step-emulsification are subjected to the balance between viscous force and surface tension. The step-emulsification is what we believe the most efficient method to generate droplets, its details are described in its chapter. In the following section, the T-junction and flow focusing which seems most closely to the step-emulsification are introduced.

T-junction.
Continuous phase is injected into the main stream channel, and the dispersed phase into a channel perpendicular to the main stream channel, droplets are formed at the intersection of the two channels. This method allows monodispersed droplets, and the result is reproducible. The droplet size and delivery frequency can be controlled by tuning the pressure or flow rate of continuous and dispersed phase, viscosity of two phases, as well as the geometry of channels [98, 145]. Different models have been proposed to explain the physics of droplet formation at a T-junction. One relies on the balance between shear stress applied by the continuous phase on the emerging dispersed phase, and Laplace pressure due to curvature of dispersed phase formed at the corner of T-junction [132]. The experimental observation leads to the fundamental image of the model, that the dispersed phase emerges from its channel, and forms a "head" in the main stream channel. The "head" stays stable whereas droplets are formed in a more downstream position (fig1.1 left). The droplet size can be predicted from the balance between shear stress $\sigma = \eta\epsilon$ and Laplace pressure $P_L = \frac{2\gamma}{r}$, where η the viscosity of continuous phase, ϵ shear rate, γ surface tension between two phases, resulting in $r \sim \frac{\gamma}{\eta\epsilon}$. This model is valide for relatively high capillary number, when the flow rate of dispersed phase is high enough for keeping the "head" stationary in the main stream channel. However at low Ca, the droplet formation can no longer be considered as been sheared off from the dispersed fluid, Garstecki et al. [53] proposed that the the dominant contribution to the dynamics of break-up arises from a pressure drop between continuous phase and dispersed phase, due to increasing resistance in the carrier flow when the dispersed phase fills the carrier channel (fig 1.1 right). The procedure is identified into four steps. Firstly, dispersed phase is pushed into the main stream channel, with pressure on the tip P_d imposed by pressure controlling set up and kept constant. The main stream channel is filled gradually by the dispersed phase, leaving a path with width ϵ (fig 1.1 right) for the continuous phase. This fact increases hydrodynamic resistance of continuous phase, and the pressure P_c increases, which pushes the dispersed phase to elongate. A drop is formed when the dispersed phase is cut off by continuous phase. The elongated length $\frac{L}{w} = 1 + \alpha\frac{Q_{in}}{Q_{out}}$, where w the channel width, α a geometrical factor which can be deduced from fitting with experimental results, Q_{in} and Q_{out} relatively flow rate of dispersed and continous phase.

Flow focusing.
Flow focusing technology in microfluidics has been frequently applied in production of not only liquid droplets [3, 88, 128, 129], but also in micro bubbles [42, 52, 146] and complex structures such as polymerized bead [98], fluid emulsion wrapped by ionic liquid [140], and double emulsions [97]. Different geometry of micro channels are designed, while relying on the same principal, that both continuous phase and dispersed phase are going through a confined area, either a cylinder orifice [128] or a rectangular [3], droplets are formed at the outlet of the confined geometry (fig 1.2). The advantages of flow focusing relies on the symmetric shear the continuous phase on dispersed phase, which generates smaller possible droplet diameter down to 100 nm [129], and narrower distribution of droplet size. Droplet size can be changed by tuning the flow rates of both phases, and high throughput of droplet can be achieved by increasing the flow rate of dispersed phase [128]. Anna et al. [3] have varied a whole range of flow rates and drawn a phase diagram, where distributed droplet

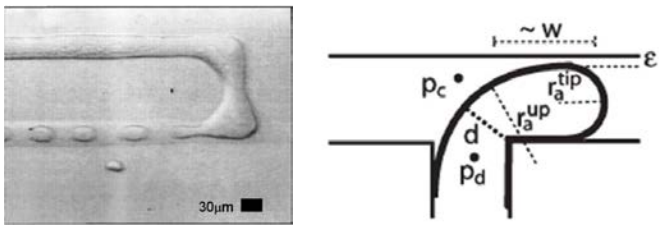

Figure 1.1: Droplets produced from T-junction. Droplets formed from a stationary "head" of dispersed phase (left), resulted from balance between shear stress and Laplace pressure, from [132]. Droplets formed at the intersection of T-junction, due to increased pressure between continuous phase and dispersed phase, caused by increasing resistance in the main stream channel (right), from [53].

diameters close to size of orifice and those much smaller than orifice, monodispersed and polydispersed droplets can also be corresponded to specific flow rates. In terms of controlling technology, pressure control is compared with flow rate control in [141]

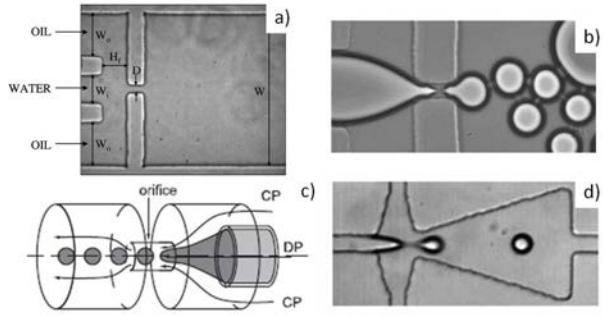

Figure 1.2: Different micro channel design of flow focusing from [3] (a,b), from [128](c), from [129](d). Both continuous phase and dispersed phase are going through a confined area, droplets are formed in the outlet.

The formation of micro bubbles by flow focusing have attracted particular attention of both experimentalists and theorists [42, 52, 145]. Gañán-Calvo and Gordillo [52] studied the physics of the breakup of gas flow, where they distinguished a region of gas filament in steady state in the upstream of breakup point, and another region close to breakup point as absolute unstable. They arrived to predict the diameter of droplets, which is independent from both flow properties such as viscosity, but depending on ratio of flow rate: $d_b/D \simeq (Q_g/Q_l)^{0.37\pm0.005}$, where D the diameter of orifice, Q_g and Q_l relatively flow rate of gas and liquid. This prediction agrees with experiments. Dollet et al.[42] reported that the formation of bubbles by flow focusing in a rectangular channel depends strongly on channel aspect ratio, an abrupt change of the aspect ratio caused break up of dispersed phase filament. The pinching kinetics is identified as a linear collapse, followed by a fast 3D pinch-off. By fitting the 3D pinch-off by $w \sim t^{1/3}$, they comes to the conclusion that the final phase of pinching is driven by inertia of both gas and liquid, instead of capillarity. This work is similar to some extent with step emulsification, due to the fact that droplets formation is caused by a sudden change of aspect ratio. However, it differs from step emulsification

method, because the aspect ratio does not reach the request of Hele-Shaw cell, that the gas filament may not be sufficiently stabilised by the fact of confining.

1.2.3 Capacity of modeling networks in cores for petroleum application

The production of microfluidic channels is capable to realise complex 2D or 3D networks following the design. A cross-section extracted from a core sample which is porous media, can be replicated on microfluidic chips. So far the experiments done to study motion of oil and aqueous solution through the cores are carried out en macro scale, retention of any components in the porous media is measured at the exit of the core, no detailed distribution of retention can be visualized. PDMS microfluidics due to its optical transparency allows the illustration of fluid motion locally in the network. This pushes the petroleum study into a micro or nano scaled field.

1.3 The objectives and organisation of thesis

The thesis is separated into three parts:
• The first part is contributed to the study of fluid slippage on solid surface with controlled hydrophilicity, using the Total Internal Reflection illumination and tracing passive fluorescent particles motion. Some factors physically bring biases to the results, such as Brownian motion, fluid shear effect, and electrostatic interactions between particles and charges solid wall. Some factors technically influence precision of result, such as fluorescent particles photo-bleaching effects, and the focal depth of the objective. In this study, all of these factors are taken into account during a Langevin simulation, which corrects the bare velocity profile. Viscosity is determined by fitting linearly the velocity profile, and compared with results measured by conventional rheometers. Slip length is determined by extrapolating the velocity profile to zero velocity. We innovate an experimental method to determine precisely position of the wall. Both the viscosity and slip length are determined with higher precision than the state of the art. Slip lengths on different surface wettability are distinguished for the first time.

• The second part is concentrated on the physics of drop production at a step. We use microfluidic technology to fabricate a channel, where fluids flow from a shallow channel into a deep pool. If two immiscible fluids are flowing parallel with each other, droplets can be formed at the intersection of shallow channel and deep pool. The driven factor of droplet formation is capillary effects. A. Leshansky has built a theoretical explanation to predict drop formation dynamics and droplets size, it also illustrates a phase transition between small droplets phase and large drops phase, as function of capillary number and aspect ratios. Experimentally, we collaborate with Leshansky to understand the physics of drop formation at the step. Our experiments have supported his theoretical study.

• The last part concerns a project sponsored by petroleum companies, they would like to develop new technologies to improve oil recovery process, since actually the quantity of recoverable oil stays 1/3 of the total capacity of the reservoirs. They want to inject nano particles into porous media underground, to let them collect information on oil geographical

distribution and quantity. The whole project is divided into three groups. The first group is in charge of conventional numerical simulation in petroleum field; the second group synthesises the nano particles which are capable to retain information on oil distribution and quantity. Our lab is in the third group, we built a micro model which simulates the porous media of rocks using microfluidic technology, the typical dimension of the channel size is 1 μm. Nano particles are injected into our model to observe in real time the penetration of these particles into networks, as well as their retention process.

Part I

Experimental study of slippage of Newtonian fluids and polymer solution

Chapter 1

Presentation of the state of the art

1.1 Slippage of Newtonian fluid

1.1.1 Theoretical expectations

Classical fluid dynamic problems consist in solving the partial differential equation Navier-Stokes equation for impressible flow

$$\rho(\partial_t + \mathbf{u} \cdot \bigtriangledown)\mathbf{u} = - \bigtriangledown p + \mu \bigtriangledown^2 \mathbf{u} \tag{1.1}$$

with the mass conservation equation for incompressible fluid: $\bigtriangledown \cdot \mathbf{u} = 0$. Most of the studies in the history have assumed that the fluid on the liquid-solid boundary satisfies the no-slip condition, that means the fluid velocity in three components equals to that of the solid in direct contact with it. By solving the Navier-Stokes equation, velocity profile of a laminar flow in a cylindrical pipe expresses in a parabola shape: $v(r) = -\frac{1}{4\eta}\frac{\Delta p}{\Delta x}(R^2 - r^2)$, with R radius of the pipe, and r the radial variable. The experiments in this thesis consist in using an Hele-Shaw cell (fig 1.1) and measure velocity profile. In such a geometry, the height of the channel is much smaller than width and length. Velocity profile assuming no-slip boundary condition is a parabola in the direction of smallest length scale:

$$v(z) = -\frac{1}{2\eta}\frac{\partial p}{\partial x}[(\frac{h}{2})^2 - z^2] \tag{1.2}$$

where h height of the channel, z the vertical variable. The shear stress and shear rate on the boundary express relatively $\sigma_w = \frac{\partial p}{\partial x}\frac{h}{2}$, $\dot{\gamma}_w = \frac{\sigma_w}{\eta}$.

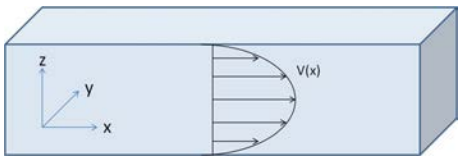

Figure 1.1: Laminar flow in rectangular channel.

Since recent years, many experimental studies have revealed apparent slippage of incompressible fluid on solid surface. These measurements delivered by elaborated precise method down to micrometric scale or nanometric scale, have challenged the assumption of no-slip

boundary condition, and restimulated many experimental, numerical and theoretical interests on it. A review of the methods of study, and discussion of the results is found in [78].

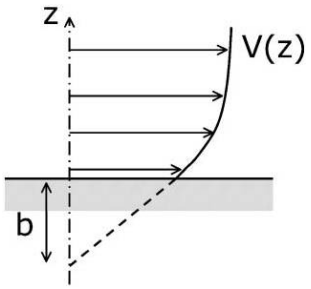

Figure 1.2: Schematic representation of the definition of the slip length b, from [12].

The theoretical studies of slip length are reviewed in [12, 78]. The geometrical definition of slip length is illustrated in fig1.2. b is the length into the solid where the velocity profile is extrapolated to zero. If the fluid velocity in direct contact with the surface is positive value, then b is a positive slip length. If the fluid is stagnated on the solid surface, or there exists a discontinuity of velocity profile in the fluid, the slip length is negative. Slip effect is proven to be tightly related with interfacial properties, by definition, slip length is dependent on a friction coefficient λ: $b = \eta/\lambda$, with η the fluid viscosity. A scaling estimation of slip length is proposed by Sendner et al.[119]. The Green-Kubo equation which relates the friction coefficient with the friction force can be estimated by $\lambda \approx \frac{1}{Ak_BT}\langle F_f^2\rangle_{equ} \times \tau$, where A is the lateral area, F_f is the total microscopic lateral force acting on the surface. τ is the typical relaxation time approximated as $\tau \sim \sigma^2/D$, with σ the microscopic characteristic length scale, and D the diffusion coefficient in the fluid. Friction force on the surface depends on interaction energy on molecular level between liquid and solid, and the rms force is estimated as: $\langle F_f^2\rangle_{equ} \sim C_\perp \rho\sigma(\epsilon/\sigma)^2$, with $C_\perp$ a geometrical factor representing roughness at the atomic level. Thus slip length b can be approximated as

$$b \sim \frac{k_BT\eta D}{C_\perp \rho\sigma\epsilon^2} \tag{1.3}$$

This scaling is proved in good qualitative agreement with molecular dynamics simulation [12, 119]. The molecular dynamics is a widely used theoretical approach to investigate fluid boundary motion [4, 11]. Its principle is based on integrating in time a series of Newton's laws, each equation corresponding to one single atom or molecule:

$$m_i \frac{d^2 r_i}{dt^2} = \sum_j F_{ij} \tag{1.4}$$

where r_i position of the atom number i, m_i the mass of the atom, F_{ij} the interaction force between atoms i and j, $F_{ij} = -\bigtriangledown_i V_{ij}$, with V_{ij} the interaction potential between atoms following Lennard-Jones potential that will be mentioned in next section. Interaction of fluid with solid is studied by adding solid atoms onto the surface, either fixed or coupled with the surface with a large spring constant. Since the contact angle of fluid with solid is highly dependent on the interaction energy between them, it is meaningful to expressed the slip length as a function of contact angle, which is experimentally easy to measure. Such a

result is reviewed in [13] containing a wide range of surfaces (fig 1.3), slip length increases while contact angle increases. A qualitative agreement can be found in a set of experimental work with high accuracy represented on the right figure. However, a quantitative agreement has not be attained. For the numerical simulations, slip length on a surface with contact angle between 100° and 120° is nearly zero, however for the experimental result, it rises up to $10 - 20\ nm$.

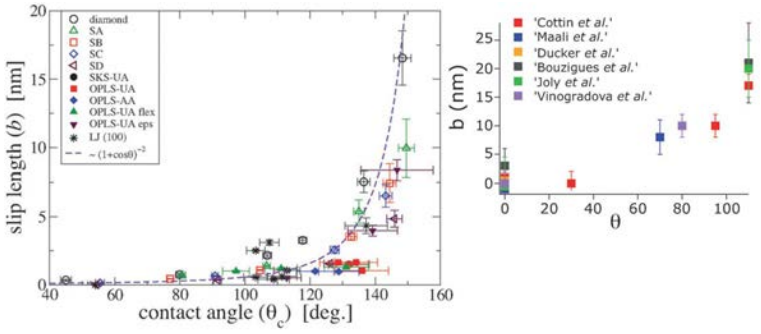

Figure 1.3: Molecular dynamics simulation of slip length dependence on contact angle (left), and experimental results which are in qualitative agreement (right). From [13].

1.1.2 What physical factors influence slippage

1.1.2.1 Roughness

Slip length has been observed to be dependent on the roughness of the solid surface. Numerous studies of flow on surface roughness of either atomic scale [51, 109, 153] or larger scale [94, 153], and either periodic [147] or random distribution of the roughness [66, 77], have reported enhanced [14, 31, 34, 147] or inhibited [66, 94, 107] slipping.

Bonaccurso et al. [14] experimentally measured the hydrodynamic drainage force, which decreases with the increasing slip length while the surface possesses higher degree of roughness. In this study a microparticle is attached to the catilever of an Atomic Force Microscope, the drainage force is measured according to the deflection of the catilever when the particle is subjected to the flow of sucrose solution next to the substrate. The boundary slip length is found to be dependent on the shear rate [34], and roughness of the surface plays a dominate role in determining a critical shear rate for the onset of slip [153]. The observation of increased slip by roughness induced superhydrophobicity has been confirmed and explained by numerical studies [31, 32, 147]. By comparing the free energy of molecules wetting the wall with those dewetting [32], slipping may occur when the following condition is satisfied $P < \gamma(1+rcos\theta_c)/a$, which, P the fluid pressure, γ surface tension of the fluid, r the ratio of real to apparent surface, θ the contact angle, and a the height of roughness element. So that for a given pressure, slipping can be induced by hydrophobic surface created by roughness, with small enough roughness height. Air bubbles have long been suspected to be the reason why slip occurs more easily on hydrophobic surface than on hydrophilic ones[39, 138]. Vinogradova [138] reported that the generation of air bubbles near the hydrophobic surfaces is caused by the enhanced concentration of gas-filled submicrocavites, which is closely related to the long-range hydrophobic interaction.

In comparison, other studies concluded that the presence of roughness suppresses slip. One of the physical reasons consists in dissipating mechanical energy at the scale of roughness, and thus increases the hydrodynamic resistance [78]. Another reason relies on the shift of effective surface position due to the presence of roughness [94]. Jansons [66] in his theoretical work studies the situation where a viscous fluid flowing on a solid surface with defects, but satisfies no-slip boundary condition in microscopic scale. These defects induce a macroscopic slip length: $\lambda \sim a/c$, where a is size of the defect, and c is fraction of the roughness. Lauga et al. [78] in their review used a simple scaling law which balances the disturbance flow created by the defects with local Stokes drag on a defect, found the same result. When c is of the order 1, the slip length has the same order as roughness size, and the situation converges to no-slip boundary condition. Ponomarev et al. [107] suggested a replacement of the layer near roughness by a stick slip layer. They obtained an effective hampering of hydrodynamic flow by the roughness, and their study of viscosity close to the surface pointed out an additional resistance in the stick layer near the roughness.

1.1.2.2 Wetting

It is widely accepted that slipping is closely related with wetting, which itself is a consequence of solid-liquid interaction at molecular scale. The phenomena of wetting is concretely discussed in [40]. The fact of wetting is descried by the spreading coefficient $S = \gamma_S - \gamma - \gamma_{LS}$ which is the difference between surface energy of an non-wetted solid surface with that wetted by the liquid. $S > 0$ represents the situation that the solid surface is totally wetted by liquid layer, while $S < 0$ means it is partially wetted. The degree of partial wetting is quantified by contact angle $\theta_c = \dfrac{\gamma_S - \gamma_{LS}}{\gamma}$.

Numerical simulations have been processed to study the influence of molecular interaction between liquid and solid on slipping effect [32]. The interactions are of Lennard-Jones type, with potential

$$V_{ij}(r) = \epsilon[(\frac{\sigma}{r_{ij}})^{12} - C_{ij}(\frac{\sigma}{r_{ij}})^{6}] \tag{1.5}$$

which σ molecular diameters, C_{ij} the interaction coefficient between two atoms i and j. The effect of interactions on contact angle is estimated by Barrat and Bocquet [4] in their work of partial wetting surfaces:

$$cos\theta = -1 + 2\frac{\rho_S C_{LS}}{\rho_L C_{LL}} \tag{1.6}$$

with ρ_S density of solid, and ρ_L that of liquid. In this work the density of the fluid molecules is found to be even in the bulk of fluid; whereas the density profile oscillates in the vicinity of the solid surface, indicating an heterogeneous distribution of fluid molecules. The slip length is found to be increased with a decreasing interaction coefficient between the liquid and solid.

In terms of theory, Tolstoi's molecular kinetics theory discussed the effect of surface energy on slip [133], it is review in [78]. Tolstoi relates the molecular diffusivity $D \sim \sigma V$ with surface energy $\gamma\sigma^2$, which σ is typical molecular size, V typical molecular displacement velocity, γ the surface tension. By considering the motion of fluid molecules, the energy consumed for the fluid to create a void position of size σ is actually the cost of surface energy. Since the surface energy of the system in the fluid bulk is different from that at the

vicinity of fluid-solid interface, the distribution of fluid molecules near surface is changed. He concluded that in total wetting system, the no-slip condition is satisfied with molecular scale uncertainty. However in partial wetting case, it comes to slip length which can reach orders of magnitudes larger than molecular size:

$$\frac{\gamma}{\sigma} \sim exp(\frac{\alpha\sigma^2\gamma(1-\cos\theta_c)}{k_BT}) - 1 \tag{1.7}$$

where α is a dimensionless geometrical coefficient. Blake [10] considered and extended Tolstoi's work, by taking into account adsorption of liquid on solid surface, in which case there is not only no-slip condition, but even more the no-slip condition occurs on a plane in the fluid. This phenomenon called "negative slip length" is illustrated on velocity profile as zero velocity extrapolated to positive Z position. It is due to strong interaction between solid surface and liquid molecules, especially in case of complex fluids.
Another theory developed by Bocquet and Barrat [11] relies on Onsager's hypothesis of linear regression of fluctuations, and use the fluctuation and dissipation theorem to derive the slip length. For different status of surfaces, the time dependent correlation function is computed, and compared with molecular dynamic simulation. The comparison leads to the determination of slip length and other fluid parameters. The slip length is given by a scaling law [78] as

$$\frac{\lambda}{\sigma} \sim \frac{D^*}{S_t c_{LS}^2 \rho_c \sigma^3} \tag{1.8}$$

where D* the normalized diffusion coefficient by the bulk diffusivity, S_t expressed the structure property of the surface, c_{LS}^2 the Lennard-Jones potential coefficient between solid and liquid. This relation reveals the nature that slip length vanishes with increasing interaction coefficient between liquid and solid.
Experimentally, the dependence of slippage on wetting property is presented by slip length vs. contact angle, which is a relatively easily controlled condition. Some of the most accurate measurements are collected in fig 1.3.

1.1.2.3 Shear rate

It has been found in several experiments that slip length is shear rate dependent. Hydrodynamic drainage force of a borosilicate sphere approaching a flat surface has been measured [34, 96], the degree of boundary slip is found to be dependent on viscosity and shear rate. The shear rate dependence of slip can be suppressed by adsorption of surfactants on the surface [60].

1.1.3 Applications of slippage

1.1.3.1 Increased permeability and reduced hydrodynamic dispersion

The presence of slip effect allows generation of enhanced permeability in porous media. In a pressure drop flow, when there is slip, the velocity of fluid is increased by a factor $1+6b/h$ compared with no slip, with b is the slip length, and h the channel characteristic length [12]. Petroleum discovery can take advantage of the slip phenomenon and inject fluids which slip on rock surfaces into the underground, so that with a constant pressure application, fluids can go further and faster. The slip efficiency can be estimated as b/h, the effect of

increased permeability becomes significant in fluid path with sub-micrometric dimension. Besides, presence of slip reduces dispersion of components (molecules, particles) in the fluid. High dispersion close to interface is due to non-slip boundary condition, where the relative difference of velocity $\Delta V = (v_{max} - v_{min})/v_{max}$ is maximized. However, this is reduced to $\Delta V = (1 + 4b/h)^{-1}$ for slipping channel [12].

1.1.3.2 Enhanced interfacial transport

Flow can be driven in a channel not only by pressure gradient, some alternative methods can generate flow at the interface of fluid and solid, this effect realises the interfacial transportation. With the presence of hydrodynamic slip, transportation can sometimes be largely facilitated. Taking the example of **electro-osmosis** [69], in which case the flow is generated by an electric field. Due to charged solid surface in contact with fluid, particles and molecules with charges in the fluid are reorganized geometrically, and form a electrical double layer near the surface. This layer is characterized by a length scale called Debye length λ_D, outside this layer the environment is electrically neutral, while inside there is an electrical potential. The fluid motion induced by stream-wise electrical field is restricted into the double layer. The velocity of a charged particle is determined by the balance between electrical force $f_e = q \cdot E = \epsilon \dfrac{V_0}{\lambda_D} E$, and the viscous drag in the fluid $f_\eta = \eta v_{eo}/(\lambda_D)$, ϵ being the dielectric permittivity of the fluid, V_0 the potential of solid surface, η the viscosity. With the presence of hydrodynamic slip, the balance transforms to:

$$\eta \frac{v_{eo}}{\lambda_D + b} \sim -\epsilon \frac{V_0}{\lambda_D} E \tag{1.9}$$

With the definition of electro-osmosis mobility $v_{eo} = -\dfrac{\epsilon\zeta}{\eta} E$, Zeta potential ζ which characterises the transport ability is expressed by:

$$\zeta = V_0 (1 + \frac{b}{\lambda_D}) \tag{1.10}$$

The amplification of interfacial transport is estimated by b/λ_D, which may be orders of magnitudes large.
The above idea can be generalised to **diffusio-osmosis** and **thermo-osmosis** [1, 2]. Taking the example of diffusio-osmosis, flow at the interface is generated by a concentration gradient of solutes, which are under short range interaction with the interface. The solutes are attracted to the surface, and squeeze the fluid in the direction opposite to the concentration gradient to reach a velocity v_s:

$$v_s = -\frac{1}{\eta} \Gamma L (1 + b/L) \frac{dc}{dx} \tag{1.11}$$

with $\Gamma = \int_0^\infty dy \cdot \dfrac{\partial \Sigma_{eq}}{\partial c}(y)$, and $L = \Gamma^{-1} \int_0^\infty dy \cdot y \cdot \dfrac{\partial \Sigma_{eq}}{\partial c}(y)$, these are length scales related with stress anisotropy, $\Sigma_{eq} = \sigma_n - \sigma_t$. L is a measure of thickness of stress-generating interface, which depends on concentration gradient (fig1.4). With presence of slip, interfacial velocity is amplified with factor b/L, which can be significant. In terms of **thermo-osmosis**, flow is generated by temperature gradient, and velocity follows the form of equation 1.11.

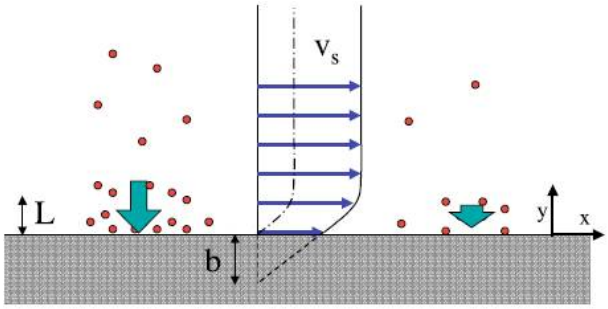

Figure 1.4: Schema of diffusio-osmosis. Solutes interact with solid surface in short range and vertically, they are attracted to the surface and form a concentrated layer with characteristic thickness L. Due to concentration gradient close to the surface, fluid is expelled in the opposite direction.

1.2 Slippage of polymers

The study of polymer flow along solid surface has significance in industrial production. For instance in the polymer extrusion procedure, flow instabilities have been observed at given shear stress range. Kalika and Denn [71] studied capillary extrusion of polyethylenes, and reported oscillation on throughput of the extruder at certain range of pressure. The oscillation is attributed to the imperfections of the surface, which induces the *stick-slip* phenomenon of the polymer flow. Vinogradov et al. [137] studied flow of polybutadiene melts and reported that above a critical shear stress the throughput of extruder jumps to a higher value, this phenomenon of *spurt* is a macroscopic interpretation of polymer slippage. The theoretical expectations and experiments on the polymer-surface interaction and its influence on polymer slippage are reviewed by Leger et al. [79].

1.2.1 Formation of polymer layer on solid surface

The discussion of polymer slippage is based on the formation of a polymer layer on the surface. The layer can be formed by chemical methods [79], by grafting the end of polymer chains with high density onto chemically treated surfaces. In the case of an attractive surface, no chemical method is needed to produce irreversible adhesion. Taking the example of PDMS melt on silica surface, polymer chains form hydrogen bonds between silanol sites of silica surface and the oxygen atoms of the backbones. The adsorption is irreversible, and allows the thickness of formed layer $h \sim N^{1/2}\phi_0^{7/8}$, where N the index of polymerization, and ϕ_0 the polymer volume fraction. To the contrary, the reversible adsorption is based on thermodynamic equilibrium near the surface, where polymer chains exchange permanently between the solid surface and the bulk [38].

Polymer molecules adsorbed on solid surface increase flow resistance, thus reduce flow rate in the capillary. Reported works utilized this fact to measure the effective hydrodynamic thickness e_H of adsorbed layer, according to equation: $e_H/R = 1-(Q_a/Q)^{1/4}$, where R the radius of the capillary, Q_a and Q the flow rate after and before the adsorption of polymer respectively [30]. De Gennes [38] constructed equilibrium concentration profile of polymers near the wall, and characterised the wall by the "free energy of sticking", which is negative

for adsorption and positive for desorption. He concluded that the effective hydrodynamic thickness depends on the largest loop of the adsorbed chain, which scales like the gyration raduis of a free polymer chain in solvent.

Previous works suggested that the presence of polymer chain on the solid induces surface roughness and suppresses slip [106, 153]. This fact expressed on the velocity profile of polymer solution close to the wall as a negative slip length [14]. Since then, no detailed work has been done in order to determine the exact negative slip length of polymer solution on the wall with satisfactory precision.

1.2.2 Theoretical and experimental study of polymer slippage on solid surface

The widely accepted theory about polymer slippage on an interface is that developed by de Gennes and Brochard [20], they assumed a situation that shear induced polymer melt flowing above a solid surface with grafted polymer chains. The density of grafting is small so as to avoid interaction between the grafted chains. Without applying a shear stress to the flowing polymer, the conformation of the tethered chains is dominated by entropy, and exist in shape of mushrooms. Once been applied a shear stress σ, the state of entanglement and disentanglement between flow polymer and grafted chains induces different slip length and surface velocity. Three regimes have been distinguished. At shear stress smaller than a critical shear stress σ^*, the flowing system is under entangled regime. The structure near the surface can be approximated as a cylinder with length L and diameter D, which consists of the elongated tethered chain with a number of flowing chains entangled with it. This situation can be described by equating the elastic force $F_{el} = \frac{3kT}{R_0^2}L$ with viscous force $F_{vis} = \eta V(R_0^2 + L^2)^{1/2}$, with R_0 the entropy dominated coil size of grafted chain, and V the velocity on the surface (i.e. the slip velocity). The elongation L increases with surface velocity, until the state of entanglement is not stable any more, this critical surface velocity is $V^* = \frac{kT}{\eta Z a^2}$, where Z the index of polymerization of the tethered chain. At $\sigma > \sigma^*$, a much weaker friction is exerted between flowing chains and tethered ones. The friction can be approximated as a sum of contribution of single monomers according to Rouse model. By equating this friction with elastic force, the smaller elongation L_R is obtained with $L_R = L^*\frac{V}{V_1}$, where $V_1 = V^*\frac{\eta}{\eta_1 N_e^{1/2}}$, with η_1 the viscosity of liquid of monomers, N_e the number of entanglement of tethered chains. In this marginal regime, flowing chains disentangle and re-entangle with tethered chains, resulting in a jump of surface velocity at critical shear stress. In the regime of strong shear flow, the shear stress grows even higher, the flowing chains disentangle with tethered chains, the slip velocity continues increasing with shear stress, but the slip length stays independent from the slip velocity. The force balance which describes the three regimes is summarized by [20]:

$$k_m V + \frac{\nu kTL(V)}{R_0^2} = \sigma = \eta\frac{V}{b(V)} \tag{1.12}$$

where $k_m V$ is the monomer friction in Rouse model. The relation between shear stress and surface velocity, and that between surface velocity and slip length are plotted in fig 1.5. Since de Gennes and Brochard considered Newtonian fluid, there is direct correspondence

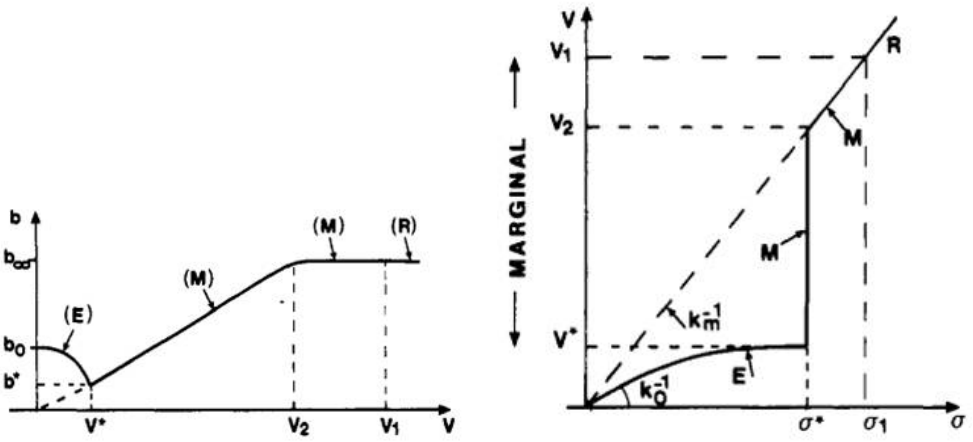

Figure 1.5: slip length vs surface velocity (left) and surface velocity vs shear stress (right) for entangled regime, marginal regime and disentangled regime. From [20].

between shear stress and shear rate. Mhetar and Archer [92] took into account the changes in configuration and relaxation dynamics of the tethered chains, and proposed a more sophisticated model in qualitative agreement with that of de Gennes and Brochard, but instead 5 regimes are identified.

The prediction of 3 regimes have been confirmed by experiments [61, 79, 92]. Hervet and Leger used Near Field Laser Velocimetry to detected velocity of flowing polymers, subjected to a Couette shearing. The upper plane with non zero velocity is grafted with large density to avoid slippage, the lower plane keeps immobile and is grafted with PDMS chains to investigate the slippage of flowing polymer, and their interaction with the grafted chains [61]. Results are slown in fig 1.6. At low velocity of upper plane, there always exists slippage on the lower plane, as the measured velocity is higher than its counterpart by assuming no-slip condition (the lower dashed line). Slip length is the extrapolated length which stays independent from slip velocity with a precision of the order of μm. At marginal regime, the entangled chains on the solid surface reach their limit length and disentangle. The chains are restored under elastic force and re-entangle with flowing chains. Both slip velocity and slip length jump to higher values. Finally in disentangled regime, the flow of polymer reacts like a block flow with slip velocity equaling to applied velocity, slip length is independent from slip velocity. During the whole procedure, applied velocity and slip velocity cover several order of magnitudes, whereas the slip length jumps between two orders of magnitudes. Hervet and Leger in turn studied the influence of surface grafting density on the critical shear rate which triggers the marginal regime. There exists a specific grafting density, corresponding to the largest critical shear rate. The explanation is that at small grafting density, chains do not overlap and act independently on the friction with flowing chains. While the grafting density reaches a critical value, the penetration probability of flowing chains into the tethered layer decreases, which makes disentanglement easier. Mhetar and Archer [92] obtained similar results by studying flow of polybutadiene melts over clean silica glass surface. They discovered the critical shear stress on the onset of marginal regime $\sigma^* \approx 0.2 \pm 0.02 G_e$, where G_e is the plateau modulus measured by a rheometer. This discovery allows the determination of σ^* from bulk rheological measurement. All authors

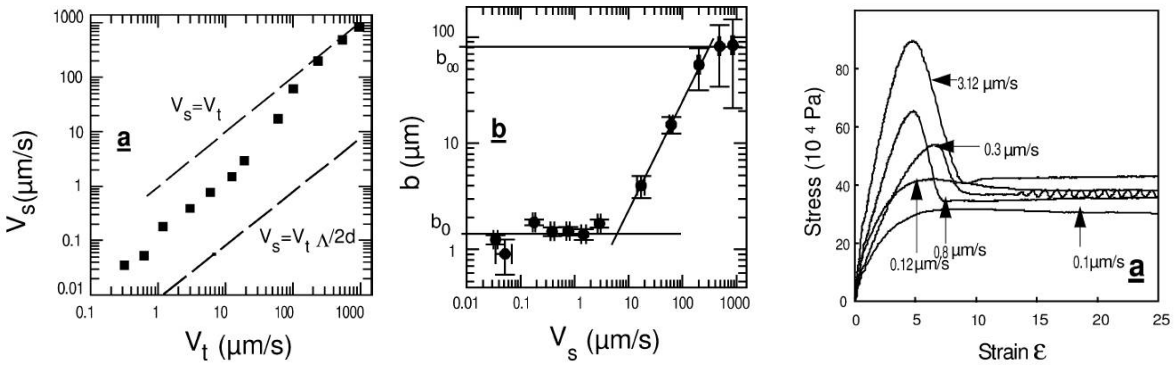

Figure 1.6: Typical results for slip velocity (left) and slip length (middle), of PDMS melt (M_w = 970 kg/mol) flowing on a silica surface grafted with PDMS chains (M_w = 96 kg/mol), and at a fixed surface density. Three regimes are well defined. Oscillation of shear stress at intermediate shear rate in stick-slip regime (right). SBR melt with molecular weight 135 kg/mol flowing on adsorbed layer of SBR chain with molecular weight 50 kg/mol, from [61].

have observed an oscillation of shear stress at certain range of applied shear rate, which is the evidence of the existence of polymer stick-slip motion on the surface, during which the chain disentangle and re-entangle to induce the oscillation of shear stress. Wang and Drda [139] studied pressure driven capillary flow of polymer melt, and confirmed the mechanism of stick-slip is related with the entanglement state between free chains and grafted chains. They identified several factors which influence the slip effect. Firstly, higher temperature makes the critical shear stress at stick-slip transition occurs at higher value. Secondly, the slip length decreases when molecular weight gets smaller. Thirdly, by comparing polymer flow on bare surface with modified surface, They come to the conclusion that the slip of polymer chain is tightly related with process at molecular level between polymer chain and the surface.

1.2.3 Motivation of study polymer slippage on solid surface

Considering the theoretical and experimental studies of polymer slippage on solid surface previously mentioned, the slip length are claimed to be positive in the order of 1 μm at low shear rate. Besides, adsorbed polymer chain on the solid is claimed to induce surface roughness and inhibit slip. The slip length is tightly related with polymer chain interaction with the solid surface (ie. repulsion, adsorption, etc.). TIRF method provides the opportunity to study velocity profile of polymer solution in the area close to solid surface within 500 nm, so that to illustrate polymer behaviour in this zone. One of the aims of this present thesis is to show for the first time 3-D velocity field of polymer solution, and correlate it with the interaction mechanism between polymer chain and solid surface.

1.3 Experimental methods of investigation of slippage

Summary

In this chapter the experimental methods aimed at slip length determination are reviewed.

The indirect methods are based on measurements of quantities which are affected by the presence of slippage. Some of this methods require pre-estimated values of fluid property, which allows the induction of slip length. The most efficient method is based on Surface Force Apparatus [33], which does not need information about fluid property, and provide a resolution of measurement $\sim 2\ nm$. A common backdrop of the indirect methods consists of the impossibility to study flow profile deeper into the fluid, so that these methods are restricted to simple homogeneous fluid. The study of complex fluids which exhibits specific flow profile requires direct methods which allow in-situ measurements.

The direct methods rely on tracking the motion of passive tracers in the fluid. Since the tracers have certain size distribution and possess a number of charges on the surface, their diffusion, hydrodynamic interaction with the fluid and with the solid surface will introduce biases on the measured fluid velocity. Corrections need to be elaborated. The resolution on the direction normal to the solid surface is a principal challenge to overcome in order to obtain highly resoluted slip length. These methods will be discussed in detail below.

1.3.1 Indirect methods

1.3.1.1 Method based on pressure-flowrate measurement

This method is based on the fact that slippage generates a larger flow rate through an orifice or a micro channel while the pressure drop between the entry and the exit is maintained constant. The slip length b can be inferred from the following equation, considering the case of a rectangular cross-sectioned channel [26]:

$$Q = \frac{2wh^3}{3\mu}\frac{\Delta p}{L} + 2hw \cdot u_{slip} \tag{1.13}$$

Where Q is the flow rate, Δp the pressure drop in the channel, w, h, L relatively width, height and length of the channel, μ viscosity of fluid, u_{slip} the slip velocity. The first term on right hand side of equaton 1.13 denotes flow rate of Poiseuille flow, the second term denotes that of slippage. Experimentally, pressure Δp is applied, and flow rate Q is measured, slip length u_{slip} is induced by equation 1.13. The slip length b is calculated by $b = u_{slip}/\dot{\gamma} = \frac{\mu Q L}{2\Delta p w h^2} - \frac{h}{3}$, with $\dot{\gamma}$ the shear rate. By using this method, several studies confirm the theoretical prediction that the fluid does not present slip length on wetting surface; whereas on non-wetting surface with contact angle between $70°C$ and $135°C$, the slip length raises up to positive value, and extends in a large range between 5 nm and 70 nm according to different studies [78]. Choi et al reported water flowing on hydrophobic surfaces with slip length varying linearly with shear rate [26]. Cheng and Giordano studied slip length with some classical fluids flowing in nano pores. The experiments of water show agreement with the non-slipping condition; whereas several organic fluids indicate significant slip length while being confined in nano pores smaller than 100 nm [24]. Cheikh and Koper studied the stick-slip transition of surfactant solution in the nano pores, and found the slip length remains around 20 nm independent from surfactant concentration. The fact of slip is related to the reorganization of adsorbed surfactant bilayers from an entangled structure to independent layer flowing on one another [23].

As indicated by equation 1.13, slip length is deduced basing on the pre-estimated fluid properties such as viscosity, and channel geometry. Repeated experiments has shown a

resolution of slip length at $\pm 5\ nm$ [26]. However, the accuracy of slip length may also be influenced by other facts such as pressure dependent viscosity, viscous heating, and uncertainty on the exact channel height. The method based on flow rate by changing pressure is restricted to studies of fluids with exclusive known parameters.

1.3.1.2 Method based on surface force measurement

The stream-wise hydrodynamic force exerted on a sphere which is approaching perpendicularly to the solid surface with velocity V is expressed by the formula: $F_h = 6\pi\eta r V \frac{r}{h}$ with η fluid viscosity, r sphere radius, h the separation distance. This formula is based on no-slip boundary condition on the surface, however this force may be modulated with presence of slippage [6, 14, 33]. The author applied Vinogradova's theory [138], which incorporated slip boundary condition into the drainage force formula: $F_h = \frac{6\pi\eta r^2 V}{h} f^*$, with f^* a correction factor for slip on both surfaces

$$f^* = \frac{h}{3b}[(1 + \frac{h}{6b})\ln(1 + \frac{6b}{h}) - 1] \tag{1.14}$$

the slip length b is adjusted to fit the experimentally measured drainage force with theory at various value of separation distance. An increasing slip length is found to decrease the drainage force on the sphere, and this fact is more pronounced at higher shear rate and higher viscosity. Cho et al. [25] use this method to study slippage of polar liquid on hydrophobic surface, and find that at high contact angle, the slip length decreases with increasing polar moment of liquid, instead of depending on wetting property.

The advantage of measuring slip length by surface force apparatus consists firstly in high resolution. The displacement of plane and the relative displacement between sphere and plane are determined by nano sensors within resolution of $1\mathring{A}$. Slip length is determined with an error bar of 2 nm [33]. The second advantage is that the hydrodynamic boundary condition does not depend on pre-estimated values of liquid properties such as viscosity, diffusivity of optical tracers. However, this method only provides fluid motion on the surface, but does not deliver velocity profile near the plane surface. For the studies of complex fluids, which may exhibit complicated structure such as block flow or shear banding, the method based on surface force measurement encounters its limitation.

1.3.1.3 Method based on streaming potential

This method consists in using ζ-potential of solid surface on contact with liquid, it has provided a measurement of slip length at 0 nm on wetting surface, and 5-8 nm on partial wetting surface with contact angle $80° - 90°$ [27].
The ζ-potential is defined as the electric potential between the double layer and the bulk. Its important role on the potential $\Psi(z)$ of a position close to the surface is given by:

$$\Psi(z) = 4k_BT/e\tanh^{-1}[\tanh(e\phi_0/4k_BT)]exp(-z/\lambda_D) \tag{1.15}$$

where ϕ_0 the surface potential, considered as ζ-potential if the double layer is approximated as part of the particle. λ_D the Debye length [65]. λ is a characteristic length which describes

the extend of electronic double layer. It is strongly dependent on charge distribution near the surface:

$$\lambda_D = (\frac{\epsilon_r \epsilon_0 k_B T}{\sum_{j=1}^{N} n_j^0 q_j^2})^{1/2} \tag{1.16}$$

where ϵ_r the relative dielectric constant, $\epsilon_0 = 8.85 \cdot 10^{-12} F/m$ the dielectric constant in vacuum, n_j^0 mean concentration of charge of species j, and q_j the number of charges of species j.

The ongoing of an electrolyte flow in a capillary induces a convection of ions in the direction of the stream, which generates currant and potential. By connecting the entrance and exit of the capillary with two electrodes which are integrated into a electrical circuit, the potential and current corresponded to each pressure drop in the capillary can be measured. The streaming potential is the potential extrapolated to zero net current, it is expressed by Helmholtz-Smoluchowski equation:

$$\Delta E = \frac{\epsilon_0 \epsilon_r \zeta}{4\pi\eta K} \tag{1.17}$$

Where $K = l/\pi r^2 R_s$ is the electrical conductivity of the solution in the capillary with length l. With the presence of slippage, the streaming potential is corrected by a factor $1 + \gamma\eta\kappa$, where $\gamma = v_s/\tau_s$ the slippage coefficient, with v_s the slip velocity and τ_s the shear stress on a solid surface, η the viscosity, $1/\kappa = \lambda_D$ the Debye length. Churaev et al [27] used this method to detect variation of slippage following the attachment and detachment of air bubbles on the solid surface.

This method is applicable for slippage of electrolyte solutions on solid surface. Like other indirect methods, it is restricted to homogeneous fluid, and incapable to provide information of local flow near the surface.

1.3.1.4 Method based on TIR-FRAP (Total internal reflection-Fluorescence recovery after photo-bleach)

The method TIR-FRAP [105] was developed to investigate fluid slippage close to the wall. The principal of this measurement relies on the dynamic of fluorescent intensity recovery, after the photo-bleaching of particles initially in the investigation zone. The photo-bleaching is induced by a vertical strong beam, in order to set the intensity to threshold; after that the totally reflected beam turns on, the intensity of newly convected particles is collected by the photon multiplier (fig 1.7).

The speed of intensity recovery depends on shear rate, with higher shear rate correspondent to faster recovery. The experimental result is fitted by a theoretical work, which relates the concentration of detected particles with convection, photo-bleaching and diffusion.

$$\frac{\partial C}{\partial t} + V_x \frac{\partial C}{\partial x} - D\frac{\partial^2 C}{\partial^2 x} + k_B C = 0$$

where C concentration indicating the total intensity, D diffusion coefficient, k_B first order bleaching constant, $V_x = \dot{\gamma}(z + b)$, with $\dot{\gamma}$ the effective shear rate. The addition of a stearid acid causes the adhesion of this molecule on the surface, which induces a higher slip length and effective shear rate with an increasing time of its incubation. This phenomenon is expressed on the intensity recovery curve by increasing the speed of recovery.

Since the total internal reflection allows illumination within a characteristic penetration length $\sim 100\ nm$, and the signals are collected being the sum of intensity of all particles,

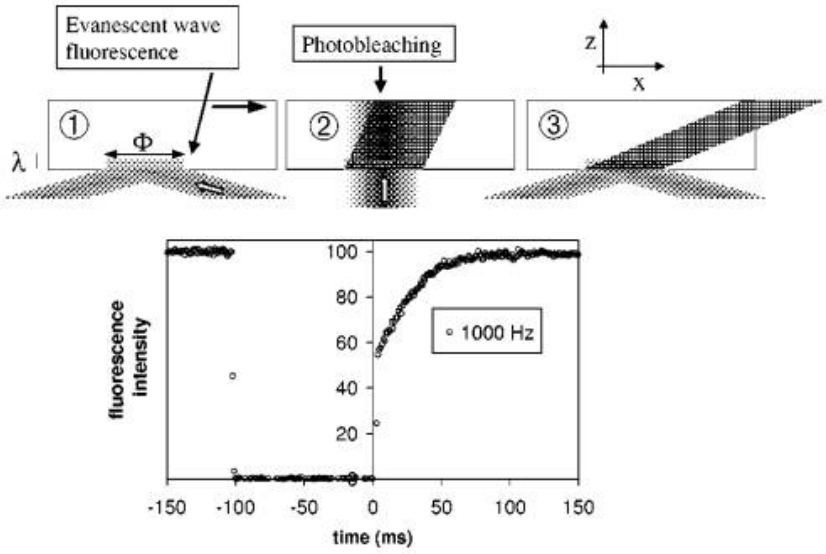

Figure 1.7: Procedure of TIR-FRAP velocimetry, from [105]. The evanescent laser beam and vertical strong laser beam are turn on alternatively to record the intensity recovery, and photo-bleaching of the particles.

the probed thickness should be no greater than 100 nm. The resolution on slip length measurement is ± 100 nm, which is not satisfying compared with other indirect methods.

1.3.2 Direct methods

1.3.2.1 Method based on PIV (Particle image velocimetry)

The PIV method is an useful technique to study of the local flow everywhere in a channels, by performing statistical measurement of tracer particles motion in the fluids. It has been applied to the measurement of slip length on surfaces with different wetting property, and delivers slip length with smaller error bars than conventional methods [70, 134]. This method uses fluorescent particles seeded in the fluid as passive tracers, to detect fluid velocity at a certain layer of height. In the work of Joseph and Tebeling, a piezo-electric device is used to control of depth at which the objective is focused, particles detected in this layer are averaged on height and velocity. Particles adsorbed on the surface serves to the determination of the position of the solid surface. Intensity measurements are taken at several depth close to the surface, and a Lorentzian law is used to fit the intensity profile induced by adsorbed particles, so as to know the distance between the intensity pick and the solid surface. The overestimated velocity very close to the wall is caused by hindered diffusion of particles close to the wall [114]. The obtained velocity profile (fig 1.8) is fitted by a parabolic function which corresponds to theoretical prediction, and the slip length is obtained as the depth position by extrapolating the velocity to zero. Tretheway et al. [134] found a slip length on hydrophobic surface ~ 1 μm. Joseph and Tabeling [70] found slip lengths are below 100 nm with precision ± 100 nm on both hydrophilic and hydrophobic surfaces.

This method allows a direct investigation of flow profile, so that can be applied to study

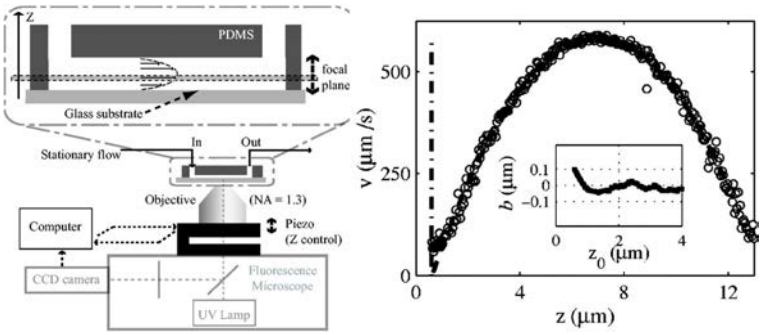

Figure 1.8: Set-up of PIV measurement on velocity profile (left). Obtained parabolic velocity profile (right).

complex fluid flow, which may exhibit unconventional profiles than Poiseuill flow, such as block flow; or to polymer flows which has special properties such as shear banding. However, as the objective is focused at a specific altitude and there are particles in the zone with certain depth, the diffraction limited intensity detection causes the uncertainty of altitude, which is reported as $\pm 100\ nm$ in [70].

1.3.2.2 Method based on TIRF (Total Internal Reflection Velocimetry)

The method is based on an evanescent wave created at the interface of solid and liquid, by the total reflection of laser (fig 1.9). The characteristic length p of the evanescent wave is determined by the incident angle of the laser, and the intensity of the wave decreases exponentially with the depth of its penetration.

$$p = \frac{\lambda_0}{4\pi}[n_2^2 \sin^2\theta - n_1^2]^{-1/2} \tag{1.18}$$

$$I = I_0 exp(\frac{-z}{p}) \tag{1.19}$$

Where λ the incident laser wave length, n_2 the refractive index of solid medium, n_1 the refractive index of liquid medium, θ the incident angle, I_0 the intensity of emitted fluorescence at position of the interface. The evanescent wave illuminates a small portion of the fluid very close to the wall, within 0 to 1 μm, so that the intensity of the particles out of focus is not detected, which makes the single particle tracking velocimetry is possible. Fluorescent particles are seeded into the fluid and excited by the evanescent wave, their emission fluorescence is supposed to be proportional to the excitation intensity. According to the intensity of emitted fluorescence, the particles' depth in the fluid can be estimated. However the fluorescence is related with their size distribution and number of fluophores contained inside each particle. These will bring biases to the calculation of the particle Z position. Particles displacement with fluid motion is recorded by camera and calculated by algorithms, thus to deduce the velocity. This method allows a more precise insight into the fluid motion very close to the interface, and the estimation of slippage on the surface.

The TIRV method has been significantly developed during the past decade. [17, 56, 57, 62, 63, 64, 68, 81, 82, 83, 114, 115, 116, 150]. Breuer fixed an interval of intensity, so as to fix the depth of investigation, to make a statistical particle tracking method. He obtained the distribution of apparent velocity at different shear rate. The plot of apparent velocity vs. shear rate is extrapolated to zero shear rate to induce the slip length by equation

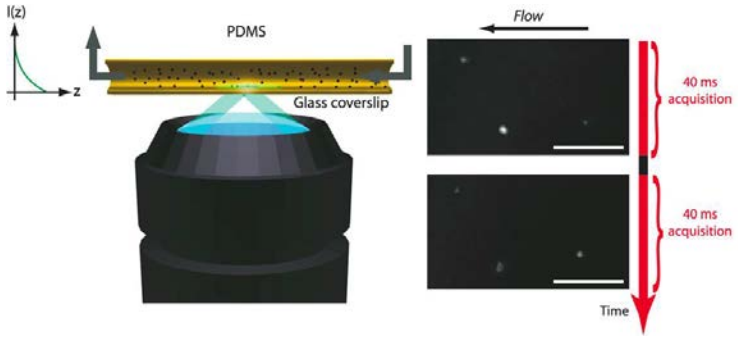

Figure 1.9: Total reflection of laser on the solid-liquid interface creates evanescent wave, which penetrates into the fluid, and illuminates the layer of thinner than 1 μm. Fluorescent particles in the fluids are excited by the wave and emits intensity, which allows their depth determination. From [17]

.

$< u >= (b + W)\dot{\gamma}$, where $< u >$ the average of apparent velocity of particles, b the slip length, W the investigation depth, and $\dot{\gamma}$ the shear rate [26, 68]. The slip length is found to be dependent on surface wetting property. It is from 26 to 57 nm on hydrophilic surface, and from 37 to 96 nm on hydrophobic surface. This result significantly reduces the previously published slip length with the order of 1 μm, however, its accuracy is limited by the few number of points on the velocity vs. shear rate plot, and the incomplete knowledge of penetration length, which leads to 150 nm of maximum error. Breuer extends the scope of this method by studying slip length in electrolyte solutions, which concludes that the electrostatic and electrokinetic effects has no influence on the slip length [62]. The effort of making more precise determination of fluid motion is done by using smaller tracers, such as molecular tracer and quantum dots [56, 57].
Yoda took advantage of the special property of evanescent wave-the exponentially decreased intensity with depth-to explore the single particle tracking method. She divided the observation field vertically into three layers, and made statistical measurement in each layer to deliver the average height and velocity. Using this method, the first velocity profile is published [82, 83]. Due to the few number of point on the velocity profile plot, the slip length could difficultly be induced by simply fitting the velocity profile and extrapolates to zero velocity.
Breuer and Yoda in their concrete study of TIRV method, have mentioned several physical factors which bring bias to the fluid motion. They will be discussed in the following subsections.

1.3.2.2.1 Particle size distribution induced bias on nano-velocimetry The intensity emitted by a particle does not solely dependent on its depth. Due to the polydispersity of the particle size, a bigger particle far from the wall may emit the same intensity with a smaller particle closer to the wall. This induces a bias on the depth determination. Supposing the particle size follows a Gaussian distribution, the probability density function is:

$$P(r) = P_0 exp[-\frac{(r/a - 1)^2}{\sigma_r^2}]$$

Where P_0 a normalization constant, a the average radius, and σ_r the standard deviation of radius distribution. Considering the particles are filled with fluophores in their volume, and by incorporating the exponential decreasing of intensity of evanescent wave, the PDF of a particle with intensity I^e at depth h is written:

$$P(I^e, h) = \frac{\alpha}{(I_0)^{2/3}} exp\{-\frac{[\sqrt[3]{(I^e/I_0)e^{(h-a)/d}} - 1]^2}{\sigma_r^2}\} \tag{1.20}$$

Where α a normalization constant, h the particle depth, and d the penetration length of evanescent wave. By fixing an investigation depth to $0 < h/a < 3$, and supposing an evenly distributed medium, the PDF of intensity is illustrated for different standard deviation of particle size distribution [64]. A deformation of intensity PDF is aggravated with an increasing polydispersity of particles. Breurer thus concluded that it is challenging to study fluid motion based on single particle tracking method, because of particle size induced bias on depth determination.

1.3.2.2.2 Diffusion induced bias on nano-velocimetry Particles exhibit asymmetric Brownian motion when they are close to the wall, because of the enhanced hydrodynamic drag force. The diffusion coefficient far from the wall is described by Stokes-Einstein equation $D_0 = \frac{k_B T}{6a\pi\eta}$. Whereas the diffusion is hindered next to the wall, and the parallel diffusion coefficient $D_{\parallel}$ is described by the Method of Reflection [55] when $Z > 2$:

$$\frac{D_{\parallel}}{D_0} = 1 - \frac{9}{16}(Z)^{-1} + \frac{1}{8}(Z)^{-3} - \frac{45}{256}(Z)^{-4} - \frac{1}{16}(Z)^{-5} + O(Z)^{-6} \tag{1.21}$$

and for $Z < 2$ with an asymptotic solution [54]:

$$\frac{D_{\parallel}}{D_0} = -\frac{2[\ln(Z-1) - 0.9543]}{[\ln(Z-1)]^2 - 4.325\ln(Z-1) + 1.591} \tag{1.22}$$

The hindered diffusion coefficient in the normal direction is written as [8, 18]:

$$\frac{D_{\perp}}{D_0} = \frac{6(Z-1)^2 + 2(Z-1)}{6(Z-1)^2 + 9(Z-1) + 2} \tag{1.23}$$

Where $Z = z/a$ with a the particle radius. Experimentally, the hindered diffusion coefficients can be determined by doing statistical calculation of particles displacement. The parallel coefficient $D_{\parallel}$ is deduced from the ensemble average of radial displacement ΔR of particles:

$$< \Delta R >^2 = \pi D_{\parallel} \Delta t$$

where Δt is the time interval between consecutive image acquisitions. The perpendicular coefficient $D_{\perp}$ is calculated from

$$< (\Delta z)^2 > - < \Delta z >^2 = 2D_{\perp}\Delta t$$

where $< \Delta z >$ is the ensemble average of particle vertical displacement. The measured hindered diffusion coefficients are found to be coherent with the theories [62, 64, 68].
The hindered diffusion impacts significantly the measurement of fluid motion by TIRV method because of the thin illumination depth of evanescent wave. Particles drop in and

out of the luminous region continuously due to vertical Brownian motion, which causes mistakes on particle identification. The resultant physical parameters of the fluid can be discussed in terms of investigation depth and the time interval. Sadr et al. [115] studied particle trajectory with Langevin equation, which describes the temporal change in acceleration due to stochastic force. The hindered diffusion shows qualitatively its effect on trajectory. A FFT correlation-based interrogation algorithm and a Gaussian peak-finding algorithm are applied to determine particle displacement. The particle-mismatch percent ξ is found to increase with time interval (fig 1.10). However the average displacement error can be maintained negligible for $\zeta < 40\%$, which means a time interval $\Delta t < 10a^2/D_\infty$ is recommended in order to minimize the displacement error.
Sadr et al. [114] numerically studied the hindered diffusion impact on average vertical position $< z >$, by using the Fokker-Planck method, which describes the evolution of probability distribution of the z-position. The density of particles $f(z,t)$ is expressed in a diffusion equation, taking into account the vertical Brownian motion:

$$\frac{\delta f(z,t)}{\delta t} = \frac{\delta}{\delta z}(D_\perp(z)\frac{\delta f(z,t)}{\delta z}) \tag{1.24}$$

with initial condition as particles evenly distributed in $a \leq z \leq Z$, where a the particle radius and Z depth of investigation field. The boundary condition is by assuming the vertical diffusion into the wall is impossible: $D_\perp(z)\frac{\delta f}{\delta z}\ |_{z=a}= 0$. The statistical calculation of average $< z >$ position considers only the particles which are situated on z at both moment $t = 0$ and $t = \Delta t$, a PDF function $P(z)$ is used to define this restriction. The $< z >$ is calculated as $< z >= \int_a^\infty zP(z)dz$. The measured $< z >$ is found to be more accurate at small time interval and large investigation depth, for the reason that less particles drop in and out of the region along with less mismatching probability. Fig 1.10(b) compares the $< z >$ measurement between numerical calculation of Fokker-Planck method, with experimental result from artificial images. The deviation induced to the measurement is due to hindered Brownian motion in the first two layers, where the hindered diffusion is specially pronounced.

1.3.2.2.3 Shear induced bias on nano-velocimetry Particles with diameter 100 nm cannot be considered as a dot in the fluid, their displacement under effect of hydrodynamic force cannot totally reflect fluid motion. Shear flow near the wall induces rotation of particles, which causes the translational velocity lower than the fluid velocity. The translational velocity v under shear rate S has been proposed in [54], for large $Z = z/a$ far from the wall:

$$\frac{v}{zS} = 1 - \frac{5}{16}Z^{-3} \tag{1.25}$$

and for small Z:

$$\frac{v}{zS} = \frac{0.7431}{0.6376 - 0.2\ln(Z-1)} \tag{1.26}$$

For intermediate Z, a cubic approximation was proposed [103]:

$$\frac{v}{zS} = (\frac{1}{Z}exp\{0.68902 + 0.54756[\ln(Z-1)] + 0.072332[\ln(Z-1)]^2 + 0.0037644[\ln(Z-1)]^3\}) \tag{1.27}$$

Huang et al. applied these expressions in Langevin simulation [56], and confirmed an underestimation of fluid velocity due to the shear induced hindered motion.

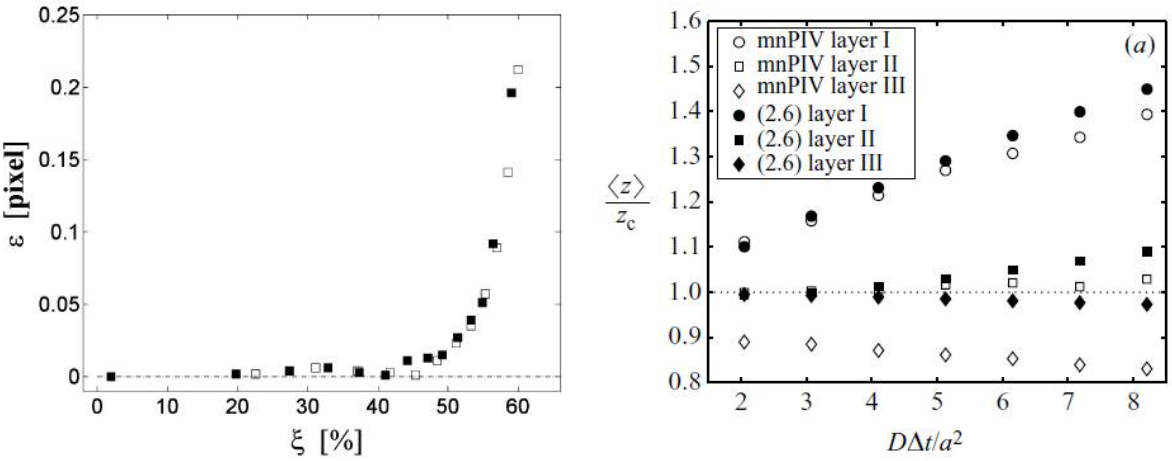

Figure 1.10: Influence of hindered diffusion on measurement of ensemble average of displacement (a), and on vertical position $< z >$ (b). Where ϵ the average displacement error, ξ the mismatching percentage determined by time interval, and $D\Delta t/a^2$ the normalized time interval.

1.3.2.2.4 Electrostatic force and Wan der Waals force induced bias on nano-velocimetry The particles are fabricated with surface coating, which shows negative charges, so as the solid wall. There exists electrostatic repulsion between the particles and the wall [83]. This causes the non-uniform distribution of particles close to the wall, which biases velocity average value towards where particles are relatively more concentrated, so that overestimate velocity. Li et al.[81] considered this effect in their study of Multilayer nano velocimetry, by determining the averaged Z position $\bar{Z} = \frac{\int zC(z)dz}{\int C(z)dz}$, instead of taking the geometrical center of each layer. The corrected slip length corresponds better to the classical considered no slip boundary condition for ordinary fluids.
The particle-wall interaction is described by the sum of electrostatic repulsion and Van der Waals force, defined by the DLVO theory [99]:

$$H = \frac{B_{pw}}{k_B\Theta} K e^{-K(Z-1)} + \frac{A_{pw}}{6k_B\Theta}[-\frac{1}{(Z-1)^2} - \frac{1}{(Z+1)^2} + \frac{1}{Z-1} - \frac{1}{Z+1}] \tag{1.28}$$

where $K = \kappa a$ with κ inverse of Debye length, A_{pw} Hammaker's constant for a spherical particle near a flat wall, B_{pw} a contant which regulates the electrostatic repulsion:

$$B_{pw} = 4\pi\epsilon\epsilon_0 r_0 \left(\frac{k_B\Theta}{e}\right)^2 \left(\frac{\hat{\zeta_p} + 4\gamma\Omega\kappa r_0}{1 + \Omega\kappa r_0}\right) \left[4\tanh\left(\frac{\hat{\zeta_w}}{4}\right)\right] \tag{1.29}$$

where

$$\hat{\zeta_p} = \frac{\zeta_p e}{k_B\Theta} \quad ; \quad \hat{\zeta_w} = \frac{\zeta_w e}{k_B\Theta} \quad ; \quad \gamma = \tanh\left(\frac{\hat{\zeta_p}}{4}\right) \quad ; \quad \Omega = \frac{\hat{\zeta_p} - 4\gamma}{2\gamma^3} \tag{1.30}$$

Θ is the fluid temperature, ζ_p and ζ_w are relatively ζ-potential of particles and of the wall. Huang et al. implemented the electrostatic and Van der Waals force, the shear effect, and Brownian motion into their Langevin simulation [56] . They found the overestimation of particle velocity with respect to fluid velocity at small time interval is caused by shear and

DLVO forces, which are enhanced close to the wall; Whereas at large time interval, the overestimation diverges due to the aggravating particle mismatching caused by the drop in and out. This effect is more pronounced at small investigation depth.

1.3.2.2.5 Slip length determination Two groups of researchers have reported slip length measurement by TIRF method. Huang et al [64] did not induce it by extrapolating velocity profile to zero velocity. Slip length is determined by fitting the curve of apparent velocity vs. shear rate to slopes of expected apparent velocities if a certain slip length is present. Slip length ranges from 26 to 57 nm in the case of hydrophilic surface, and 37 to 96 nm for hydrophobic surface. The difference between hydrphobic and hydrophilic surfaces is confirmed, however as the datas show, slip length is given with high resolution $\sim \pm 30$ nm. Li and Yoda [81, 83] initiated the Multi-layer Tracking Velocimetry, in which the flow field with total depth $\sim 500\ nm$ is divided into three layers, particles in each layer contribute statistically to the average velocity and depth of the layer. Velocity profiles are plotted (fig 1.11), slip length can be obtained by fitting linearly the velocity profile, and extrapolate to the depth where velocity is zero. Slip length on hydrophilic and hydrophobic surfaces are measured and resolution is claimed to be ± 30 nm. However, due to large distribution of intensity of particles even at the same altitude, the authors divide the investigation depth into three layers, so that there are only three points on the velocity profile. Being lack of theoretical correction on the altitudes and velocity, it is impossible to deduce a reliable slip length with high resolution based on three points on velocity profile.

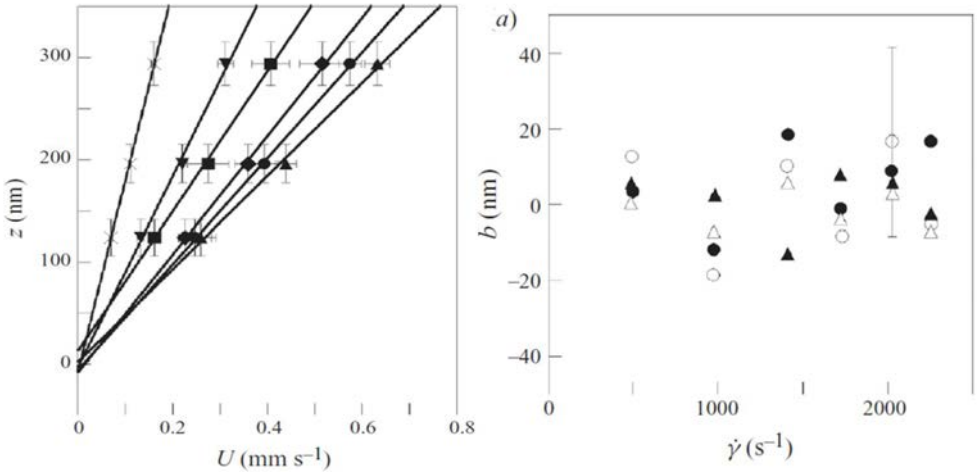

Figure 1.11: Velocity profile of 2 mM CH_3COONH_4 on hydrophilic surface (left), and slip length vs. shear rate for the Poiseuille flow of $2mM$ ($\circ$) and $10mM$ ($\bullet$) CH_3COONH_4 and $2mM$ ($\triangle$) and $10mM$ (black triangle) of NH_4HCO_3 on hydrophilic surface (right), from [81]. The maximum standard deviation of slip length measurement is claimed to be in average 30 nm.

1.3.3 Motivation of high resolution slip length measurement based on TIRF method

The previously mentioned indirect and direct methods for the measurement of slip length have their pros and cons. The most precise determination among the indirect methods is the surface apparatus based method [33], which attain an accuracy of ±2 nm. However, these indirect methods fail to illustrate velocity profile further into the fluid, so that cannot be utilised to study complex flow which exhibits local structures. The study of velocity profiles requires direct methods, among which the multi-layer nano PTV [81] reported the highest resolution merely at ±30 nm.

Aiming at measurement of slip length at higher resolution than the state of the art, in this present thesis, we combine experimental and numerical works, by using the most advanced equipments so far and innovative wall position determination, and Langevin simulation for correcting the biases induced by Brownian motion, shear effects and particle size distribution. The resultant accuracy is reduced to ±5 nm for sucrose solution and around ±10 nm for water. The effect of surface hydrophobicity on slip length is clearly illustrated.

Chapter 2

Experimental study of slippage of Newtonian fluid and polymer using TIRF method

2.1 Experimental setup

2.1.1 Illumination setup

The illumination system is sketched in fig 2.1. The components information are listed in (table 2.1). A laser beam is initiated from a Sapphire laser (Coherent Sapphire 488-50) with wavelength 488 nm at output power 350 mW. This paralleled beam goes through an objective with magnification X10 to be focused on the focal plane (2). An orifice (3) is placed on the same focal plane to let pass only the focused light. A lens with focal length 150 mm (4) is placed behind the orifice, with its focal plane superposed with that of the objective X10. The beam comes out from this lens being paralleled again but with an enlarged diameter at 2 cm. These three components are fixed on a horizontal rail, in order to align them in the transversal direction, and be free to adjust them in the horizontal direction. The implementation of these three components is for producing perfectly paralleled laser beam with enlarged diameter, and eliminating lights due to unparalleled incidence and diffraction. The paralleled beam goes through a diaphragm (5), which is fixed on the table during the first time of alignment of the laser, and serves as a reference point of the beam. For the future laser alignment, the (2)(3)(4) components will be sliding on the rail in order to make the beam go through this diaphragm perpendicularly. The component (6) is a mirror which reflects the beam 90° and incident onto a lens (8) to be focused on its focal plane; this focal plane is shared by the lens (8) and the objective of the microscope. There is a dichroic mirror with splitting wave length 510 nm situated between the lens (8) and the objective, in order to reflect the incident laser beam up to the objective. The component (6) and (8) are fixed on a motor in order to be moved together horizontally without relative displacement, the motor is regulated by a commercial provided LABVIEW program. The fact of moving components (6) and (8) horizontally does not impede the laser beam to be focused on the focal plane of the objective, but results in a displacement of focusing point away from the optical central line of the objective, which induces an angle of incidence different from 90° relatively to the microchannel (fig 2.2).

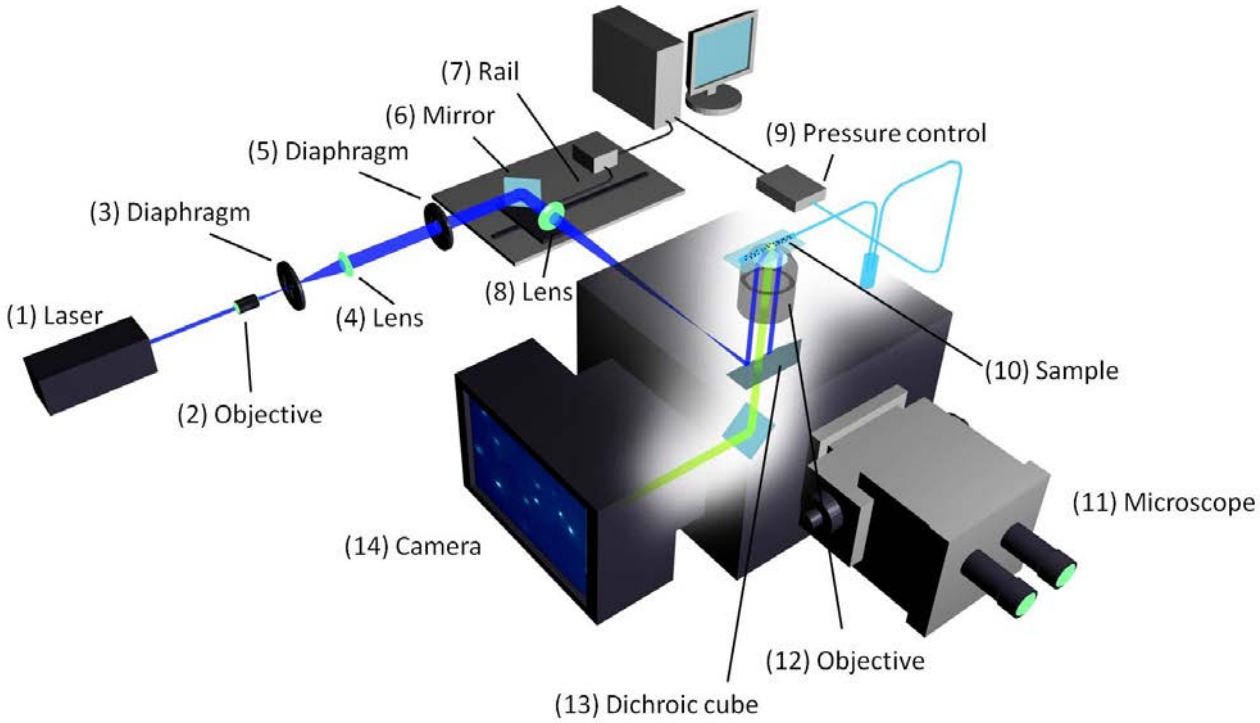

Figure 2.1: Laser setting up of TIRF experiments.

The advantage of using an objective for TIRF measurement relies in the convenience of sending incident light at a supercritical angle without a prism, and retrieving fluorescence information at the same time. The objective has magnification $100X$ and a high numerical aperture $N_a = 1.46$. The numerical aperture fixes the maximum half angle of the cone of light. It is expressed as: $N_a = i \times \sin(q)$, where i the index of refraction of the working medium of the objective, which the immersion oil ($i = 1.518$), which has equal index of refraction with the lens of the objective and glass slide, q is the half angle of the maximum light cone which is 74.1°. The critical total reflection angle at the interface of water and glass slide is about 61.4° with index of refraction of water at 1.3327; and for the interface of sucrose solution 40%wt and glass slide is 67.1° with index of refraction of sucrose solution at 1.3981. The objective with numerical aperture $N_a = 1.46$ has large enough half cone angle to produce total internal reflection in our case of study. Another advantage of using objective with large numerical aperture and oil immersion consists in the increasing number of orders of diffraction collected by the lens, which reduces the size of Airy disk of diffraction, and increases the resolution of the lens.

2.1.2 Acquisition setup

The Andor Neo sCMOS camera is utilized for the acquisition of data (fig 2.1). Its advantages compared with the previously served CCD cameras are described as follows. Firstly, the sCMOS camera offers the lowest noise floor, but providing an unparalleled 1 electron rms typical read noise floor, without amplification technology. It is capable to work with a good sensitivity at 16 bits, which means 65536 grey levels. It allows the distinction of

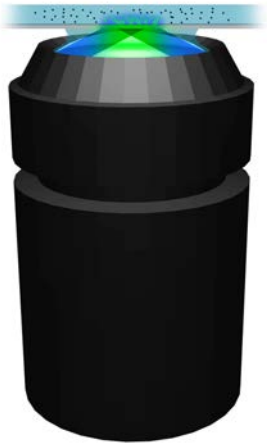

Figure 2.2: Total internal reflection of laser beam on the interface of glass slide and experimental liquid.

two slightly different intensities. Secondly, by applying the "rolling shutter mode", different lines of the arrays are read out at different moment. If a full image with $1024 * 1024$ pixels are taken, the line in the edge will be read 10 ms later than the line in the middle; In the experiments, an image of $512 * 512$ pixels are taken, so there exists a maximum of 2 ms of delay among the different lines. Considering the fact that the time of exposure is 2.5 ms, all the line will be read out during the exposure time. There is no time gap between two successive exposures, so that no information is lost. The fastest frame rate and lowest read out noises are achieved in this mode. Thirdly, the camera provides 4 GB of on-head image buffer, which overcomes the limitation of frame rate due to the eventually low write rate of hardware, and enables frame rates up to 400 images per second. Fourthly, the camera offers a FPGA generated hardware timestamp with the precision of 25 ns, which is 1% of the exposure time, and has neglected effect on the velocity calculation. Lastly, the main difference between a sCMOS and CCD camera relied on the number of amplifier related to the pixels. The number of photons captures on the pixels are translated into tension and amplified. A CCD camera has only one amplifier for all of the pixels, so that the ratio of amplification is constant; whereas a sCMOS camera has one amplifier for each pixel, so that a slight difference of amplification rate is inevitable. For the Andor sCMOS camera used in the experiments, the difference of amplification rate is 0.1% in intensity, which induces 0.1% error of altitude calculation, corresponding to 0.1 nm, which is a negligible effect in the experiments.

2.1.3 Pressure applying setup

The fluid injection is controlled by a pressure applying setup Fluigent (fig 2.1)(9). The maximum pressure is 1000 mbars, with precision 0.1% of the total scale, equals to 1 mbar. The minimum pressure applied in water experiment is 20 mbars, which means the source of error due to the pressure set up introduces to the stress calculation with error at maximum 5% for water, and 1% for 40%wt sucrose solution, which in turn leads to maximum error of

Table 2.1: Components of illumination setup

Number	Component	Manufacturer	Model	Remark
1	laser	Coherent	Sapphire 488-50	350 mW
2	objective 10X	Achro	10/0.25	f=0.17
3	Diaphragm	Newport		
4	lens	Newport	Flat mirror, Pyrex	f=150 mm
5	diaphragm	Newport		
6	mirror	Newport	Flat mirror, Pyrex	
7	rail	Newport	new step NSA12	
8	lens	Thorlabs	LMR2/M	
9	pressure controller	Fluigent	MFCS-FLEX	Maximum pressure: 1 bar
11	microscope	Leica	DMIRM	
12	objective 100X	Leica		numerical aperture=1.46
13	dichroic mirror	Leica	set I3	splitting wave length 510 nm
14	camera	Andor	Neo sCMOS	4GB internal memory

deduced viscosity at 5% and 1% relatively.

2.1.4 Studied solutions and seeding particles

De-ionised water and 40%wt of sucrose solution are studied. The particles utilized in the experiments are Fluospheres from Invitrogen (Carboxylate modified 100 nm Yellow-Green Fluorescent particles F8803, solid 2%, i.e. $3.6 \cdot 10^{13}$ particles/ML). The excitation wave length peak appears at 488 nm, and the emission peak at 510 nm (fig 2.3). The particle concentration seeded in 40%wt sucrose solution is 0.0004% solid, and 0.002% solid in water, so as to have 10 to 20 particles detected in each frame.

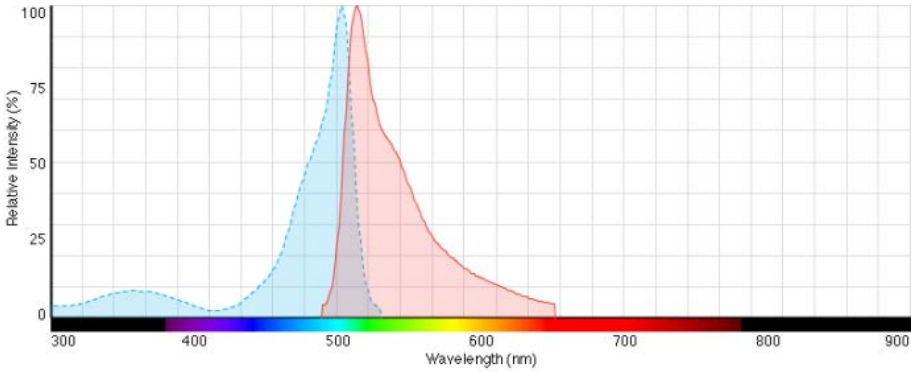

Figure 2.3: Fluorescent particles excitation and emission spectrum.

2.1.5 Channel geometry

The dimension of the channel is 8.8 cm in length, 183 μm in width and 18.3 μm in height. The channel is designed to be in snail shape in order to economize space. The curved parts

has negligible influence on fluid property, because the $Re \approx 10^{-3}$, so that the inertia is neglected.

2.1.6 Preparation of surfaces

Both hydrophilic and hydrophobic surfaces are studied. Hydrophilic surfaces are prepared by treating glass slides with Piranha solution, i.e. 30% volume of hydrogen peroxide and 70% volume of sulfuric acid heated at $300°C$ during 30 min. The obtained slide is combined with PDMS channels with plasma treatment to form a closed structure ready for experiment.

Hydrophobic surfaces can be obtained by coating a layer of n-octadecyltrichlorosilane (OTS) by liquid phase or gas phase on a slide treated by piranha solution. The specifique choice of Trichlorosilane allows the formation of monolayer on the hydrophilic surface (fig 2.4). Optimal experimental conditions and kinetics of monolayer growth are reported in litteratures [22, 43, 76, 111, 122]. The presence of water layer on hydrophilic surface favours the formation of $Si-OH$ group and the adhesion on the surface [22]. However, exceeding presence of water causes condensation of molecules and surfaces highly roughened [76]. The choice of solvent during silanisation on liquid phase is crucial, because the competition between silane molecules and solvent molecules influences the coating quality, this competition is dependent on polarity and shape of solvent molecules [43]. Close packed monolayers are reached if the reaction happened at low enough temperature [22].

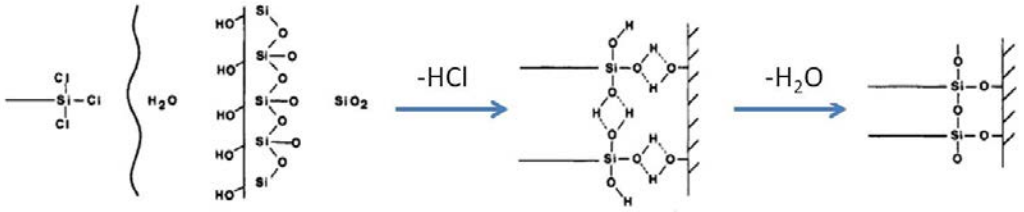

Figure 2.4: Chemical procedure of reaction during OTS coating on a hydrophilic surface. Presence of a water layer activates the reaction.

The procedure of silanisation on **gas phase** is as following:
•Glass slide is treated by plasma to be activated.
•Treated slides are put into a petri dish, in which a small reservoir containing several drops of n-octadecyltrichlorosilane can also be found. Anhydrous crystals are distributed in the petri dish for avoiding the influence of water vapour. During the procedure, the petri dish is sealed by parafilm. Silanised slides are taken out in the end of two hours.

The prodecure of **liquid phase** is described as below, all procedure is manipulated under hood:
•A reactor made from glass with three outlets is cleaned, and purged with N_2 gas to eliminate water vapour.
•Glass slides after been treated with piranha liquid is taken out and dried by N_2 gas. Then subjected to UV light in ozone environment, for further cleaning. Taken out from UV ozone,

the slides are put into reactors, with N_2 continuously purging the system.
•0.1 ml n-octadecyltrichlorosilane (in forms of liquid at $22°C$) is injected into a bottle of 150 ml Toluene, and mixed. The mixture is injected into the reactor with glass slides on the bottom. A balloon containing N_2 gas is connected with the reactor, in order to guarantee the inert environment. (fig 2.5)
•The reaction takes two hours. Slides are taken out, rinsed with toluene and dried with N_2.

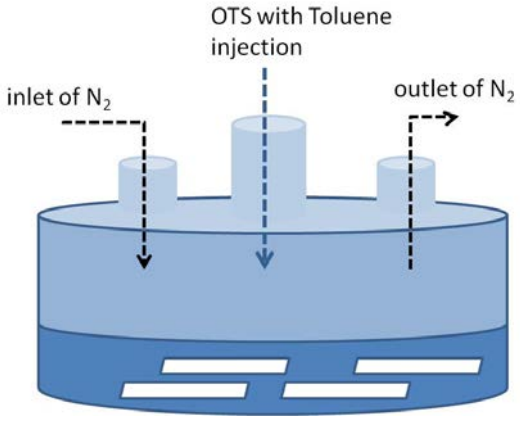

Figure 2.5: Glass slides are treated by mixture of OTS in Toluene in sealed reactor, under environment of N_2 flow.

The thickness of the coated hydrophobic layer by liquid phase is 20 $\mathring{A}$ measured by ellipsometry. Roughness of coating with liquid and gas phase are measured by atomic force microscopy (fig 2.6). The liquid phase gives a much smoother surface, with height distributing around 0 nm with semi-height 1.3 nm; while the gas phase gives a highly roughened surface, with "hills" on the surface, which does not allow the determination of the exact wall position (fig 2.7). The experiments of moving particles are made on smooth hydrophobic surfaces realised by silanisation of liquid phase.

The contact angle of a drop of de-ionized water on the coated layer is 105°, measured by a surface tension determination setup KRUSS (fig 2.8). The hydrophobic slide is combined with channel printed on NOA. The choice of NOA channel instead of PDMS channel is for avoiding combination by plasma treatment, which risks bringing destruction of the coated hydrophobic surface.

2.2 Measurement technique

2.2.1 Incident angle measurement

A glass hemisphere (with refractive index equals to that of glass slide and immersion oil) is put on the objective. The incident laser goes through the hemisphere without being refracted. The out coming laser is projected onto a milimetric paper in forms of an elongated spot. The center of the spot is located for incident angle calculation. The relation among the incident angle θ_i, height of the spot on the milimetric paper H and the distance between

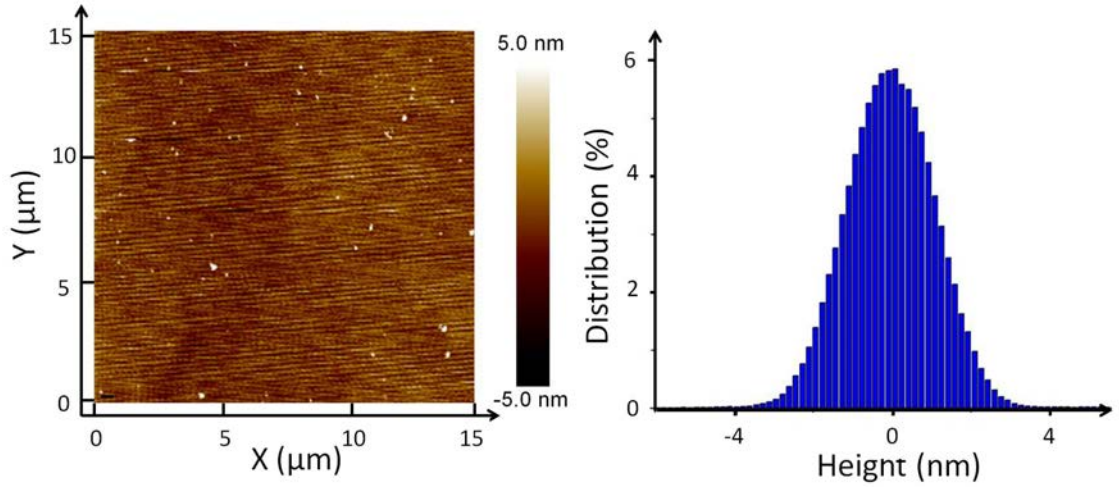

Figure 2.6: State of hydrophobic surface coated on glass slide by n-octadecyltrichlorosilane on liquid phase, thickness measured by AFM (left), and RMS (right) indicating the roughness distributes around 0 nm with ± 1.3 nm at semi-height.

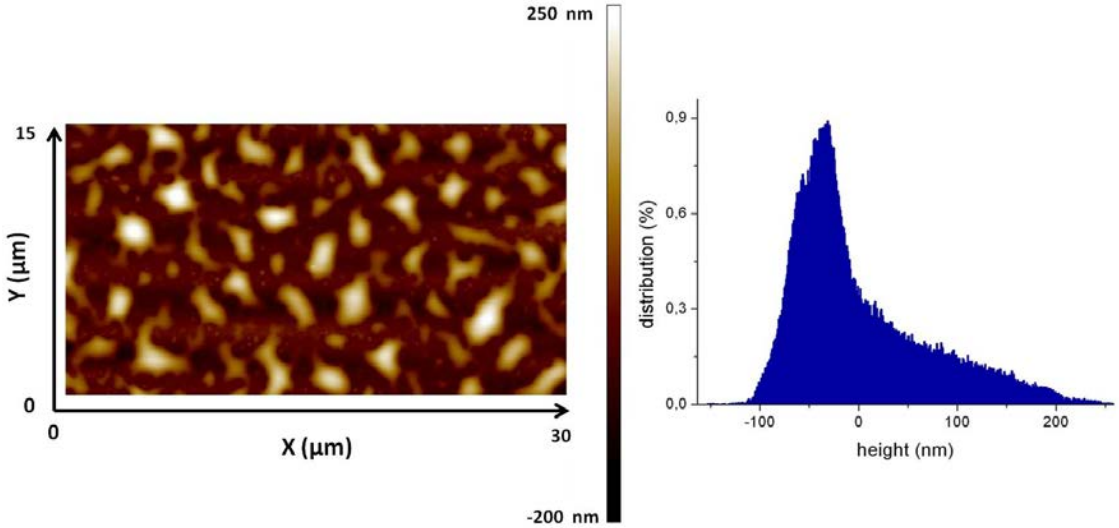

Figure 2.7: State of hydrophobic surface coated on glass slide by n-octadecyltrichlorosilane on gas phase, thickness measured by AFM (left), and RMS (right) indicating a highly roughened surface.

the milimetric paper to the objective L is expressed as: $\tan(\frac{\pi}{2} - \theta_i) = \frac{H}{L}$ (fig 2.9). The precision of the spot central height measurement is at ± 0.5 mm, which introduces an error of 1 nm to the penetration length, approximately 0.7%. Since the laser incident angle is adjusted each time before experiments, the penetration length changes from one experiment to the other. This is taken into account during the data analysis.

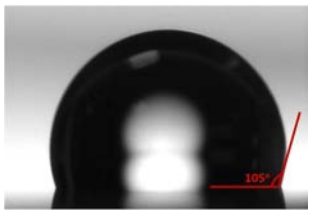

Figure 2.8: Contact angle measurement of silanised hydrophobic surface by liquid phase.

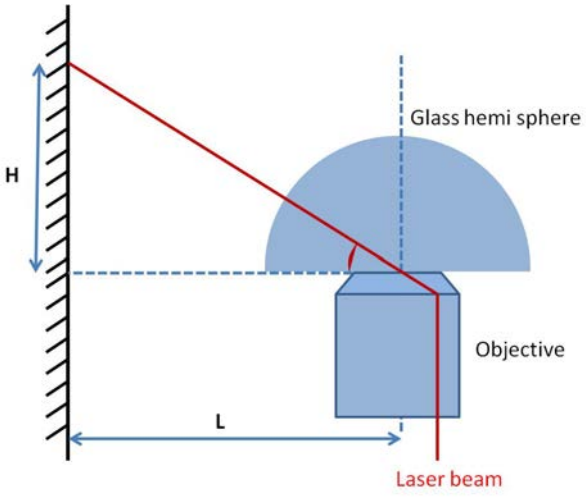

Figure 2.9: Side view of method of measuring laser incident angle. An hemisphere made of glass is put on the objective of TIRF, laser is not refracted because the optical index of the hemisphere and lens of the objective is adapted through immersion oil. Laser spot is projected onto a milimetric paper, where the height can be measured with precison $\pm 0.5\ mm$. The distance between objective and the board $L = 57.2\ cm$.

2.2.2 Acquisition of data

Sample is injected into channels by pressure. Under "live mode" of the camera, focus can be adjusted by either turning the focus button on the microscope, or by a piezoelectric connected to the objective, the latter is with precision $\pm 100\ nm$, which is more accurate. The well focused position is determined by illustrating clearly the particles with strongest emission light, i.e. those most close to the solid-liquid interface. Since the objective has field depth $\approx 350\ nm$, together with the manual adjusting of focusing, the exact position of focus may vary from experiment to another, and with an interval of uncertainty. This will be discussed in the following sessions. After focusing, the camera is tuned to "overlap mode", which allows zero gap time between two acquisitions, and the record begins. 2000 images were taken for one experimental run, which corresponds to duration of 5 seconds. For each applied pressure, 6 experimental runs are taken to ensure a high enough number of detected particles, which will contribute to the statistics of the data analysis. Within the 5 second of recording, no defocusing of the objective is believed to occur. Fig 2.10 shows an example of recorded images.

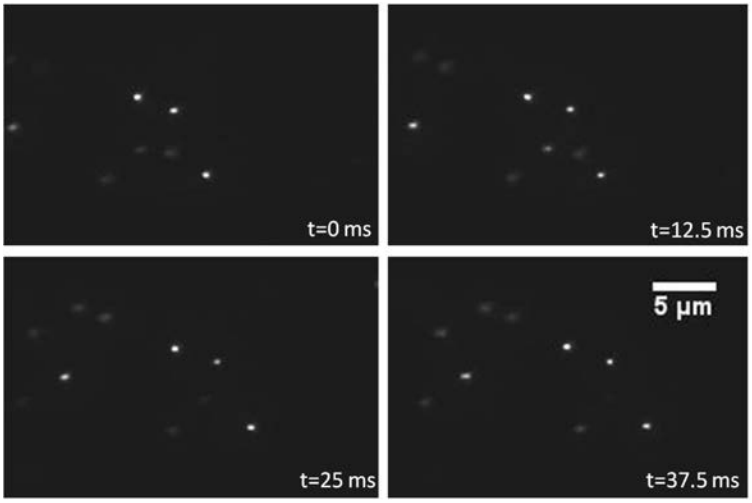

Figure 2.10: A montage of recorded images in TIRF experiments. Flow is from left to the right. Particles with different intensities demonstrate their difference on height. The time gap from one image to another is 12.5 ms, corresponding to 5 frames.

2.2.3 Laser waist and intensity calibration

The intensity of detected particles is not only determined by their height in the channel, but also affected by the heterogeneous illumination of laser on the experimental zone. For this reason the particles intensity should be normalized by laser illumination intensity. Fluoresceine solution is injected into the channel to have an illuminated screen under laser excitation. 2000 images are recorded during 5 seconds. The intensity at each pixel is averaged among the 2000 images. One example of the laser form is shown in fig 2.11.

2.3 Detection method

The recorded information is a serie of images with spots at different intensity. Since the particle size is smaller than wavelength of emission, these spots are actually diffraction image of fluorescent light through the aperture of objective. The Point Spread Function which is the response of optical system can be approximated by 2-D Gaussian distribution. In this study, we adopt the method proposed by Bonneau et al. [15] for the intensity detection and particle centre localization. The method consists in convolution of the detected intensity distribution with a template, which possesses 2-D Gaussian form.

The PSF has standard deviation $\sigma_{PSF} = R_A/3$, with $R_A \approx 1.22\lambda/2N_A$ being the radius of Airy disc, and N_A the numerical aperture of the objective. In the situation where $\lambda = 512\ nm$, $N_A = 1.45$, with size of a pixel= 65 μm, we have $\sigma_{PSF} \approx 72\ nm \approx 0.011$ pixels. The template G with Gaussian form is discretized on a support of 5×5 pixels, with G^m the mean intensity over the support, and G^σ its standard deviation. The intensity peak is identified via the normalized cross-correlation method. The factor which illustrates cross-

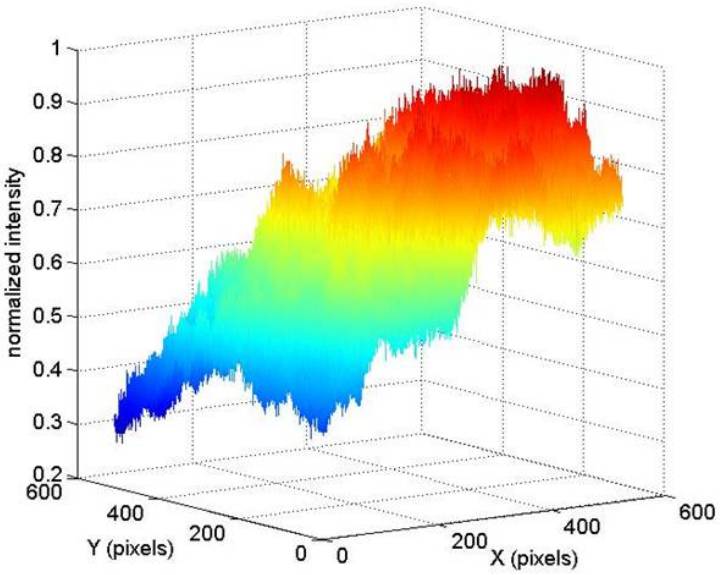

Figure 2.11: The shape of laser print at the total reflection is recorded by injecting fluoresceine homogeneous solution into the channel. These data will be served to the normalisation of particle intensity during analysis.

correlation image $\gamma_{|z}$ results from a convolution of detected intensity with the template:

$$\gamma|_z = \frac{(I_{|z} - I^m_{|z}) * (G - G^m)}{I^\sigma_{|z} G^\sigma} \tag{2.1}$$

Where $I_{|z}$ being the image detected for a particle, $I^m_{|z}$ the average intensity of $I_{|z}$, and $I^\sigma_{|z}$ its standard deviation. The correlation maximas are considered as candidates for detected particles, filtration of noise and location refinement are applied to reach a sub-pixel estimation of particle centre localization. The resolution reaches 0.1 pixel which corresponds to 650 nm for a signal-to-noise higher than 10 [15]. This resolution corresponds to 6.5 nm in the channel.

2.4 Analysis procedure

A customer made MATLAB program is utilized to analyse the detected particles intensity and displacements, in order to deliver the velocity profiles. The analysing procedure is divided into the following steps.

2.4.1 Numerical data treatment

Normalized intensity

The structure which contains the particles x and y position, their intensity at different

frame, and the number of particles detected in each frame is opened by the program as initial information. Intensity of each particle detected in every image frame is withdrawn by the background noise of the camera which is fixed at 103 grey levels; and then be normalized by the laser intensity at its pixel position.

Particles displacement
The particles displacement dx and dy in the PIV experiments are calculated by correlation in two successive frames [70]. In this study of TIRF, however, since the velocity close to the wall is small, and the time delay between two frames is short, the displacement of one particle from one image to the next is much shorter than the distance between two particles detected, considering that the number of particles detected in one image is around 15 in a window of $33 * 33\ \mu m$. Thus an algorithm is implicated to identify the same particle which appeared in two successive images and deduce its displacement, taking into account the estimated displacement and the diffusion effect. For each particle detected in image i, the longitudinal and transversal displacement dx and dy from it to all the particles in image $i + 1$ are calculated. For each pair of (dx, dy), the probability that these two particles in two images are actually the same particle in two frames is expressed as: $P(j) = exp(-(dx - j)/L^2) * exp(-dy/L^2)$, where L the diffusion length, j a vector of estimated displacement, P is the maximum of $P(j)$, which delivers the maximum probability of the two particles being the same one. The probability P of the particle in image i with other particles in image $i + 1$ are all calculated and constructed a matrix of probabilities. The maximum value in the matrix indicates the most probable pair in two successive image frames being the same particle. The displacements dx and dy are noted, and the intensity of the particle is the average of the intensities in the two frames $I = (I_i + I_f)/2$. These data are added into the table of results for the future statistical calculation, which takes into account the particle pairs with probability $> 90\%$.

Statistical treatments
The x and y position of each detected particle, together with their intensity and displacements dx and dy are listed in a table, which usually contains more than 20 000 particles data. Noting that one single particle which appeared N frames during the film acquisition contributes to $N - 1$ number of statistical data. The particles are sorted in an order of decreasing value of intensity. 1000 particles are grouped into one slice for statistics. That means each point on velocity profile represents an average of 1000 datas. The velocities are calculated via $V = dx/2.5\ ms$.

2.4.2 Determination of position of the wall

The intensity of particles on the wall I_0 gives the relative distance between moving particles and the wall. Li and Yoda [83] brought the particles to the wall by electrostatic forces using 10 mM of $CaCl_2$ solution. However, due to photo bleaching property of the particles, the intensity on the wall will depend on the time of illumination. In this session, we innovate a method of measuring I_0 before photo bleaching.

The microfluidic channel is chosen to be the same as in the experiments of velocity measurements, the laser incident angle is also set to be the same. 0.05 M of NaCl is dissolved in the sample. This concentration of salt is observed to be the most suitable, for both bring

the particles stick on the surface, and avoid the particles from forming aggregates, which would otherwise significantly cause the overestimation of measured intensity. The sample is injected into the micro-channel by pressure during several minutes in order to bring enough particles in the channel. After that the pressure is set to zero for the particles near the wall touch and stick on the wall due to Brownian motion. During the particles injection period, the laser was off to avoid photo bleaching previously to the measurement. At the end of procedure, a large number of particles stick on the wall to ensure an enough number of events for the statistic.

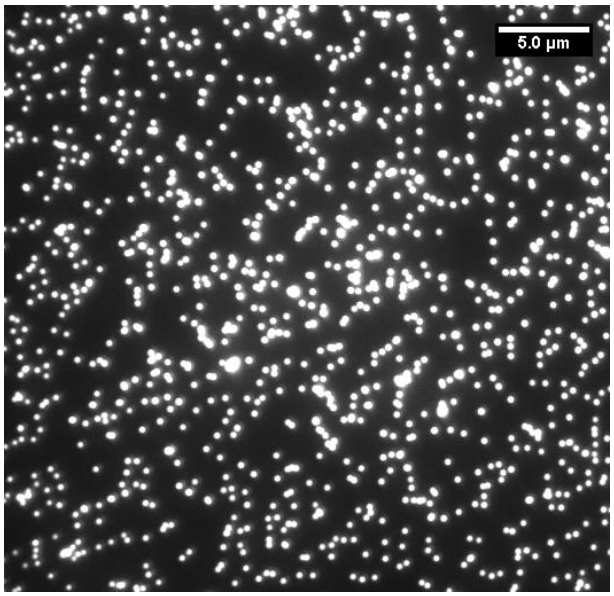

Figure 2.12: Particles stick to the wall due to the fact of adding 0.05 M NaCl into the liquid in order to screen the charge distribution on the surface. A such image is recorded to have an average intensity of particles on the wall, which serves to the determination of wall position.

During the data acquisition, a hand-made shutter is closed firstly to cut the laser stream and avoid it from shining into the micro-channel. The objective of the microscope is placed at the position of the channel, which contains the particles. However, the fact that whether the particles are in the focal plane of the objective cannot be guaranteed. The following is the solution that we innovated. The camera acquisition is firstly begun, the hand-make shutter opened to let the laser pass; the manual focusing is proceeded during the camera acquisition. The advantage of this method is that the camera recorded the whole procedure of focusing, so that the time between the laser switching on and that of the good focusing can be easily deduced from the film; Considering that this time delay can be varied across a wide range due to different manual focusing speed, by repeating a large number of this kind of operation, a plot of the photo-bleaching kinetics can be constructed. An example of well focused image extracted from one of the films is shown in fig 2.12. From the figure we observe that most of the particles are mono-dispersed, however, there is a negligible number of them which have larger sizes and exhibit significant higher intensity than the others. For these particles which are obviously in form of aggregates, we neglect them during the analysis of particles intensity distribution.

The analysis process starts with manually sorting out the well focused images from the film taken previously. For each film, the frame number on which the laser was switched on, and the well focused image frame number were noted so as to calculate the time of illumination. The grey value of the background noise of the camera is 103, which is also the case in the experiments of moving particles. The detected intensity is firstly subtracted by the background noise of camera, then be renormalized by the laser shape. The obtained result is a collection of structures, each structure presents an well focused image, with particles positions, intensities, and particle numbers.

The previous result continues being analysed to illustrate the distribution of particles intensities on a histogram with 200 bins. The distribution is nearly Gaussian, with nonetheless several single events at high intensity. This is due to the aggregates of particles which emit fluorescence with size to the power of cube. Such a distribution can be analyzed theoretically. Assuming that the bleaching process is the same for all the particles, the intensity I emitted by a particle of size r, located at $z = r$, and illuminated by the laser beam for a time t, is given by the formula :

$$I = I_B(t) \left(\frac{r}{r_0} \right)^3 \tag{2.2}$$

in which $I_B(t)$ is a function that characterizes the bleaching process, assumed to apply uniformly on the particle population, independently of their sizes. In this expression, we do not take into account the fact that the particles, being of different sizes, have their centers located at different distances from the wall and therefore are illuminated with slightly different intensities. The corresponding error is on the order of $(\sigma r/p)^2$ i.e 10^{-4}. Assuming further a normal distribution for the particle size, with standard type deviation σ, one obtains the probability density function (pdf) of the intensity emitted by an ensemble of particles located at $z = r$ at time t:

$$p_W(I,t) = \frac{r_0}{3 I_B(t) \sigma_r \sqrt{2\pi}} \left(\frac{I_B(t)}{I} \right)^{2/3} \exp - \frac{\left(\left(\frac{I}{I_B(t)} \right)^{1/3} - 1 \right)^2}{2\sigma_r^2} \tag{2.3}$$

Our expression is slightly different from [64], because we restaured a factor $I^{-2/3}$ coming from a variable change, that was not taken into account. Fig 2.13 shows intensity distribution of sticking particles at four time steps, which agree well with the experiment. By comparing the theory and the experiments, we can extract σ_r and $I_B(t)$ at each time. Regarding σ_r , the values range between 8-9% at all times, which is compatible with the data provided by the constructor (5% for the size dispersity). As mentioned in [64], the standard deviation we obtain incorporates fluctuations in the particle size, number of fluorophores and quantum efficiencies. This may explain why it stands above the sole size dispersity stated by the constructor.

The evolution of $I_B(t)$ with time is shown in fig 2.14, we obtain an exponentially decreasing function. This behavior reflects that, in the range of time we consider, two time constants are needed to describe the bleaching process, consistently with the literature [123, 124]. Song et al. studied the photobleaching kinetics of a thin fluorescein layer under microscopy, they reported that depending on fluorescein concentration and complex structure of fluorescein

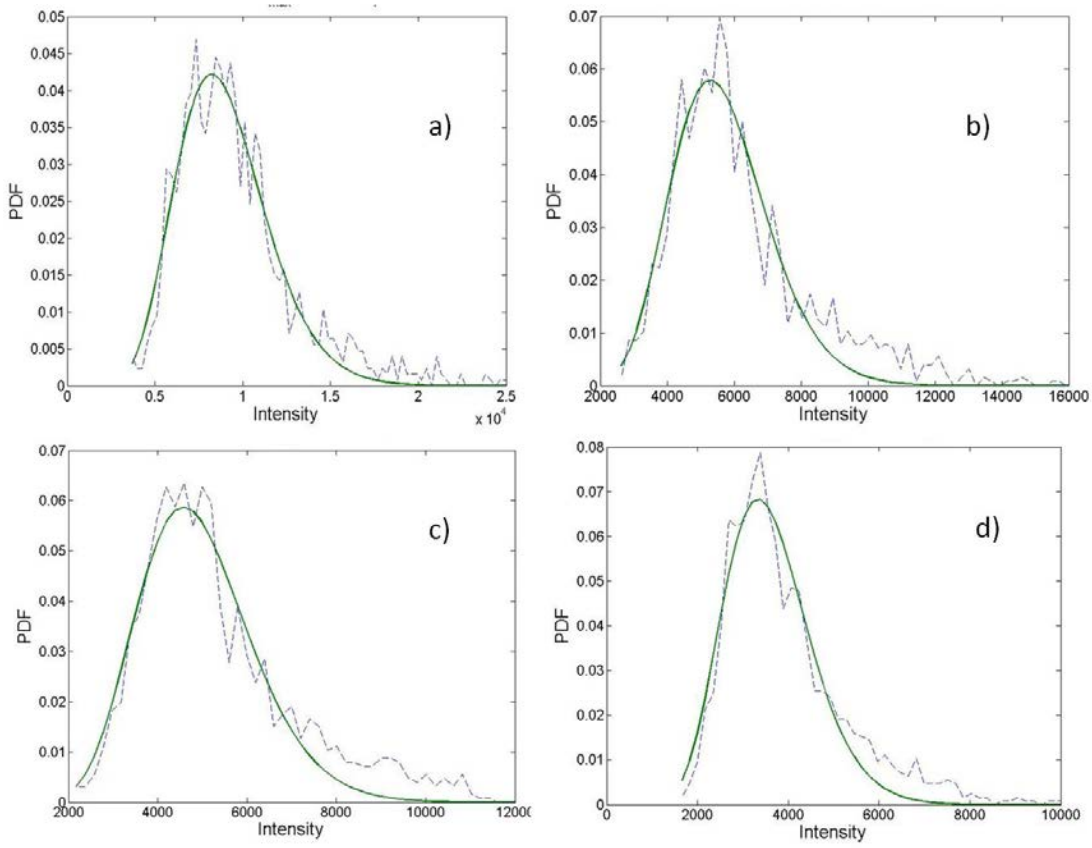

Figure 2.13: Intensity distribution of particle sticking on the hydrophilic surface, in sucrose solution of 40%wt, at four different time step during their photo bleaching. The average intensity $I_B(t)$ and standard deviation σ are obtained through fit. At $t = 0\ s$ (a), $I_B(t) = 8731$, $\sigma_r = 0.098$; at $t = 69\ ms$ (b), $I_B(t) = 5536$, $\sigma_r = 0.087$; at $t = 161\ ms$ (c), $I_B(t) = 4801$, $\sigma_r = 0.088$; at $t = 3680\ ms$ (d), $I_B(t) = 3510$, $\sigma_r = 0.09$.

molecules are bounded with, the photobleaching kinetics can no longer be described by a single-exponential behaviour. Their simulation shows that the non-single-exponential kinetics is caused by the oxygen-independent, proximity-induced triplet-triplet or triplet-ground state dye reactions of bound fluorescein in microscopy. By fitting the data by the formula

$$I(t) = A_1 e^{-t/t_1} + A_2 e^{-t/t_2} \tag{2.4}$$

with free parameter A_1 and A_2 relatively the amplitude of the two exponentials, t_1 and t_2 the characteristic times. One obtains the fitting results as shown in table 2.2. Taking the example of sucrose 40%wt solution. The I_0 is obtained as $I_0 = A_1 + A_2$, so that the average I_0 on hydrophilic surface is 8583, the average I_0 on hydrophobic surface is 6349. Another method of I_0 determination relies on the direct measurement of intensity at $t = 0$ s. Using this method, I_0 on both surfaces is an average of a number of events taken in the same experimental condition, so that $I_0 = 8584$ for hydrophilic surface, and $I_0 = 6448$ on hydrophobic surface. The two methods give consistent average values of I_0. The second method being the direct method of I_0 determination, has an error of ± 123 grey values, which introduces ± 2 nm of confidence interval to the slip length measurement.

Surface	A_1		t_1		A_2		t_2	
	value	95% CI	value	95% CI	value	95% CI	value	95% CI
sucrose hydrophilic	2283	±359	22.4	±9.5	6300	±223	675	±49
sucrose hydrophobic	1801	±200	46	±12	4548	±112	1195	±61
water hydrophilic	2052	±2482	307	±1114	5264	±2576	1368	±1040
water hydrophobic	808.6	±83	92.6	±22	3180	±74	2395	±201

Table 2.2: Double exponential fitting result of photo bleaching kinetics, with mean values and 95% confidence interval.

2.4.3 Influence of finite particle size in evanescent field on the altitude determination

Since the particles diameter (100 nm) and the characteristic penetration length of the evanescent wave (130 nm) are comparable, the particle cannot be assumed to be a point in the evanescent field, and its center on maximum intensity should be identified. The calculation takes the assumption that the fluophores in each particle is distributed homogeneously in the spherical volume. A sphere is separated into 100 layers parallel to the wall. The fluorescence intensity emitted by each layer i is written as:

$$F(i) \sim [V_{cap}(i) - V_{cap}(i-1)] \cdot I_0 \cdot exp(\frac{-z}{p}) \tag{2.5}$$

With V_{cap} the volume of a cap of a sphere expressed as $V_{cap} = \frac{\pi h}{6}(3a^2 + h^2)$, where h height of the cap, a the radius of the base of the cap. The intensity of each layer is plotted in fig 2.15, with particle sticking on the wall, 100 nm, and 200 nm far from the wall. The maximum of intensity stays at 42 nm from the bottom, smaller than 50 nm which is the geometrical center of the particle.

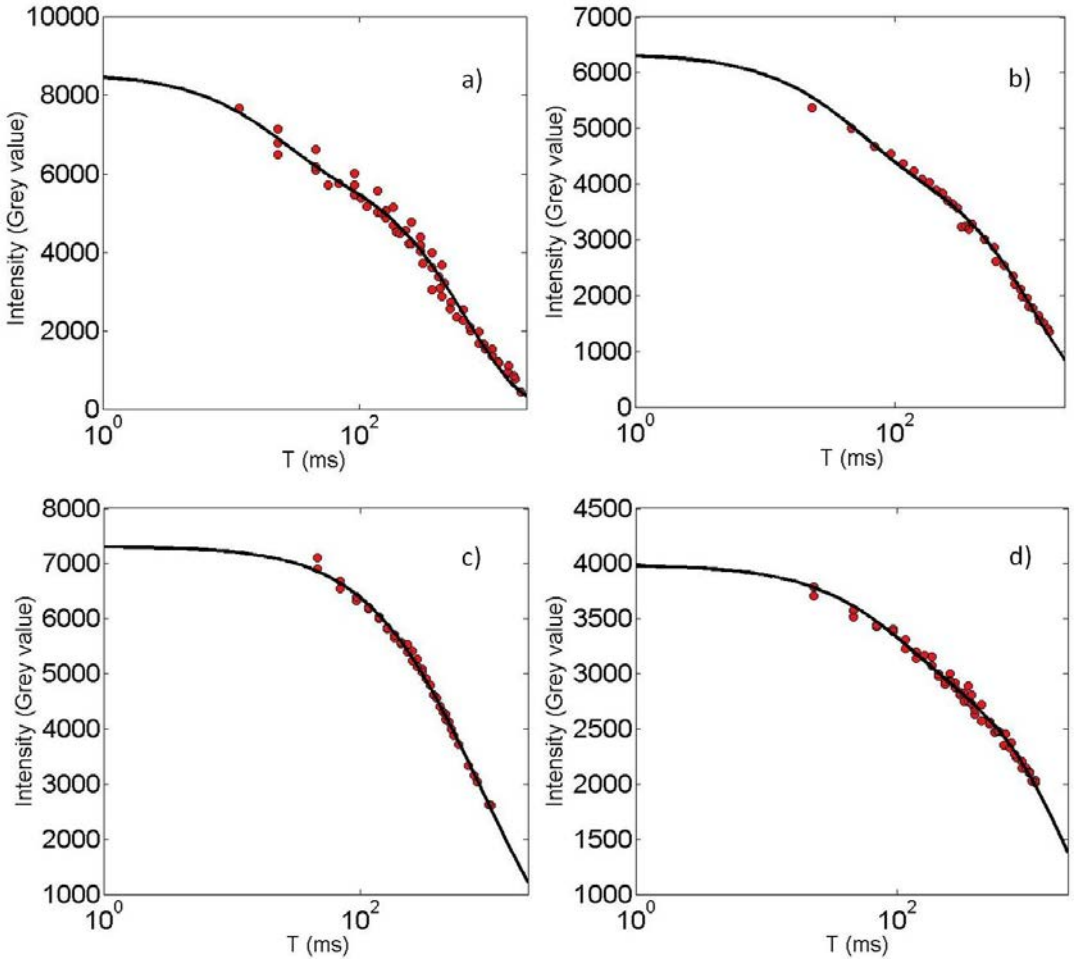

Figure 2.14: Kinetics of particles photo bleaching in sucrose solution on hydrophilic surface (a) and hydrophobic surface (b), that in water on hydrophilic surface (c) and on hydrophobic surface (d). The kinetics can be described by double-exponential laws, the intersection of the two exponential constant occurs at around 100 ms. I_0 is obtained by extrapolating the curve to $t = 0$ s.

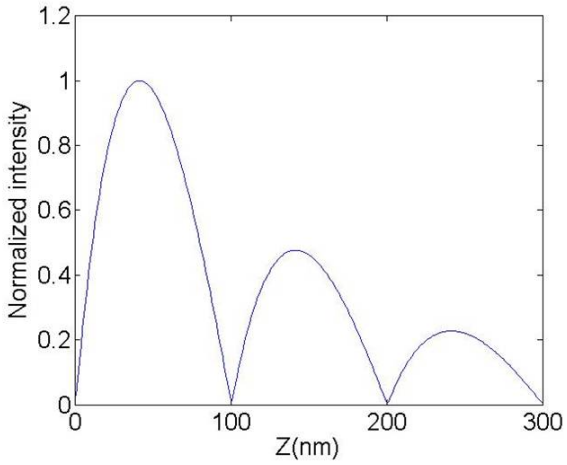

Figure 2.15: Intensity of fluorescence emitted by layers at different height of a sphere, the sphere is situated 0 nm, 100 nm, and 200 nm from the wall, and excited in the field of evanescent wave.

Even though the intensity pick is situated at 42 nm from the bottom of a particle, the formula for particle altitude calculation $z = a + p\ln(I_0/I)$ stays valuable when $a = 50$ nm as the radius of the particle. Because the particle velocity represents the fluid velocity at the same altitude with the geometrical centre of the particle.

2.4.4 Influence of bleaching on flowing particles

Since the particles exhibit photo bleaching process after they are exposed to light within the order of millisecond, the photo bleaching induced intensity decay may generate error in the calculation of flowing particles' altitudes. During the analysis procedure, supposing each displacement of the particles is counted as one contribution to the total statistics. Therefore, if one particle has remained in the camera detection vision for N frames, it contributes to N-1 times to the statistics of velocity and altitude, with each time different quantity of bleached intensity. Its intensity decay due to continuous photo bleaching may lead to bias on the velocity profile. Fig 2.16(a) shows the distribution of number of appearance frames of the particles in one set of experiment containing 2000 images. More than half of the particles appeared for only two frames, then jumped out from our field of investigation due to Brownian motion in vertical direction. Those disappeared particles do not emit intense enough fluorescence for itself to be detected, it is reasonable to consider that they don't receive intense excitation light, and thus do not pursue photo bleaching. However, there are several particles which remain in the field of investigation for a number of frames. Their influence on the lost intensity, and thus to the error of altitude should be analysed. The fraction of lost intensity normalized by total number of events l versus frame number N is expressed by:

$$l(N) = \frac{1}{T} \cdot n \cdot \sum_{N_f=2}^{N} \frac{I_0 - I(N_f)}{I_0}$$

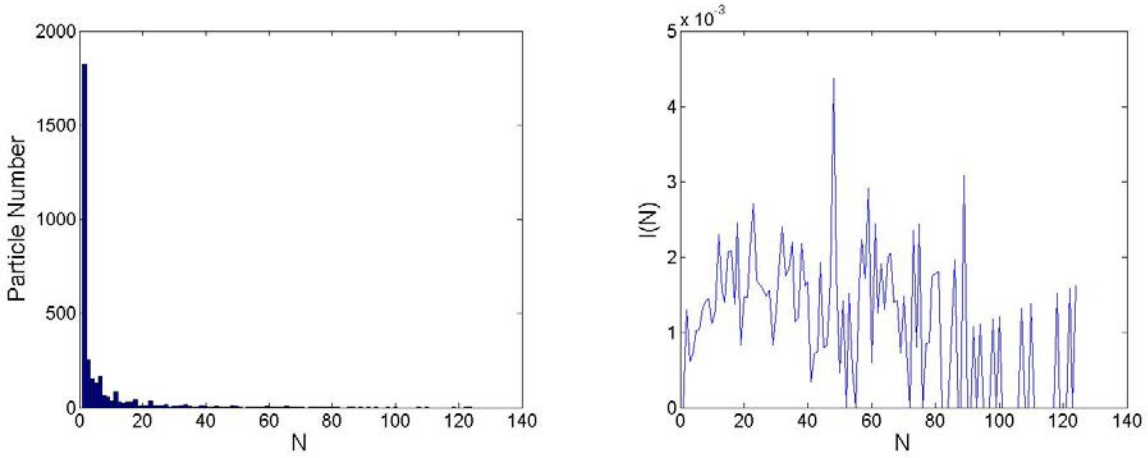

Figure 2.16: Effect of bleaching on the lost intensity. (a) plots the distribution of number of particles which appeared for a certain number of frames N, (b) the fraction of lost intensity due to bleaching vs. number of frames

Where T the total number of events contributed to the velocity calculation, usually in the order of 10^4, n the number of particles which appeared for N frames, $I(N_f)$ the intensity of the particle at N_f^{th} frame, determined experimentally as double-exponential law, by measuring the bleaching kinetics of particles sticking on the wall. The distribution of lost intensity fraction attributed by different number of appearance frames is plotted in figure 2.16(b). Each number of appearance frame introduces in average 0.15% of intensity lost due to photo bleaching, which is negligible. The total intensity lost may however be significant, for example it raises to 13.45% of initial intensity. This error of intensity detection can be related to the altitude error by $z = -p \log \frac{I}{I_0}$, and the maximum error brought by the photo bleaching can reach up to 18 nm, if we do not add a process of filtration on the number of appearance frame during the analysis. The altitude accuracy will attain within 2 nm, if only the particles which appeared for 2 frames are taken into account for the velocity and altitude calculation.

In order to determine experimentally the bias on velocity profile brought by bleaching effect, the particles which appeared during only two frames are sorted out for the calculation of velocity profile. For doing this, a home made MATLAB program is used to construct a table, in which the trajectory and intensity of each particle at all time steps are listed. The particles which appeared during only two frames, and first two frames of those which appeared more than three frames are taken into account. Fig 2.17 shows the comparison between velocity profiles using all particles with that using only particles appearing during two frames. The two curves superpose with each other with the 95% confidence intervals. If the bleaching has a significant effect on the determination of particles altitude, the velocity profile "with only 2 frames" would be expected to be situated at smaller Z position than that "with all frames" at a given value of velocity. However this effect is not observed. Thus the bleaching effect is not as significant as estimated, and so that be neglected.

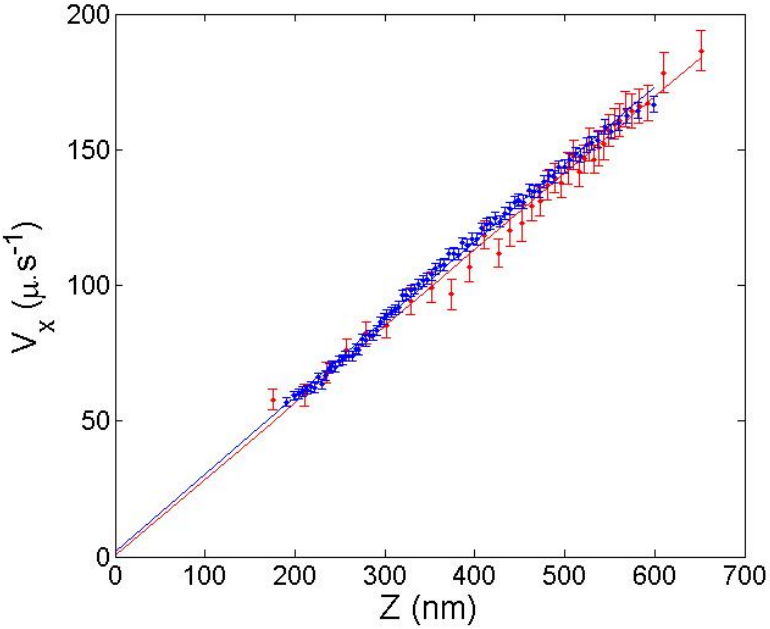

Figure 2.17: Velocity profile calculated by taking into account particles with all number of frames (blue), compared with particles with only first two frames (red). The two profiles superpose within 95% confidence interval, and have negligible difference on slip length.

2.4.5 Influence of focusing on particle altitude determination

Three dimensional intensity distribution around focal plane

It is well known that the intensity distribution of a well focused circular source in the focal plane is described by Fraunhofer diffraction on the aperture of the lens. Since during the experiments the procedure of focusing is controlled manually, it is necessary to consider not only intensity distribution in the focal plane, but also in axial direction around the focal plane. Details are introduced in [16, 59]. As a summary, consider the situation that light is going through the aperture of objective and tends to converge to the axial focal point O (fig 2.18). We are interested in the intensity disturbance on the point P in the neighbourhood of point O. The focal distance is f, the radius of the aperture is a, position of point P in cylindrical coordination is (z, r). Two variables are introduced:

$$u = \frac{2\pi}{\lambda}(\frac{a}{f})^2 z, \qquad v = \frac{2\pi}{\lambda}(\frac{a}{f})r \tag{2.6}$$

Taking into account that numerical aperture of the objective is $N_a = na/f$, and wave length of laser in the vacuum $\lambda_0 = n\lambda$. For points in the geometrical focal plane $u = 0$, intensity distribution is:

$$I(0, v) = (\frac{2J_1(v)}{v})^2 I_0 \tag{2.7}$$

with I_0 the intensity of well focused image on point O. $J_1(v)$ the Bessel function of order 1. Whereas in the axial direction, the intensity distribution writes:

$$I(u, 0) = (\frac{sin(u/4)}{u/4})^2 I_0 \tag{2.8}$$

The first zero of this function gives at $u = 4\pi$, corresponding to the maximum depth of foculisation $\triangle z = \pm\frac{2n\lambda_0}{N_a^2}$.

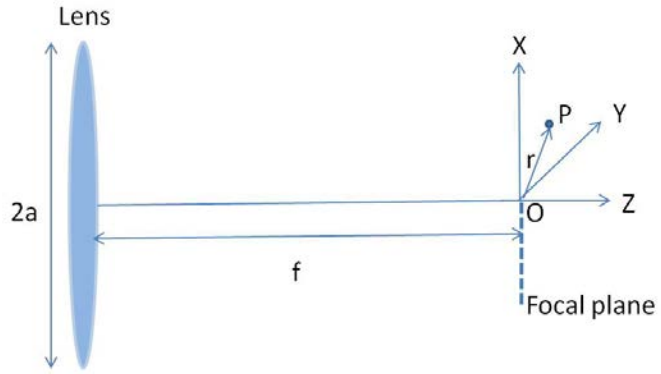

Figure 2.18: Sketch for diffraction at circular aperture of an objective.

Depth of field and effect of out-of focus

The resolution of intensity detection in the axial direction is dependent on the depth of field D_f. The D_f of the objective represents the distance along the optical axe over which a point object can be displaced while keeping its intensity detected without being much attenuated. As proved previously, the numerical aperture N_a is a strong determining factor of the depth of field:

$$D_f = \frac{n\lambda_0}{N_a^2} + \frac{ne}{N_a M} \tag{2.9}$$

where n the optical index between the objective and the fluid, which in our case the immersion oil with $n = 1.518$; λ_0 the wave length in the vacuum which is 488 nm; M the magnification of the objective equals to 100. The first term of the equation comes from the diffraction. While second comes from optical geometry, however this term is negligible in front of the first one. By using an objective with $N_a = 1.46$, the depth of field in our case raises to $D_f = 348$ nm. The intensity along optical axe at a distance z from the focal plan can be approximated by a Lorentzian law [9, 100], with width at semi height D_p:

$$I(z) = \frac{I_{focus}}{1 + (\frac{2z}{D_p})^2}, \tag{2.10}$$

where I_{focus} is the intensity of a focused particle.

In the experiments, the D_p is kept constant. However, due to the manual focusing, the exact position of focal plane is guaranteed with ± 50 nm along the optical axe. This introduces aberration of intensity determination, so that has to be clarified for each experiment. The effect of different position of focal plane z_p is illustrated in fig 2.19. During these experiments, four different focal plane position have been tested. The "correct focus" position is considered to be the best focal position, and applied to all of the experiments of velocity profile determination. It corresponds to letting the particles most close to the wall been well focused visually. Its precision is ± 50 nm along optical axe, due to the precision limitation of piezo-electric at 100 nm.

By comparing the velocity profile of "correct focus" experiment (black) with that been focused 200 nm higher (red), when the focal plane is 200 nm above "correct focus" one, the particles with higher velocity appear situated at smaller altitude z, corresponding to stronger intensity (fig 2.19(left)). This means the particles with high velocity is well focused when the focal plane is fixed at higher altitudes. Identically, the velocity profile with focal plane fixed at 400 nm above the "correct focus" position (green) shows even stronger intensity of particles at high velocity, and much weaker intensity of particles at low velocity. In this case, the particles close to the wall with low velocity are severely badly focused. Moreover, if the focal plane is placed 200 nm lower than the "correct focus" position (blue), only the particles with small altitude are well focused, the others are detected with intensity much attenuated due to defocusing. The plot of intensity distribution supports the previous statement (fig 2.19(right)). Comparing the intensity distribution between "correct focus" (black) with 200 nm higher than "correct focus" (red), the black one is focused closer to the wall, so that better focussed on particles with higher intensity, that is why the "correct focused" one detects more particles at high intensity, but less particles at lower intensity than at 200 nm above "correct focus". Identically, the green curve results from focusing 400 nm above "correct focus" position, it is focused particularly on particles far from the wall, so that with low intensity. The green curve of intensity distribution detects much larger number of low intensity particles than other focus position, and much lower number of high intensity particles.

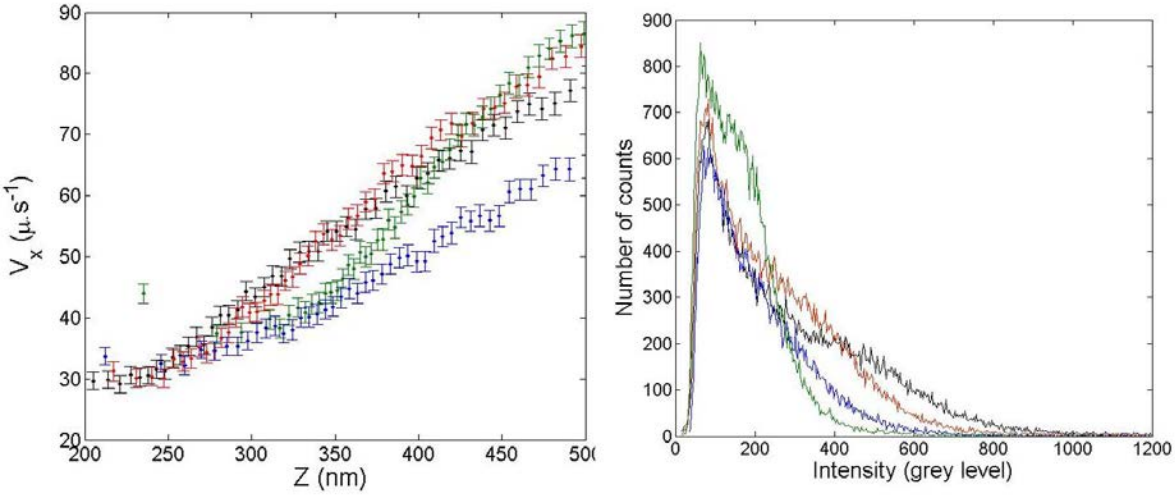

Figure 2.19: Velocity profile (left) and intensity distribution (right) corresponding to different focusing position during experiments (left), correctly focused (black), +200 nm (red), +400 nm (green), −200 nm (blue).

This test of defocusing effect indicates that the correct position of focal plane (black) allows the particle with $z < 400$ nm been qualitatively well focused; however the particles with $z > 400$ nm are defocussed, and their altitude cannot be deduced directly from the detected intensity, but needs to be adjusted considering the defocusing effect. For this purpose, fitting with a control experiment has been made in order to deduce the position of focal plane and depth of focus of the experiments. Theoretical velocity profile of fluid subjected to shear

stress σ and with viscosity η is firstly plotted as: $V(z) = \frac{\sigma}{\eta}z$. The corresponding intensity in well focused case can be calculated as $I_{focus} = I_0 exp(-z/d)$ by law of evanescent wave. Taking into account defocusing effect, the detected intensity is

$$I(z) = I_0 \cdot exp(-\frac{z}{d}) \cdot \frac{1}{1 + [\frac{2(z - z_p)}{D_p}]^2} \tag{2.11}$$

with d penetration length of evanescent wave, z_p the position of focus, and D_p the depth of focus. Vertical position of particles are calculated via evanescent law, and reconstruct the velocity profile resulting from defocusing. This predicted velocity profile is fitted with experimental result in the same condition with z_p and D_p as free parameters. One obtain that $D_p \approx 350$ nm and $z_p \approx 300$ nm. For the experiments, particles altitude is corrected according to equation 2.11 with z_p and D_p as fixed parameters.

2.4.6 Electrostatic forces

Since particles are coated with carboxylate groups COOH, the dissociation (e.g., COO^- on the surface and H^+ in the aqueous solution) results in a negatively charged surface. Silanol groups of glass slide dissociate into (SiO^-) and H^+, also renders the glass surface negatively charged under water environment. The two surfaces repulse with each other, causing a non-uniform distribution of particles close to the wall. This depletion phenomenon has been observed in previous studies [81]. The physical mechanism is as follow: when surface is negatively charged while the fluid far from the surface is neutral, there exists the electrostatic double layer in the vicinity of the surface (fig 2.20), where the layer out of the negative charged layer is positively charged, to satisfy the global neutral requirement. So that a local electric field is created near the surface with a difference of potential between two layers. All negatively charged particles situated in the extend of this field are repulsed further from the surface. The electric potential Φ is related with a thermodynamic description of a system of mobile charges, the Poissons-Boltzmann equation 2.12, which comes from a combination of Poisson equation and the Boltzmann equation. Poisson equation describes the electrical potential in a dielectric medium $\bigtriangledown^2\Phi(r) = -\frac{\rho}{\epsilon_r\epsilon}$, where ρ the charge density in the medium. Boltzmann equation describes the probability of an isolated system to be in thermodynamic equilibrium with a certain energy. In electrolyte solution, it is expressed as: $n^+ = n_\infty exp(\frac{q\Phi}{k_B T})$, with n_∞ concentration of ions in the bulk solution. Detail explanation can be found in [80, 127].

$$\bigtriangledown^2 \Phi(r) = -\frac{1}{\epsilon_r\epsilon_0}\sum_{j=1}^{N} q_j n_{j\infty} exp(-\frac{q_j\Phi(r)}{k_B T}) \tag{2.12}$$

where r the distance from the wall, ϵ_r the dielectric constant of the dispersion medium 80.1 for water at $20°C$, ϵ_0 the permittivity of free space $8.85 \cdot 10^{-12} F/m$, N number of charge species, q_j number of charges of j^{th} specie, $n_{j\infty}$ concentration of j^{th} specie in the bulk solution, k_B the Boltzmann constant, and T absolute temperature. The Poisson-Boltzmann equation can be linearised to be the Debye-Hückel equation (2.13) if electrical energy of an ion is much smaller than thermodynamic energy ($q\Phi \ll k_B T$), with the second term at

RHS vanishes because of neutral bulk solution.

$$\bigtriangledown^2 \Phi(r) = (\sum_{j=1}^{N} \frac{n_{j\infty} q_j^2}{\epsilon_0 \epsilon_r k_B T}) \Phi(r) - \frac{1}{\epsilon_r \epsilon_0} \sum_{j=1}^{N} n_j^0 q_j \tag{2.13}$$

By defining the Debye length as $\lambda_D = (\frac{\epsilon_r \epsilon_0 k_B T}{\sum_{j=1}^{N} n_{j\infty} q_j^2})^{1/2}$, the PB equation can be written as: $\Phi(r) = \zeta exp(-r/\lambda_D)$, with ζ electric potential at the shear plane. λ_D is thus a characteristic length of the electric double layer.

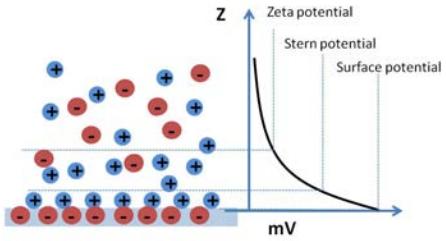

Figure 2.20: Sketch of electrostatic double layer. Surface is negatively charged, with positive ions adsorb on it. Zeta potential is the potential at the limit of double layer.

In the experimental conditions, the Debye length can be calculated. The sample is made from deionised water, sucrose grains and fluorescent particle suspension from Invitrogen (F8803). The charges are considered as mainly introduced by the fluorescent sample. The concentration of charges in initial particle product is 0.3207 meq/g, which is equivalent to 0.3207 $mmol/ml$. In the sample subjected to experiments, particles initial suspension is diluted as 1.3 $\mu l/5ml$, correspondent to charge concentration $C = 8.3382 \cdot 10^{-5}$ $mmol/ml$, so that Debye length using the equation $\lambda_D = (\frac{\epsilon_r \epsilon_0 k_B T}{2e^2 N_a C})^{1/2}$ gives $\lambda_D \approx 37$ nm.

The ζ-potential is another important factor to characterize the surface electric property, it is the electrical potential on the shear plane of double layer. ζ-potential can be induced by measurement of electrophoretic mobility μ_e in an electrophoresis experiment. Because the particles are charged on the surface, they can be induced to movement via an application of electrical field. The mobility is defined as $\mu_e = v/E$, with v the motion velocity, and E the electrical field. Its relation with ζ-potential is $\mu_e = \frac{\epsilon_r \epsilon_0 \zeta}{\eta}$, with η dynamic viscosity of the dispersion medium (Pa.s). In the case of "thick double layer", where the Debye length is not much smaller than particle diameter, it is approximated as:

$$\mu_e = \frac{2\epsilon_r \epsilon_0 \zeta}{3\eta} \tag{2.14}$$

An electrophoresis measurement has been done by a Malvern Instrument, using a sample of particle suspension in deionised water. Results show mobility $\mu_e = -2.974 \pm 3.195$ $\mu mcm/Vs$, which induces ζ-potential $\zeta = -37.9 \pm 40.8$ mV at $25°C$.

To estimate the charge number per particle,

$$\sigma = -\int_0^{\infty} \rho dx \tag{2.15}$$

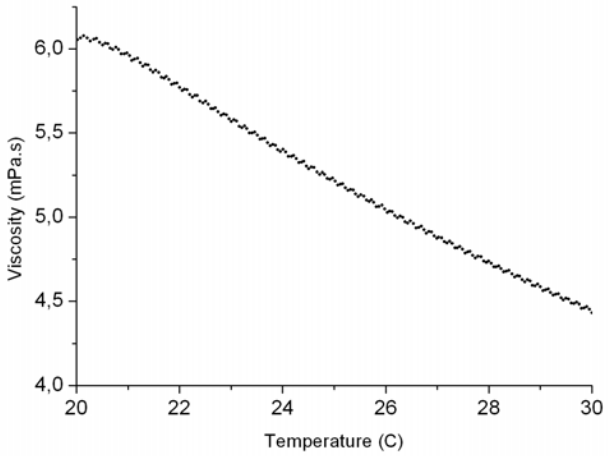

Figure 2.21: Variation of viscosity at changing temperature is measured by conventional Couette rheometer, at fixed shear rate at 50 s^{-1}.

with σ the charge surface density. Incorporating the Poisson equation into equation 2.15, charge number can be expressed as $\sigma = -\epsilon_r\epsilon_0(\frac{d\Phi}{dx})_{x=0}$. Linearising this equation, we have charge density on the glass slide surface: $\sigma \sim \frac{\epsilon_r\epsilon_0\zeta}{\lambda_D} \approx 6.9 \cdot 10^{-4} C/m^2 \equiv 4.3 \cdot 10^{15}\ charges/m^2$. The charge number on a spherical surface is estimated as [80]: $Q = \frac{4\pi\epsilon_r\epsilon_0 r}{e}(1 + \frac{r}{\lambda_D})\zeta$, which gives $Q = 236$ per particles.

The previously estimated ζ potential and charge number per particle will be used in Langevin simulation which incorporates electrostatic repulsion between the wall and the particles. These factors will be adjusted in order to better fit the experiments with simulation, but still within the qualitative agreement with values estimated in this section.

2.4.7 Rheological determination of solution viscosity

In order to verify the precision of TIRF method on the viscosity measurement, viscosity of sucrose (40%wt) is measured by conventional rheometer as function of temperature, at fixed shear rate 50 s^{-1}. Result is shown in figure 2.21.

2.5 Results

2.5.1 Raw results before correction

The preliminary results of velocity profiles on hydrophilic surface and hydrophobic surface are shown in fig 2.22. The profiles are fitted linearly in order to obtain the measured shear rate, which is the tangent of the fit, and deduce the measured viscosity $\eta = \sigma/\gamma$, where σ the shear stress applied by pressure controlling in the channel $\sigma = \frac{\Delta P \cdot h}{2L}$, which is invariant along depth of the channel. Since the microchip system consists of not only the

channel but also connecting tubes, their hydrodynamic resistance needs to be calculated, in order to have the distribution of pressure drop in each part. For a channel with rectangular cross section, with length $L = 8.8\ cm$, width $W = 183\ \mu m$, and height $h = 18.3\ \mu m$, hydrodynamic resistance is expressed as:

$$R_h \approx \frac{12\eta L}{Wh^3(1 - 0.63\frac{h}{W})} \tag{2.16}$$

For the sucrose solution at $40\%wt$ with viscosity approximately 5 $mPa.s$, hydrodynamic resistance in the channel is $R_h = 5.31 \cdot 10^{15}\ \frac{Ns}{m^5}$. Taking into account that the channel entry is connected to sample container by tygon tubes, hydrodynamic resistance in the tube with a circular cross section is expressed as:

$$R_h = \frac{8\mu L}{\pi R^4} \tag{2.17}$$

Where $R = 250\ \mu m$ the internal radius of the tube, $L = 20\ cm$ length of the tube. Hydrodynamic resistance in the tygon tube is $R_h = 6.5 \cdot 10^{11}\ \frac{Ns}{m^5}$, which is 4 orders of magnitudes smaller than that in rectangular channel, so that the pressure applied by the pressure controlling machine equals to the pressure drop in the rectangular channel.

Measured viscosity are shown in the fig 2.23(right), and compared with the value measured by conventional rheometer (fig 2.21). Two series of experiments have been done on hydrophilic surfaces, at temperature $T = 27.5°C$ corresponding to viscosity $\eta = 4.8\ mPa.s$, and temperature $T = 25°C$ corresponding to viscosity $\eta = 5.2\ mPa.s$. One serie of experiment has been done on hydrophobic surface at temperature $T = 26°C$, corresponding to viscosity $\eta = 5\ mPa.s$. Comparaison between viscosity measured by rheometer and TIRF method before correction is shown in Table 2.3. The comparison indicates that the viscosity measured by TIRF method without any correction being made gives $6\% - 15\%$ of error from result of rheometer, which is taken as the reference value.
Slip length is deduced from equation: $b = \frac{dV}{d\gamma}\ |_{z=0} = \frac{V_s}{\gamma}$, and is shown in fig 2.23(left). The average slip length without any correction being made is $b \approx 25\ nm$ on hydrophilic surface, and $b \approx 50\ nm$ on hydrophobic surface (Table 2.3). This result is incoherent with many reported works, in which the flow velocity on hydrophilic surface does respect the no-slip boundary condition.

Table 2.3: Raw results of viscosity and slip length, without correction by Langevin simulation. The η_{rheo} is the viscosity measured by conventional rheometer, where serves as reference value. The errors represents 95% confidence interval.

Sample	Surface	T ($°C$)	η_{rheo} (mPa.s)	η_{tirf} (mPa.s)	Slip length (nm)
sucrose $40\%wt$	Hydrophilic	27.5	4.8	5.55 ± 0.16	26.34 ± 4.9
		25	5.2	5.51 ± 0.19	30.2 ± 5.9
	Hydrophobic	26	5	5.29 ± 0.13	46.2 ± 3.4
water	Hydrophilic	25	0.89	0.886 ± 0.04	21.3 ± 8.4
	Hydrophobic	23.5	0.92	0.954 ± 0.036	65.7 ± 9.4

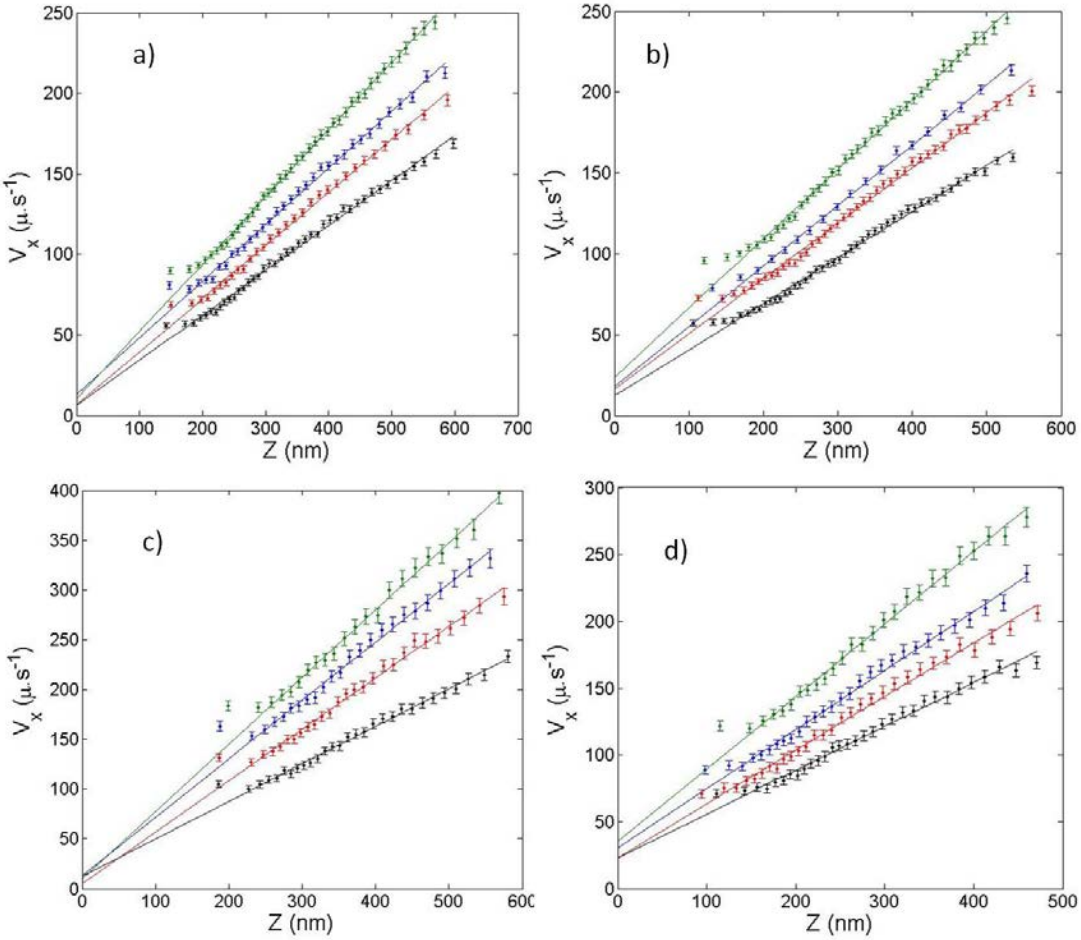

Figure 2.22: Velocity profile of sucrose on hydrophilic surface(a) and on hydrophobic surface(b), water on hydrophilic surface (c) and on hydrophobic surface (d), without taking into account factors which may bring bias to the velocity profile determination. Laser penetration length is $d = 124\ nm$ for sucrose experiments and 135 nm for water experiments. For sucrose on hydrophilic surface(a), the colours represents 140 mbars (black), 170 mbars (red), 195 mbars (blue), and 230 mbars (green). For sucrose on hydrophobic surface(b), the colours represents 145 mbars (black), 175 mbars (red), 195 mbars (blue), and 235 mbars (green). For water on hydrophilic surface(c), the colours represents 32 mbars (black), 42 mbars (red), 52 mbars (blue), and 62 mbars (green). For water on hydrophobic surface(d), the colours represents 30 mbars (black), 37 mbars (red), 42 mbars (blue), and 52 mbars (green). The error bars represent 95% confidence interval.

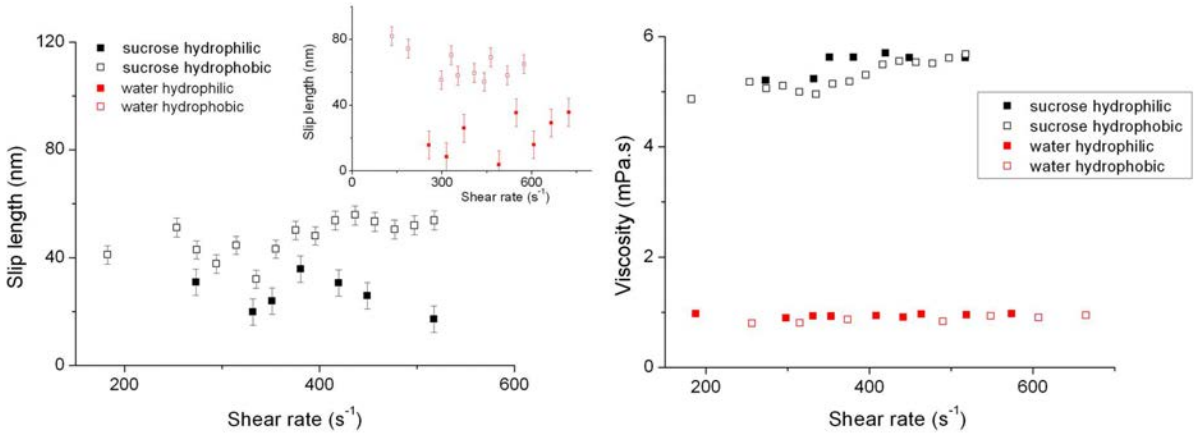

Figure 2.23: Raw results of slip length (left) and viscosity (right) without correction by Langevin simulation, for sucrose 40%wt solution on hydrophilic and hydrophobic surface, and water on hydrophilic surface and on hydrophobic surface.

A backdrop of the direct methods of measuring fluid profile using seeded particles is that particles do not reflect perfectly fluid motion, with the presence of particles Brownian motion, their interaction with charged surface, and their velocity difference from fluid velocity due to the fact that their size is not infinitesimal small. The accuracy of TIRF measurement is not only influenced by the physical factors, but also by limitations of the optical set-up, such as the depth of focusing of the objective. In the next section, we will use the Langevin simulation to explain the biases caused by various factors, and correct the experimentally measured velocity profile.

2.5.2 Langevin simulation

The Langevin simulation describes particles displacements based on stochastic equations [47]. It is based on a set of expression of Newton's law, equating the change in momenta $p_i = m_i v_i$ to the forces that particle i is subjected to. Ermak and McCammon [47] have used this method to calculate displacement of Brownian particles taking into account of hydrodynamic interaction force between particles. Huang et al [56] used it to illustrate the effect of hindered mobility and depletion of particles near solid wall, and its implication on nano-velocimetry.

The discretized displacements at each time step i are written in non-dimensionalized form, with $X = x/r_0$, $Y = y/r_0$, $Z = z/r_0$ stands for coordinates normalized by particle radius r_0:

$$X_{i+1} = X_i + F(Z_i) \cdot Pe \cdot Z_i \cdot \delta T + S\left(0, \sqrt{2\beta_x(Z_i)\delta T}\right) \tag{2.18a}$$

$$Y_{i+1} = Y_i + S\left(0, \sqrt{2\beta_y(Z_i)\delta T}\right) \tag{2.18b}$$

$$Z_{i+1} = Z_i + \left.\frac{d\beta_z}{dZ}\right|_{Z_i} \delta T + H(Z_i)\beta_z(Z_i)\delta T + S\left(0, \sqrt{2\beta_z(Z_i)\delta T}\right) \tag{2.18c}$$

Where the Peclet number $Pe = \frac{\dot{\gamma}a^2}{D_0}$, with $\dot{\gamma}$ the fluid shear rate and D_0 the diffusion coefficient in the bulk, which is estimated by the Stokes-Einstein relation $D_0 = \frac{k_B T}{6\pi\eta r_0}$. The terms describing fluid advection $F(Z_i)$, Brownian motion $\beta(Z_i)$ and electrostatic interaction between particles and solid wall $H(Z_i)$ are as following:

$$F(Z_i) = \frac{U(z_i)}{z_i\dot{\gamma}} \quad ; \quad \beta(Z_i) = \frac{D(Z_i)}{D_0}; \quad H(Z_i) = \frac{F_{pw}(Z_i)r_0}{k_B\Theta} \quad ; \tag{2.19}$$

$F(Z_i)$ is a factor which describes the difference of velocity between particles close to the wall and the real fluid velocity. Near wall shear effect causes the particles undergo rotation, and the translational velocity is slightly lower than the local fluid velocity [54]. The expression of $F(Z_i)$ is suggested according to particle distance from the wall by equations 1.25, 1.26 and 1.27.
The factor $S\left(0, \sqrt{2\beta(Z_i)\delta T}\right)$ describes displacement by Brownian motion, normally distributed with the diffusion length $\sqrt{2\beta(Z_i)\delta T}$ as standard deviation. Particles close to the wall exhibit hindered Brownian motion due to hydrodynamic effects, the hindered diffusion coefficients are expressed by equation 1.21, 1.22 and 1.23.
$H(Z_i)$ describes interaction between particles and the wall, mainly under electrostatic repulsion. In this study, the Van der Waals force is neglected, because the length scale of Ver der Waals interaction is much smaller than that of our investigation range. The expressions of electrostatic forces are written in equation 1.29 and 1.30.

The numerical simulation is done by Loïc D'eramo. During the simulation, 3D positions of the particles are calculated temporally. As initial condition, the fluid field is separated vertically into 23 layers, each layer possesses 500 particles randomly distributed. Experimentally the exposure time of the camera is 2.5 ms, which means the position of particles are averaged during 2.5 ms. The simulation divides 2.5 ms into 50 time steps. In each time step i, the factors $F(Z_i)$, $\beta(Z_i)$ and $H(Z_i)$ are updated and incorporated into the Langevin equations 2.18 for the calculation of X_i, Y_i and Z_i. The X-position is averaged during 50 time steps and for 500 particles, and the displacement is obtained. The averaged Z-position serves to the calculation of the apparent intensity.
Experimentally, as the apparent intensity is not only determined by particle Z-position, but also influenced by the focal depth of optical objective, the intensity of particles situating out of the focal place will be under estimated, as expressed by equation 2.11. During the simulation, this fact is taken into account, the entire equation for the calculation of the apparent intensity reads:

$$I(z) = I_0 \cdot (\frac{r}{r_0})^3 exp(-\frac{z}{d}) \cdot \frac{1}{1 + [\frac{2(z - z_p)}{D_p}]^2} \tag{2.20}$$

with I_0 intensity emitted by a particle with radius r_0 situated on the wall. z being the Z-position calculated by the Langevin Simulation. The apparent Z-position of particles is deduced from the apparent intensity. The simulation is executed with several physical coefficients which cannot be measured very precisely in the experiments, but are chosen within a reasonable range. They vary slightly from one experiment to another, and are listed in table 2.4. z_p standing for the position of objective focusing is fixed in the range of

$300 \pm 50\ nm$. As the particles are subjected to electrostatic repulsion from the wall, there are few particles situated within the range from the wall to $z = 200\ nm$. Manual operation focuses to the visible particles appearing in mass and most close to the wall, so that most reasonably around $z = 300\ nm$. The precision of piezo-electrical device limits the range of focusing within $\pm 50\ nm$. The Debye length λ_D is mainly determined by ionic strength close to the surface. We estimate $\lambda_D \approx 37\ nm$ using the charge concentration in the commercial particle suspension. Since the fluids are susceptible to be polluted by impurities to which the Debye length is sensible, it is possible that Debye length is varied in experiments. In the case of aqueous solution on hydrophilic surface which serves as a calibration test, the simulated apparent positions are most close to experimentally measured ones with Debye length fixed around 25 nm. ζ-potentials of the particle and the wall are fixed with the same manner, and are within a reasonable range. The simulated apparent velocity profile is compared with theoretical fluid velocity profile in figure 2.24. Thus a correction method is deduced.

Table 2.4: Physical coefficients fixed in the Langevin simulation. z_p stands for position of the focal plane, λ_D the Debye length, ζ_w and ζ_p are relatively ζ-potential on the solid surface and on particle surface.

Sample	sucrose			water	
Surface	hydrophilic		hydrophobic	hydrophilic	hydropphobic
Temperature ($^\circ C$)	27	25	26	25	23.5
z_p (nm)	250	300	320	360	200
λ_D (nm)	27	22	18	25	10
ζ_w (mV)	-77	-77	-77	-77	-77
ζ_p (mV)	-25	-25	-25	-25	-25

2.5.3 Results after correction

Details of the corrected results are shown in the attached paper, in which both results for sucrose solution 40%wt and water are illustrated, on hydrophilic and hydrophobic surfaces. As a resume for the result, we achieved a determination of slip length with unprecedented accuray: $\pm 5\ nm$ for sucrose solution and $\pm 10\ nm$ for water. The slip length on hydrophilic and hydrophobic surfaces are distinguished. On hydrophilic surfaces, slip lengths for sucrose and water are around 0 nm, while on hydrophobe surface, the slip lengths are 32 nm and 57 nm. The measurements on hydrophilic surfaces serve as a verification of the accuracy of our method, because it is widely accepted that the no-slip boundary condition is valid on hydrophilic surfaces[13]. In addition, the viscosity after correction agrees better with that measured by conventional rheometer. Statistical results are resumed in table 2.5 for sucrose solution, and table 2.6 for water.

2.5.4 Results with Polyethylene solution on hydrophilic surface

Polyethylene oxide (PEO) polymer solution has been subjected to slip length measurement by TIRF. A PEO molecule is illlustrated by its chemical expression: $H-(O-CH_2-CH_2)_n-$

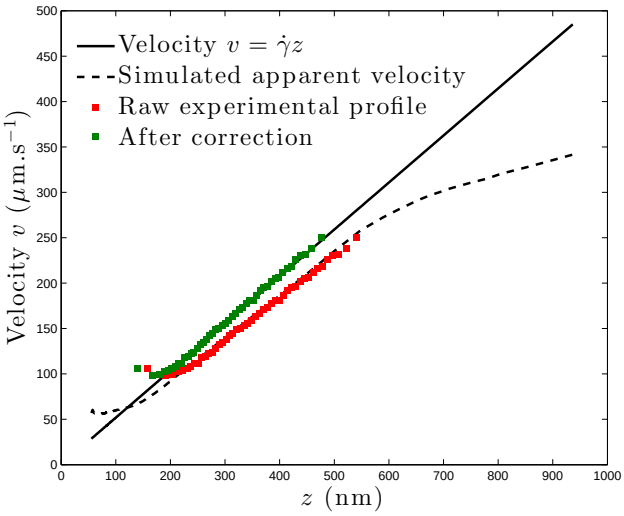

Figure 2.24: Correction from the apparent velocity profile to final velocity profile. Simulated apparent velocity profile (dashed line) deviates from theoretical fluid velocity profile (solid line), because of particles Brownian motion, electrostatic interaction with the wall, slowing down due to shear effects close to the wall, and out-of-focus due to limited focal depth of the optical objective. Experimentally measured apparent velocity profile (red) agrees well with the simulated one (dashed line), and the corrected velocity profile (green) agrees with the theoretical fluid profile (solid line).

OH. The 2g/l of PEO 5MDa solution was made by desolving PEO powder (Sigma-Aldrich) by deionized water, with agitation 80 r/min at 20°C during 7 days. The oxygen stom easily forms hydrogen bonds with H in water, which makes it ideal chain dissolved in water. Near a glass surface, the molecules form hydrogen bonds with silanols, inducing adsorption.
The molecular size 5 MDa corresponds approximatedly to the number of polymerization $n = 114000$. In diluted regime, the morphology of polymer chains is dominated by entropy, they exist in the solution in the form of coils and are independent from each other. PEO monomer has effective length $a \approx 0.35\ nm$ [58], the gyration radius is estimated as $R_F = aN^{0.59}$ [48], which is 340 nm. While the polymer concentration is increased, the solution enters the semi-diluted regime, where the chains are highly overlapped with each other. Between two points of entanglement, the chain can be approximated as blobs, and the solution can be considered as a coil composed of many such blobs [131]. The boundary between the diluted and semi-diluted regimes is the overlap concentration C^*. Viscosity of solution at different concentrations varie 1000 times while the concentration is increased by 10 times in the vicinity of C^* (See thesis of Dr. Philippe Nghe). It is defined on an order of magnitude, rather than on a specific number. The quantitative determination of C^* is as following:

$$C^*(\sqrt{2}R_F)^3 = \frac{M}{N_A} \tag{2.21}$$

Where M the molar mass of the polymer, N_A being the Avogadro number. In the case of 5 MDa PEO polymer, $C^* \approx 0.074\ g/L$. Note that the estimation C^* is exact to the level of order of magnitude. We use the solution of PEO 5MDa at $2g/L$, which is 27 times of C^*, to study the slip effect of polymer solution on hydrophilic surface. According the

Surface	Hydrophilic		Hydrophobic
Temperature ($°C$)	27	25	26
η_{rheo} (mPa.s)	4.9	5.2	5
$\frac{\eta_{raw}-\eta_{rheo}}{\eta_{rheo}}$	12.56%	6.75%	5.77%
$\frac{\eta_{corr}-\eta_{rheo}}{\eta_{rheo}}$	2.7%		0.66%
b_{raw} (nm)	28.0 ± 5.4		46.2 ± 3.4
b_{corr} (nm)	1 ± 5		32.4 ± 5

Table 2.5: Viscosity and slip length measured by TIRF before and after correction, on hydrophilic and hydrophobic surfaces, for **sucrose solution** at $40\%wt$. η_{rheo} stands for viscosity measured by conventional rheometer, η_{raw} is the apparent viscosity measured by TIRF before correction, η_{corr} is the viscosity after correction, b_{raw} and b_{corr} stand for slip lengths before and after correction.

Surface	Hydrophilic	Hydrophobic
Temperature ($°C$)	25	23.5
η_{rheo} (mPa.s)	0.89	0.92
$\frac{\eta_{raw}-\eta_{rheo}}{\eta_{rheo}}$	0.5%	3.7%
$\frac{\eta_{corr}-\eta_{rheo}}{\eta_{rheo}}$	2.8%	0.1%
b_{raw} (nm)	21.3 ± 8.4	65.7 ± 9.4
b_{corr} (nm)	9 ± 10	55 ± 9

Table 2.6: Viscosity and slip length measured by TIRF before and after correction, on hydrophilic and hydrophobic surfaces, for **water**.

viscosity measurement by conventional rheometer at different concentration of polymer, at $C = 27C^*$, the viscosity is experiencing an abrupt increase with concentration. The volume fraction in the bulk is $\phi_b = \frac{Na^3}{R_F^3} \approx 1.2 \cdot 10^{-4}$, and the correlation length of the solutoin in the bulk $\xi_b = a\phi_b^{-3/4} \approx 300$ nm, in the same order of the gyration radius.

The velocity profiles after correction is collected in figure 2.25, and the extrapolated slip length is shown in figure 2.26 (left). It is clear that PEO solution at the overlap concentration exhibits a negative slip length on hydrophilic surface, the value is $b \approx -60\ nm$, independently from applied shear rate within one order of magnitude. The corrected viscosity is averaged at the value of 3.66 mPa.s, which is still 9% overestimated than the value measured by conventional rheometer at $25°C$. The reason may be attributed to temperature regulation of rheometer, since the viscosity of PEO solution is very sensitive to temperature. The final results are collected in table 2.7.

This result is consistent with previous published ones [14, 106, 153], that polymer solution flowing above an adsorbed layer exhibits negative slip length. It is coherent with the state-

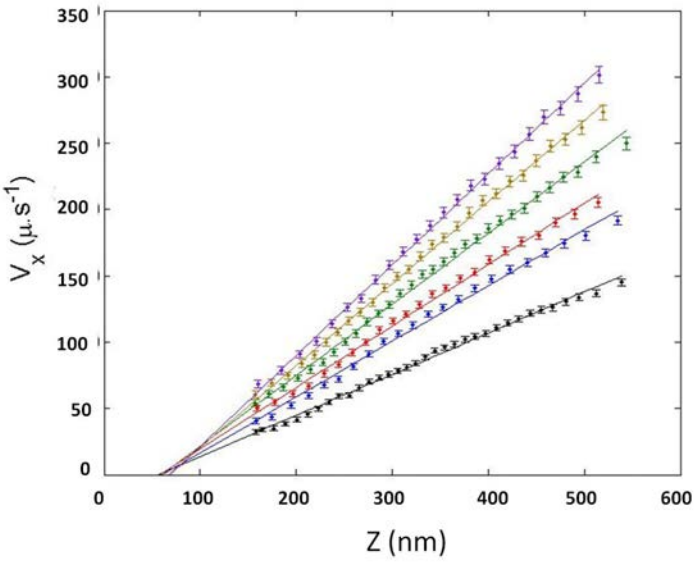

Figure 2.25: Velocity profiles after correction for PEO 5 MDa solution at $2g/L$ on hydrophilic surface. The colors correpond to 115 mbars (black), 145 mbars (blue), 160 mbars (red), 190 mbars (green), 220 mbars (yellow), and 250 mbars (purple).

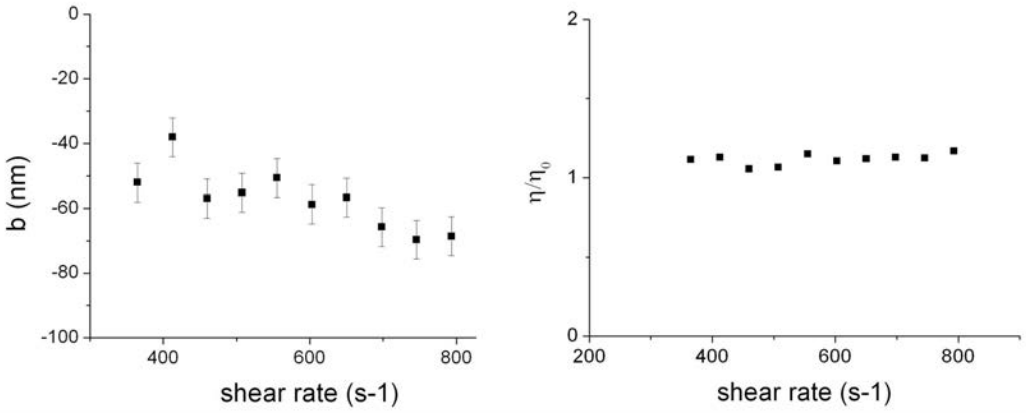

Figure 2.26: Result after correction for PEO $2g/l$ solution. PEO solution exhibits negative slip length (left), measured with 6 nm errors for 95% confidence interval. Viscosity measured by TIRF normalized by that measured by rheometer (right) is around 1.09.

ment of de Gennes [38] that the thickness of effective hydrodynamic layer above which the polymer solution flows is of the same order of largest loop dimension on the surface, also with the gyration radius in a good solvent ($R_F \approx 340\ nm$). The altitude most approximated to the wall is concentrated in monomer in the case of attractive wall. The adsorption of monomers is energetically favourable, and the energy to counteract it is $Nf\gamma_1 a^2$, with N the number of polymerization, γ_1 the surface tension between polymer chain and the surface, f the fraction of adsorbed monomers, and a size of the monomer. Even though it is based on assuming weak interaction, the fact that N being large induces strong adsorption. With the increased altitude, monomer concentration decreases gradually to the bulk concentration.

Temperature ($°C$)	η_{rheo} (mPa.s)	$\frac{\eta_{raw}-\eta_{rheo}}{\eta_{rheo}}$	$\frac{\eta_{corr}-\eta_{rheo}}{\eta_{rheo}}$	b_{raw} (nm)	b_{corr} (nm)
25	3.35	18.8%	9%	-48.4 ± 5.7	-57.2 ± 6

Table 2.7: Viscosity and slip length of $2g/l$ PEO 5MDa solution measured by TIRF before and after correction, on hydrophilic surface. The error bar is determined by the 95% confidence interval.

The adsorbed chains have conformation in loops, with the fraction of adsorbed monomer $f = a/D$, where D is the effective thickness of adsorbed chains [37].

This measurement demonstrated that TIRF method achieves a precise determination of polymer solution negative slip length on hydrophilic surface, with unprecedented accuracy. The study can be extended to more concentrated polymer solution, to study the performance of entangled polymer chains near the surface. Such measurements have been performed by other methods [61], with a positive slip length 1 μm at low shear rate. These studies emphasize on the slip regime transition at increasing shear rate when the bulk chains disentangle with tethered chains. However, they failed to illustrate the negative slip fact near the wall with nanometer accuracy. The study of velocity profile by TIRF can also be extented to fluids which form complex structures while being sheared, to deliver a 3D mapping in nanoscale.

2.6 Conclusion

In this part of thesis, we have developed a methodology, based on the Total Internal Reflection Velocimetry, to determine precisely fluid motion within 200-800 nm from the wall. We achieved unprecedented resolution on particle altitude, horizontal velocity, and wall position determination. We took into account biases induced by Brownian motion, shear effect, electrostatic repulsion, photo-beaching, and defocusing, via a Langevin simulation, biases are corrected. We achieved a determination of slip length with accuracy ± 5 nm for sucrose solution and ± 10 nm for water solution. The distinguishment of slippage on hydrophilic and hydrophobic surfaces is clear, with sucrose solution on hydrophilic surface 1 ± 5 nm, and on hydrophobic surface 32 ± 5 nm, with water on hydrohilic surface 9 ± 10 nm, and on hydrohobic surface 55 ± 9 nm. This method being applied to PEO 5MDa solution at $2g/l$ demonstrates a negative slip length -57 ± 6 nm, due to adsorbed layer on the surface. The TIRF based nanovelocimetry can be extented to study of flows near the wall, with complicated structures and flow profiles.

Near-wall nanovelocimetry based on Total Internal Reflection Fluorescence with continuous tracking

Zhenzhen Li [1*], Loïc D'eramo [1*] †, Choongyeop Lee [1], Fabrice Monti [1], Marc Yonger [1], Patrick Tabeling [1]
Benjamin Chollet [2], Bruno Bresson [2], Yvette Tran [2]

[1] MMN, CNRS, ESPCI Paris-Tech, 10 rue Vauquelin, 75005 Paris, France
[2] PPMD-SIMM, CNRS, ESPCI Paris-Tech, 10 rue Vauquelin, 75005 Paris, France

(Received ?; revised ?; accepted ?. - To be entered by editorial office)

The goal of this work is to make progress in the domain of near-wall velocimetry. The technique we use is based on the tracking of nanoparticles in an evanescent field, close to a wall, a technique called TIRF (Total Internal Reflection Fluorescence)-based velocimetry. At variance with the methods developed in the literature, we permanently keep track of the light emitted by each particle during the time the measurements of their positions ('altitudes') and speeds are performed. A number of biases affect these measurements: Brownian motion, heterogeneities induced by the walls, statistical biases, photobleaching, polydispersivity and limited depth of field. Their impacts are quantified by carrying out Langevin stochastic simulations, in a way similar to Guasto & Breuer (2009). By using parameters calibrated separately or known, we obtain satisfactory agreement between experiments and simulations, concerning the intensity density distributions, velocity fluctuation distributions, and the slopes of the linear velocity profiles. Slip lengths measurements, taken as benchmarks for analysing the performances of the technique, are carried out by extrapolating the corrected velocity profiles down to the origin along with determining the wall position with an unprecedented accuracy. For hydrophilic surfaces, we obtain 1 ± 5 nm for the slip length in sucrose solutions, and 9 ± 10 nm in water, and for hydrophobic surfaces, 32 ± 5 nm for sucrose solutions and 55 ± 9 nm for water. The errors (based on 95% confidence intervals) are significantly smaller than the state-of-the-art, but more importantly, the method demonstrates for the first time a capacity to measure slippage with a satisfactory accuracy, while providing a local information on the flow structure with a nanometric resolution. Our study confirms the discrepancy already pointed out in the literature between numerical and experimental slip length estimates. With the progress conveyed by the present work, TIRF based technique with continuous tracking can be considered as a quantitative method for investigating flow properties close to walls, providing both global and local information on the flow.

† Email address for correspondence: loic.deramo@espci.fr [*] *both authors contributed equally*

1. Introduction

Velocimetry techniques based on Total Internal Reflection Fluorescence (TIRF) have enlightened our understanding of the behaviour of Newtonian flows and particles near boundaries. The method was pioneered by Yoda (Zettner & Yoda 2003; Sadr *et al.* 2004, 2005; Li *et al.* 2006; Sadr *et al.* 2007; Li & Yoda 2008, 2010) and Breuer (Jin *et al.* 2004; Huang *et al.* 2006*a*; Guasto *et al.* 2006; Huang & Breuer 2007; Guasto & Breuer 2009; Huang *et al.* 2009), and further developed or used by several authors (Kazoe *et al.* 2013; Bouzigues *et al.* 2008). It consists in seeding the fluid with fluorescent nanoparticles and operate in an evanescent field near a wall/liquid interface. In such conditions, the fluorescent particles emit a light whose intensity is expected to decrease exponentially with their altitudes (i.e. their distances to the wall) and it becomes envisageable, by translating intensities into distances, to determine the location of each of them with respect to the wall without being subjected to diffraction limit. With the cameras available today on the market, the theoretical resolution of the technique is subnanometric, but in practice, for a number of reasons that will be explained later, the best resolution reported thus far in the literature is 30 nm (Li & Yoda 2010). Still this represents an improvement by more than one order of magnitude in comparison with well resolved techniques such as μPIV (micro Particle Image Velocimetry) (Santiago *et al.* 1998; Meinhart *et al.* 1999; Joseph & Tabeling 2005*a*; Tretheway & Meinhart 2002; Zheng *et al.* 2013).

Reaching nanometric resolutions on the local measurement of velocity, diffusion constant, speed distributions, etc. is a breakthrough for flow instrumentation. It opens the possibility to analyse nanoflows in a great variety of contexts (Hu & Li 2007; Sparreboom *et al.* 2009; Mijatovic *et al.* 2005). Examples concern lubricating films in concentrated emulsions and foams (Kimura & Okada 1989; Schmid & Wilson 1995; Briceo & Joseph 2003), depleted layers in polymer solutions (De Gennes 1981; Vincent 1990), grain dynamics in microgel concentrated suspensions (Sessoms *et al.* 2009; Meeker *et al.* 2004), Debye layers(Bouzigues *et al.* 2008), grafted brush structure (de Gennes 1980; Murat & Grest 1989), polymer melt near-wall behaviour (Brazhnik *et al.* 1994; Brochard & De Gennes 1992), etc.). TIRF based velocimetry has thereby the potential to open new interesting avenues in fluid dynamics research.

Nonetheless, TIRF based velocimetry suffers from a number of limitations and artefacts that have been analysed by a number of investigators (Huang *et al.* 2006*a*; Huang & Breuer 2007; Choi *et al.* 2003; Sadr *et al.* 2005, 2007; Li & Yoda 2010). The main problems are the followings:

• *Brownian wandering* Nanoparticles are subjected to Brownian motion while the exposure times, or the delay times between two successive captures are limited by the performances of the camera. During the exposure time τ (typically, one or two ms) particles explore a region equal $\sqrt{2D\tau}$, in which D is the diffusion coefficient of the particle in the fluid. Using Einstein estimate of the diffusion constant, one finds that there is an optimal scale l_{opt}, defined by

$$l_{opt} = \left(\frac{kT\tau}{3\pi\mu}\right)^{1/3} \tag{1.1}$$

for which particle radius equals to Brownian standard type deviation (here, k is the Boltzmann constant, T the absolute temperature, μ the fluid viscosity). Particles much smaller than l_{opt} develop large Brownian excursions and therefore probe large volumes. Particles larger than l_{opt} also degrade the resolution because of their size. Therefore, expression 1.1 provides a reference scale for establishing the spatial resolution that TIRF based velocimetry can achieve. It turns out that the best resolution achieved to-day (30

nm) coincides, in terms of order of magnitude, with l_{opt}. In the future, progress on the spatial resolution of TIRF based velocimetry will obviously be facilitated by progress in camera technology, but to-day the possibility of improving the situation with the existing cameras is worth being considered.

• *Biases induced by the heterogeneities of the spatial distribution of the particles.* The distribution of particles is not homogeneous in space, which generates difficulties in the interpretation of the averaged measurements. In aqueous solutions, and in typical situations, the colloidal particles seeding the flow are negatively charged and the wall develops negative surface charges. A Debye layer builds up, repelling the colloids and thus depleting the near wall region in particles (Oberholzer *et al.* 1997). Dielectrophoretic effects, pointed out recently by Yoda (Cevheri & Yoda 2014) may also contribute to shape the heterogeneity field. Other sources of inhomogeneities in the spatial distributions of the particles are diffusion gradients, inducing a drift oriented away from the wall, and closer to the walls, short range forces (Koch 1989). Since all measurements involve spatial averaging, either for statistical reasons, or because of Brownian wandering, the interpretation of the averages obtained with such heterogeneities is delicate. In the present state of the art, Yoda (Li & Yoda 2010; Li *et al.* 2006) partitioned the space into three regions, assuming homogeneity in each of them. The velocity profiles obtained with this approach, being composed, for reasons linked to Brownian motion, of only three points in the 200-500 nm range (Li & Yoda 2010), are modestly resolved. One question is whether it is possible to improve the situation, for instance by reducing the size of the intervals over which averages are determined, while ensuring acceptable statistical convergence and controlling or reducing statistical biases.

• *Polydispersity of the particle characteristics.* The particles currently used in the TIRF velocimetry experiments have polydispersivities in size, quantum efficiency and numbers of incorporated fluorophores. Since the determination of the position relies on intensity measurements, this variability impacts the accuracy at which the particles can be localized. This difficulty can in principle be eliminated by carrying out statistical averaging, provided that the heterogeneity issue raised above can be addressed. In practice, using 100-200 nm fluorescent particles, for which polydispersivity lies between 5 and 10% is acceptable, while using 20 nm, with polydispersitivities between 20-30% is problematic.

• *Position of the wall.* Determining the wall location accurately is critical, since errors made at this level impact directly the accuracy of the slip length determination. Determining the wall location necessitates separate measurements that must be made in situ, in order to keep the flow geometry and the instrumentation environment unchanged. One of the techniques consists in enhancing adsorption by adding salt (and then suppressing electrical screening), and measuring the intensity distribution of the particles adsorbed onto the wall (Li & Yoda 2010). In the present state-of-the-art, these measurements are subjected to significant uncertainties, due, mostly, to an inaccurate analysis of the bleaching process.

• *Relating particle speeds to flow speeds.* Even though the particle positions and speeds were accurately determined, the information would be not sufficient for determining the flow. Close to a wall, owing to various phenomena well documented in the literature (hindered diffusion, slowing down,...) the particle speed is not equal to the flow speed. Models must therefore be developed to convert particle speed data into flow speed data.

To-day, TIRF velocimetry has enlightened our understanding of the behaviour of Newtonian fluids close to a wall by establishing the structure of the velocity profiles and investigating how particles are transported. However, the biases and artefacts discussed above severely affect its capability to discuss slippage phenomena. The quantity charac-

terizing slippage is the slip length, i.e., for TIRF based velocimetry, the length obtained by extrapolating the velocity profiles down to zero (thus the "extrapolated slip length"). Slip length measurements have attracted the interest of a community for more than one decade and it is now well documented for the case of Newtonian fluids (Bocquet & Barrat 2007; Bocquet & Charlaix 2010*a*). Slip lengths can be taken to benchmark different techniques. At the moment, the best accuracy (based on standard type deviation) obtained on the slip length measurements by TIRF is ± 30 nm (Li & Yoda 2010; Huang *et al.* 2006*a*). This limited accuracy ranks TIRF velocimetry well below SFA (Cottin-Bizonne *et al.* 2005*a*), which currently achieves ± 2 nm, and other methods, such as pressure drop measurements (Choi *et al.* 2003) which achieves ± 5 nm. Worse, the actual TIRF-based slippage measurements do not allow to distinguish between hydrophilic and hydrophobic surfaces (Li & Yoda 2010); in another work (Huang *et al.* 2006*a*) slip lengths lying between 26 and 57 nm are found for hydrophilic surfaces, which disagrees with the generally accepted view that there is no slip on such surfaces. By failing to demonstrate a capacity to measure slip lengths with a satisfactory accuracy, one must admit that, at variance with most velocimetry techniques, TIRF-based nanovelocimetry cannot be envisioned yet as a quantitative tool for exploring flows in near-wall regions.

The objective here is to make progress on TIRF based nanovelocimetry. By using a new methodology, based on continuous tracking of the particles, along with improving the precision of some determinations, we succeeded to significantly improve the performances of TIRF based nanovelocimetry in terms of spatial resolution and measurement accuracy. In a nutshell, coupled to the accurate determination of the wall position, along with Langevin simulations for estimating the systematic biases, we reached a ± 5 nm on the slip length measurements in sucrose solutions and a ± 10 nm in water (based on 95% confidence intervals). This represents a substantial improvement compared to the state-of-the-art (Li & Yoda 2010). With these improvements, we demonstrate for the first time that TIRF based velocimetry is an outstanding *quantitative* tool for exploring flow behaviors in the first hundreds nanometers near a wall.

2. Description of the experimental set-up

The illumination system is sketched in figure 1. A laser beam (1) is initiated from a Sapphire laser (Coherent Sapphire 488-50) of wavelength 488 nm at output power 350 mW. This paralleled beam goes through an objective with 10X magnification (2) to be focused on the focal plane. A diaphragm (3) is placed on the same focal plane with 10 μm of diameter to let pass only the focused light. A lens (4) with focal length 150 mm is placed behind the orifice, with its focal plane superposed with that of the 10X objective. The beam comes out from this lens being paralleled again but with an enlarged diameter at 2 cm. The implementation of (2)(3)(4) is for producing perfectly paralleled laser beam with enlarged diameter, and eliminating lights due to unparalleled incidence and diffraction. The paralleled beam goes through a diaphragm (5), which is fixed on the table during the first step of alignment of the laser, and serves as a reference point of the beam. The component (6) is a mirror which reflects the beam at 90° and incident onto a lens (8) to be focused on its focal plane; this focal plane is shared by the lens (8) and the objective of the microscope. There is a dichroic filter cube (510 nm) situated between the lens (8) and the objective, in order to reflect the incident laser beam up to the objective. The component (6) and (8) are fixed on a rail in order to be moved together horizontally without relative displacement, the rail is regulated by a home made Labview program. The fact of moving components (6) and (8) horizontally does not impede the laser beam to be focused on the focal plane of the objective, but results in a displacement of focusing

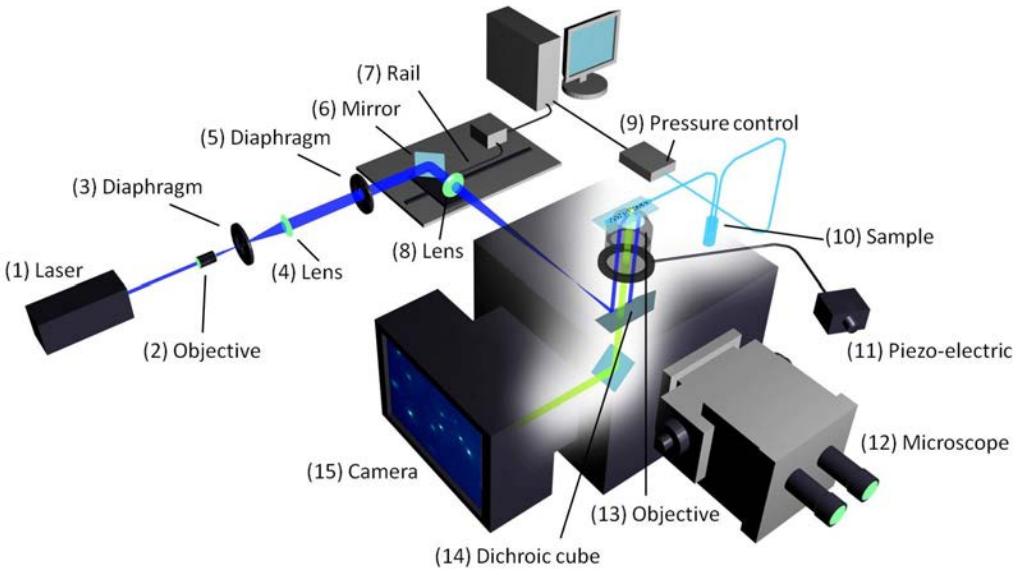

FIGURE 1. Scheme of the TIRF setup. A laser beam is collimated through a high numerical aperture objective (100X, NA=1.46) with an incidence angle higher than the critical angle for total reflection. Laser is focused in the back focal plane of the objective with an achromatic doublet (focal length=200 mm) and the incidence angle is tunable by displacing a mirror in the optical path. The evanescent wave created within the channel restricts fluorescence to tracers (dots over the glass slide) in the vicinity of the surface, which is collected by the high-speed camera.

point away from the optical line of the objective, which induces an angle of incidence different from 90° relatively to the micro channel.

The advantage of using an objective for TIRF measurement relies in the convenience of sending incident light at a supercritical angle without a prism, and retrieving fluorescence information at the same time (see Selvin & Ha (2008)). The objective has magnification 100X and a high numerical aperture at 1.46. The numerical aperture is expressed by the following equation:

$$\mathrm{NA} = n_i \sin(\Theta) \tag{2.1}$$

where n_i is the refractive index of the working medium of the objective, i.e. immersion oil ($n_i = 1.518$). Θ is the half-angle of the maximum light cone ($\theta = 74.1°$). The total reflection critical angle at the interface of water and glass slide is about 61.4° with the refractive index of water at 1.3327; and for the interface of sucrose solution at 40w% and glass slide it is 67.1° with the refractive index of sucrose solution at 1.3981. The incidence angle is measured by a glass hemisphere, which projects the light spot onto millimetre paper. This angle θ is:

$$\theta = \arctan(H/L) \tag{2.2}$$

where L is the horizontal distance between the objective and the millimetre paper board. The light spot height H is measured with a 1 mm precision, which corresponds to an error of 1 nm on the penetration length, i.e. less than 1% error on its determination.

Another advantage of using objective with large numerical aperture and oil immersion consists in the increasing number of orders of diffraction collected by the lens, which reduces the size of the Airy diffraction disk, and increases the lens resolution.

The expression of the evanescent field we apply reads, within the liquid:

$$I = I_0 \exp(-z/p) \tag{2.3}$$

in which z is the distance from the glass/liquid interface (i.e. the channel wall), p is the field depth of penetration and I_0 is the intensity of the evanescent field at $z = 0$. We use an Andor Neo sCMOS camera for the acquisition of data. It has several advantages. Firstly, it is able to work with a good sensitivity at 16 bit, which means 65 536 grey levels accessible, and so allows the distinction of two slightly different intensities. Secondly, by using the *rolling shutter mode*, we can benefit from this lower noise and acquire data at high frame rate (400 fps), as 512*512 pixels pictures are taken during the experiments, with a 2.5 ms exposure time. Operated in *overlay* mode, there is no time gap between two successive exposures, so that no information is lost. Thirdly, the camera provides 4GB of on-head image buffer, which overcomes the limitation of frame rate due to the eventually low write rate of hardware, and enables frame rates up to 400 images per second. Fourthly, the camera offers a FPGA generated hardware timestamp with the precision of 25 ns, i.e. 1% of the exposure time, which has a negligible effect on the velocity calculation. Lastly, this sCMOS camera has an amplifier for each pixel, so that there might be a slight difference of amplification rate. However, the difference of amplification rate is 0.1% in intensity, which induces 0.1% error of altitude calculation, corresponding to 0.1 nm, which is a negligible effect in the experiments. The fluids are injected with a MFCS-FLEX pressure controller by Fluigent. The maximum pressure is 1000 mbar, with 1 mbar precision (0.1% of full scale). The minimum pressure applied in water experiment is 20 mbar, which means that the source of error due to the pressure controller introduces an error on the stress calculation of maximum 5% for water, and 1% for 40w% sucrose solution, inducing a maximal error on the deduced viscosity of 5% and 1% respectively. DI water (DIW) and 40w% of sucrose solution in DIW are studied. Fluospheres particles from Invitrogen (carboxylate modified 100 nm Yellow-Green Fluorescent particles F8803, solid 2w%, 3.6×10^{13} particles/ml) are used as tracers. Their peak excitation and emission wavelengths are 505 nm and 515 nm. The particle concentration seeded in 40w% sucrose solution and DIW are respectively 0.0004w% and 0.002w% solid, so as to have up to 10 particles detected in each frame. The channel dimension is $L = 8.8$ cm in length, $w = 183$ μm in width and $h = 18.3$ μm in height. With these dimensions, the hydrodynamic resistance has the right order of magnitude to operate with flow speeds well adapted to our particle tracking system. The channel is designed in a coil shape in order to save space. With a Re on the order of 10^{-3}, inertia is neglected and the small turning points of the channel does not induce any recirculation nor instabilities. Both hydrophilic and hydrophobic surfaces are studied. Hydrophilic surfaces are prepared by treating glass slides with Piranha solution (30v/v% hydrogen peroxide and 70v/v% of sulfuric acid) heated at 300° C until degassing ends. The obtained slides are bonded to PDMS channels with O_2 plasma treatment. Hydrophobic surfaces are obtained by coating a layer of n-octadecyltrichlorosilane on a slide treated by Piranha solution (McGovern *et al.* 1994). The coated hydrophobic layer is 20 Å thick according to ellipsometry measurements. The contact angle of a DIW drop on the coated layer is 105°, measured by a surface tension determination setup KRÜSS DSA30. The roughness of the coated surface is measured by Atomic Force Microscope (figure 2): the relative roughness distributes around 0 ± 1.3 nm at half-height. The hydrophobic slide is combined with channel printed in NOA (Bartolo *et al.* 2008). NOA-made channels are preferred to PDMS to avoid the alteration of the hydrophobic coating by the plasma exposition.

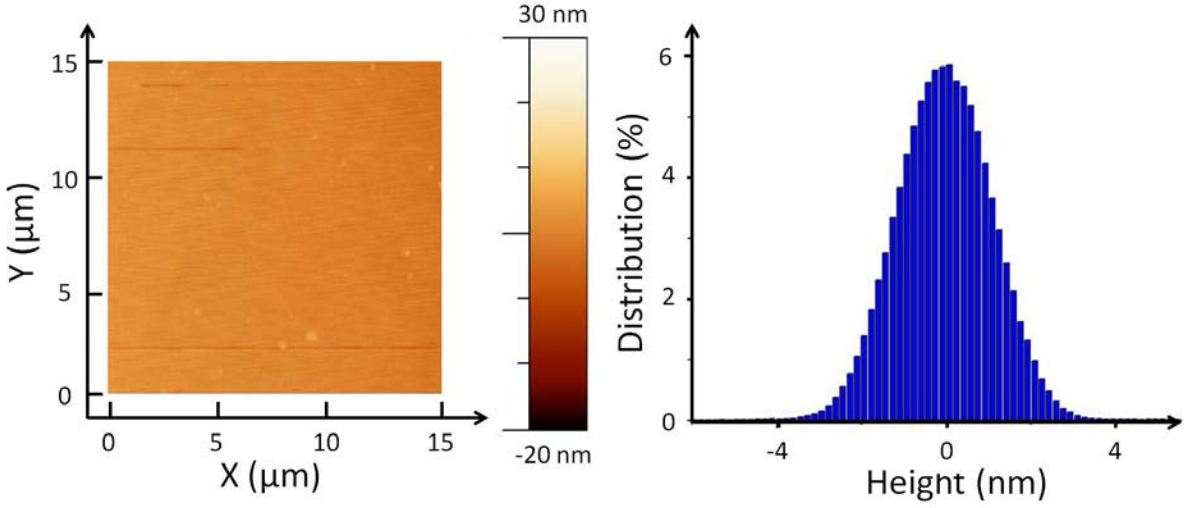

FIGURE 2. State of hydrophobic surface coated on glass slide by n-octadecyltrichlorosilane, thickness measured by AFM (left), and RMS (right) indicating the roughness distributes around 0 ± 1.3 nm at half-height.

sample	$\dot{\gamma}(s^{-1})$	$V(\mu m/s)$	Re	Pe	$\mu(mPa.s)$
Sucrose 40%w	200-600	560 - 1500	$[2;7] \cdot 10^{-3}$	0.5-1.8	6.2
Water	200-800	560 - 1800	$[10;40] \cdot 10^{-3}$	0.1-0.5	1

TABLE 1. Experimental conditions and non-dimensional numbers. $\dot{\gamma}$ the fluid shear rate. Reynolds number is defined as $Re = \rho V H/\mu$ and Peclet numbers defined as $Pe = \dot{\gamma} r_0^2/D_0$ (Guasto & Breuer 2009), where V is the average velocity of fluid in the channel, ρ density of the fluid, H height of the channel, D_0 diffusion coefficient of particles in the fluids calculated by Stokes-Einstein equation, and r_0 the particle radius. Viscosity μ is measured by conventional rheometer at $20^{\circ}C$.

3. Method of measurement of the particle locations and speeds

During the acquisition, for each five seconds long experimental run, 2000 images are taken; and for each applied pressure, 6 runs are carried out to ensure a high enough number of detected particles around 80000, which will contribute to the statistics of the data analysis. The measurement of the intensity is the averaged intensity $\bar{I}$ over the exposure time of the camera τ, with $\tau = 2.5$ ms. In this process, no particle is lost from the observation, since the two intervals of time are strictly consecutive. This represents a crucial difference with previous work (e.g. Huang *et al.* (2006*a*), Li & Yoda (2008)). The experimental conditions and characteristic numbers are summarized in table 1. An interesting quantity that we used in the discussion of the results is the shear rate $\dot{\gamma}$ which is determined by the following formula:

$$\dot{\gamma} = \frac{h\Delta P}{2\mu L} \tag{3.1}$$

where ΔP is the applied pressure and μ the fluid viscosity.

A custom made Matlab program is used to analyze the detected particles intensity and displacements. We use the tracking method developed by Bonneau *et al.* (2005).

The subpixel x and y locations are obtained by convoluting the detected intensity spot with a 2-D Gaussian template, with standard deviation $\sigma \approx 1.1$ pixels, and discretized on a support of size 5×5 pixels^2. The accuracy of coordinates determination is 0.1 pixels with a signal-to-noise ratio greater than 10 (Bonneau *et al.* 2005). This represents a spatial resolution of 6 nm. In this study of TIRFM, since the velocity close to the wall is small, and the time delay between two frames is short, the displacement of one particle from an image to the next one is much shorter than the distance between two detected particles, considering that the number of particles detected in one image is around 10 in a window of 33*33 μm. Thus an algorithm is implicated to identify the same particle which appeared in two successive images with a nearest neighbour search (Guasto & Breuer 2009), taking into account the estimated displacement and the diffusion effect. The technique is efficient, and mismatches are extremely rare events.
After particles identification, displacement between two successive frames can be calculated with a theoretical resolution of $6\sqrt{2} \approx 8$ nm. The time averaged velocity $\bar{V}_X$ and $\bar{V}_Y$ are calculated by displacement divided by time gap 2.5 ms. The time averaged intensity $\bar{I}$ is subtracted by camera background noise, and then normalized by the laser-only intensity at the pixel position. The apparent intensity of one identified particle $\bar{I}_{app}$ is the average between two successive frames: $\bar{I}_{app} = (\bar{I}_1 + \bar{I}_2)/2$ where $\bar{I}_1$ and $\bar{I}_2$ are respectively the time averaged intensity measured in the first frame (called frame 1) and in the next one (called frame 2). In general, because of Brownian motion, the particle in frame 1 has not the same altitude as in frame 2. In order to check the effect of the altitude fluctuations on the results, we have compared velocity profiles constructed with a selection of particles travelling less than 50 nm in altitude between frames 1 and 2, with profiles obtained with particles travelling up to 200 nm in altitude between the same frames. We found that the two profiles are undistinguishable. We thus did not introduce any rule of selection of particles at this level.
The apparent altitude $\bar{z}_{app}$ of the particle is inferred by using the following expression derived from (2.3):

$$\bar{z}_{app} = p \log \frac{I_0}{\bar{I}_{app}} \tag{3.2}$$

in which I_0 is the intensity emitted by a particle located at the wall, a crucial parameter deserving a separate measurement (see section 6).

The above formula allows to estimate the measurement accuracy of the apparent altitude and the resolution, i.e the capacity to distinguish between the altitudes of two strictly identical particles. Error estimates on I_0 (see below) and p being on the order of 2 nm, z_{app} is determined with a similar accuracy. On the other hand, with the camera we use and with a 10:1 signal to noise ratio, the altitude resolution we obtain is an amazing 10^{-1} nm. In practice however, the resolution is limited by statistical constraints (see below).

After these measurements are carried out for each individual particle, we proceed to statistical averaging over many particles. First, all the particles are sorted out according to their apparent altitudes $\bar{z}_{app}$. A box is an interval, along the z axis, which contains particles whose apparent altitude belongs to the interval.The box sizes represents the spatial resolution at which the velocity profile is measured. Throughout the experiments, we take box sizes on the order of a few nanometres for distances larger than 200 nm from the wall. At less than 200 nm from the wall, box sizes can reach 50 nm. The reason is that we impose that each box includes $N = 1000$ particles, so as to guarantee statistical convergence. Thereby, since there are only a few particles very close to the wall, the box sizes must be increased in that region, at the expense of the resolution.

The statistically averaged velocities and apparent altitudes, calculated in each box, are determined by the relations:

$$< \bar{V}_X > = \frac{1}{N} \sum_N \bar{V}_X \qquad ; \qquad < \bar{V}_Y > = \frac{1}{N} \sum_N \bar{V}_Y \qquad ; < \bar{z}_{app} >= \frac{1}{N} \sum_N \bar{z}_{app} \tag{3.3}$$

in which X and Y are respectively the streamwise and cross-stream coordinates, and $\bar{V}_X$ and $\bar{V}_Y$ the corresponding time averaged speeds. The summations are carried out in each box over the 1000 particles belonging to it. The raw velocity profile is defined as $< \bar{V}_X >$ vs. $< \bar{z}_{app} >$.

4. Langevin modeling of the particle trajectories and intensity measurements

In this section, we describe the stochastic Langevin equations we used to interpret our measurements. We used the same approach as Huang *et al.* (2006*b*). We consider here a population of spherical particles, with a mean radius r_0 and size dispersion σ_r, assuming a normal distribution for the radius r:

$$p_R(r) = \frac{1}{\sigma_r \sqrt{2\pi}} \exp - \frac{((r/r_0) - 1)^2}{2\sigma_r^2} \tag{4.1}$$

These particles are transported by a pure no-slip shear flow $V(z) = \dot{\gamma} z$ (where $\dot{\gamma}$ is the shear rate) close to a wall located at z=0.

The stochastic Langevin equations assign coordinates $x(t)$, $y(t)$, $z(t)$, to each particle center at time t. The particles interact with the surface charges at the wall. We must introduce zeta potentials ζ_p and ζ_w for the particles and the wall respectively to describe this effect. We neglect van der Waals forces, which act on scales much smaller than those we consider here (we checked that adding them does not affect the results of the paper). For the sake of simplicity, we work with dimensionless quantities, using the following dimensionless variables $X = x/r_0$, $Y = y/r_0$, $Z = z/r_0$ and $T = t/(r_0^2/D_0)$. Thus, $\delta T = \delta t/(r_0^2/D_0)$ is the dimensionless time increment taken for the integration of the trajectories. The discretized equations that describe the particle dynamics, originally written by Ermak & McCammon (1978), are :

$$X_{i+1} = X_i + F(Z_i)\ Pe\ Z_i\ \delta T + S\left(0, \sqrt{2\beta_x(Z_i)\delta T}\right) \tag{4.2a}$$

$$Y_{i+1} = Y_i + S\left(0, \sqrt{2\beta_y(Z_i)\delta T}\right) \tag{4.2b}$$

$$Z_{i+1} = Z_i + \left.\frac{d\beta_z}{dZ}\right|_{Z_i} \delta T + H(Z_i)\beta_z(Z_i)\delta T + S\left(0, \sqrt{2\beta_z(Z_i)\delta T}\right) \tag{4.2c}$$

in which the streamwise (β_x and β_y) and cross-stream (β_z) diffusion coefficients are defined by :

$$\beta_x(Z) = \beta_y(Z) = 1 - \frac{9}{16}Z^{-1} + \frac{1}{8}Z^{-3} - \frac{45}{256}Z^{-4} - \frac{1}{16}Z^{-5} + O(Z^{-6}) \tag{4.3a}$$

$$\beta_z(Z) = \frac{6(Z-1)^2 + 2(Z-1)}{6(Z-1)^2 + 9(Z-1) + 2} \tag{4.3b}$$

The other dimensionless functions are defined by the following expressions:

$$F(Z_i) = \frac{U(z_i)}{z_i\dot{\gamma}} \quad ; \quad H(Z_i) = \frac{F_{pw}(Z_i)r_0}{k_B\Theta} \quad ; \quad Pe = \frac{\dot{\gamma}{r_0}^2}{D_0} \tag{4.4}$$

in which $U(z_i)$ is the fluid longitudinal velocity of a particle at the height z_i.

Assuming that the wall particle interaction is described by DLVO theory, we obtain the following expression for $F_{pw}(Z_i)$:

$$F_{pw}^{el} = 4\pi\epsilon\frac{r_0}{\lambda_D}\left(\frac{k_B\Theta}{e}\right)^2\left(\frac{\hat{\zeta_p}+4\gamma\Omega\kappa r_0}{1+\Omega\kappa r_0}\right)\left[4\tanh\left(\frac{\hat{\zeta_w}}{4}\right)\right]\exp\left(-\frac{z-r_0}{\lambda_D}\right) \tag{4.5}$$

where

$$\hat{\zeta_p} = \frac{\zeta_p e}{k_B\Theta} \quad ; \quad \hat{\zeta_w} = \frac{\zeta_w e}{k_B\Theta} \quad ; \quad \gamma = \tanh\left(\frac{\hat{\zeta_p}}{4}\right) \quad ; \quad \Omega = \frac{\hat{\zeta_p}-4\gamma}{2\gamma^3} \tag{4.6}$$

and in which k_B is the Boltzmann constant, $\epsilon = \epsilon_w\epsilon_0$ is the dielectric constant of water, ζ_p and ζ_w are zeta potentials of the particles and the wall respectively, and λ_D is the Debye length.

The stochastic displacement of the particles due to Brownian motion is represented by the S function, following a normal distribution with a zero mean value and the dimensionless diffusion length $L = \sqrt{2\beta(Z)\delta T}$ as its standard deviation.

The total fluorescence intensity I emitted by the particle at time t_i must then be calculated. Here, we consider that the particle is at some distance z_f from the object plane of the objective. Bleaching is neglected, owing to the fact that the time of interest (2.5 ms) is much smaller than the fastest bleaching time (see section 6). The total intensity emitted by the particle, being proportional to the incident light intensity it collects, is thus given by the following expression:

$$I(Z) = I_0\left(\frac{r}{r_0}\right)^3\exp\left(-\frac{z}{p}\right)\frac{1}{1+\left(\frac{z-z_f}{P_c}\right)^2} \tag{4.7}$$

Where the parameters have the following definition:

- I_0 is the intensity emitted by a particle of radius r_0 located at the wall, i.e. at $z = r_0$, whose center is placed at the image plane of the camera sensor, i.e. at $z = z_f$.
- P_c is the depth of field of the optical system that images the particles (Joseph & Tabeling 2005*b*). This parameter is estimated with the following formula (4.8) :

$$P_c = \frac{n\lambda_0}{\mathrm{NA}^2} + \frac{na}{\mathrm{NA}\ M} \tag{4.8}$$

in which n is the refractive index of the working medium ($n = 1.518$), λ_0 the excitation wavelength ($\lambda_0 = 488$ nm), a the pixels size of the CMOS sensor ($a = 65$ nm), NA the numerical aperture of the objective (NA = 1.46) and M the magnification (100X). The formula gives 348 nm for P_c. z_f represents the position of the image plane of the camera sensor, which is estimated to be 350 nm. The choice of this value is supported by calibration experiments (see appendix 13). The effect of defocusing has not be considered thus far by the previous investigators, which seems justified by the fact that their objectives have smaller numerical apertures.

The procedure we use mimics rigorously the experimental methodology. It decomposes into the following steps:

- We generate particles whose initial positions span a range of altitudes between 100 nm and 700 nm, with uniform distributions. This interval corresponds to the range of altitudes within which particles are detected in the experiment. Outside this range, the

particles are not detected either because of the existence of a depletion or the signal they emit is indistinguishable from the noise.

• Each particle wanders in space, and reaches some position (say, 1) after a time τ equal to the exposure time of the camera, i.e. 2.5 ms. This position is calculated by using equations 4.2. After another time τ, the particle reaches a second position (say, 2) which is calculated in the same way.

• For each particle, the intensity $I(Z)$ is temporally averaged between the initial time $t = 0$ and $t = 2\tau$, the result being I_{app}. A similar procedure applies for the altitude, leading to z_{mean} and for the horizontal coordinates of the particle.

• The apparent altitude z_{app} is calculated similarly as in equation 3.2. The formula is:

$$z_{\rm app} = r_0 + p \log \frac{I_0}{I_{app}} \tag{4.9}$$

Note that $z_{\rm app}$ is generally different from z_{mean}.

• The horizontal displacement vector of the particle between its mean positions 1 and 2 is calculated. The components of this vector are divided by the separation time (i.e. τ) to obtain the components of the apparent fluid speed, V_{xapp} and V_{yapp} as a function of z_{mean}.

• Boxes similar to the experiment are defined (see section 3). The quantities or interest (altitudes, speeds) are further averaged out statistically over thousands of particles located in each boxes. Distributions are also obtained.

A final remark concerns the stationarity of our simulations. They are not stationary, since in the course of time, the particles tend to diffuse away. Nevertheless, the escape is extremely slow (its characteristic time is a fraction of seconds, i.e. several hundreds of times the time we consider here, τ). The escape process is also slow with respect to the speed of establishment of the Debye layer, which takes only a fraction of τ to build up. Therefore, on the time scales we consider in the simulations, the leak of particles we evoke here can be neglected.

5. Using Langevin simulation to correct altitudes and speeds

Now we make use of the simulations to discuss the relation between the apparent altitude $z_a = < z_{\rm app} >$ and the apparent longitudinal speed $V_a = < V_{xapp} >$ (where the brackets mean statistical averaging in the boxes). In fact, each apparent quantity is a function of $< z_{mean} >$. Therefore, by eliminating $< z_{mean} >$, we can plot V_a in function of z_a, thus mimicking the experimental measurements we perform. The plot is shown in figure 3.

One sees that the apparent profile $V_a(z_a)$ departs from the true profile $V(z_a) = \dot{\gamma} z_a$. Close analysis shows that as a whole, the apparent profile is shifted towards the right by a few nanometers, for reasons related to the coupling between Brownian fluctuations and convexity of the function $I(z)$. On the other hand, the lower part of the apparent profile is curved upwards. This is due to the depletion in particles in the Debye layer. More explicitly, the explanation is the following: with the values we have taken in the simulations shown in figure 3, the Debye layer thickness is 22 nm. In such conditions, the depletion in particles is perceptible up to 150 nm. Particles located in the depleted layer develop smaller excursions near the wall than far from it. It follows that their apparent altitude, calculated from the nonlinear equation 4.9, is underestimated, while their apparent speed is overestimated. These particles thus stand apparently closer to the wall than they are, and move apparently faster than they do. This artefact gives rise

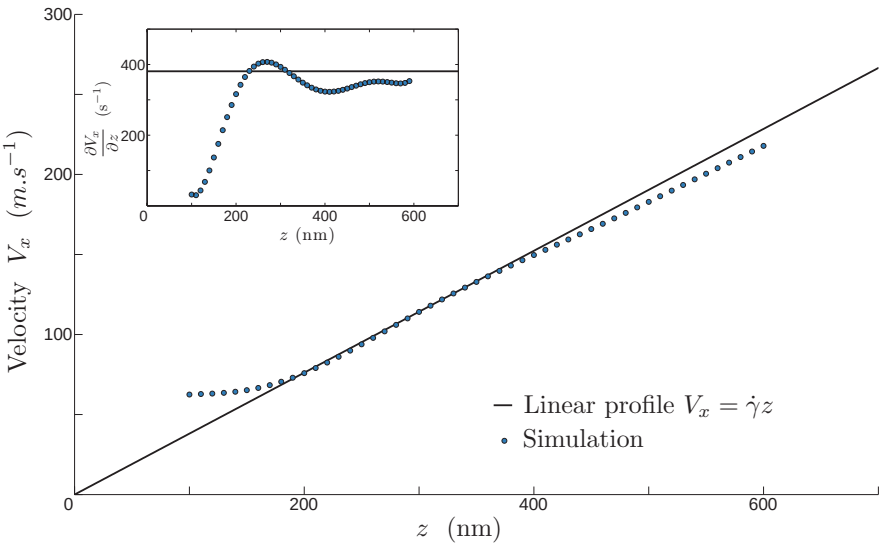

FIGURE 3. Simulated velocity profiles of sucrose $40w\%$ solution on an hydrophilic surface for an inlet pressure $p = 195$ mbar. The parameters of the simlation are $\lambda_D = 22$ nm, $P_c = 348$ nm and $z_f = 300$ nm, and $p = 124$ nm. Inset shows the local slope of the velocity profile.

to an apparent profile $V_a(z_a)$ that tends to level off as the wall is approached.
Another deviation between the apparent and expected profiles is visible at large distances, where the upper part of the profile is curved downwards. This effect originates in the fact that as we move farther from the wall, the particles become more and more unfocussed and consequently, they seem farther than they are. A consequence of defocussing is a slope reduction (down to 20%), which gives rise to an overestimate of the in situ viscosity when determined from formula 9.1. Note that these biases are small in amplitude. The consequence is that we do not need an outstanding accuracy on the calculation of the biases to correct the experimental data.

In practice, we use the function $V_a(z_a)$ to convert apparent velocity profiles into corrected profiles, which are expected to approach the "true"velocity profiles.

6. Experimental determination of I_0

I_0 is a crucial parameter that necessitates an accurate measurement. In order to measure this parameter, we analysed populations of particles physically adsorbed to the wall, thus located at $z = r$. Adsorption of many particles onto the wall is achieved by adding 0.05 M NaCl to the working fluid, thus lowering the repelling electrostatic barrier between the particle and the wall. In our method, which is different from Li & Yoda (2010), we first turn off the laser, maintain a flow, and wait for a few minutes, (i.e. in the black). This time is sufficient for the adsorption process to reach an equilibrium state, where all particles are immobilized. Then we turn the laser on, tune manually the objective position so as the particles lie in the focal plane of the TIRF objective. Throughout the procedure, a film is taken so that the instant at which the laser is switched on, along with the time at which the first well focused image of the particles is captured are known with a 23 ms accuracy. No significant amount of particles gets adsorbed to the wall nor desorbs during the time the analysis is carried out. This hypothesis is checked directly on the movie. The inset of figure 4 shows an intensity distribution obtained 138 ms after the laser is switched on.

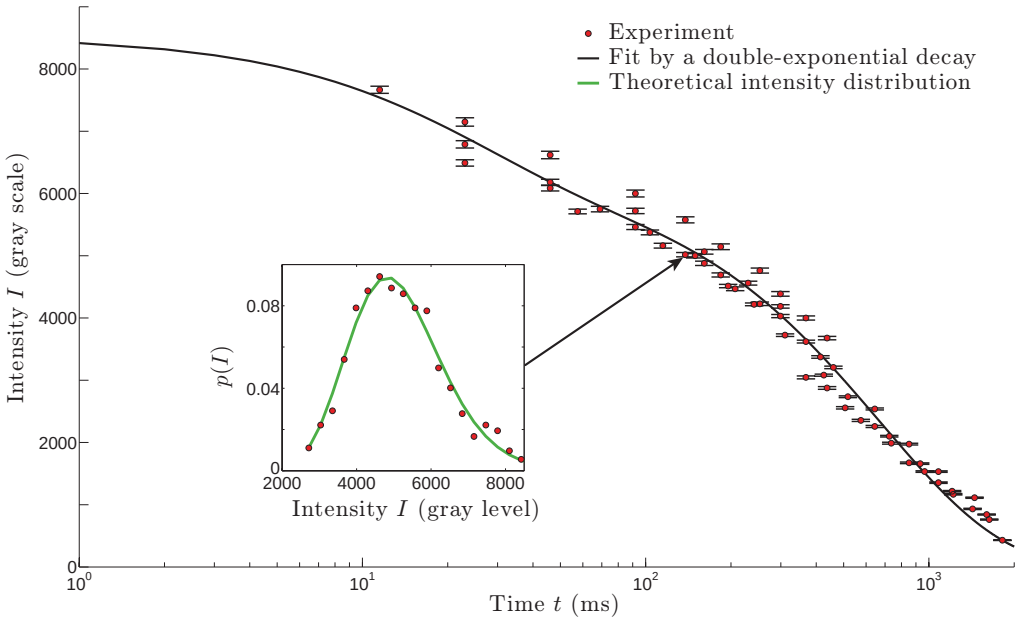

FIGURE 4. Temporal decay of the intensity $I_B(t)$ emitted by particles physically adsorbed onto the wall, whose center are thereby approximately located at $z = r$. Experimental results are fitted by equation 6.3 which corresponds to double-exponential photo-bleaching kinetics (Song *et al.* 1995, 1997), with A, B, t_1, and t_2 as free parameters. The fit parameters are $A = 2283 \pm 359$ grey values, $B = 6300 \pm 223$ grey values, $t_1 = 22.4 \pm 9.5$ ms, $t_2 = 675 \pm 49$ ms. The fit includes data obtained at $t < 1$ ms. In the insert, the red dots represent, for time $t = 138$ ms, the intensity distribution emitted by the population of particles located at the surfaces; in the same insert, the green line is a fit based on equation 6.2, from which $I_B(t)$ and σ_r are determined.

Such a distribution can be analysed theoretically. Assuming that the bleaching process is the same for all the particles, the intensity I emitted by a particle of size r, located at $z = r$, and illuminated by the laser beam for a time t, is given by the formula :

$$I = I_B(t) \left(\frac{r}{r_0} \right)^3 \tag{6.1}$$

in which $I_B(t)$ is a function that characterizes the bleaching process, assumed to apply uniformly on the particle population, independently of their sizes. In this expression, we do not take into account the fact that the particles, being of different sizes, have their centers located at different distances from the wall and therefore are illuminated with slightly different intensities. The corresponding error is on the order of $(\sigma_r r/p)^2$ i.e. 10^{-4}. Assuming further a normal distribution for the particle size, with standard type deviation σ_r, one obtains the probability density function (pdf) of the intensity emitted by an ensemble of particles located at $z = r$ at time t:

$$p_W(I,t) = \frac{r_0}{3 I_B(t) \sigma_r \sqrt{2\pi}} \left(\frac{I_B(t)}{I} \right)^{2/3} \exp - \frac{\left(\left(\frac{I}{I_B(t)} \right)^{1/3} - 1 \right)^2}{2\sigma_r^2} \tag{6.2}$$

Our expression is slightly different from Huang *et al.* (2006*a*), because we restored a factor $I^{-2/3}$ coming from a variable change, that was not taken into account. The inset of figure 4 shows that this distribution agrees well with the experiment. By comparing

the theory and the experiments, we can extract σ_r and $I_B(t)$ at each time. Regarding σ_r , the values range between 8-9% at all times, which is compatible with the data provided by the constructor (5% for the size dispersity). As mentioned in Huang *et al.* (2006*a*), the standard deviation we obtain incorporates fluctuations in the particle size, number of fluorophores and quantum efficiencies. This may explain why it stands above the sole size dispersity stated by the constructor.

The evolution of $I_B(t)$ with time is shown in figure 4. We obtain an double-exponentially decreasing function, well represented by the following formula:

$$I_B(t) = Ae^{-t/t_1} + Be^{-t/t_2} \tag{6.3}$$

This behaviour reflects that, in the range of time we consider, two time constants are needed to describe the bleaching process, consistently with the literature (Song *et al.* 1995, 1997) and at variance with Li & Yoda (2008). Figure 4 is important for the measurement we make, because it allows to check that the direct measurement of I_0 (i.e that done at $t < 1$ ms, not represented on the figure), is in excellent agreement with the value $I_B(0)$ obtained with the fit. In practice, by repeating measurements at small times, the errors on the direct measurement of I_0 are estimated on the order of $\pm$ 123 gray levels, which, translated in z-position by using formula 2.3, leads to a $\pm$ 2 nm accuracy.

In Li & Yoda (2008, 2010) the photo bleaching kinetics of fluorescent particles was not analysed with such a degree of precision. This induced a substantial error on the average value of I_0, and therefore on the measurement of the slip length.

7. Analysis of the intensity distributions and comparison with the Langevin simulations

The analysis of intensity distributions of populations of particles seeding the flow allows to confront our simulation to the experiment. The distributions shown in figure 5 represents an experiment made with a sucrose solution. The distribution is strongly skewed. There are sharp peaks on the left side, and bumps on the right wing.

The left side of the distribution represents the contributions of the dimmest particles, i.e. those located far from the wall. If particles were uniformly distributed in space, the evanescent form of the intensity field would induce a hyperbolic function for the intensity distribution, which is consistent with the observed shapes of the central part of $p(I)$. Below a certain level, no particle is detected anymore, and the distribution level collapses. The largest intensity levels probe the closest distances to the wall. The abrupt decrease of $p(I)$ at high intensity levels is linked to the existence of depleted layers in the vicinity of the wall. These depleted layers result from the action of hindered diffusion and electrostatic repulsion.

The simulation represents well the overall shape of the observed distributions. There are some discrepancies on the left side of the distribution, where the distribution of the dimmest particles seem to be imperfectly reproduced by the theory. We suggest that the discrepancy is due to the crude modeling of the conditions for which the particles cease to be observable by the camera. On the other hand, there are only small differences on the right part of the distribution, which correspond to the brightest particles, i.e those located closer to the wall. This suggests that the simplifications made in the theoretical representation of this region are acceptable. One weakness of the DLVO theory we used is that the particles are assumed pointwise, while they occupy a significant fraction of the Debye layer. Another weakness is that some parameters (such as the ζ potentials of the walls and particles) are poorly known. Still, from the viewpoint of the intensity distributions, these approximations seem acceptable.

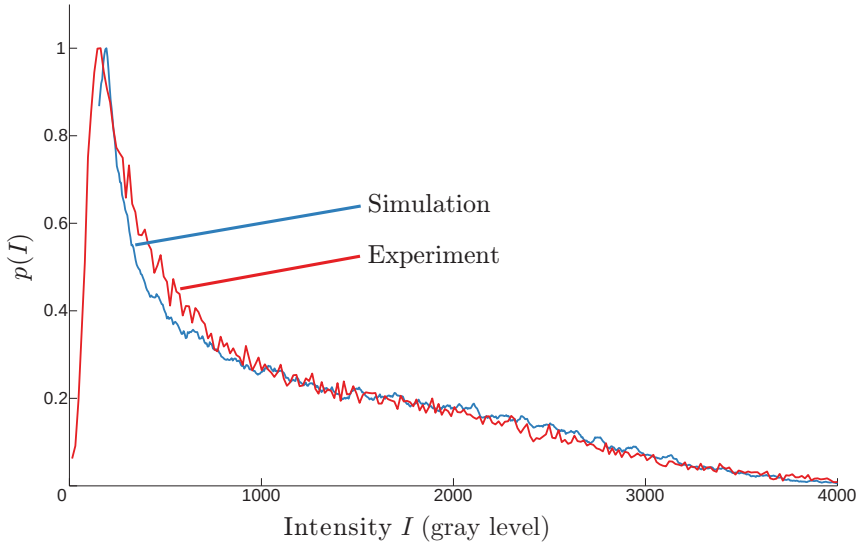

FIGURE 5. Experimental (red line) and related simulated (blue line) intensity distributions in the case of 40w% sucrose solution. Both situations correspond to an inlet pressure of 140 mbar. The simulation parameters are $\lambda_D = 22$ nm, $P_c = 348$ nm, $z_f = 300$ nm, $p = 124$ nm.

As a whole, the agreement can be considered as satisfactory. This is an important observation, which supports the idea that our Langevin model represents well the experiment, and thereby can provide reliable estimates of the existing biases. We also tested the robustness of the agreement with respect to changes in the parameters of the simulations. The lower range of intensities is sensitive to the size of the pack of particles we took for prescribing the initial conditions of the simulation. Likewise, in the upper range of intensity levels, a similar comment can be made regarding the sensitivity of the form of the distribution to the choice of the Debye layer thickness λ_D. Nonetheless, although quantitative differences may exist when the simulation parameters are not adequately chosen, the structures of the calculated distributions shown in figure 5 are robust. Moreover, changing the aforementioned parameters within a realistic range of values does not affect the velocity profiles outside the Debye layer. As a consequence, for the rest of the paper, we will concentrate ourselves on a range of altitudes lying between 200 nm and 600 nm for sucrose, 150 nm and 500 nm for water, for which the particles are sufficiently far from the wall to be insensitive to the detailed characteristics of the Debye layer, and more generally, for which the simulated velocity profiles are robust with respect to moderate changes of the simulation parameters.

8. Analysis of the velocity distributions and comparison with the Langevin simulation

A typical transverse velocity distribution (i.e. along y), averaged across the z interval 100 – 600 nm, is shown in figure 6, and compared with the Langevin simulation. Both agree well.

It is interesting to note that V_y distribution is more peaked than a Gaussian curve, indicating that small V_y events are more probable than they would be for a Gaussian process. In fact, here, we look at the travelled distance along y made by a large number of particles launched at the origin, after a time τ. Within the range of time we considered, the process apparently keeps the memory of the initial condition, giving rise to a cusp of

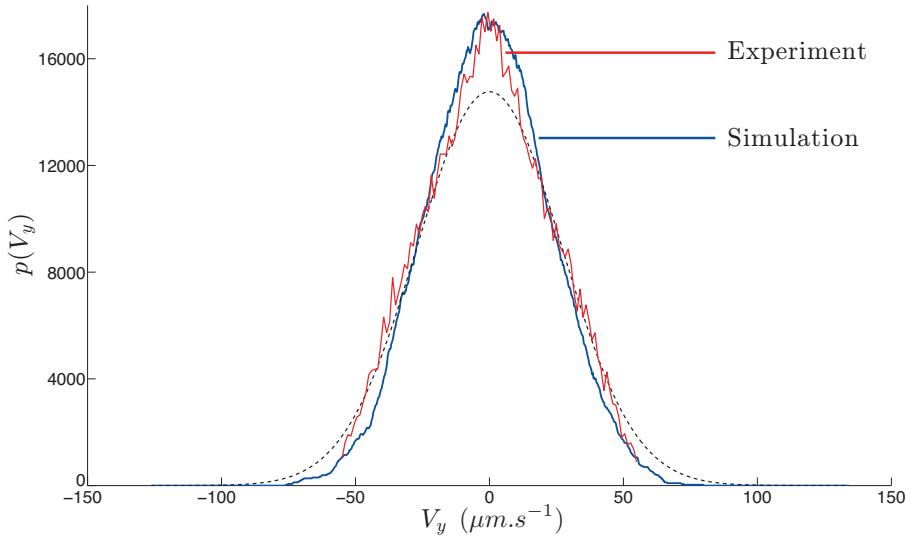

FIGURE 6. Transverse velocity V_y distribution. Red and blue lines correspond respectively to experimental and simulated data. The dotted line is the Gaussian distribution with standard deviation $\sigma_v = \left(\frac{2D}{\tau}\right)^{\frac{1}{2}}$.

the pdf around the origin. Since the distribution is not Gaussian, the diffusion constant associated to the V_y distribution, is given by the following formula:

$$D = \frac{{\sigma_v}^2 \tau}{\alpha} \tag{8.1}$$

with σ_v being the standard deviation corresponding to the Gaussian distribution and $\alpha \approx 1.2$. Applying this formula in the experiments, we found diffusion constants in satisfactory agreement with the expectations.

9. Raw velocity profiles and raw viscosities

The raw velocity profiles $V_x(z_a)$ are shown in figure 7 for the sucrose solution and water, pressures, as a function of the apparent altitude z_a. These profiles represent the raw data we obtained, i.e. those without corrections. Between 200 nm and 500 nm, the profiles are approximately linear in z_a. This is explained by the fact that on the scales we consider, the curvature of the Poiseuille profile is not visible and consequently, the profiles must be straight.

Nonetheless, on looking in more detail, there is a systematic tendency to curve downwards above 500 nm. This is mainly due to defocussing, that weakens the intensity emitted by the particles, and in turn, increases their apparent altitude. Below 200 nm, the profiles tends to level off. This effect is due to the existence of a depletion zone close to the Debye layer, that favours a systematic underestimate in the measurement of the particle altitude and overestimated of speeds, as explained previously. According to the simulation, the levelling off effect is more pronounced when the Debye length is increased. This effect tends to vanish out as we move away from the walls, where the electrostatic force is out of scale, and particle concentration distribution tends to be homogeneous.

From the measurements of the profile slopes, in regions located between, typically, 200 and 600nm (where both electrostatic and defocussing biases are reduced), one may determine an apparent viscosity μ_a, through the formula (see 3.1):

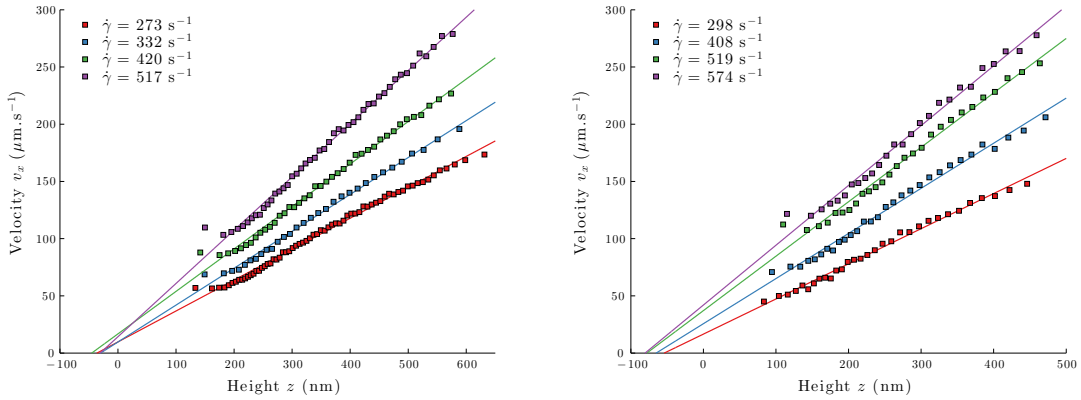

FIGURE 7. Uncorrected velocity profiles obtained with a 40w% sucrose solution, over a hydrophilic surface (left), and with water over a hydrophobic surface (right), for different pressures. Linear fits are made between 200 and 600 nm for sucrose and 150 and 500 nm for water.

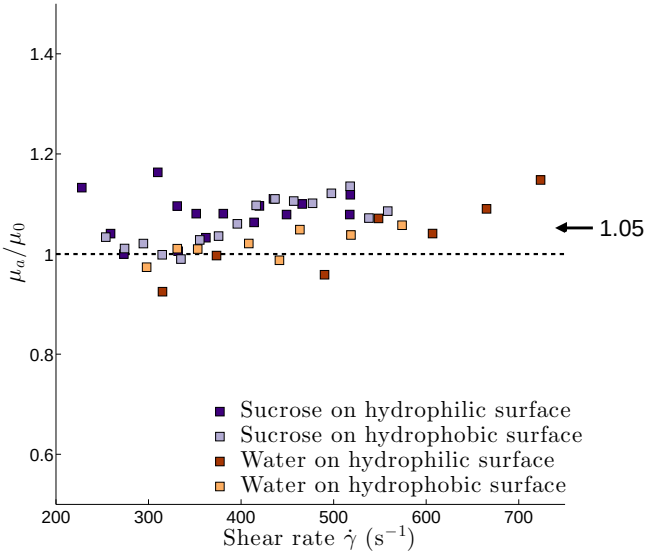

FIGURE 8. Uncorrected measurements of the ratio between the *in situ* apparent viscosity μ_a (see 9.1) over the bulk viscosity μ_0, determined independently with a rheometer. The mean deviation between the apparent and the bulk viscosity is 5%.

$$\mu_a = \frac{h\Delta P}{2\dot\gamma\ L} \tag{9.1}$$

The measurements are shown in figure 8. There are fluctuations (presumably linked to the $\pm$ 50 nm uncertainties on the determination of the location of the focal plane) but it appears that viscosities systematically tend to stand above the expected values, by amount on the order of 5%. The existence of this bias along with the order of magnitude of its importance, supports the analysis made in a precedent section.

10. Corrected velocity profiles and corrected viscosities

Figures 9 and 10 show the same set of data, but corrected, using formulas based on figure 3. The corrected data is close to the raw data, typical differences being on

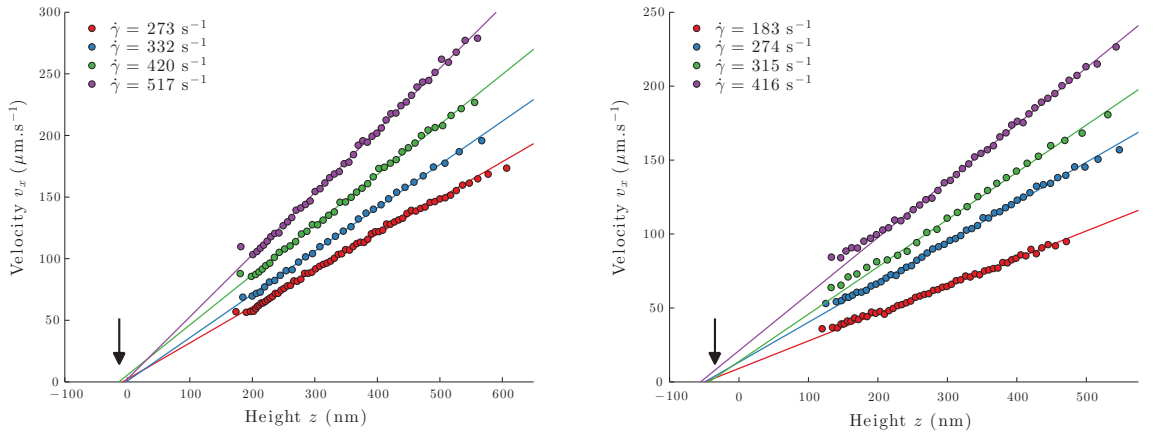

FIGURE 9. Corrected velocity profiles obtained with sucrose solution 40w%, on hydrophilic surface (left), and hydrophobic surface (right), for different pressures. The linear fit are calculated between 200 nm and 600nm. For hydrophilic walls, all profiles converge to a no-slip condition; with hydrophobic walls, they confirm the existence of slippage, with a slip length of 35 $\pm$ 5 nm.

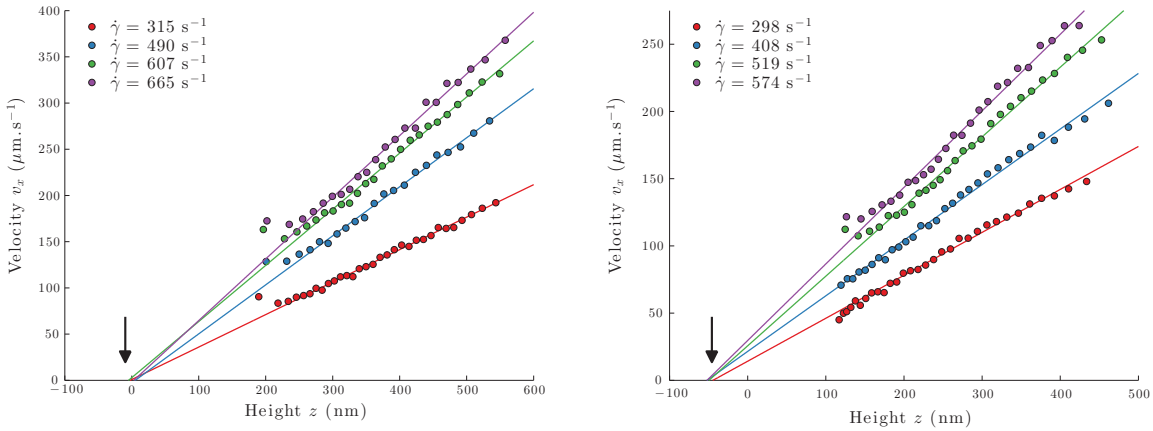

FIGURE 10. Corrected velocity profiles obtained with water, on hydrophilic surface (left), and hydrophobic surface (right), for different pressures. The linear fits are calculated between 250 nm and 500 nm for the hydrophilic case and 150 and 500 nm for the hydrophobic one.

the order of 10%. The corrected profiles are straight above about 200 nm, indicating that the tendency to curve down, as a result of defocussing, has been captured by the Langevin simulation and satisfactorily corrected. Moreover, the tendency to level off at small altitudes is less pronounced on the corrected than on the raw profiles.

The viscosities, obtained by using formula 9.1, with shear rates estimated by fitting linearly the corrected profiles, are significantly closer to the expected values, the remaining discrepancy being on the order of 1%, as shown on figure 11. These results, associated to the remarks previously made on the shapes of the corrected profiles, support the validity of our method of correction.

11. Slip length measurements

We are now in position to carry out slip length measurements. As for the viscosity, slip lengths are obtained by fitting the corrected velocity profiles with straight lines, usually restricting ourselves to the 200 – 600 nm range, and extrapolate them down to the z axis. The (extrapolated) slip lengths are then measured as a function of the shear

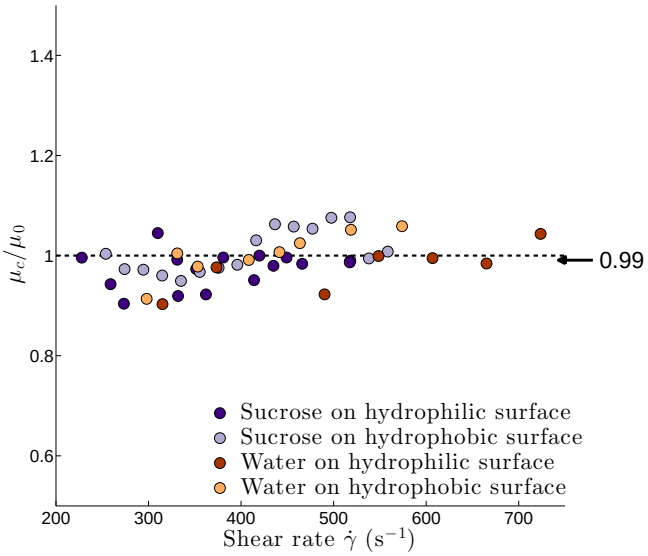

FIGURE 11. Data showing corrected values of the *in situ* measured viscosity μ_c divided by the bulk viscosity μ_0 determined independently. The graph includes data obtained with hydrophilic and hydrophobic walls. The mean statistical deviation is 1%.

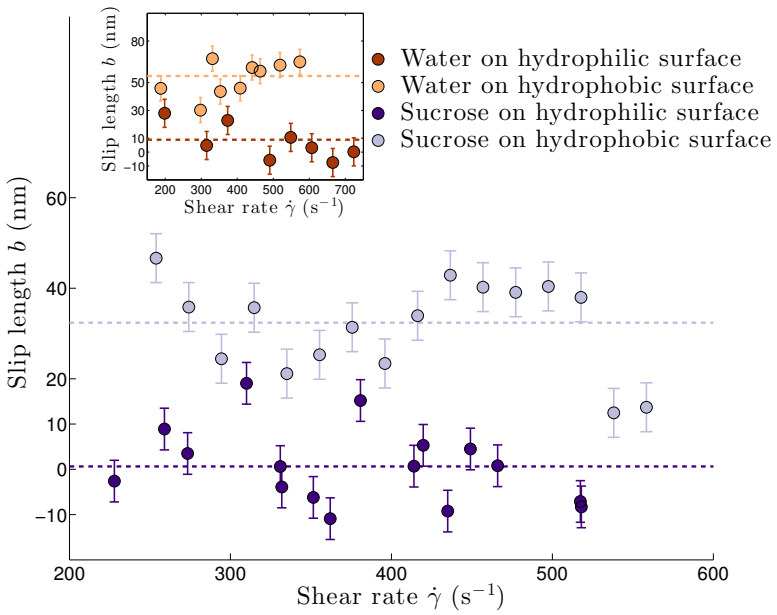

FIGURE 12. Slip lengths measurements, obtained with the sucrose solution. The insert is the case of water. In all cases, one can easily detect a difference between hydrophilic (dark dots) and hydrophobic (light dots) walls.

rate by localizing the intersections of this line with the horizontal axis, using the fit expressions.

The results are plotted in figure 12, for hydrophilic, hydrophobic walls, using water and sucrose. For hydrophilic walls, one obtains, both for water and sucrose solutions, a slip length indistinguishable from zero. For hydrophobic walls, the slip lengths are clearly above the horizontal axis. It thus appears that the nature of the wetting property of the

		Sucrose 40%w		Water	
surface		hydrophilic	hydrophobic	hydrophilic	hydrophobic
b	(nm)	1	32	9	55
Δb	(nm)	5	5	10	9
Error on viscosity	(%)	2.7	0.6	2.8	0.1

TABLE 2. Summary of our measurements made on slip lengths and viscosity errors

wall (i.e. whether it is hydrophilic or hydrophobic) is well captured by our slip length measurements, a result still not established firmly in the literature with TIRF based velocimetry, owing to the importance of the experimental uncertainties reported in the corresponding papers.

Taking the rule of 95% confidence interval, and neglecting possible variations with the shear rate of the measured quantities - an hypothesis being acceptable owing to the small range of flow rate we explored - we obtain 1 ± 5 nm and 9 ± 10 nm for hydrophilic walls (for the case of sucrose and water *resp.*) and 32 ± 5 nm and 55 ± 9 nm for hydrophobic walls (again for sucrose and water respectively). This estimate of the errors does not include that made on I_0, which was found close to 2 nm (see Section 6), and which therefore can be neglected if we assume statistical independency. The hydrophilic data agrees well with the literature (Cottin-Bizonne *et al.* 2005*b*). Hydrophobic slip lengths stand somewhat above the published values, but stay in the right order of magnitude. With our present understanding of slippage phenomena, it is impossible to claim that there is an universal curve linking slip lengths to wetting angles, that would be totally independent of the detail of the surface physico-chemistry of the wall. Our data may suggest that the slip lengths lie in a region of the slip length-contact angle plot, rather than on a line, the spread being nurtured by slight differences in the surface physico-chemistry of the boundaries.

12. Conclusion

The first outcome of this paper is about the technique. We showed that nanoPTV technique, associated to Langevin stochastic calculations, achieves unprecedented accuracies ($\pm$ 5 nm) on the determination of slip lengths, while delivering a local information, with an outstanding resolution of $\pm$ 6 nm. This marks a substantial progress as compared to the state of the art, where error bars were such that it was difficult to draw out a firm conclusion on the existence of slippage over hydrophilic or hydrophobic walls.

The reason why we succeeded to improve the accuracy of the technique is probably linked to a number of improvements concerning the determination of the wall position, the spatial resolution along with statistical conditions of measurement. It is remarkable that our Langevin simulations indicate that, with the methodology we took, systematic errors exist, but their amplitudes are small. This suggests that continuously tracking the particles represents, from the standpoint of the performances of the technique, an advantage in comparison with previous techniques. The sum of the improvements we made leads to determine the velocity profiles more accurately and consequently determine the corresponding extrapolated slip lengths with a much better accuracy.

We envision applications of our approach to non Newtonian flows, such as polymer so-

lutions, microgels concentrated suspensions or living micelles, where the technique can readily be applied. These systems, in particular the polymer solutions, deserve a confirmation of slippage measurements made in the past with less sophisticated techniques.

Moreover, our work leads to interesting results concerning slip lengths. The slip lengths we found for hydrophobic surfaces have the same order of magnitude as the literature. They also stand much above the numerical simulations. We thus confirm the unresolved discrepancy between experiments and numerical simulations (Bocquet & Charlaix 2010*b*). It challenges our understanding of the flow dynamics at nanometric distances from an interface, which in turn questions our ability to understand the physics of transport at solid/liquid interfaces in many systems, including natural ones. Owing to its importance, this unresolved issue deserves being addressed experimentally with different techniques, owing to the formidable difficulties that must be faced to perform quantitative measurements in a range of scales that touch or pertain to the nanofluidic realm.

Acknowledgments The authors thank L. Bocquet, E. Charlaix, C. Cottin-Bizonne, T. Kitamori, D. Lohse, Z. Silber-Li, M. Tatoulian, and C. Ybert for fruitful discussions and exchanges. Support from AEC, ESPCI, CNRS and UPMC is acknowledged.

Appendix A. Experiments dedicated to check the analysis of the defocussing effect

In order to support the theoretical analysis of the effect of defocusing made in section 4, we carried out dedicated experiments. We moved the position of the focal plane z_f by translating the TIRF objective with a piezo actuator (P-721 PIFOC nanopositioner controlled by E-662 LVPZT servo-amplifier, PI). At each position, we determined velocity profiles. Here, red and blue dots represent experimental data obtained with a 40w% sucrose solution for an hydrophilic wall, for two different z_f, 200 $\pm$ 50 nm and 600 $\pm$ 50 nm. The results are fitted with an expression derived from equation 4.7 :

$$V_x(z_{app}) = \dot{\gamma}\left[z_{app} - p\log\left(1+\left(\frac{z_{app}-z_f}{P_c}\right)^2\right)\right] \qquad \text{(A 1)}$$

which captures the essence of the theoretical description made in section 4. As shown in figure 13, we found that formula A 1 captures well the effect, within a range of altitudes where it is expected to apply, i.e., outside the Debye layer. These experiments provided an experimental check of the theoretical description of the defocusing effect made in section 4.

In practice, we tuned z_f between 200 and 360 nm in our Langevin model so as to minimize the curvature observed at long distances on the velocity profiles. The interval of z_f that is chosen is justified by the experimental procedure we took, which consists in adjusting the position of the objective to obtain a number of bright particles well in focus. Owing to the existence of a depletion in the Debye layer, the particles we focus on with this procedure are located, typically, between 200 and 400 nm from the wall.

REFERENCES

Bartolo, Denis, Degr, Guillaume, Nghe, Philippe & Studer, Vincent 2008 Microfluidic stickers. *Lab on a Chip* **8** (2), 274.

Bocquet, Lyderic & Barrat, Jean-Louis 2007 Flow boundary conditions from nano- to micro-scales. *Soft Matter* **3** (6), 685.

Bocquet, Lyderic & Charlaix, Elisabeth 2010*a* Nanofluidics, from bulk to interfaces. *Chemical Society Reviews* **39** (3), 1073.

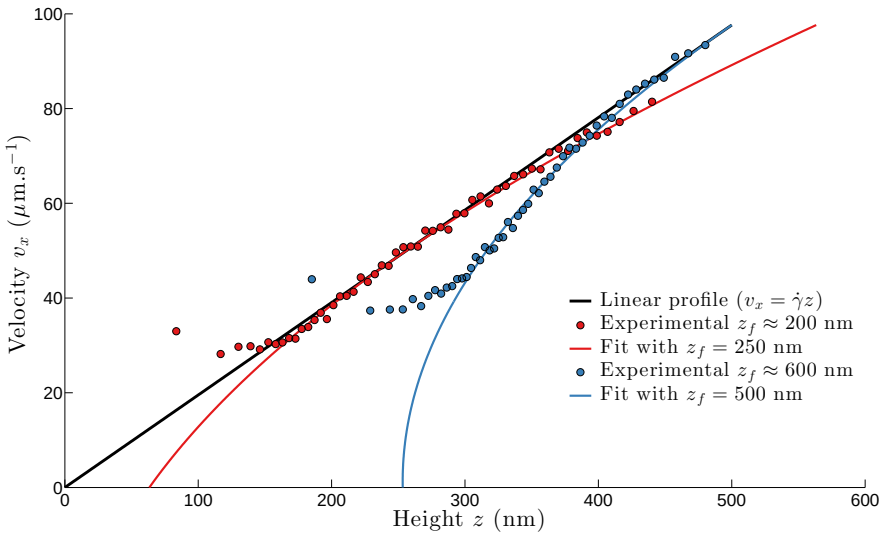

FIGURE 13. Experiments showing the velocity profiles obtained at different positions of the TIRF objective, thus at different z_f. Red dots are obtained for $z_f \approx 200$ nm and blue dots correspond to $z_f \approx 600$ nm. Full lines show good agreement between experimental data and equation A 1 within a range of altitudes where it is expected to apply, for the depth of field $a = 348$ nm of the objective.

BOCQUET, LYDERIC & CHARLAIX, ELISABETH 2010*b* Nanofluidics, from bulk to interfaces. *Chemical Society Reviews* **39** (3), 1073.

BONNEAU, S., DAHAN, M. & COHEN, L.D. 2005 Single quantum dot tracking based on perceptual grouping using minimal paths in a spatiotemporal volume. *IEEE Transactions on Image Processing* **14** (9), 1384–1395.

BOUZIGUES, C. I., TABELING, P. & BOCQUET, L. 2008 Nanofluidics in the debye layer at hydrophilic and hydrophobic surfaces. *Physical Review Letters* **101** (11), 114503.

BRAZHNIK, PAVEL K., FREED, KARL F. & TANG, HAI 1994 Polymer melt near a solid wall. *The Journal of Chemical Physics* **101** (10), 9143–9154.

BRICEO, M. I. & JOSEPH, D. D. 2003 Self-lubricated transport of aqueous foams in horizontal conduits. *International Journal of Multiphase Flow* **29** (12), 1817–1831.

BROCHARD, F. & DE GENNES, P. G. 1992 Shear-dependent slippage at a polymer/solid interface. *Langmuir* **8** (12), 3033–3037.

CEVHERI, NECMETTIN & YODA, MINAMI 2014 Electrokinetically driven reversible banding of colloidal particles near the wall. *Lab on a Chip* .

CHOI, CHANG-HWAN, WESTIN, K. JOHAN A. & BREUER, KENNETH S. 2003 Apparent slip flows in hydrophilic and hydrophobic microchannels. *Physics of Fluids (1994-present)* **15** (10), 2897–2902.

COTTIN-BIZONNE, C., CROSS, B., STEINBERGER, A. & CHARLAIX, E. 2005*a* Boundary slip on smooth hydrophobic surfaces: Intrinsic effects and possible artifacts. *Physical Review Letters* **94** (5), 056102.

COTTIN-BIZONNE, C., CROSS, B., STEINBERGER, A. & CHARLAIX, E. 2005*b* Boundary slip on smooth hydrophobic surfaces: Intrinsic effects and possible artifacts. *Phys. Rev. Lett.* **94** (5), 056102.

DE GENNES, P. G. 1981 Polymer solutions near an interface. adsorption and depletion layers. *Macromolecules* **14** (6), 1637–1644.

ERMAK, DONALD L. & MCCAMMON, J. A. 1978 Brownian dynamics with hydrodynamic interactions. *The Journal of Chemical Physics* **69** (4), 1352–1360.

DE GENNES, P. G. 1980 Conformations of polymers attached to an interface. *Macromolecules* **13** (5), 1069–1075.

GUASTO, JEFFREY S. & BREUER, KENNETH S. 2009 High-speed quantum dot tracking and velocimetry using evanescent wave illumination. *Experiments in Fluids* **47** (6), 1059–1066.

Guasto, Jeffrey S., Huang, Peter & Breuer, Kenneth S. 2006 Statistical particle tracking velocimetry using molecular and quantum dot tracer particles. *Experiments in Fluids* **41** (6), 869–880.

Hu, Guoqing & Li, Dongqing 2007 Multiscale phenomena in microfluidics and nanofluidics. *Chemical Engineering Science* **62** (13), 3443–3454.

Huang, Peter & Breuer, Kenneth S. 2007 Direct measurement of anisotropic near-wall hindered diffusion using total internal reflection velocimetry. *Physical Review E* **76** (4), 046307.

Huang, Peter, Guasto, Jeffrey S. & Breuer, Kenneth S. 2006*a* Direct measurement of slip velocities using three-dimensional total internal reflection velocimetry. *Journal of Fluid Mechanics* **566**, 447–464.

Huang, Peter, Guasto, Jeffrey S. & Breuer, Kenneth S. 2006*b* Direct measurement of slip velocities using three-dimensional total internal reflection velocimetry. *Journal of Fluid Mechanics* **566**, 447–447.

Huang, Peter, Guasto, Jeffrey S. & Breuer, Kenneth S. 2009 The effects of hindered mobility and depletion of particles in near-wall shear flows and the implications for nanovelocimetry. *Journal of Fluid Mechanics* **637**, 241–265.

Jin, S., Huang, P., Park, J., Yoo, J. Y. & Breuer, K. S. 2004 Near-surface velocimetry using evanescent wave illumination. *Experiments in Fluids* **37** (6), 825–833.

Joseph, Pierre & Tabeling, Patrick 2005*a* Direct measurement of the apparent slip length. *Physical Review E* **71** (3), 035303.

Joseph, Pierre & Tabeling, Patrick 2005*b* Direct measurement of the apparent slip length. *Phys. Rev. E* **71** (3), 035303.

Kazoe, Yutaka, Iseki, Keizo, Mawatari, Kazuma & Kitamori, Takehiko 2013 Evanescent wave-based particle tracking velocimetry for nanochannel flows. *Analytical Chemistry* **85** (22), 10780–10786.

Kimura, Yoshitsugu & Okada, Kazumi 1989 Lubricating properties of oil-in-water emulsions. *Tribology Transactions* **32** (4), 524–532.

Koch, Donald L. 1989 On hydrodynamic diffusion and drift in sheared suspensions. *Physics of Fluids A: Fluid Dynamics (1989-1993)* **1** (10), 1742–1745.

Li, Haifeng, Sadr, Reza & Yoda, Minami 2006 Multilayer nano-particle image velocimetry. *Experiments in Fluids* **41** (2), 185–194.

Li, Haifeng & Yoda, Minami 2010 An experimental study of slip considering the effects of non-uniform colloidal tracer distributions. *Journal of Fluid Mechanics* **662**, 269–287.

Li, H. F. & Yoda, M. 2008 Multilayer nano-particle image velocimetry (MnPIV) in microscale poiseuille flows. *Measurement Science and Technology* **19** (7), 075402.

McGovern, Mark E., Kallury, Krishna M. R. & Thompson, Michael 1994 Role of solvent on the silanization of glass with octadecyltrichlorosilane. *Langmuir* **10** (10), 3607–3614.

Meeker, S. P., Bonnecaze, R. T. & Cloitre, M. 2004 Slip and flow in soft particle pastes. *Physical Review Letters* **92** (19), 198302, WOS:000221540900065.

Meinhart, C. D., Wereley, S. T. & Santiago, J. G. 1999 PIV measurements of a microchannel flow. *Experiments in Fluids* **27** (5), 414–419.

Mijatovic, D., Eijkel, J. C. T. & van den Berg, A. 2005 Technologies for nanofluidic systems: top-down vs. bottom-upa review. *Lab on a Chip* **5** (5), 492.

Murat, Michael & Grest, Gary S. 1989 Structure of a grafted polymer brush: a molecular dynamics simulation. *Macromolecules* **22** (10), 4054–4059.

Oberholzer, Matthew R., Wagner, Norman J. & Lenhoff, Abraham M. 1997 Grand canonical brownian dynamics simulation of colloidal adsorption. *The Journal of Chemical Physics* **107** (21), 9157–9167.

Sadr, Reza, Hohenegger, Christel, Li, Haifeng, Mucha, Peter J. & Yoda, Minami 2007 Diffusion-induced bias in near-wall velocimetry. *Journal of Fluid Mechanics* **577**, 443–456.

Sadr, Reza, Li, Haifeng & Yoda, Minami 2005 Impact of hindered brownian diffusion on the accuracy of particle-image velocimetry using evanescent-wave illumination. *Experiments in Fluids* **38** (1), 90–98.

Sadr, R., Yoda, M., Zheng, Z. & Conlisk, A. T. 2004 An experimental study of electro-osmotic flow in rectangular microchannels. *Journal of Fluid Mechanics* **506**, 357–367.

Santiago, J. G., Wereley, S. T., Meinhart, C. D., Beebe, D. J. & Adrian, R. J. 1998 A particle image velocimetry system for microfluidics. *Experiments in Fluids* **25** (4), 316–319.

Schmid, Steven R. & Wilson, William R. D. 1995 Lubrication of aluminum rolling by oil-in-water emulsions. *Tribology Transactions* **38** (2), 452–458.

Selvin, Paul R & Ha, Taekjip 2008 *Single-molecule techniques: a laboratory manual*. Cold Spring Harbor Laboratory Press Cold Spring Harbor, NY:.

Sessoms, David A., Bischofberger, Irmgard, Cipelletti, Luca & Trappe, Vronique 2009 Multiple dynamic regimes in concentrated microgel systems. *Philosophical Transactions of the Royal Society A: Mathematical, Physical and Engineering Sciences* **367** (1909), 5013–5032, PMID: 19933125.

Song, Loling, van Gijlswijk, R. P. M., Young, I. Ted & Tanke, Hans J. 1997 Influence of fluorochrome labeling density on the photobleaching kinetics of fluorescein in microscopy. *Cytometry* **27** (3), 213223.

Song, L., Hennink, E. J., Young, I. T. & Tanke, H. J. 1995 Photobleaching kinetics of fluorescein in quantitative fluorescence microscopy. *Biophysical Journal* **68** (6), 2588–2600.

Sparreboom, W., van den Berg, A. & Eijkel, J. C. T. 2009 Principles and applications of nanofluidic transport. *Nature Nanotechnology* **4** (11), 713–720.

Tretheway, Derek C. & Meinhart, Carl D. 2002 Apparent fluid slip at hydrophobic microchannel walls. *Physics of Fluids (1994-present)* **14** (3), L9–L12.

Vincent, Brian 1990 The calculation of depletion layer thickness as a function of bulk polymer concentration. *Colloids and Surfaces* **50**, 241–249.

Zettner, C. & Yoda, M. 2003 Particle velocity field measurements in a near-wall flow using evanescent wave illumination. *Experiments in Fluids* **34** (1), 115–121.

Zheng, Xu, Kong, Gao-Pan & Silber-Li, Zhan-Hua 2013 The influence of nano-particle tracers on the slip length measurements by microPTV. *Acta Mechanica Sinica* **29** (3), 411–419.

Part II

Physics of drop formation at a step

Chapter 1

Introduction

1.1 Droplet production in 2D geometries or 2D geometry with discontinuity

1.1.1 From dripping to jetting

A fluid forced through an orifice surrounded by another immiscible fluid will break into drops by two ways. Either it forms drops at the end of the orifice, following the mechanism of dripping; or it forms a stream into the continuous phase, and breaks into drops further from the end of the orifice, which is called jetting. The transition between these two phases is influenced by factors such as viscosity, surface tension, flow rates of both fluids. Clanet and Lasheras [28] studied the case where the Bond number Bo plays an important role. Utada et al. [136] studied the case where viscosity of inner phase is 10 times smaller than that of outer phase. The transition from dripping to jetting is related with Weber number $W_{in} = \rho_{in} d_{tip} u_{in}^2/\gamma$ of inner phase, and the Capillary number $C_{out} = \eta_{out} u_{out}/\gamma$ of outer phase. A jetting state is favoured when the inner phase is under large inertial force and large viscous shear stress from the outer phase.

Our study of drop formation at a step presents a similar but different situation. Both fluids are co-flowing from a confined channel into a reservoir, drops are formed at the end of confined channel. The mechanism should be included into that of dripping, however with two distinguished phases: the step emulsification and large drops.

1.1.2 Pinching mechanism and drop size

Both theoretical and experimental works have been focused on the dynamic of pinching when a drop detaches from the nozzle or from a jet. They are reviewed in [46]. Breaking off of the drop from its initial thread is motivated by surface tension, which is the source of perturbation and tends to minimize surface energy. In the case of a jet, the fact of pinching is generally agreed to be dominated by Rayleigh instability. Assuming the fluid velocity at the nozzle is perturbed by a sinusoidal function

$$v_{nozzle} = v_j + \epsilon(\frac{\gamma}{\rho r_0})^{1/2} sin(2\pi f t) \tag{1.1}$$

where v_j the speed of the jet, and r_0 the unperturbed radius, ϵ the amplitude of small perturbation, $u_0 = (\frac{\gamma}{\rho r_0})^{1/2}$ the capillary velocity. The wave length λ can be tuned by driving frequency f, as $\lambda = v_i/f$. The dimensionless wave number $x = 2\pi r_0/\lambda$ is found by Rayleigh to play a crucial role in the development of instability, as $x = 0.697$ is a mode the most fast amplified. At low viscosity, the time scale on which surface perturbations grow is $t_0 = (\rho r_0^3/\gamma)^{1/2}$, since pinching is under the balance between surface tension and inertia. In the case of dripping, the necking effect is initiated by an outside force such as gravity in the case of dripping faucet [93], or flow rate in the case of fluid going through a capillary nozzle [136]. The Rayleigh instability serves to the final breaking off.

In terms of numerical simulation, many studies have involved the inviscid, irrotational flow for the case of low viscosity, Stokes flow for the case with high viscosity, and Navier-Stokes equation with comparable inertia and viscosity [46]. Scheele and Meister [118] performed an overall force balance on a drop during dripping or jetting. They found that below a critical nozzle velocity where the drop pinches at the tip of nozzle in forms of dripping, drop size is determined by the forces balance; while above this critical nozzle velocity, drop size is determined by stability dynamics. Tyler[135] used Rayleigh's instability theory and assumed that wave developed on the interface of two fluids is due to disturbance of the nozzle, and drop volume is determined by the wavelength. Other related studies [19, 74] have attempted to predict drop size and jet length. Richards [110] extended the study of Schelle and Meister, and performed numerical simulation by involving all forces such as viscous force, buoyancy, surface tension, inertial force, jet contraction, velocity profile relaxation, etc. into the calculation, avoiding presumption of dominant forces. This direct simulation allows prediction of drop size and jet length without separating the phenomena of drop production into different phases.

The profile of fluid during capillary pinching exhibits self-similar property [84, 151], independent from initial conditions. The shape in the last stages before breaking up is a cone with a sharp tip for inviscid fluid, and a thread for viscous fluid [120].

1.2 Production of droplets by step emulsification

A number of experimental studies have demonstrated that the step emulsification method is robust in forming droplets with sub-micron dimension, small size distribution, and easier to be paralleled during the procedure. Kobayashi et al. [75] applied the principal of step emulsification to the mass production of droplets, by designing a large number of holes through which dispersed phase flow and formed droplets in the outlets. High throughput and less than 6% size variation are achieved. Shui et al. [121] used a micro chip, in which two immiscible fluids are going through an Hele-Shaw cell with height less than 1 μm, and formed droplets at the intersection with a micro channel. The authors designed two flow rate regulators connected to both inlets of two fluids, to achieve tiny flow rate in the nano channel. Droplets size are found to be merely dependent on nano channel height. Priest et al.[108] studied droplet formation of two immiscible fluids co-flowing from a confined channel into a deep pool. According to different flow rate of both fluids and ratio of flow rate, three phases have been identified on a phase diagram: T-junction, step emulsification and jet. In the step emulsification regimes, droplet size is controlled by flow rate ratio and shallow

channel height. Droplet throughput is controlled by flow rate of dispersed phase. However, no explanation in terms of fluid dynamics was given. Sugiura et al. [126] used the step emulsification method to produce monodispersed droplets with less than 5% size deviation. The mechanism is claimed to be determined by the minimization of surface energy. Malloggi et al.[87] firstly confirmed the observation that droplet size is a function of shallow channel height. In addition, they studied more closely into the droplet formation, they discovered that the dispersed phase stream narrows during droplet formation, the width of the tip is a function of capillary number defined as: $C_a = \dfrac{6\eta U l_0}{\gamma h}$, where η the viscosity, U the velocity of dispersed phase in shallow channel, l_0 the upstream width of the dispersed stream, γ surface tension between two phases, and h height of shallow channel.

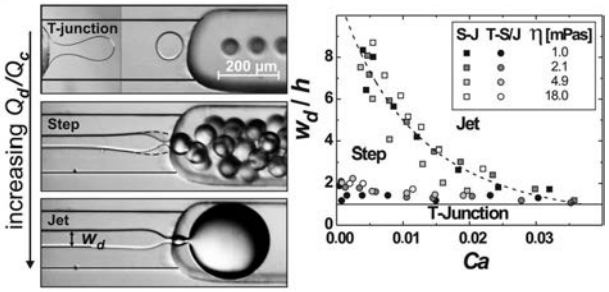

Figure 1.1: Drop formation studied by Priest et al. [108], where three regimes T-junction, step emulsification and jet are discovered, which depend on flow rate of both phases (left). Phase diagram distinguishing three regimes is plotted (right). Capillary number defined as $C_a = \eta U/\gamma$ is an important factor.

The previous studies have mostly been concentrated on experimental work of droplet production, few has been interested in physical mechanism. Our study collaborated with A. Leshansky intends to fill this gap.

1.3 Theories developed for understanding drop formation at a step

1.3.1 Previous theories on step emulsification

Dangla et al. [35] studied mechanism of step emulsification from the point of view of equivalence between fluid curvature in shallow channel with that of the bulb formed downstream of the step. They considered the situation that fluid which was confined in shallow channel flows into a less confined channel. While the bulb radius is increasing, its curvature eventually reaches a critical curvature $\kappa^* = 2/h$, with h the height of the shallow channel. After that the fluid in the shallow channel begins necking and the bulb breaks from the thread. This study achieved explaining the surface tension induced droplet formation at a step, by experimentally imposing the curvatures in both confined channels. However, it fails to distinguish the step emulsification phase with the large bubble phase while the reservoir is not confined.

Malloggi et al. [87] gave a theoretical prediction for a more genralised step emulsification production, without imposing curvature, and with distinguishment of step emulsification of small droplets and large drops phases. They defined a capillary number: $Ca \sim \frac{\mu U l_0}{\gamma b}$ and illustrated that the tip width of dispersed phase before breaking into droplets increases with the Ca. The theory is based on the experimental observation, that the dispersed phase stream narrows in the vicinity of the step, and forms a tongue-shape while delivering droplets (fig 1.2) [87]. A in-plane curvature indicates a pressure jump between the two liquids, and its formation is explained qualitatively as follow: The dispersed phase does not wet the channel, and be surrounded by a wetting fluid, both liquids flow from a shallow channel into a deep reservoir. Due to the difference of wetting between the two fluids, under the effect of a confined channel, there forms a meniscus between the two fluids, this out-plane curvature makes the pressure in dispersed phase higher than that in continuous phase, approximated to Laplace pressure $\frac{2\gamma}{b}$, with γ surface tension between two fluids and b height of shallow channel. However in the reservoir, the pressures are assumed to be equal. This means the dispersed phase has to accelerate to satisfy a higher pressure gradient. By mass conservation, the section of the inner fluid reduces near the step.

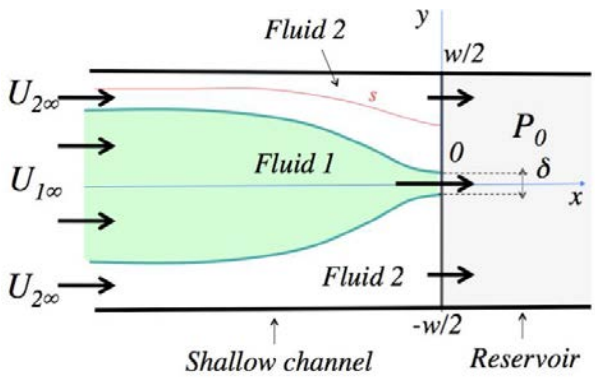

Figure 1.2: Schema of theoretical analysis of dispersed phase narrowing in the vicinity of step. The tongue tip formation is capillary effect induced.

The following theory developed by A. Leshansky, will illustrate the transition between these two phases, and droplet size dependence on other experimental conditions such as aspect ratio and flow rates.

1.3.2 Low-Ca approximative theory (by A. Leshansky)

The "Low C_a approximative theory" is developed by A.M. Leshansky and L.M. Pismen. They continue using the concept of Malloggi et al. [87], and defined two new non-dimensioned numbers:

$$Ca = \frac{12 U_{oil} \mu_{oil}}{\gamma * b} \tag{1.2}$$

with U_{oil}, μ_{oil}, γ and b relatively the velocity and viscosity of oil, surface tension between two phases and height of the shallow channel. What to mention is that the Ca is independent from the velocity of the continuous phase. Another number k is the relative viscous

importance between the two phases.

$$k = \frac{U_{water}\eta_{water}}{U_{oil}\mu_{oil}} \tag{1.3}$$

The Low-C_a asymptotic theory consists in applying the quasi-static approximation assuming gentle variation of the fluid tip width $l(x)$ in the axial direction, and derive a single non linear ODE governing the interface shape. For laminar flow at low Re, Navier-Stokes equation of two phases reduces to:

$$v_1 = -\frac{b^2}{12\mu_1} \qquad v_2 = -\frac{b^2}{12\mu_2} \tag{1.4}$$

After Hele-Shaw approximation, they become:

$$q_1 = -\frac{b^3 l}{12\mu_1}\frac{\partial p_1}{\partial x} \qquad q_2 = -\frac{b^3(w-l)}{12\mu_2}\frac{\partial p_2}{\partial x} \tag{1.5}$$

with q_1 and q_2 flow rate of two phases, p_1 and p_2 longitudinal pressure drop in two fluids, μ_1 and μ_2 viscosity of two fluids, and w the width of shallow channel. Since the pressure jump between two phases is induced by the in-plane and out-plane curvature, it can be expressed in form of $p_1 - p_2 = \frac{2\gamma}{b} - \frac{\gamma l_{xx}}{(1+l_x^2)^{3/2}} \approx \frac{2\gamma}{b} - \gamma l_{xx}$ for gentle variation in width $l_x \ll 1$. By differentiating with respect to x and introducing scaled variables, the full expression for interfacial curvature when the transversal variation of the thread profile near the step is not negligible:

$$\epsilon^{-1}\partial_\xi\left(\frac{\eta_{\xi\xi}}{(1+\eta_\xi^2)^{3/2}}\right) = \frac{1}{\eta} - \frac{k}{1-\eta} \tag{1.6}$$

When the gentle variation in the transversal direction near the step is assumed, equation 1.6 can be simplified as:

$$\epsilon^{-1}\eta_{\xi\xi\xi} = \frac{1}{\eta} - \frac{k}{1-\eta} \tag{1.7}$$

where $\epsilon = C_a(\frac{w}{b})^2$ with $\frac{w}{b}$ the aspect ratio, $\eta = l/w$ with l the tongue width of dispersed phase, $\xi = x/w$, with x longitudinal coordinate, k defined previously as relative viscous importance between two fluids. By assuming that the thread profile near the step deviates slightly from η_∞, we can write $\eta = \eta_\infty + \tilde{\eta}$, where $\tilde{\eta} \ll \eta_\infty$ is a small perturbation. Equation 1.6 and 1.7 can be linearlized as:

$$\epsilon^{-1}\tilde{\eta}_{\xi\xi\xi} + \frac{(1+k)^3}{k}\tilde{\eta} = 0 \tag{1.8}$$

Three boundary conditions are corresponded to equation 1.6, 1.7 and 1.8. First, the upstream width of the inner thread is determined by flow rates and viscosities of both phases, which results in as $\xi \to -\infty$:

$$\eta_\infty = \frac{l_\infty}{w} = \frac{1}{1+k} \tag{1.9}$$

Second, $\eta' = 0$ at the outlet as the tongue pinches to a minimum value. Third, as the pressure in the inner phase and outer phase equals at the outlet, η'' is defined as the balance between in-plane curvature $\frac{\gamma l_{xx}}{(1+l_x^2)^{1/2}}$ and out-plane curvature $\frac{2\gamma}{b}$, which induces

$\eta_{\xi\xi} = \dfrac{2w}{b}$.
An asymptotic solution is proposed in the condition when $\epsilon \ll 1$:

$$\eta \approx \frac{1}{1+k} + \alpha e^{-\lambda\xi} + \beta e^{1/2\lambda\xi}\cos(\frac{\sqrt{3}}{2}\lambda\xi) + \gamma e^{1/2\lambda\xi}\sin(\frac{\sqrt{3}}{2}\lambda\xi) \tag{1.10}$$

where $\lambda = \dfrac{(1+k)\epsilon^{1/3}}{k^{1/3}}$. $\alpha = 0$ is imposed by the first boundary condition. γ is chosen to be zero, and β is varied to satisfy the second and third boundary condition.

1.3.2.1 Transition from step emulsification to large drops

It has been observed in previous experimental studies that the production of drops exhibits a transition from step emulsification to large drops [87, 108]. The transition occurs abruptly at a specific capillary number defined in (fig 1.1) for each upstream width of inner phase. However, no analytical explanation has been provided so far. The theory developed by Leshansky and Pismen fills this gap.
In the Hele-Shaw cell near the step, $\eta \sim b/w \ll 1$, so that the second term of right-hand-side of equation 1.7 is negligible in front of first term. The equation can be simplified by rescaling $\eta = \hat{\eta}C_a^2(w/b)$, and $\xi = \hat{\xi}C_a$, which gives:

$$\hat{\eta}\hat{\eta}_{\hat{\xi}\hat{\xi}\hat{\xi}} = 1 \tag{1.11}$$

with boundary condition $\hat{\eta}_{\hat{\xi}\hat{\xi}} = 2$ at $\hat{\xi}_*$. In reality, the in-plane curvature and the out-plane curvature do not exactly balance with each other in the outlet of shallow channel, this results in the boundary condition $\eta_{\xi\xi}$ at ξ_* not exactly equals to $\dfrac{2w}{b}$, but $c\dfrac{2w}{b}$, with c a constant factor corresponding to experimental condition. So that the rescaled boundary condition reads $\hat{\eta}_{\hat{\xi}\hat{\xi}} = 2c$ at transition. The tongue width at the position of step is $\eta \approx b/w \sim Ca^{*2}(w/b)$, so that

$$Ca^*(w/b) = Const. \tag{1.12}$$

This result suggests that the transition can be described by a critical capillary number Ca^*, which multiplied by the aspect ratio of shallow channel equals to a constant value. The $Const$ is a function of c.

1.3.2.2 Droplet formation dynamics

The previously discussed asymptotic solution provides a prediction of inner phase profile near the step, with a static solution at the moment just before a droplet is delivered. In this section, a scaling law is suggested to predict the dynamic of pinching.

While a tongue width narrows, a strong transversal displacement has taken place (fig 1.3), and the assumption of unidirectional flow does not hold any more. From Navier Stokes equation at small R_e: $\bigtriangledown p = \mu\bigtriangledown^2 v$, its transversal component allows the approximation: $v \sim (dp/dy)b^2/\mu_{oil}$, where dp/dy the pressure gradient between dispersed phase and continuous phase. This pressure gradient is induced by Laplace pressure due to out-plane curvature $2\gamma/b$. At the position of the step, the in-plane curvature $\gamma h_{xx} \sim \gamma w_{i\infty}/l_0^2$ balances with the out-plane curvature. This suggests $dp/dy \sim \gamma/l_0^2$, where l_0 the longitudinal distance over

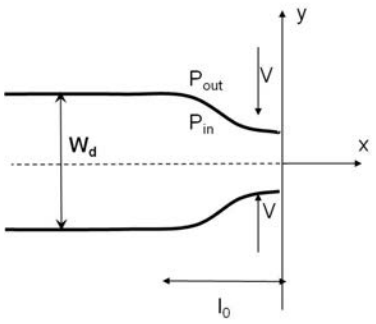

Figure 1.3: Sketch of pinching of inner phase profile near the step. A strong transversal motion undertakes at the tip of the tongue.

which the thread deforms transversally. According to the asymptotic solution of equation 1.7 at small ϵ:

$$l_0 \approx (\frac{k}{\epsilon})^{1/3} w_{i\infty} \tag{1.13}$$

where $w_{i\infty}$ the upstream width of the thread determined by flow rate ratio of two fluids $w_{i\infty} = w/(1+k)$, with w shallow channel width. Thus transversal velocity can be expressed by: $v \sim \gamma b^2/l_0^2\mu_{oil} \sim (1+k)^2/k^{2/3}$. The time of pinching is considered as $t_{drip} = w_{i\infty}/v \sim w\gamma\mu_{oil}/(l_0/b)^2$, so that

$$t_{drip} \sim C_a^{-2/3} \tag{1.14}$$

1.3.2.3 Droplet size prediction

Since the inner phase exhibits a strong deformation while producing a droplet into the reservoir, it is reasonable to attribute the droplet volume to the tongue tip deformation. A scaling law from the point of vue of surface energy is suggested to the prediction of droplet size.

During one cycle of droplet production, the oil thread firstly moves towards the step due to pressure gradient, and at the same time deforms from a sharper shape to a blunter shape (fig 2.4 from a) to b)). This fact increases the interface between oil phase and aqueous phase, so that costs the system with surface energy. The variation of surface is estimated as:

$$\Delta S_{a\to b} \sim 2w_{i\infty}l + 2bl \tag{1.15}$$

where $w_{i\infty}$ the upstream width of the oil thread, l the length over which the thread moves forward to the step, and b the height of shallow channel. The first term corresponds to the in plane surface increment during the deformation, and the second corresponds to the out plane surface increment. The delivery of a droplet is energetically favourable if the surface increment during deformation is larger than the droplet spherical surface $\Delta S_{a\to b} > S_{drop} = 4\pi r^2$. More over, the increment of volume of oil thread during deformation is estimated as $V_{a\to b} \sim w_{i\infty}bl$, which equals to the droplet volume $V_{a\to b} = V_{drop} = 4\pi r^3/3$. Solving the equation of the volume together with that of surface, the radius of smallest droplet is:

$$r_{drop} = \frac{3bw_{i\infty}}{2(b + w_{i\infty})} \tag{1.16}$$

Taking into account that k is related with oil thread upstream width as $\frac{w_{i\infty}}{w} = \frac{1}{1+k}$, and aspect ratio $\alpha = w/b$, the smallest droplet diameter normalized by shallow channel height b is expressed as:

$$\hat{d}_{drop} = \frac{3}{1 + \frac{(1+k)}{\alpha}} \tag{1.17}$$

The result indicates that the smallest droplet diameter that can be achieved by this method is $\hat{d}_{drop} \leq 3b$, in agreement with work of Malloggi et al.[87].

1.3.3 Motivation of the project

In the following study of step emulsification, we collaborate with A. Leshansky to understand the physics behind the step emulsification. We will explain for the first time, with experiments and theoretical development, the transition between step emulsification and large drop phases, predict the droplet size, pinching dynamics during the droplet formation, and tongue profiles during pinching process. We found the agreement between experiments and theory.

Chapter 2

Experimental study of step emulsification

2.1 Experimental setup

In the experiments, the dispersed phase is fluorated oil, and the continuous phase is water with sodius dodecyle sulfate (SDS) at concentration 23.4 g/l. The surface tension at the interface of this two fluids is measured as 19.17 mN/m at this concentration of surfactant, by using pendant drop method on an instrument for interfacial chemistry measurement (KRÜSS). The device is fabricated by PDMS molded from a silicon wafer with motifs realised by the method of photolithography. Since there are three different channel height corresponding to different position in the micro system, aligning techniques are necessary during the photolithography. A thin layer of PDMS is spin coated on a glass slide, and combined with the molded PDMS by plasma treatment, to achieve a four-wall PDMS channel. The device geometry is sketched in fig 2.1, it contains three entries, the one in the middle is for oil, and the two on the sides are for surfactant aqueous solution. Each of these two fluids flows through firstly an array of filters before arriving to the confined channel. This design facilitates elimination of dusts, impurities, and PDMS pieces during experimental preparation. The height of confined channel is fixed at 4.3 μm, and the aspect ratio is 8.8 and 32.6, by changing width of the channel. The width of the reservoir is 200 μm and its height is 180 μm. The flow rates are controlled with syringe pump (Nemesys) and injected by glass syringes of maximum volume 250 μl (SGE). The phenomenon are observed on a microscope (Leica) and recorded by a fast camera (Photron) at from 1000 to 15000 images per second.

2.2 Transition from step emulsification to large drops

After arriving to the shallow channel, oil is flowing in the middle position, with surfactant aqueous solution on each side. The width of oil far upstream from the step can be controlled by varying both flow rates of the two phases. The observation is focused on the upstream of the shallow channel, where the width of oil keeps constant at a fixed flow rates of two fluids, and independent from the presence of the step. Depending on flow rate of inner fluid, two phases are observed. Firstly at small flow rate Q_{oil}, small droplets are formed at a high frequency (fig 2.2), the droplets diameter is the order of shallow channel height, and

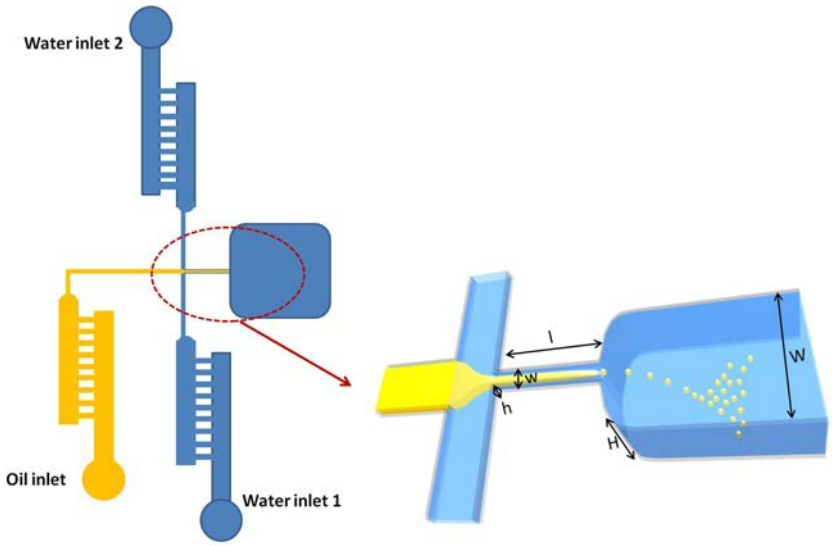

Figure 2.1: A micro chip is designed for droplet formation experiment at a step. Three inlets are connected to a in-situ filters (left), for eliminating impurities. After the filter, three streams of fluid water-oil-water will co-flow in the shallow channel, and to form drops when they reach the edge of the pool (right). Dimensions of the filters are: $h = 4.3\ \mu m$, $w = 50\ \mu m$; that of the shallow channel are $h = 4.3\ \mu m$, $w = 50\ \mu m$ and $150\ \mu m$; that of inlet channels are $H = 10\ \mu m$, $W = 300\ \mu m$, that of the chamber is $H_c = 180\ \mu m$, $W_c = 200\ \mu m$.

the frequency varies from several hundreds to thousands in our experimental condition, this procedure is named step emulsification. Whereas when the flow rate of oil exceeds a critical value, large drops are formed at low frequency. Seemann et al. observed qualitatively the same phenomenon [108].

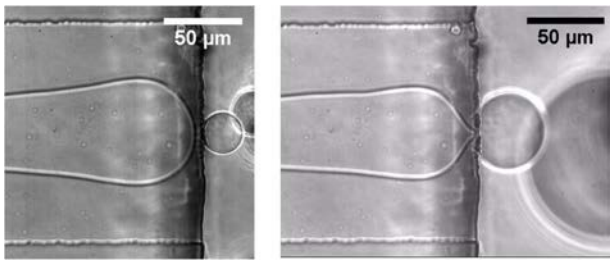

Figure 2.2: Small droplets are formed at the intersection of shallow channel and deep chamber while flow rate of dispersed phase is smaller than a critical value (left). While large drops are formed above this critical value. The transition from one phase to the other is abrupt.

In order to study the transition from the step emulsification to the large drop regime, we apply the definition of Leshansky on capillary number: C_a in equation 1.2, and the relative importance of viscous force between outer and inner phase: k in equation 1.3. Experimen-

tally, k is firstly kept constant and C_a is changed. In other words, the flow rate ratio of the two phases is kept constant, and both flow rates are varied proportionally. The width of oil in the upstream is noted, as well as the values of C_a around the transition. The same procedure is done for different values of k, and two different aspect ratio of shallow channel are tested. Fig 2.3 shows the phase diagram of the transition, plotted on upstream width of oil as function of C_a. For a fixed aspect ratio, there is a critical capillary number C_a^*, below which step emulsification is observed, and above which large drops are formed. This critical capillary number is independent from upstream width of oil, so that independent from k and flow rate of outer phase. However C_a^* is a function of aspect ratio. If the capillary number is rescaled by $C = U_{oil}\mu_{oil}/\gamma$, all the points around the transition collapse together and are consistent with results of Priest et al. [108].

To better identify the important factors on the transition, a variable change between two different definition of capillary number is realised. The definition of capillary number C_a and that of C gives equation 2.1:

$$\frac{w_d}{b} = \frac{A}{C} \tag{2.1}$$

with $A = \frac{1}{12} C_a \frac{w}{b}$, where w_d the upstream width of dispersed phase, b and w the shallow channel height and width. Fig 2.3(right) shows $\frac{w_b}{b}$ as function of C, and the points around the transition can be fitted by a reverse proportional function $\frac{w_b}{b} = \frac{0.38}{C}$, which means A is the constant 0.38. This result confirms Leshansky's prediction that the transition is defined by a critical capillary number C_a^*, which times the aspect ratio of the shallow channel equals to a constant (equation 1.12), and experiments suggests that the constant is 0.38.

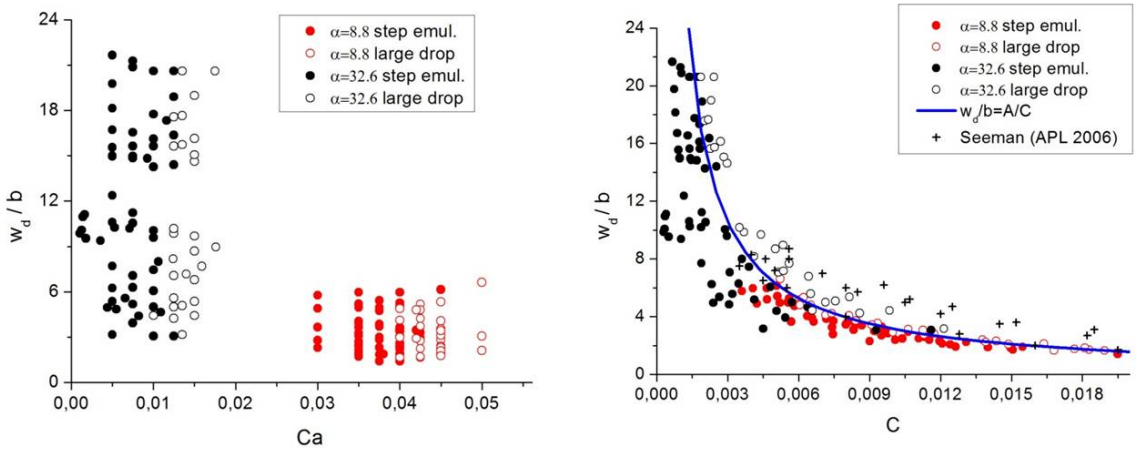

Figure 2.3: Transition from step emulsification to large drop regime is defined by a critical capillary number C_a^*, which is dependent on aspect ratio (left). Profile of transition can be fitted by a reverse proportional function, indicating that C_a^* times the aspect ratio equals to 0.38.

2.3 Step emulsification-dynamics of pinching

During the step emulsification, small droplets are formed at the step with high throughput. The whole precess is recorded by a fast camera, characteristic images are shown in fig2.4. The process is distinguished into two parts. Before a), the dispersed phase stream move forward towards the step, due to constant pressure gradient imposed by flow rate. During this period, little transversal movement can be observed, and the upstream width is kept constant. From a) to b), the stream continues move forward, but with a slight widening in the transversal direction, until it reaches the step. From b) to c), the tongue tip narrows and forms a neck, a droplet is delivered into the reservoir. It takes some time for the tongue to pinch with a certain dynamics, during this time the influx of dispersed phase supplies the droplet to grow. In this section, the physically measurable quantities during the pinching dynamic are assessed, comparison with Leshansky's scaling prediction will be performed.

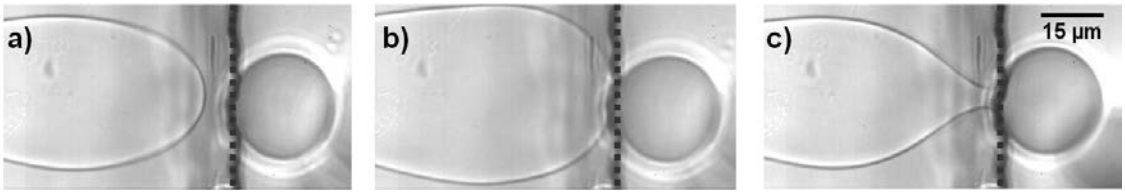

Figure 2.4: Procedure of a droplet formation. Dispersed phase stream moves forward due to imposed pressure gradient, and widens while approaching the step (a to b), then pinches to deliver a droplet (b to c). After a droplet is broken up from the stream, the stream retrieves rapidly to recover the state of a).

Capillary pinching dynamics

In the step emulsification regime, the pinching process is initiated by capillary force, and ended up by breaking of the droplet from the tongue. The dynamics of the pinching process is recorded by a fast camera, and the influence of upstream width on the velocity of pinching is assessed. Fig 2.5(a) illustrates the situation when the tongue forms a neck during pinching, and the tongue width temporal variation indicated by the arrow is measured. Fig 2.5(b) shows that the width reduction during time can be fitted by a linear function, until the tongue width reaches the value of the channel height. It means that the pinching process keeps a constant velocity, which depends on the upstream width of the tongue. The smaller upstream width exhibits faster pinching velocity, synergistic with smaller initial width to pinch, leading to a even shorter pinching time.

The time during which the dispersed phase stream pinches (b to c in fig2.4) is measured at different Ca with aspect ratio 8.8, shown in fig2.6. As the scaling law predicted by Leshansky in equation 1.14, the pinching time t_{drip} is of the order of $Ca^{-2/3}$, this scaling is confirmed by experiments on two different values of k. The transversal velocity vs. k is plotted in the inset of fig2.5, in consistence with the scaling prediction that the transversal velocity $v = w_{i\infty}/t_{drip}$ is an increasing function of k.

Contribution of deformation and influx to droplet volume

In order to investigate into determining factor on the droplet volume, the volume variation in each step of fig2.4 is studied. Firstly from a) to b), the thread elongates to reach

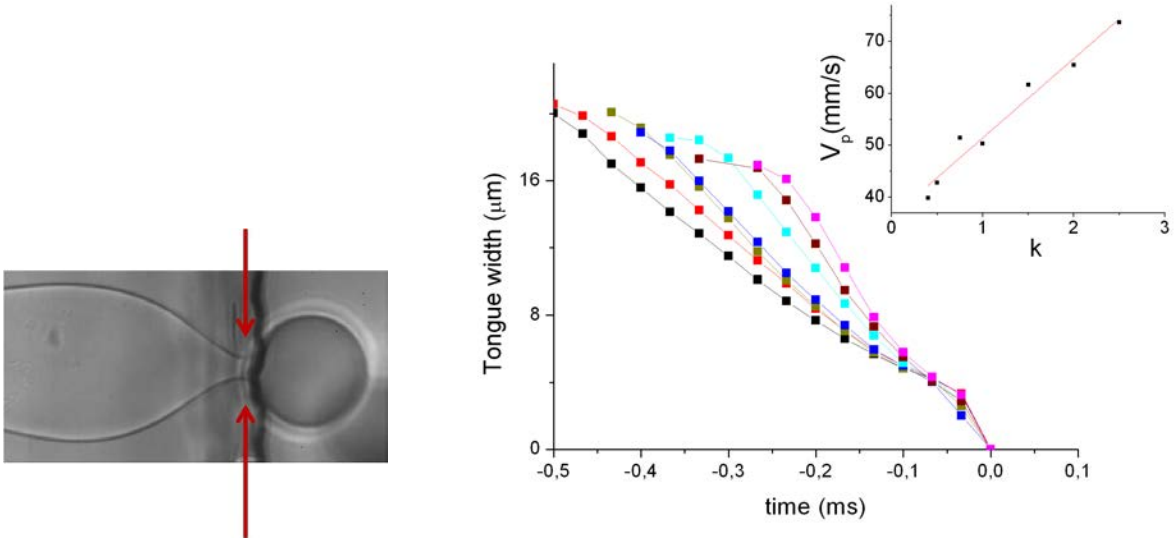

Figure 2.5: The dynamics of pinching and pinching velocity depending on upstream width. (a) shows the tongue which forms a neck during pinching, and the width variation of the neck is measured during time. (b) plots the temporal width reduction at different upstream width, and the dependence of pinching velocity on upstream width. $Ca = 0.03$, and Aspect Ratio $\alpha = 8.8$. The colours from black to purple indicate k=0.4, 0.5, 0.75, 1, 1.5, 2, 2.5, with $k = \frac{Q_{out}\eta_{out}}{Q_{in}\eta_{in}}$, increasing upstream width with smaller k. The inset of (b) shows the linear fit of pinching velocity vs. k with $V_p = 15.3k + 36$ at fitting $Adj.R - Square = 0.96$.

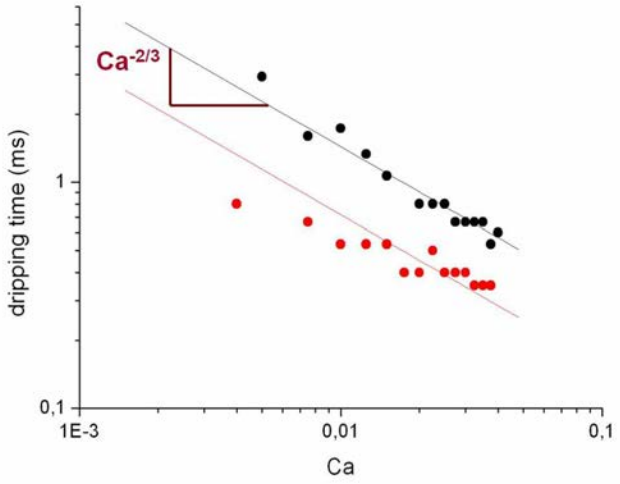

Figure 2.6: Dependence of pinching time on C_a at k=0.5 (black) and k=2 (red), and at aspect ratio $\alpha = 8.8$. The function can be fitted by $t_{drip} \sim Ca^{-2/3}$ as predicted by scaling law.

the position of step under controlled pressure gradient. Besides longitudinal movement, a transversal displacement occurs, which makes the tread deforms from a sharper shape(a) to a wider and blunter shape(b). Since the channel is shallow and satisfies Hele-Shaw requirement, the thread is under highly confined state. So that the volume variation from a) to b) is induced by a thread deformation, and can be calculated by measuring surface variation $\triangle S$ and multiplied by shallow channel height b: $V_{deform} = \triangle S \cdot b$. While from b) to c), the thread takes a certain time t_{drip} to pinch, during this time flow under imposed pressure gradient flux into the droplet. The associated volume V_{influx} can be described as the product of pinching time with the flow rate: $V_{influx} = t_{drip} Q_{oil}$.

Fig2.7 shows an example, fixing $k = 2$, aspect ratio $\alpha = 8.8$, the V_{deform} and V_{influx} are measured at different C_a. It is revealed that the V_{deform} decreases with increasing C_a, whereas the V_{influx} increases. This means at small enough C_a, the droplet formation is predominated by thread deformation due to capillary effect; When C_a is increased, the thread deformation tends to be less important, and the droplet volume is more and more supplied by the influx of oil during the pinching period. The droplet volume is measured independently, at the outlet of the shallow channel. Experiments find that even though the contribution of deformation and influx exchange importance with increasing C_a, the V_{deform} and V_{influx} compensate, and their sum equals to the droplet volume at all C_a. This compensation allows the C_a independent droplet volume.

$$V_{drop} = V_{deform} + t_{drip} Q_{oil} \tag{2.2}$$

A scaling law for the two volume contributions is built following the scaling prediction of Leshansky on pinching time t_{drip} (equation 1.14) and longitudinal distance l (equation 1.13), on which the inner phase width deviates from that in the upstream. The dimensionless

volume of influx reads:

$$\tilde{V_{influx}} = V_{influx}/b^3 \sim \Delta t_{drip} Q_{oil}/b^3 \sim (\frac{w_{i\infty}\mu_{oil}}{\gamma})(\frac{l_0}{b})^2 w_{i\infty}^2 b/b^3 \sim (\frac{w}{b})^{8/3}\frac{k^{2/3}}{(1+k)^3}C_a^{1/3} \tag{2.3}$$

The volume due to thread deformation can be estimated by $V_{deform} \sim w_{i\infty} lb$, so that the dimensionless volume of deformation

$$\tilde{V_{deform}} = V_{deform}/b^3 \sim (\frac{w}{b})^{4/3}\frac{k^{1/3}}{(1+k)^2}C_a^{-1/3} \tag{2.4}$$

The two pre-factors $(\frac{w}{b})^{8/3}\frac{k^{2/3}}{(1+k)^3}$ of V_{influx} and $(\frac{w}{b})^{4/3}\frac{k^{1/3}}{(1+k)^2}$ of V_{deform} is a function k and aspect ratio, indicating the critical C_a where occurs the interchange of volume contribution depends on k and aspect ratio. This is also verified by experiments.

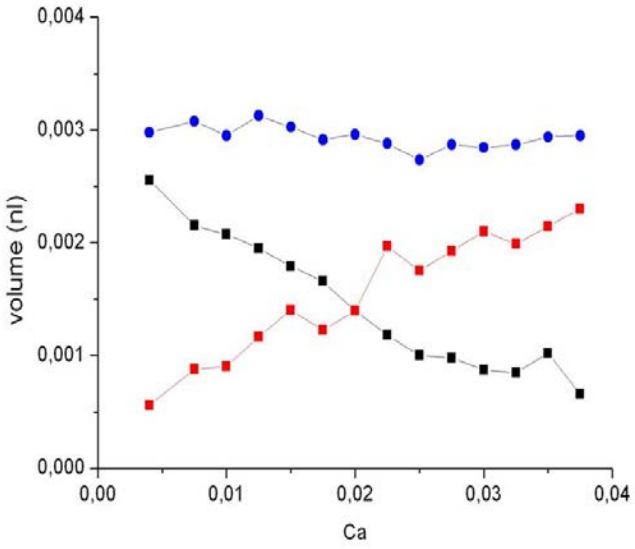

Figure 2.7: Volume due to thread deformation V_{deform} (black) decreases with C_a, whereas volume due to oil influx V_{influx} (red) increases. The two volume contribution compensate and the sum gives volume of droplet (blue), which is independent from C_a.

2.4 Droplet size

Droplet volume independent from C_a

The step emulsification method is proved to be efficient to produce monodispersed droplets [87, 108, 121]. Malloggi et al. reported that the smallest droplet diameter that can be achieved is about three times the height of the shallow channel [87]. Fig 2.8 shows the droplets volume measurement at several fixed value of k, and with increasing value of C_a (left). The droplet size is independent from C_a, but merely dependent on the value of k,

which reflects the width of oil thread in the upstream. The associated droplet delivery frequency (right) increases linearly with C_a. These results are in qualitative agreement with work of [108].

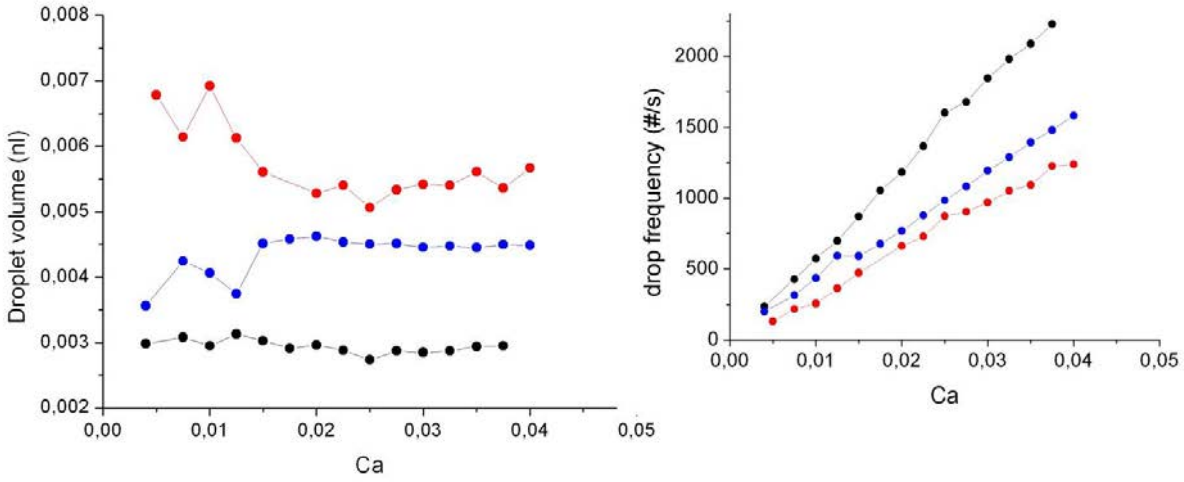

Figure 2.8: Droplet volume measurement by fixing k, and varying C_a (left). Colours corresponds to $k = 0.5$ (red), $k = 1$ (blue), $k = 2$ (black). Droplets size is independent from C_a. Corresponding droplet throughput is shown in (right).

Experiment fitted with A. Leshansky's scaling law

As shown in the previous section, that at small C_a, droplet volume is mainly contributed by the deformation of oil thread near the step, since we have just demonstrated that droplet size is independent from C_a, we can predict the droplet size in terms of deformation, by situating at low C_a. This observation provides a solid evidence to Leshansky's scaling law, which is based on the presumption that the volume of a droplet is attributed to the deformation of inner phase thread near the step (equation 1.15). The obtained result (equation 1.17) of droplet diameter has been compared with experiments in fig 2.9, in channels with aspect ratio $\alpha = 8.8$ and $\alpha = 32.6$, and for variant values of k. The experimentally measured droplet diameter is in agreement with (equation 1.17) multiplied by a factor of 2 ± 0.15.

The factor 2 ± 0.15 can be explained by the special geometry of experimental channel, which is realised by double-layer photo lithography technology, so that is asymmetric in the vertical direction. A droplet formed at the intersection of shallow channel and the reservoir is confronted by the upper wall of the deep channel, this fact inhibits the growing droplet to be vertically symmetric, and deforms the in-plane curvature of oil thread tip during its pinching in the sense to elongate time of pinching, which results in larger droplet volume.

Results and discussions can be found in the attached paper.

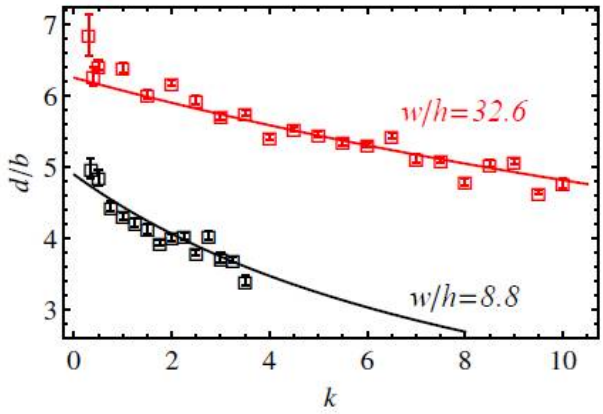

Figure 2.9: Diameter of droplets in channels with two different aspect ratios, $\alpha = 8.8$ (black), and $\alpha = 32.6$ (red). Experimental measurements (squares) are in agreement with theoretical prediction (lines) multiplied by 1.85 for α=8.8, and 2.15 for $\alpha = 32.6$.

2.5 Conclusion

In this project, we provided a comprehensive study of physics behind drop formation at a step. We defined a capillary number C_a, on which all fluid performance near the step depend. The transition point between step emulsification regime and large drop regime is defined by a critical capillary number C_a^*, which is a function of shallow channel aspect ratio. In the step emulsification regime, during droplet formation, the fact of inner phase deformation and flow rate induced dripping contribute both to a resultant droplet size. Moreover, these two contributions interchange importance while C_a is increasing. Droplet size is independent from C_a, at a fixed aspect ratio and flow rate ratio of two phases. The theory of A. Leshansky based on capillary driven low Reynolds flow in Hele Shaw cell, successfully predicts the transition between two phases, tongue profile during pinching, and with a scaling law based on surface energy, droplet size is explained with a multiplying factor. This study provides not only practical but also theoretical support to the increasing community who utilise the step emulsification method for chemical and biological application.

Step-emulsification in nanofluidic device

Z. Li[1], A. M. Leshansky[2,*] L. M. Pismen[2,3], and P. Tabeling[1]
[1] *MMN, CNRS, ESPCI Paris-Tech, 10 rue Vauquelin, 75005 Paris, France*
[2] *Department of Chemical Engineering and Russell Berrie Nanotechnology Institute, Technion – IIT, Haifa, 32000, Israel*
[3] *Minerva Center for Nonlinear Physics of Complex Systems, Technion – IIT, Haifa 32000, Israel*
(Dated: May 7, 2014)

In this paper we present a comprehensive study of the step-emulsification process for high-throughput production of (sub-)μm monodisperse droplets. The microfluidic device combines a shallow (Hele-Shaw) cell with a step-like outlet to a deep and wide reservoir. The proposed theory based on Hele-Shaw hydrodynamics provides the quasi-static shape of the free boundary between the disperse liquid phase engulfed by the co-flowing continuous phase prior to transition to oscillatory step-emulsification. At the transition the proposed theory anticipates a simple condition for the properly defined capillary number as a function of the Hele-Shaw cell geometry. The transition threshold is in excellent agreement with experimental data. A simple closed-form expression for the geometry-controlled minimal size of the droplets in step-emulsification regime, derived using simple geometric arguments also shows a very good agreement with the experimental findings.

PACS numbers: 47.55.D-, 47.55.N-, 47.61.Jd, 68.03.Cd

Introduction. Droplet-based or digital microfluidics is a fast growing interdisciplinary research area [1]. Many droplet-based microfluidic applications and technologies require high-throughput generation of monodisperse micro-droplets of controllable size. The idea to exploit the transition from confined to unconfined flow for micro-droplet generation, known as step-emulsification (SE), was first introduced in [2]. A narrow rectangular inlet channel leads to a wide and deep reservoir. The dispersed phase (non-wetting the channel walls) expands to form a tongue which grows until it reaches the step-like formation at the entrance to the reservoir. At the step the tongue expands into unconfined spherical droplet that pinches-off from the tongue. In the past years various modifications of the step-emulsification technology were studied by this group, including parallelization of inlet channels to form emulsification membrane for high-throughput droplet production [3, 4]. Other developments include droplet generation driven by a smooth "confinement gradient", i.e. gradually varying depth in [5], as opposed to a sudden (step-like) change and introduction of the co-flowing continuous phase [6–8] capable of generation of highly monosidperse μm- and sub-μm-size drops (down to attoliter droplets).

Despite the substantial technological progress, the theoretical description of SE is very limited. In [9] is was recognized that the reduction in the Laplace pressure in the tongue when the droplet expands beyond the step is responsible for the pinch-off. This mechanism was described by considering the free energy of the system. The ability of a droplet to spontaneously pinch-off/detach was calculated from the reduction in total interfacial area from before and after the droplet forms through estimating them from video images obtained using the setup described in [2]. Similar arguments were put forward in [10], where the finite element software (Surface Evolver) was used to identify the point of droplet pinch-off (as the minimum of interfacial energy) and predict the droplet size in membrane emulsification process under the assumption of quasi-static evolution.

More rigorous mathematical formulation relying on similar arguments is given in [5], whereas the explicit expression for the capillary "confinement gradient" force was derived for gently varying depth of the shallow inlet channel. It was found that, in contrast to classical gravity dripping problem (e.g. [11, 12]), the surface-tension driven droplet formation is *purely geometric*, i.e. the droplet size is independent of surface tension (provided that viscous, inertial, gravity, pressure gradients and other forces are negligibly small with respect to the surface tension forces).

In this work we shall focus on SE microfluidic technology facilitated by the co-flowing continuous phase, as was first proposed by Priest et al. [7]. In [7] an abrupt (step-like) variation in depth of the shallow Hele-Shaw (HS) channel was used to produce droplets as small as $\sim$80 μ m in diameter. No extra step-like structure of [2] is required in such case, as the confined quasi-2D tongue/stream of the inner liquid, completely engulfed by the co-flowing continuous phase is generated upstream within the HS cell at the T-junction and it extends towards the entrance to a deeper channel (i.e. "the step"). The upstream width of the engulfed tongue is controlled by the flow rate ratio of two phases and their viscosities (see the detailed analysis below). Increasing the flow rate ratio (disperse-to-continuous) they observed three distinct regimes for droplet production: (i) at low values of this ratio the breakup of the confined stream inside the shallow channel occurred right after the disperse phase is injected at the T-junction, (ii) at large values of this ratio the inner (organic) phase adopts a quasi-steady tongue shape feeding a large droplet or the balloon of the size considerably exceeding the depth of the shallow channel, until capillary instability (probably of the type described in [13])

breaks up the thread in the reservoir (the regime misleadingly named as "jetting"); (iii) at intermediate flow rate ratio the fast dripping occurs at the step yielding high-throughput production of highly monodisperse microdrops (named as "step-emulsification" regime). The transition between the regime (i) and (ii) was identified with the flow rate ratio corresponding to a critical width of the inner (organic) stream equal to the depth of the channel, i.e. diminishing the flow rate ratio the confined quasi-2D tongue becomes a cylindrical thread undergoing fast breakup due to Rayleigh-Plateau-type capillary instability.

However, the two key features of the SE process in [7] remained unanswered: (i) the mechanism/description of the capillary-number-dependent transition between SE and the "jetting" regimes; (ii) surprising controllability of the SE process: increasing the flow rates of the two fluids proportionally (i.e. increasing the capillary number) results in the linear increase in the droplet generation frequency, while the size of the produced droplets remains unaltered.

A nanofluidic SE device, capable of high-throughput production of highly monosidperse (sub-)μm size (femtoliter) drops, was later proposed by [6]. It was suggested that *capillary focusing* of the engulfed tongue tip at the step controls the size of the drops. The simplified analysis of the shape of the confined quasi-2D tongue, governed by a combination of viscous and capillary forces, showed that decreasing of the capillary number yields narrowing of the quasi-static tongue's tip in accord with the experiment.

In this paper we provide a comprehensive study of nanofluidic step-emulsification facilitated by co-flowing phases, combining theory and experiment, explaining the balloon-SE transition and offering a simple quantitative prediction for the droplet size as a function of operating parameters.

Experimental setup. The device introduced in [6] and used in this work is schematically shown in Fig. 1. Two immiscible liquids are driven through three inlets (denoted A and B in Fig. 1) towards a cross-junction and co-flow into a straight shallow (i.e. Hele-Shaw, HS) microchannel C. The inner (organic) stream does not wet the walls of the channel and thus there is a lubricating film of the continuous (aqueous) phase at the walls for all times. The two co-flowing streams arrive at a deep and wide reservoir D (as compared to a deeper channel of about the same width as the HS channel in [7]). At low enough flow rates SE regime takes place, where the tongue's tip undergoes oscillatory dripping at the step (i.e. entrance to the reservoir), generating droplets of nearly identical size. The droplet production frequency varies between tens to several kHz. In contrast to multistep splitting [14] such device allows generating microdrops of sub-μm size with very low polydispersity (less than 1% by volume) in a single step [6]. Similarly to [7],

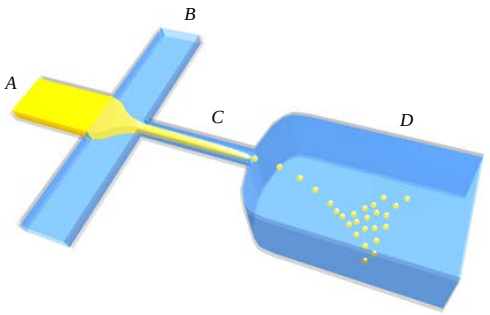

FIG. 1: Schematics of the step-emulsification nanofluidic device: inlet of disperse phase (A), inlets of the aqueous phase (B), nanofluidic Hele-Shaw channel (C), collecting reservoir (D).

increasing the flow rates of both phases results, at some point, in transition to the balloon regime.

The geometry of the of the device used in the present study is as follows: the height/depth of the HS cells is $b = 4.3$ μm, while the width was $w = 38$ μm and $w = 140$ μm (aspect ratio $w/b = 8.8$ and 32.6, respectively). The reservoir's height was 200 μm and its width 1.5 mm. The standard PDMS micro fabrication process was used. The motifs of the channels were formed on a silicon wafer by a photolithographic technology, a layer of PDMS (Sylgard) was cross-linked on the wafer, so that the motifs were printed onto PDMS. A thin layer of PDMS was spin-coated on a glass slide. PDMS with channel motif and the PDMS slide were combined by plasma treatment, which also rendered the surface hydrophilic. The channel is to be subjected to experiments immediately upon fabrication. Each inlet of the channel was connected to a syringe (SGE Analytical Science 100 μl). The flow rates of the fluids are controlled by a high-precision syringe pump (Nemesys) with minimum controlled flow rate of 1.32 nl/min. The disperse/organic phase is fluorinated oil (3M 'Fluorinert' Electronic Liquid FC3283) with dynamic viscosity of ~ 1.4 mPa·s, and the continuous/aqueous phase is the 23.4 g/l solution of Sodium Dodecyl Sulfate (Sigma Aldrich) in deionized water with viscosity of ~ 1 mPa·s. The interfacial tension of $\gamma \approx 17.86$ mN/m was measured by surface tension measuring instrument (KRUSS), using the "pendent drop" method (oil droplet immersed in the aqueous phase). The formation of droplets was recorded with a fast camera (Photron Fastcam SA3) through a Zeiss microscope.

Problem formulation. Let us start with description of the quasi-steady shape of the tongue in the balloon regime. The tongue's shape is shown schematically in Figure 2. The depth-averaged velocity fields in two immiscible liq-

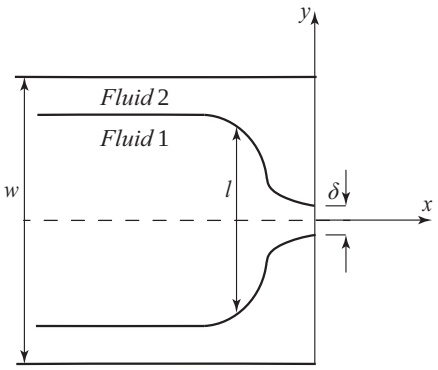

FIG. 2: Quasi-steady shape of the tongue (in the "balloon" emulsification regime) in a Hele-Shaw cell.

uids (1- inner organic phase, 2 - outer aqueous phase) are governed by the depth-averaged 2D Hele-Shaw equations

$$\boldsymbol{v}_i = -\frac{b^2}{12\mu_i}\nabla p_i, \tag{1}$$

in which $p_i(x,y)$ is the pressure in the region occupied by the fluid i of viscosity μ_i, and b is the cell depth. Here we assume that changes in the flow direction are gentle (the validity of the assumption will be discussed later based on relevant scaling) and thus the pressure across the channel width is constant (as compared to the Saffman-Taylor "finger" [15]). Thus, we can express the flow rates in both phases as (with no summation on i):

$$q_i = -\frac{b^3 w_i}{12\mu_i}\frac{dp_i}{dx}, \quad i = 1, 2, \tag{2}$$

where $w_i(x)$ is the local cell width occupied by the ith liquid.

If we define the inner fluid width as $w_1 \equiv l(x)$ and the outer as $w_2 \equiv w - l(x)$, with the channel width w, the flow rates of the two liquids (kept fixed in the experiments) read

$$q_1 = -\frac{b^3 l}{12\mu_1}\frac{dp_1}{dx}, \quad q_2 = -\frac{b^3 (w-l)}{12\mu_2}\frac{dp_2}{dx}. \tag{3}$$

At the interface between the two phases the pressure difference is equal to the capillary pressure, that is a combination of the approximately constant Laplace pressure due to a transverse (off-plane) menisci (recall that the organic inner phase does not wet the cell walls) and the pressure due to in-plane interfacial curvature varying with x,

$$p_1 - p_2 = \frac{2\gamma}{b} - \frac{\gamma\, l_{xx}}{(1+l_x^2)^{3/2}} \approx \frac{2\gamma}{b} - \gamma l_{xx}\,, \tag{4}$$

where the last approximate equality holds assuming gentle variation of the interface shape, $l_x^2 \ll 1$. Differentiating the last equation with respect to x, and substituting the pressure drop evaluated from (3) for the inner and outer liquids, we arrive at the following nonlinear ODE for the tongue's shape:

$$\gamma l_{xxx} = \frac{12\mu_1 q_1}{b^3 l} - \frac{12\mu_2 q_2}{b^3 (w-l)}\,. \tag{5}$$

Upstream from the step, at $x \to -\infty$ we have $l_{xxx} \to 0$ and $l \to w_{1\infty}$, so from (5) we can readily find the exact solution for the parallel co-flowing streams in a HS cell [18]:

$$\frac{w_{1\infty}}{w} = \frac{1}{1+k}, \quad k \equiv \frac{\mu_2 q_2}{\mu_1 q_1}. \tag{6}$$

Introducing dimensionless variables spatial $\eta = l/w$, $\xi = x/w$, Eq. (5) can written as

$$\epsilon^{-1}\,\eta_{\xi\xi\xi} = \frac{1}{\eta} - \frac{k}{1-\eta}, \tag{7}$$

where the *modified capillary number* ϵ is defined via

$$\epsilon = \frac{12\mu_1 q_1}{\gamma b w}\left(\frac{w}{b}\right)^2 \equiv \mathrm{Ca}\left(\frac{w}{b}\right)^2. \tag{8}$$

Note that the regular capillary number, $\mathcal{C} = u_{1\infty}\mu_1/\gamma$, defined with the mean upstream velocity of the inner phase $u_{1\infty}$ and used in [7], is related to Ca as $\mathrm{Ca} = 12\mathcal{C}/(1+k)$. Note also that the flow is governed by ϵ, which is equal to Ca multiplied by a large parameter $(w/b)^2 \gg 1$, emphasizing the importance of the viscous forces (due to large transverse velocity gradients) in the confined geometry. In other words, in s HS cell the flow dominated by the surface tension requires not just $\mathrm{Ca} \ll 1$, but a more restrictive condition $\mathrm{Ca} \ll (b/w)^2 \ll 1$ [22].

It can be readily seen from (7) that $l_x = \mathcal{O}(\epsilon^{1/3})$ and, therefore, the assumption of gentle variations in the flow direction requires $\epsilon^{1/3} < 1$, similarly to the well-known thin film lubrication equations (e.g. [16]). Analogous approach was applied to derive the nonlinear time-dependent ODE governing thinning of the confined symmetrical neck in the HS cell in [17]. However, in most practical cases [6, 7] ϵ is not small (even if Ca is small) due to the large factor $(w/b)^2$ multiplying Ca. One may consider using the full expression for the interfacial curvature in Eq. 4 to approximate the solution when the underlying assumption of nearly unidirectional flow (i.e. $\epsilon < 1$) is violated, yielding

$$\epsilon^{-1}\,\partial_\xi\left(\frac{\eta_{\xi\xi}}{(1+\eta_\xi^2)^{3/2}}\right) = \frac{1}{\eta} - \frac{k}{1-\eta}\,. \tag{9}$$

The parallel flow solution (6) of Eq. 7 (or Eq. 9) then reads $\eta_\infty = w_{1\infty}/w = 1/(1+k)$ as $\xi \to -\infty$.

At some distance upstream from the step, the width of the tongue η starts to deviate from constant η_∞, so

we can write $\eta = \eta_\infty + \widetilde{\eta}$, where $\widetilde{\eta} \ll \eta_\infty$ is a small perturbation. When η is close to η_∞ the Eq. 7 (or Eq. 9) can be linearized to read

$$\epsilon^{-1}\,\widetilde{\eta}_{\xi\xi\xi} + \frac{(1+k)^3}{k}\widetilde{\eta} = 0\,, \tag{10}$$

Eq. 10 can be readily solved to give

$$\eta \approx \frac{1}{1+k} + \beta \mathrm{e}^{\frac{1}{2}\lambda\xi}\cos\left(\frac{\sqrt{3}}{2}\lambda\xi\right), \tag{11}$$

where $\lambda = (1+k)\left(\frac{\epsilon}{k}\right)^{1/3}$ and β is an integration constant. In deriving (11) we used the requirement $\eta \to 1/(1+k)$ as $\xi \to -\infty$, and the invariance of the solution to the shift in the origin, so there is one free constant β. This constant is determined by the outlet conditions, i.e. $\eta_\xi = 0$ and prescribed curvature $\eta_{\xi\xi}$ at some *a priori* unknown axial distance ξ_*. If we follow [6] and assume that at the entrance to the reservoir the pressures in both phases equilibrate, and since the pressure jump across between the interface at the entrance to the reservoir is determined by Eq. 4 with $p_1 - p_2 = 0$, we arrive at $\eta_{\xi\xi} = 2(w/b)$ at the step at ξ_*. Note that this assumption is reasonable for a large droplet (with negligible Laplace pressure) inflating in the reservoir in the "balloon" regime. For a finite size droplet, however, a more general condition would be $\eta_{\xi\xi} = 2c(w/b)$ at ξ_*, where the dimensionless parameter $c \le 1$ is controlled by the complex geometry of the neck connecting the quasi-2D tongue and the emerging 3D droplet.

Balloon-SE transition and phase diagram. Our experimental findinds confirm that near at transition threshold the critical tongue's width is about the height of the HS cell, $\delta \sim b$. Figs. 3*a*, *b* show the scaled width of the tongue δ/b in the quasi-static balloon regime vs. $\mathrm{Ca} = \frac{12\mu_1 q_1}{\gamma b w}$ in two HS cells with the aspect ratio $w/b = 8.8$ and 32.6, respectively, for different values of k. It can be readily seen that in each cell, the transition to dripping occurs at the critical $\mathrm{Ca}_* = 0.042$ and 0.0125, respectively, for all k's so that $\delta/w \simeq 1$. Increasing Ca above Ca_* yields steadily growing width of the quasi-2D tongue, with rate of the grows depending on k. These results indicate that the capillary instability of the cylindrical jet as $\delta \sim b$ is likely to be responsible for the transition from the quasi-steady "balloon" regime to oscillatory SE regime. Similar mechanism was suggested to be operative in breakup of the narrow tongue, i.e. $w_{1\infty} \sim b$, upstream well inside the HS cell at low Ca's in [7].

The above experiments indicate that the transition occurs at some critical Ca_* that only varies the cell aspect ratio w/b and independent of k, i.e. of the upstream width of the tongue (see Figs. 4*b*,*c*). When the stability diagram is re-plotted in terms of $\frac{w_{1\infty}}{b} = \left(\frac{w}{b}\right)\frac{1}{k+1}$ vs. the standard capillary number, $\mathcal{C} = u_{1\infty}\mu_1/\gamma = \mathrm{Ca}(1+k)/12$, it appears to be independent of the cell aspect ratio, w/b, as both boundaries in Figs. 4*b*,*c* collapse into a single curve in Fig. 4*a*. The phase diagram in Fig. 4*a* also agrees well with the earlier results of [7]. The generic nature of the transition curve in Fig. 4*a* can be realized as follows. Given the relation between the critical Ca_* and $\mathcal{C}_*$, the transition threshold is given by

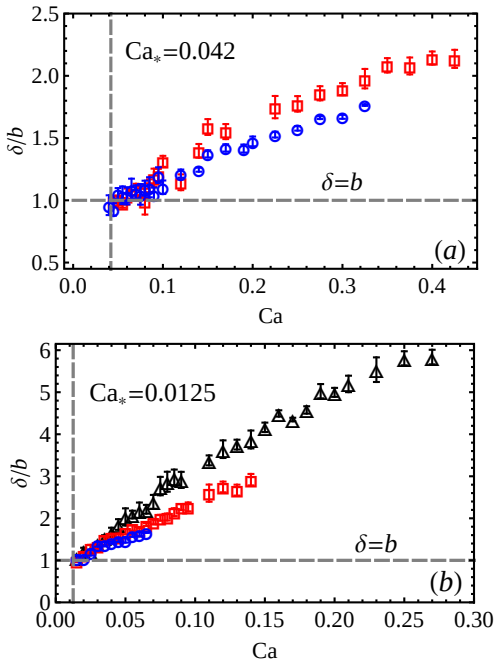

FIG. 3: The scaled tongue width at the outlet δ/w vs. Ca in a balloon regime in a HS cell (a) $w/b = 8.8$ and $k = 0.5$ (□), $k = 1$ (○); (b) $w/b = 32.6$ and $k = 1$ (△), $k = 3$ (□), $k = 6.5$ (○); the dashed lines denote the transition threshold to step-emulsification regime corresponding to $\delta \simeq b$.

$$\frac{w_{1\infty}}{b} = \frac{A}{\mathcal{C}_*}\,, \tag{12}$$

where $A = \frac{1}{12}\mathrm{Ca}_*(w/b)$, with Ca_* being the constant critical capillary that only varies with the aspect ratio. For the results (12) to be universal, (i.e. independent of the aspect ratio), we expect that $\mathrm{Ca}_*(w/b) = \mathrm{Const}$. Indeed, for $w/b = 32.6$ the critical capillary is $\mathrm{Ca}_* \approx 0.012$, while for $w/b = 8.8$ it was found that $\mathrm{Ca}_* \approx 0.042$, making the product $\mathrm{Ca}_*(w/b)$ equal to 0.39 and 0.37, respectively. Therefore the SE-balloon universal transition boundary is described by

$$\mathrm{Ca}_*\left(\frac{w}{b}\right) \simeq 0.38\,, \tag{13}$$

or alternatively by (12) with $A \approx 0.032$.

Actually, (13) readily follows from scaling of the derived ODE (7) (or Eq. 9) governing the quasi-steady

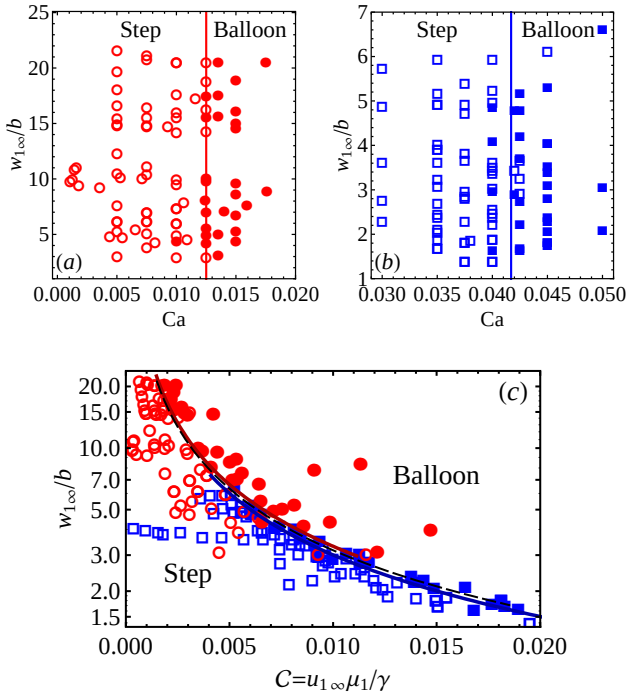

FIG. 4: Phase diagrams; the void symbols correspond to the SE regime and the filled symbols to the "balloon" regime; squares and circles stands for the channel aspect ratios $w/b = 8.8$ and $w/b = 32.6$, respectively; (a) in terms of Ca for $w/b \simeq 32.6$, the vertical line stands for transition threshold $\mathrm{Ca}_* \simeq 0.0125$;(b) in terms of Ca for $w/b \simeq 8.8$, the vertical line stands for transition threshold $\mathrm{Ca}_* \simeq 0.042$; (c) in terms of the scaled upstream width tongue width $w_{1\infty}/w$ vs. the regular capillary number $\mathcal{C}$ (log-linear plot); the solid (red and blue) lines are the boundaries re-drawn from Figs. (a) and (b), the dashed (black) line is the transition threshold (12) with $A = 0.032$.

tongue shape in the balloon regime. Near the transition the second term in the RHS is small with respect to the first one when $\eta \sim b/w \ll 1$ (for $w/b \gg k$). At the HS cell outlet at $\xi = \xi_*$ we have $\eta_{\xi\xi} = 2\mathrm{c}(w/b)$, where c is a dimensionless constant. To eliminate ϵ and w/b from the equation and the boundary condition at the cell outlet we re-scale the tongue width and the axial distance as $\eta = \widehat{\eta}\mathrm{Ca}^2(w/b)$ and $\xi = \widehat{\xi}\mathrm{Ca}$ to yield $\widehat{\eta}\widehat{\eta}_{\widehat{\xi}\widehat{\xi}} = 1$ and $\widehat{\eta}_{\widehat{\xi}\widehat{\xi}} = 2\mathrm{c}$ at $\widehat{\xi}_*$. At the transition threshold the tongue width approaching the HS cell depth, $\eta \approx (b/w) \sim \mathrm{Ca}_*^2(w/b)$, or just $\mathrm{Ca}_*(w/b) = \mathrm{Const}$, where the value of the Const is unique provided that c at the transition threshold is not varying with k. This is in agreement with (13).

Quasi-static tongue shapes. Besides predicting the correct transition threshold, the above theoretical model can also be used to compute the quasi-static shapes of the tongue in the "balloon" regime, treating c as fitting parameter. We use the asymptotic upstream solution (11) to derive a consistent set of initial conditions (η, η_ξ and $\eta_{\xi\xi}$, all depending on β) for the numerical integration of Eq. 9 as initial value problem. Thus, (9) is integrated in the direction of increasing ξ up to some (*a priori* unknown) position ξ_* by "shooting" method, i.e. fitting the value of β so that $\eta_{\xi\xi} = 2c(w/b)$ at $\xi = \xi_*$ whereas $\eta_\xi = 0$. The resulting value of $\eta(\xi_*)$ yields the width of the tongue at the nano-fluidic HS cell outlet in the quasi-steady balloon regime. The value of c giving the critical width $\eta = b/w$ at ξ_* determines the critical (negative) in-plane curvature of the tongue at the baloon-SE transition.

The sample results are depicted in Fig. 5a for $k = 0.5$, cell aspect ratio $w/b = 8.8$ for several values of ϵ: 3.48 (black), 20 (red) and 50 (blue). The fixed value of $c = 0.33$ was found to fit the critical outlet width $\eta(\xi_*) = b/w \approx 0.11$ at the balloon-SE transition at $\epsilon_* \approx 3.48$. The qualitative agreement with the experimental results (see Figs. 3) and the prediction of the analytical theory in [6] is evident: the width of the tongue tip increases with the increase in Ca, i.e. high surface tension yields better "capillary self-focusing". Note that we used $c = 0.33$ for all ϵ, while in practice upon increasing the capillary number above ϵ_* in the balloon regime, the value of c also increases, i.e. yielding higher (negative) in-plane curvature at the outlet. Recall that the limiting value $c = 1$ assumed in [6] corresponds to the maximal in-plane curvature $\eta_{\xi\xi} = 2(w/b)$. While full 3D numerical simulation (e.g. using VoF method, [19, 20]) are required in general to determine c in a self-consistent fashion, we fit the value of c numerically to best-fit the shape to the experimentally measured profiles (see Fig. 5b) showing excellent agreement between the two.

Computing the critical profiles at $\mathrm{Ca}_* = 0.38$ corresponding to $\eta(\xi_*) = b/w$ (e.g. see the solid curve in Fig. 5a) for the HS cell with $w/b = 32.6$, we found that for k varying in the wide range $k = 0.5 \div 5$ the critical in-plane curvature varies only slightly in a narrow interval $\eta_{\xi\xi} \approx 21.6 \pm 2.3$, corresponding to $c \approx 0.33 \pm 0.03$ in agreement to our previous scaling arguments for the transition threshold (13). *Therefore, decreasing Ca yields "capillary focusing", i.e. narrower outlet width of the quasi-2D tongue, δ, while the transition to oscillatory SE regime occurs at critical* Ca_* *at which* $\delta \approx b$.

Droplet size prediction in SE regime. The periodic evolution process of the droplet generation in step-emulsification regime is shown in Figs. 6. First, the tongue flows under the applied pressure gradient in the HS cell towards the step (Fig. 6a,b). The time $\Delta t_{a\to b}$ it takes for the tongue to reach the step is controlled by the flow rates of both phases. After the tongue reaches the step (as in Fig. 6b) the inner fluid is pushed into the reservoir forming a droplet, the droplet formation is accompanied by the fast narrowing of tongue's tip and considerable transverse velocities (see Fig. 6 b,c). The previous assumptions of nearly unidirectional flow in this case

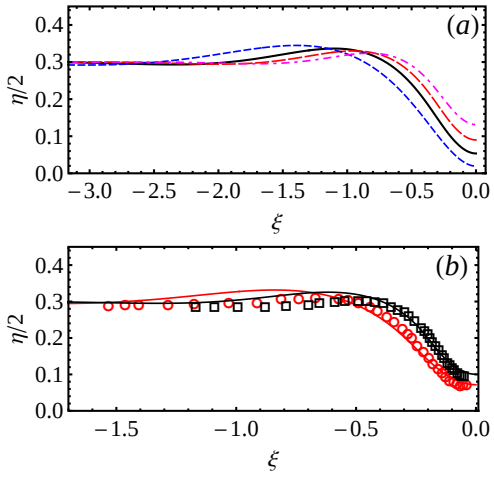

FIG. 5: The tongue shapes: (a) numerically found tongue profiles for $k = 0.67$ and $w/b = 8.8$ for 4 different values of the modified capillary number ϵ: $\epsilon = 1.5$ (short dashes), $\epsilon_* = 3.49$ (solid), $\epsilon = 6$ (long dashes) and $\epsilon = 10$ (dash-dotted). The short-dashed profile results in $\eta < b/w \approx 0.11$ at the outlet, meaning that it is unstable and $\epsilon = 1.5$ belongs to the SE regime. The interfacial curvature at the outlet ($\xi_* = 0$) is set to $\eta_{\xi\xi} = 5.85$ (corresponding to $c = 0.33$) for all shapes; (b) comparison to experiment in HS cell with $w/b = 8.8$ for $k = 0.67$: $\epsilon \simeq 7.7$ ($\circ$) and $\epsilon \simeq 19.4$ ($\square$). The fitted values of c are 0.45 and 0.62, respectively.

are obviously violated and the developed quasi-steady theory does not apply in SE regime. We denote by the *dripping time* the time is takes for the tongue at the step to deform up to the pinch-off, i.e. $\Delta t_{b\to c} \equiv \Delta t_{\rm drip}$. As we discussed in the introduction the driving force behind the step-emulsification process is the surface tension or *confinement gradient* [5] whereas the formation of the unconfined 3D droplet at the step reduces the total interfacial area/energy. Droplet formation is accompanied by the reduction of the inner pressure p_1 and thinning/squeezing of the neck feeding the droplet by a higher outer pressure p_2. The neck in Fig. 6c eventually pinches-off (presumably due to a capillary instability), followed by a very fast retreat/recoil of the tongue within the HS cell as shown in Fig. 6a.

The volume of the droplet formed in between Figs. 6b,c has two contributions: one from the deformation of the tongue, pushing some liquid out during the time between 'b' and 'c', and the second is due to constant inner liquid influx, equal to the dripping time, $\Delta t_{\rm drip}$, times q_1:

$$V_d = \Delta V_{\rm def} + \Delta t_{\rm drip}\, q_1. \qquad (14)$$

The first term due to tip narrowing can be estimated from mass conservation as a difference between tongues' volumes in Figs. 6b and 6a (i.e. volume increment),$V_{\rm def} = V_b - V_a$, assuming very fast retreat so that the volume of the tongue in 'c' and 'a' is the same.

Depending on the upstream width of the tongue (k), the relative importance of these two terms can interchange, e.g. for $k < 1$ (wide tongues) the second term (due to influx) is dominant while for $k > 1$ (narrow tongues) the first term (due to deformation) is dominating, can be seen in experiments. Both terms on the RHS of (14) depend on the flow conditions. It is reasonable to assume that for narrow tongues, the second term in (14) is small (the influx due to q_1 through a narrow tongue is small during $\Delta t_{\rm drip}$) and the droplet size is mainly controlled by the deformation of the tongue. In [7] in Fig.2b the experimental results correspond to $k \approx 2.1$, while our experiments indicate that at $k \sim 2$ the contribution of the influx to the volume is only about 20% of the droplet volume. For wider tongues the contribution of the 2nd term on the RHS in (14) to the droplet volume could be considerable, e.g. our experiments suggest it is about 75% for $k = 0.5$. Analogously, for low Ca, the 1st term is expected to contribute the most to the droplet volume, while for high Ca the 2nd term should be dominant. However, our experiments show (in accord with previous works, e.g. [7],[8]) that the droplet volume is independent of Ca for a fixed flow rate ratio q_2/q_1 (i.e. fixed k). More detailed analysis of the experimental data verify that the Ca-dependent contributions to the droplet volume from both terms in the RHS of (14) cancel out, i.e.

$$\Delta V_{\rm def} \sim V_d(1 - \alpha {\rm Ca}^{\nu}), \quad \Delta t_{\rm drip}\, q_1 \sim \alpha V_d {\rm Ca}^{\nu}, \qquad (15)$$

where α, ν are some dimensionless constants. Our experimental results show that both $\Delta t_{a\to b}$ and $\Delta t_{\rm drip}$ depend on Ca, as intuitively expected for confined flow governed by interplay of viscous and capillary forces. These two times are shown in Fig. 7a in a HS cell with $w/b = 8.8$ for $k = 2$ as a function of Ca ($\circ$ and $\triangle$). These results demonstrate that $\Delta t_{\rm drip} \sim Ca^{-0.4}$ while $\Delta t_{a\to b} \sim {\rm Ca}^{-1.6}$. Their sum gives a dripping period $T \sim {\rm Ca}^{-1}$ ($\square$).

The corresponding individual experimentally measured volumes $\Delta V_{\rm def}$ and $\Delta t_{\rm drip} q_1$ are depicted vs. Ca in Fig. 7b. The deformation volume was estimated as $\Delta V_{\rm def} = \Delta S_{\rm def} b$, where $\Delta S_{\rm def} \approx S_b - S_a$ is the corresponding surface area increment (see Figs. 6a,b). Since $\Delta t_{\rm drip} \sim Ca^{-0.4}$ and $q_1 \sim$ Ca, the volume due to influx $\Delta t_{\rm drip} q_1 \sim {\rm Ca}^{\nu}$ with $\nu \approx 0.6$ as can be readily seen (long-dashed line). The deformation volume $\Delta V_{\rm def}$ follows the second Eq. (15) so that the total droplet volume is constant, $V_d \approx 2.9$ pL, and independent of Ca.

Since the size of the generated droplet in the SE regime is independent of Ca, obviously the frequency of their production, f (i.e. number of droplets per unit time), should grow linearly with Ca (or with q_1 in [7]). Indeed, from mass conservation $f = q_1/V_d$. Re-writing q_1 via Ca we obtain $f = \mathcal{K} Ca$, where the proportionality constant $\mathcal{K} = \gamma b w/2\pi\mu_1 d^3$. The experimental results depicted in Fig. 8 confirm the linear growth of f with Ca in agreement with previous results [7]. Analogously, the dripping

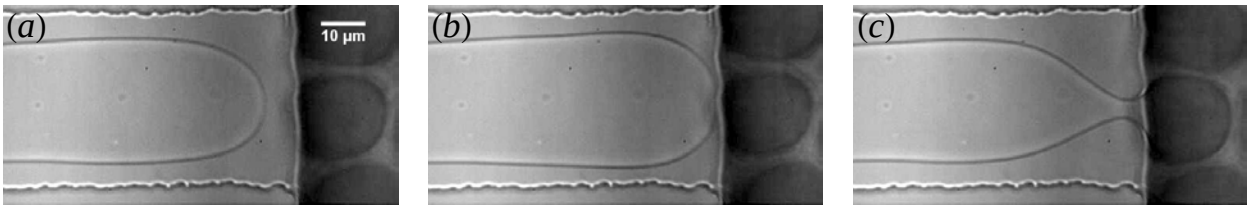

FIG. 6: The step-emulsification breakup regime observed in experiments using fluorinated oil (inner phase) in water (outer phase); the time progresses from left to right. The scale bar is the same for all figures. (a) the tongue right after the droplet pinch-off and retreat; (b) the tongue just reached the step; (c) the tongue shape right before pinch-off and retreat;

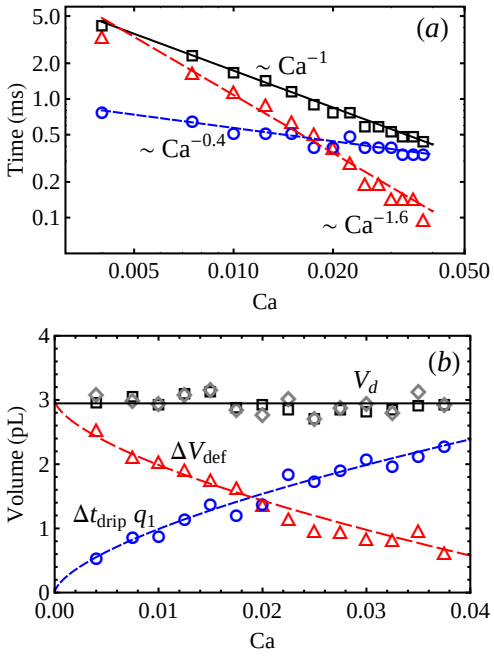

FIG. 7: Characteristics of step-emulsification regime in HS cells with $w/b = 8.8$ for $k = 2$: (a) the droplet formation times (ms) vs. Ca (log-log plot): $\Delta t_{a\to b}$ (△), $\Delta t_{\rm drip}$ (○); full time period $T = 1/f$ (□). The lines are the best power-law trends. (b) Individual volumes (picoliter) vs. Ca: deformation volume $\Delta V_{\rm def}$ (△), influx volume $\Delta t_{\rm drip} q_1$ (○), their sum $\simeq 2.98 \pm 0.14$ pl (◇) and measured droplet volume $V_d = 2.95 \pm 0.11$ pl (□). The dashed (short and long dashes) are the Eqs. 15, respectively, with $\alpha \simeq 6.2$ and $\nu \simeq 0.63$.

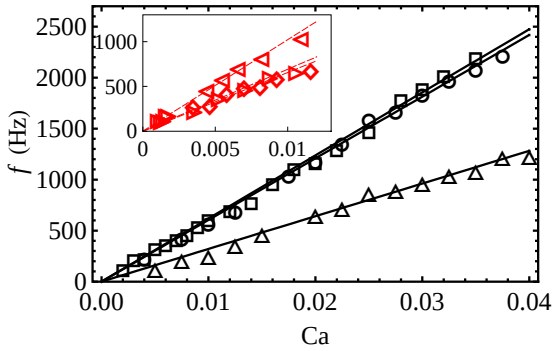

FIG. 8: The droplet production frequency, f, in SE regime vs. Ca in HS cells with $w/b = 8.8$: $k = 0.5$ (△), $k = 2$ (○), $k = 2.5$ (□); the inset shows the results for $w/b = 32.6$: $k = 1$ (◇), $k = 2.5$ (▷) and $k = 5.2$ (◁). The continuous lines are the best linear fits.

period $T = 1/f \sim {\rm Ca}^{-1}$ in agreement with Fig. 7a (□, solid line). *Thus, even though the dynamics within the HS cell is governed by the combination of the viscous and capillary forces (making the balloon-SE transition threshold Ca-dependent, see Figs. 4), this dynamics seem to be slaved to the droplet formation in the reservoir controlled entirely by the surface tension as the viscous forces are negligibly small.*

Leaving aside the intriguing question concerning cancelation of the Ca-dependent contributions to the droplet volume, we shall focus on the limit $Ca \to 0$ where the droplet volume is controlled predominantly by tongue deformation, i.e. $V_d \approx \Delta V_{\rm def}$. In this case it is reasonable to assume that the droplet is spontaneously formed once the total interfacial energy (i.e. area) is lowered, i.e. droplet formation is favored thermodynamically. Simple arguments based on comparison of corresponding interfacial areas and volumes yield the critical droplet size. $V_{\rm def}$ can be estimated from mass conservation as a difference between tongues' volumes in Figs. 6b and 6a (i.e. volume increment), $V_{\rm def} = V_b - V_a$, assuming very fast retreat so that the volumes of the tongue in 'c' and 'a' are essentially the same, $V_a \approx V_c$. In such case we need to compare the interfacial area in 'b' with that in 'c', where the latter is equal to the area of the tongue in 'a' plus the surface area of the droplet produced. Let us denote by ℓ the distance over which the tongue retreats backward into the HS cell after breakup, i.e. from 'c' to 'a' (or advances from 'a' to 'b'). therefore the increment in the interfacial area ("new" interface) between 'a' and 'b' (assuming that no deformation occurs, just translation

of the tongue forward) reads

$$\Delta S_{a\to b} \approx 2w_{i\infty}\ell + 2\ell b\,,$$

where the first term stands for the in-plane surface and the 2nd term for the area of the off-pane menisci. On the other hand, the surface area of the droplet is just $S_{\rm d} = \pi d^2$. Conservation of mass requires that the volume difference $\Delta V_{a\to b} \approx w_{1\infty}\ell b$ should be equal to the volume of the produced droplet, $V_d = \pi d^3/6$. The breakup of droplet is favorable when $\Delta S_{a\to b} \gtrsim S_d$. Solving the equation $\Delta S_{a\to b} = S_d$ together with mass conservation constraint, $\Delta V_{a\to b} = V_d$ yield the diameter of the *smallest* droplet and the corresponding distance ℓ

$$d = \frac{3bw_{1\infty}}{(b+w_{1\infty})}\,, \quad \ell = \frac{9b^2\pi w_{1\infty}^2}{2(b+w_{1\infty})}\,. \tag{16}$$

Using the upstream parallel-flow solution, $\frac{w_{1\infty}}{w} = \frac{1}{1+k}$, the scaled droplet diameter d/b reads

$$\frac{d}{b} = 3\left[1 + \frac{(1+k)}{w/b}\right]^{-1}\,. \tag{17}$$

This results indicates that the diameter d of the smallest droplet that can be produced in SE regime varies between $\approx 2b \div 3b$. This is in qualitative agreement with previously experimental observations reporting the smallest droplet diameter two to three times the height the inlet channel height [4, 6, 8]. The narrower inner streams (i.e. lower $w_{1\infty}$ and higher k) or/and larger aspect ratio w/b results in smaller droplets.

Using this solution we obtain that the interfacial area increment $\Delta S_{a\to b} \sim d^3/b$, while the interfacial area of the produced droplet is quadratic in its diameter, $S_d \sim d^2$. Therefore, production of small droplets with diameter smaller than that in Eq. (17) is unfavored since interfacial area increases. The size of the droplet produced in experiments using channels with two different aspect ratios $w/b = 8.8$ and $w/b = 32.6$ seem to agree well with the prediction in (17) multiplied by a factor of ≈ 2. The comparison is provided in Fig. 9 showing excellent agreement between the theory and the experiment. Note that the proposed geometric construction of the tongue shape is only approximate (i.e. going from 'a' to 'b' the tongue does not simply advances to the right, but also inflates) and thus the appearance of the constant multiplicative factor ≈ 2 varying slightly with the cell aspect ratio is not surprising. However, the agreement between the simple theory (17) and the experimental results for a particular HS cell with given aspect ratio is excellent in a wide range of k. For wide tongues (e.g. $k = 0.5$) the theoretical prediction (17) somewhat underestimates the droplet size. Wide tongues require small capillary number $\mathcal{C}$ and thus low flow rate of the continuous phase q_2 in the SE regime (see the phase diagram in Fig. 4*a*) and generated droplets are not conveyed fast enough further downstream in the reservoir following their pinch-off.

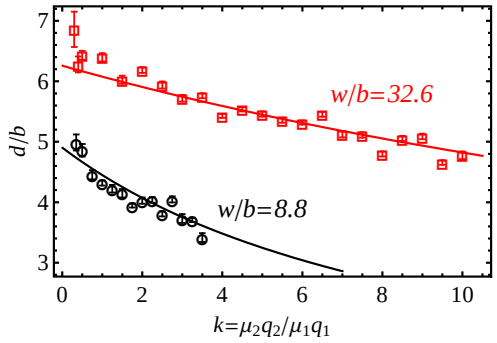

FIG. 9: The diameter of the droplets, d/b, produced by step-emulsification in the HS cells with two aspect ratios: $w/b = 8.8$ (black circles) and $w/b = 32.6$ (red squares). The solid lines are the prediction in Eq. (17) multiplied by 1.85 and 2.15 respectively.

Thus formation of the droplets is affected by their crowding near the step. The disturbance due to crowding yields relatively large variance in the measured droplet size at $k = 0.5$.

Concluding remarks. Here we provide a comprehensive experimental and theoretical study of the step-emulsification process in a microfluidic device composed of a shallow nanofluidic (Hele-Shaw) cell connected to a deep and wide reservoir. The theoretical model based on depth-averaged Hele-Shaw hydrodynamics yields the nonlinear ODE for the quasi-static shape of the confined tongue of the disperse liquid, engulfed by the co-flowing continuous phase, prior to transition to the oscillatory step-emulsification regime. At the transition threshold, the developed theory suggests a very simple condition for the critical capillary number, Ca $(w/b) =$ Const, in a complete agreement with experimental data showing that Const ≈ 0.38. The computed tongue shapes, determined by fitting the curvature of confined tongue of the disperse liquid at the outlet, are in excellent agreement with the experimental results. The closed-form expression for the smallest size of the droplets produced in step-emulsification regime is found using simple thermodynamic and geometric arguments as a function of flow rates, viscosities of both phases and geometry of the Hele-Shaw cell. This prediction shows an excellent agreement with experimental findings.

Acknowledgement. A.M.L. acknowledges the support of the Israel Science Foundation (ISF) via the grant #1319/09 and Joliot Chair visiting position at Ecole Supérieure de Physique et Chimie de Paris (ESPCI). Z.L. and P.T. acknowledge CNRS and ESPCI for their support.

* Electronic address: lisha@technion.ac.il

[1] H. A. Stone, A. D. Stroock and A. Ajdari, Engineering flows in small devices: Microfluidics toward a lab-on-a-chip, Annu. Rev. Fluid Mech. **36**, (2004); R. Seeman et al., Droplet based microfluidics, Rep. Prog. Phys. **75**, 016601 (2012).

[2] T. Kawakatsu, Y. Kikuchi, and M. Nakajima, Regular-sized cell creation in microchannel emulsification by visual microprocessing method. J. Am. Oil Chem. Soc. **74**, 317, 1997.

[3] I. Kobayashi, K. Uemura, and M. Nakajima, Controlled generation of monodisperse discoid droplets using microchannel arrays. Langmuir, **22**, 10893 (2006).

[4] I. Kobayashi, M. Nakajima, K. Chun, Y. Kikuchi, and H. Fujita, Silicon array of elongated through-holes for monodisperse emulsion droplets. AIChE J. **48**, 1639 (2002).

[5] R. Dangla, S. Cagri Kayi, and C. N. Baroud, Droplet microfluidics driven by gradients of confinement, Proc. Natl. Acad. Sci. U.S.A. **110**, 853 (2013)

[6] Malloggi, F., Pannacci, N., Attia, R., Monti, F., Mary, P., Willaime, H., Tabeling, P., Cabane, B., Poncet, P., Monodisperse colloids synthesized with nanofluidic technology. Langmuir **26**, 2369 (2010).

[7] C. Priest, S. Herminghaus, and R. Seemann, Appl. Phys. Lett. **88**, 024106 (2006).

[8] L. Shui, A. van den Berg, J. C. T. Eijkel, Scalable attoliter monodisperse droplet formation using multiphase nano-microfluidics, Microfluid. Nanofluid. **11**,8792 (2011).

[9] S. Sugiura, M. Nakajima, S. Iwamoto and M. Seki, Interfacial tension driven monodispersed droplet formation from microfabricated channel array, Langmuir **17**, 5562 (2001).

[10] M. Rayner, G. Tragardh, C. Tragardh and P. Dejmek, Using the Surface Evolver to model droplet formation processes in membrane emulsification, J. Colloid Interface Sci. **279** 175 (2004).

[11] S. D. R. Wilson, The slow dripping of a viscous fluid, J. Fluid Mech. **190**, 561 (1988).

[12] M. S. Longuet-Higgins, B. R. Kerman and K. Lunde, The release of air bubbles from an underwater nozzle, J. Fluid Mech. **230**, 365-390 (1991).

[13] J. R. Lister and H. A. Stone, Capillary breakup of a viscous thread surrounded by another viscous fluid, Phys. Fluids **10**, 2758 (1998).

[14] D. R. Link, S. L. Anna, D. A. Weitz and H. A. Stone, Geometrically mediated breakup of drops in microfluidic device, Phys. Rev. Lett. **92**, 054503 (2004).

[15] P. G. Saffman and G. I. Taylor, Proc. R. Soc. London, Ser. A **245**, 312 (1958).

[16] F. Bretherton, The motion of long bubbles in tubes, J. Fluid Mech. **10**, 166 (1961).

[17] P. Constantin, T. F. Dupont, R. E. Goldstein, L. P. Kadanoff, M. J. Shelley, and S.-M. Zhou, Droplet breakup in a model of the Hele-Shaw cell, Phys. Rev. E **47**, 4169 (1993).

[18] K. J. Humphry, A. Ajdari A. Fernndez-Nieves, H. A. Stone and D. A. Weitz, Suppression of instabilities in multiphase flow by geometric confinement, Phys. Rev. E **79**, 056310 (2009).

[19] S. Afkhami, A. M. Leshansky and Y. Renardy, 2011. Numerical investigation of elongated drops in a microfluidic T-junction, Phys. Fluids **23**, 022002 (2011);

[20] A. M. Leshansky, S. Afkhami, M.-C. Jullien, and P. Tabeling, Obstructed Breakup of Slender Drops in a Microfluidic T Junction, Phys. Rev. Lett. **108**, 264502 (2012).

[21] G. K. Batchelor, *An Introduction to Fluid Dynamics*, Cambridge Univ. Press, 1967.

[22] A similar effect of confinement on the interplay between inertia and viscous forces concerns the condition of negligible liquid inertia, $(b/w)\mathrm{Re} \ll 1$, where the Reynolds number is defined as $\mathrm{Re} = \rho b^3 |\nabla p|/\mu^2$ [21]. In other words, viscous forces dominate over inertia even at finite $\mathrm{Re} \sim \mathcal{O}(1) \ll w/b$, i.e. it is difficult to produce inertia-dominated flow in confinement.

Part III

Flow and nano particles transport in sub-micrometric models of reservoirs

Chapter 1

Project background

In the current petroleum recovery technology, only 1/3 of the discovered the oil or gas can be easily extracted, and this fraction is facing to be exhausted. The other 2/3 of reservation is known to be distributed in the network of rocks with transversal dimension on 1 μm. This complex situation challenges the existed recovery technology of the petroleum companies, some more detailed knowledge concerning about the reservoirs becomes necessary, and more advanced technology need to be developed. This induced the formation of the Advanced Energy Consortium, which consists of some companies such as Total, Schlumberger, BP, Shell, etc, getting together and support the micrometric study of flows in porous media underground. One idea is to inject nano particles into the reservoir, with the particles assumed to be "smart". For example, some nano particles undergo phase transition when they reach the water-oil interface, or when they experience temperature change. These allow to provide information about oil and gas distribution and quantity, after they are collected at the production well (Fig 1.1). The nano particles are injected with water and complex fluid, and released to porous media underground through the transmitter. By the application of pressure, they travel through the rocks and arrive at the receiver array, where their phase transition is quantified, and the distribution of oil and gas is mapped. The whole project invited 28 laboratories worldwide, which were divided into three categories according to their speciality. Some laboratories in geographical field made numerical studies about flow and particles motion in the reservoir. Others specialised in chemical synthesis are in charge of fabrication of nano particles, which are for instance quantum dots, emulsions, with specific surface coating and all necessary properties to adapt the sometimes extreme condition underground. Another group where our lab has been involved studies the mobility of nano particles. AEC support the realisation of wettability patterned network, which corresponds to the real situation underground, and the particle motion in the network.

My work is to fabricate microfluidic network with micrometric dimension (height $< 2\ \mu m$), and different wettability pattern, which is the best way today to approach the complex structure in the reservoir. We inject the nano particles into the model and study their mobility, i.e. whether they go through or are retained in the model. Particles suspension in the micro model is observed on microscope and recorded by fast camera. The advantage of this study is to have real time information about particles motion in porous media, and provide more detailed observation on micrometric scale, which cannot be realised in macroscopic core experiment. The work is divided into three parts.

• 1. Study the clogging effect of nano particles during their penetration into micro model.

• 2. By using the evanescent wave PTV technology, flow of complex fluid within 500 nm close to the solid surface is studied.
• 3. Nano particles fabricated by AEC member institutions are injected into our micro model, and been observed in real time their motion and adsorption onto the solid surface, leading to conclusion on the retention.
The rest of the chapter describes the results that we have observed.

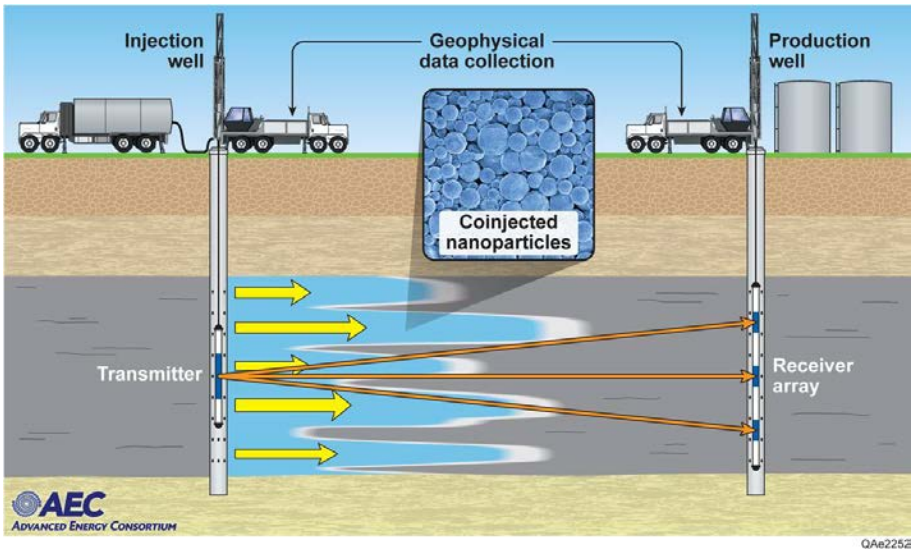

Figure 1.1: Principle idea of the AEC project. A transmitter is planted under ground on the injection well side, and a receiver array is planted on the production well side. Nano particles are injected with pushing fluid from the transmitter into the porous media underground. These nano particles are supposed to perform phase transition or deliver information while in touch with oil. After they arrive at the receiver array, their phase transition information can be detected, indicating the quantity and distribution of oil in the media they went through.

Chapter 2

Study of AEC produced nanoparticles penetration and motion in patterned microfuidic network

The main goal of the AEC project is to test mobility of AEC synthesised nano particles in the micro model with patterned wettability. Taking the advantage of the PDMS and NOA channel being transparent, all temporal motion of particles can be followed by microscope. In addition, microfluidic method allows different design of structures, which approaches the real strucutres of cores with micrometric size as well as possible.

2.1 Preliminary results

Before obtaining the realistic geometry of cores from the AEC, in order to test the feasibility of AEC nano particle penetration into microfluidic networks, a simple network of channels using PDMS (NOA works equally) was made. The network consists of many horizontal and vertical straight channels intersecting with each other (fig 2.1).The width of each channel is 14 μm, and the height of this network is 2 μm. Particle suspension is injected from one side, and exits from the other.

Retention overview Particles from AEC Netherlands member group are firstly tested. These are Quantum dots of diameter 50 nm. The range for excitation is rather broad but the photo-luminescent effect is strongest if use UV source. The emission is broad-banded as well (100 nm width at half height) centred around 570 nm. A suspension of these particles in water at concentration 8 μM is injected into our micro model with hydrophilic surface (fig 2.2 left) and hydrophobic surface (fig 2.2 right). By comparing these two different channel surfaces, one can see that hydrophobic surface causes more particle-retention in the channel, whereas hydrophilic surface finishes with less particle deposition. The deposited objects can be single particles, particle aggregations and dusts presented in the particle suspension. The deposition of single particle is caused by the attractive Van der Waals force which overcomes electrostatic repulsive force; the particle aggregates may be eliminated by sonication of the suspension before injection into the network; however the impurities are difficult to be eliminated, for example if a filter is used for getting rid of the dusts, lots of particles will also be caught in the filter. A suggestion was made for member groups to

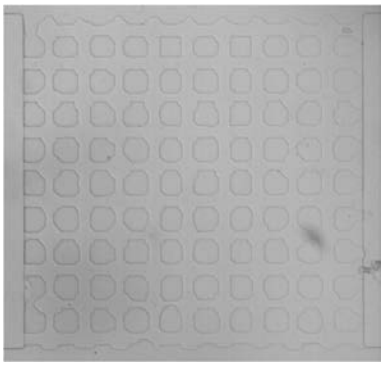

Figure 2.1: Network model made from PDMS, the width of each channel is 15 μm and the height 2 μm.

fabricate the nano particles as mono-disperse and containing fewer impurities as possible.

Dynamic of particle retentions is also investigated. Fig 2.3 shows fluorescent area

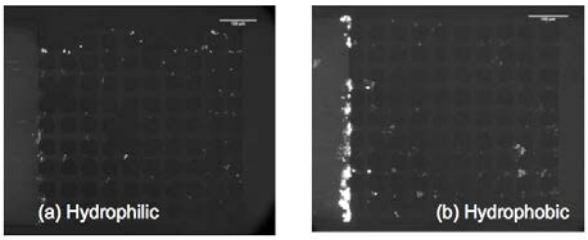

Figure 2.2: QD of diameter 50 nm penetration into micro metric network model. The network was initially filled with water so that the background was black at $t = 0$. Gradually the background becomes slightly enlightened, indicating that fluorescent particles penetrates into the network. Some particles or particles aggregates are deposited on the wall of the network, illustrated as dots with intense light. Hydrophilic network (left) has less particles deposited on the surface so that less retention. More retention is observed in hydrophobic network (right).

indicating (at least partially) the amount of deposited particles and plotted the variation of fluorescent areas as function of time. Hydrophilic channels causes retention of particles slower than hydrophobic channels.

Retention length. In order to investigate further retention phenomena, particle suspension is injected into a single straight channel. The distribution of fluorescent intensity versus position along the channel length is plotted in fig 2.4. One can see that within a length scale of the order of 100 μm, the fluorescent intensity is equally distributed, for either hydrophilic (left) or hydrophobic (right) channels. There are several rare events represented by a large pick of intensity, which is caused by deposited particles or aggregates on the channel wall. This observation suggests that the length of retention is longer than the scale of 100 μm.

As a summary, the experiment of transport of quantum dots synthesized by the AEC is feasible. Indeed the same study can be performed on all kinds of particles, provided they emit fluorescence in some range of wavelength (preferentially compatible with our excitation/detection system.) Several issues emerged from the retention studies are, firstly, dust should be eliminated from the sample. Dust particles often stick in the network. They

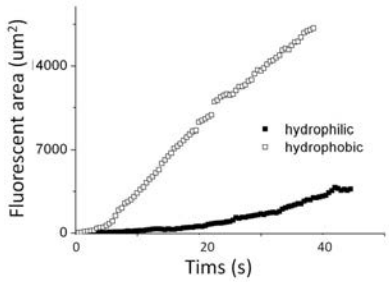

Figure 2.3: Increase of fluorescent area in the network as function of time, for hydrophilic surface and hydrophobic one. Hydrophobic surface causes more retention of particles than hydrophilic surface at each moment.

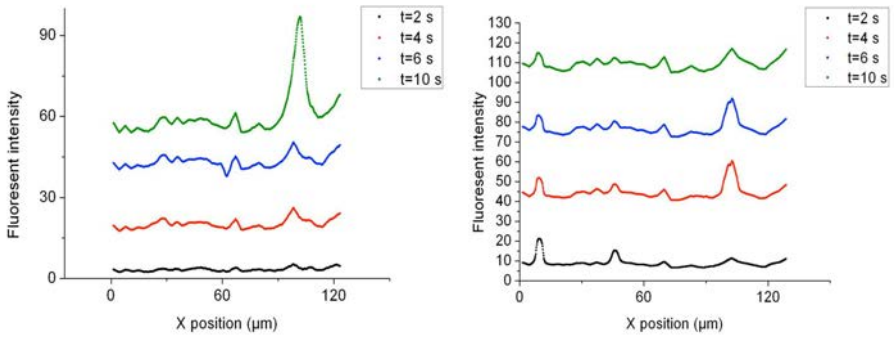

Figure 2.4: Fluorescent particles distribution in a single channel during suspension flowing into the channel. The fluorescent intensity in both hydrophilic (left) and hydrophobic (right) channels is equally distributed, except some rare events such as deposition of particles on the wall, illustrating on this graph by a pick of intensity.

represent a source of deposition for the other particles. Secondly, the particle suspension should be stable to avoid clusters, because they may trigger the development of retention phenomena. One can draw conclusion that most of the particles get through the system, with some of them stick in it. It is however difficult to be quantitative, as long as the differentiation between dust retention and intrinsic NP retention is clear. These issues have certainly to be addressed in order to draw out firm conclusion on the transport properties of NP synthesized by AEC.

2.2 Transport of nano particles in micro models with patterned wettability

Patterning technology In order to fabricate the micro model which simulates as well as possible the porous media of cores, the micro channels need to be patterned with different wettability. This part of work is mainly accomplished by Hervet Willaime. The principal is summarized as below.

The technology of patterning was developed at ESPCI by Studer and Bartolo, and applied in this project to PDMS network with 1.3 μm dimension. The idea is based on the following

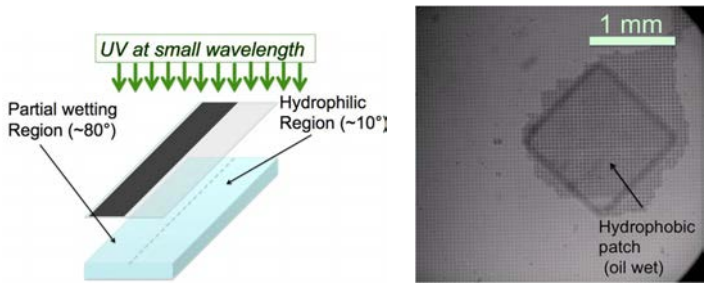

Figure 2.5: Principal technology of wettability patterning using a mask (left), it is possible to obtain hydrophilic and non hydrophilic regions on the same substrate, with a spatial resolution on the order of a few micrometers. Typical result after patterning (right). A microfluidic network, 1.3 μm high, made in PDMS. The square sides are 100 μm. The region inside the square is untreated (therefore left globally hydrophobic), while the rest of the system is subjected to the action of the 250 nm UV illumination (thereby hydrophilic). The wettability pattern is revealed by a flow of water (white) avoiding the square patch.

observation (fig 2.5 left): A PDMS chip is subjected to a beam of 250 nm UV light which modifies its wettability, and switches it from non hydrophilic to hydrophilic. This observation allows to pattern the wettability of PDMS substrates. In practice, a quartz plate (transparent to UV) is placed at the bottom wall. On one side of this plate, a SU8 layer is spincoated and patterned on it. SU8 being opaque to UV, this layer works as a mask. After this step is done, a PDMS network is combined with the quartz plate by plasma treatment on the other side of the plate. Owing to the small heights to be achieved, hard PDMS is used so as to avoid collapse of the structure onto the quartz plate. After the system is made, the system is heated for several hours in an oven, so as to ensure that PDMS has returned to hydrophobicity. Then the system is insolated under a 250 nm UV collimated beam so as to selectively impose hydrophilicity for certain regions of the system (part been insolated by UV). This step typically takes 70 mins. After this step is completed, the system is ready to use. (fig 2.5 right) shows a typical result of patterning, in which the hydrophilic zone is well distinguished from hydrophobic one.

Application of AEC synthesized nano particles. The microfabricated systems is shown in fig 2.6 (left). The geometry comes from a X ray picture of a cut of core samples, provided by Dr K.Thomson from AEC group. Even though the core is in three-dimension, the cut is chosen so as a net flow can be driven through the micro model. A PDMS based micro model is constructed according to this geometry, experiments are done in three situations: homogeneous hydrophilic network, homogeneous hydrophobic network, and that with patterned wettability. For the third situation, a periodic wettability pattern is imposed, and shown in fig 2.6 (right).

Minute quantities of particles are injected into the micro model. This task is achieved thanks to the implementation of external valves, as shown in fig 2.7. The liquid (i.e water or brine) without particles is driven from top to bottom. It can be controlled by actuating the first valve. A second valve allows to inject a few nanoliters of the nano particle suspension. This volume represents several times the "pore volume". By doing this, we reproduce typical conditions of particle testing achieved in core flow experiments. Without the valves, the minimum volume of injection would have been thousand times the "pore volume", which would not be representative of what is done in the field of oil industry. Fig 2.8 shows that

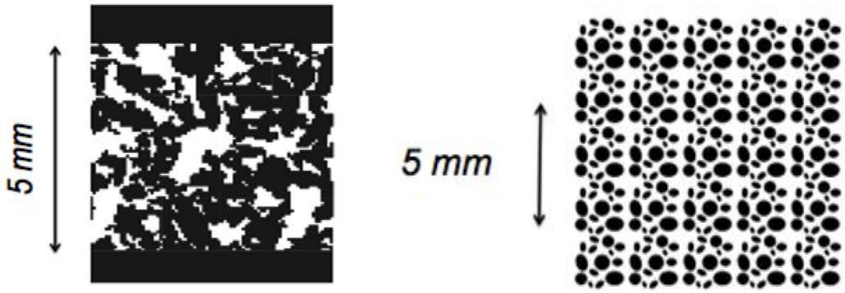

Figure 2.6: Core structure projected on two-dimension (left), provided by AEC member group. The black zones represent empty areas where fluid can go through, and the white areas are solid in core, so that PDMS in the micro model. A PDMS channel is fabricated according to this geometry, with height in the porous media 1.3 μm, and that in entry and exit 14 μm. The mask for periodic wettability patterning (right) is designed by Hervet Willaime. The parts of PDMS channel covered by the black patterns will be avoided to UV insolation, and keep the hydrophobicity.

the injection can be repeated periodically. At the entry and the outlet of the micro system, intensity measurements are carried out, detecting groups of fluorescent particles injected in the micro model, and going out of it.

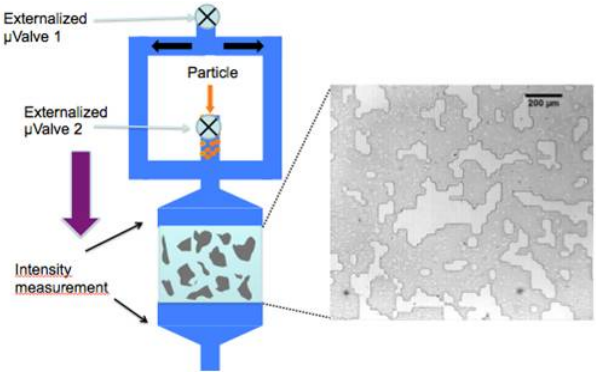

Figure 2.7: The liquid without particles is driven from top to bottom, along two parallel channels (coloured in blue). They arrive in the shallow part of the micro system (light blue with grey spots), i.e. the micro model. This micro model has the geometry mimicking a reservoir configuration. A second valves injects, periodically, a solution incorporating the particles to be tested. The operation can be repeated at will. All the valves are externalized, i.e. integrated on different microfluidic devices.

Result summary. The nano particles tested from AEC group is: 1. CeSeS quantum dot/Neodol in API brine with diameter 90 nm, from Michael Wong. 2. InP core, ZnS shell, quantum dots with thiol PEG5000 with diameter 40 nm, from Daniel Turkenburg. 3. $Fe_3O_4 - PEG$ 3.4K, with diameter 45 nm, from Joyce Wong. The area of the static fluorescent spots appearing in the micro model is measured as a function of time. The area

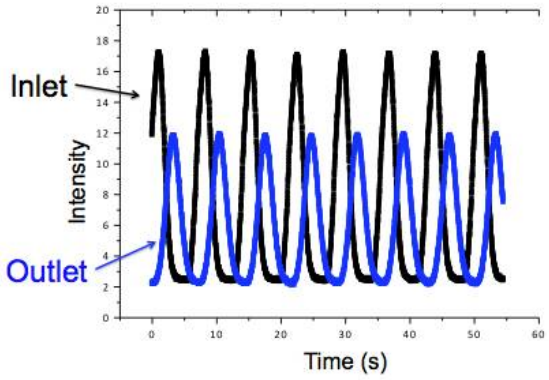

Figure 2.8: At the entry and the outlet of the micro system, intensity measurements are carried out, detecting blobs of fluorescent particles injected in the micro model (black) and going out of it (blue). The injection impulsion is short, so that there is no plateau visible on the diagram. The intensity at the outlet is lower than that at the entry, because dilution of water or brine.

characterizes the amount of deposited particles. Typical evolutions of this area, obtained for particles of Dr. Michael Wong as an example, is shown in fig 2.9, for different wettabilities conditions. The hydrophilic surface causes retention of particles faster than hydrophobic channels or patterned micro models. Having tested the particles from AEC groups, we conclude that most of the particle can go through the micro model, with certain fraction retained in the porous media. The retention is due to deposition of particles, aggregates and dusts, which result in extrinsic clogging.

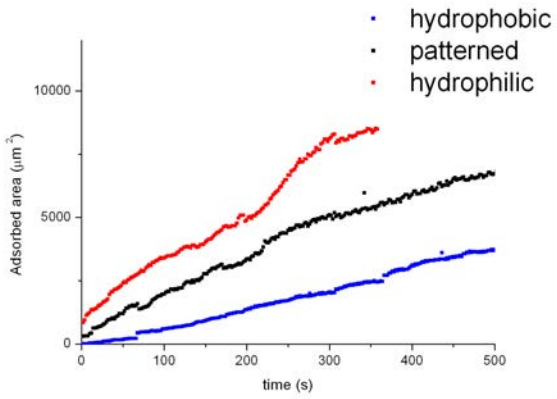

Figure 2.9: Evolution of fluorescent area in the network as function of time, for hydrophilic, patterned and hydrophobic conditions. Hydrophilic surface causes more retention of particles than hydrophobic and patterned surfaces. The particles come from M. Wong's lab.

2.3 Conclusion

We successfully build a 2D micro model, which mimics the complex structure of porous media underground with characteristic length at microscale. We took advantage of the

microfluidic technology, to realize different surface wettability, including hydrophilic, hydrophobic and patterned surfaces. Thanks to the transparency of PDMS material, fluid motion in the micro model can be observed in real time, and serves to predict what happen in realistic underground. We collaborated with 5 labs in the AEC group in the domain of particles synthesizing. Their particles motion are tested in the micro model, retention states have been quantified. We have proved that the microfluidic is a convenient technology to perform penetration test of nanoparticles before they are applied to the Enhanced Oil Recovery.

Appendices

Appendix A

Clogging of polystyrene particles in microfluidic channels

A.1 Introduction

The penetration of particles into micro model is firstly impeded by clogging of the particles in the channels. The physical mechanisms involved in the clogging are numerous and still not understood. Few studies have been dedicated to this problem, and mostly deal with isolated aspects of the question, such as the particle size, the influence of organic matter or specific surface properties [50, 102], or the structural organization of the filter cakes resulting from clogging [104]. Most of these works were conducted on whole filters or granular media. Conversely, Wyss et al. [144] conducted a study at the single-pore level, based on model experiments in microfluidic channels, in order to better control the many parameters at play. Wyss et al. [144] thus investigated clogging by modelling the porous media via a network of microfluidic Polydimethylsiloxane (PDMS) channels (fig A.1). Micron-sized polystyrene particles were injected into a serie of parallel channels, and a mean clogging time was measured (averaged over the whole chip).

They showed that in their model experimental setup, for a given particle/surface interaction, clogging was governed by the relative geometries of the channels and particles (fig. A.1, right). Their macroscopic measurements, conducted for different channel sizes and particle diameters, allowed them to determine a typical lengthscale ϵ, within which particles stick to the channel walls (see definition of ϵ in the inset of fig. A.1, right). The values were compatible with a Debye layer thickness, which was an encouraging result. Nonetheless, we are at a preliminary stage both on the experimental and theoretical sides, and much remains to do in order to reach an adequate level of understanding of clogging in micro models.
In this chapter, we present experiments of the different phenomena involved, following the single-pore approach of Wyss et al. [144]. The influence of particle size relative to the channel dimension, that of the surface state, and clogging mechanism are studied.

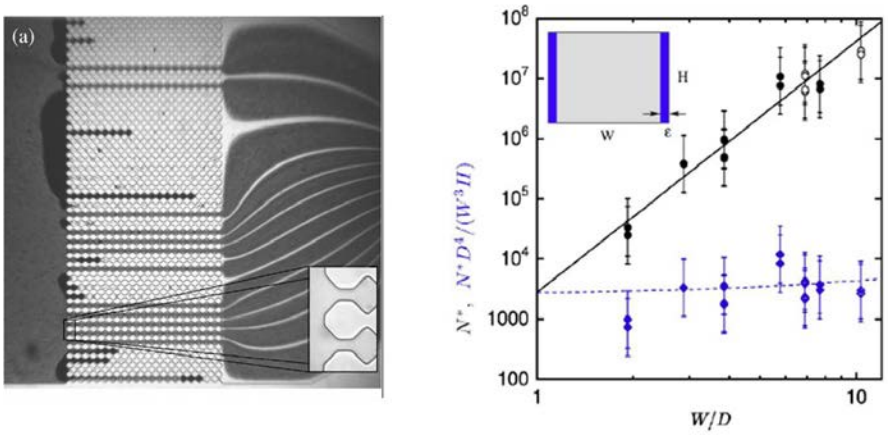

Figure A.1: Single-pore level study by Wyss et al. [144] Left: Picture of their experiment (Channel width: $W = 20\ \mu m$, height: $H = 25\ \mu m$). The particles (diameter: $D = 4\ \mu m$) appear in black. Right: Number N of particles going through the channel before clogging (black), as a function of the geometric ratio W/D. N^*, number of particles rescaled by the geometric quantity $D^4/(W^3H)$ (blue). Circles: experimental data; lines: theoretical prediction.

A.2 Experiments on clogging

The design of the microchannels used to study the clogging of microparticles is simple. The microfluidic chips are composed of 25 paralleled straight channels (width: 20 μm, height: 25 μm, length: 1 mm). The channels are replicated from a double-layered lithographied mold, where the height at the level of channels is 25 μm, whereas the height at the level of chambers is 50 μm in order to prevent clogging from occurring at places other than the channels. Before experiments, the channels and connection tubes are rinsed by ethanol, isopropanol and milipore water, for minimizing the effect of dusts and PDMS debris on the clogging result. The entire micro system preparation is done under hood. Suspension of polystyrene particles with diameter 5 μm are injected into the micro system, microscope is used to observe the clogging procedure, which is also recorded by fast camera. Fig A.2 shows a typical experiment of clogging. Particles move from left to the right, and get clogged over time. Two measurable quantity of this experiment are the time when a channel is clogged, and the position where clogging occurs. Statistical measurement is made at different surface property, concentration and confinement.

A.2.1 Extrinsic clogging

We define extrinsic clogging the phenomenon that the clogging of a channel is caused by the arrival of an unexpected dust, instead of by particles. When a dust has dimension comparable to that of the cross section of a channel, the clogging of this channel is dominated by the dust, and the time and position of clogging is independent from particle concentration, neither the surface state. The extrinsic clogging is often observed at large channel cross section and small particles, where the intrinsic clogging due to particles occurs so late that the arrival of a dust terminates the experiment. Fig A.3 shows an example of extrinsic clogging. During the experiment, the width of channels is fixed at 20 μm and the height

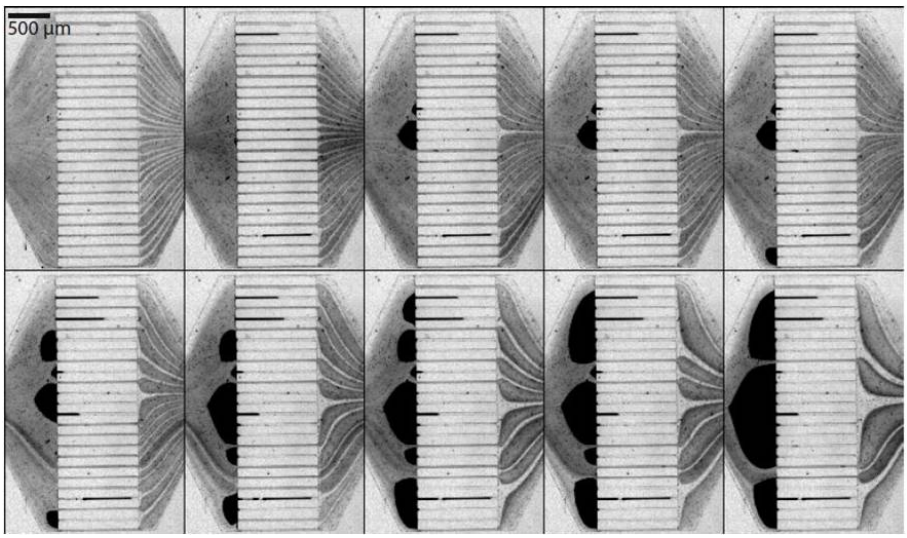

Figure A.2: Snapshots from a typical clogging experiment. A suspension of PS particles in water is injected into a serie of parallel straight channels (width $W = 20\ \mu m$, height $H = 25\ \mu m$, length $L = 1\ mm$; particle diameter $D = 5\ \mu m$). Time interval: $80s$. The particles appear in black.

is varied, the concentration of particles varies in the range of $1\%wt$ and $10\%wt$. We empirically found out that the extrinsic clogging occurs when channel height is above $4 - 5$ times the diameter of the particle. This result is inconsistent with Wyss et al. [144], where no microscopic observation was made on the local of clogging. In their model, all clogging phenomena, irrespective of particle concentration and confinement level, are attributed to successive deposition of particles on the channel surface. The category extrinsic clogging is dominated by singular events, which is out of scope of our study on clogging mechanism.

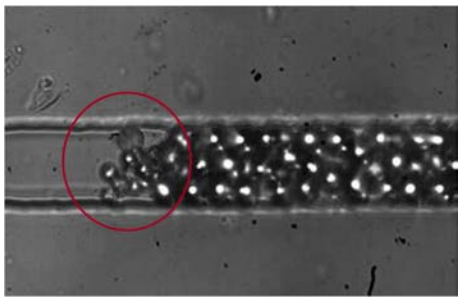

Figure A.3: A typical extrinsic clogging, where the channel is clogged by a dust indicated by red circle.

A.2.2 Intrinsic clogging

Surface influence. In order to study the intrinsic mechanism of clogging, the channels dimension is fixed at width $W = 20\ \mu m$, height $H = 18\ \mu m$, length $L = 400\ \mu m$, which is confined enough to make the intrinsic clogging occur fast, and to prevent the extrinsic clogging from taking the place. Particles with diameter $5\ \mu m$ at $10\%wt$ is used to make a preliminary test of surface property, and decide the proper surface to be used in the

following study of clogging mechanism. Hydrophilic surface after plasma treatment and hydrophobic surface are compared. In the hydrophilic surface, time of clogging ranges from the order of 10 s to 100 s, the relative long clogging time with large distribution and weak reproducibility shows that clogging is most probable due to arrival of unexpected singular events, such as dusts. More over on the distribution of clogging position, most of the channels are clogged at the entry, which corresponds to large dusts been stopped at entry (fig A.4). Whereas in hydrophobic case, clogging time concentrated on the order of 1 s, and the position of clogging is distributed around 30 μm from the entry. Both measured result and recorded film indicate that the clogging is caused by synergy of deposited particles on the channel surface with confinement effect, this is what we called intrinsic clogging. Thus for the following experiment, only hydrophobic surfaces are utilised.

Particle concentration influence. The influence of particle concentration on the

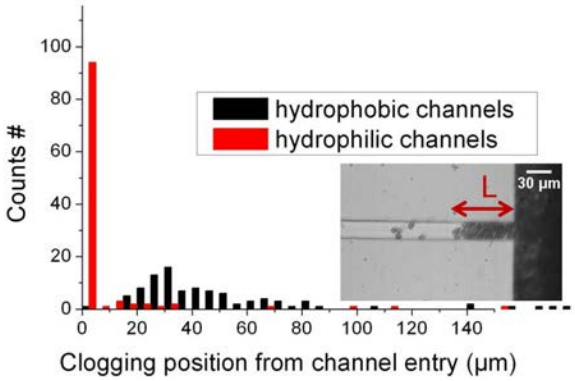

Figure A.4: Number of clogged channel vs. clogging position for hydrophilic channel and hydrophobic channel. Most of hydrophilic channels are clogged at entry, and are classified in category of extrinsic clogging. Whereas clogging position in hydrophobic channels distributes around 30 μm, indicating the particle-surface interaction induced clogging, so called intrinsic clogging. Inset is an example of intrinsic clogging.

clogging time is firstly studied. Channel geometry stays invariable, pressure is applied at 15 $mbars$, PS particles with diameter 5 μm is added with $0.01MNaCl$ in order to screen the double electrical layer near the solid surface, decrease the electrostatic repulsion between surface of channel and particle, thus to make the particles easily stick on the wall. This method accelerates deposition, so that the intrinsic clogging. Fig A.5 shows the clogging time decreases with particle concentration, which is in qualitative agreement with Wyss et al.[144]. It is also observed that the $10\%wt$ is a critical concentration, below which the clogging time is of the order of 100 s with large distribution, and drops to the order of $1s$ above this concentration.

Particle deposition induced clogging. In intrinsic clogging, some particles deposit on the channel surface, while others go through the channel. While the local deposition number increases to a certain level, the confinement in this area triggers the clogging of the channel. The effect of particle deposition on clogging time is measured in this section. The number of deposited particles along time is counted by ImageJ. Since the particles are not transparent, only the projection in two-dimension of deposited particles are counted, it is unfortunately unable to know the volumetrically retained particle number in the channel. However, this measurement still provides an important insight into the adsorption induced

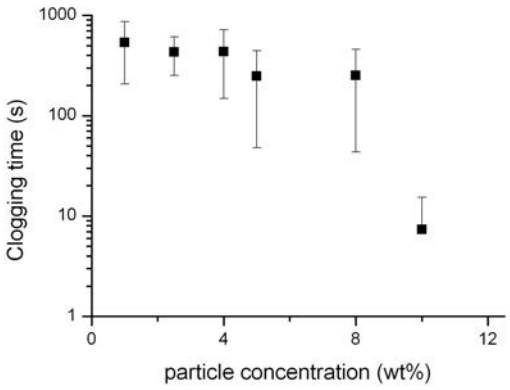

Figure A.5: Clogging time vs. particle concentration, when PS particles with diameter 5 μm with $0.01 MNaCl$ penetrating into channels with width $W = 20$ μm, height $H = 25$ μm, length $L = 400$ μm. Pressure $P = 15$ $mbars$. $10\%wt$ is a critical concentration between long time of clogging with large time distribution, and fast clogging with small time distribution.

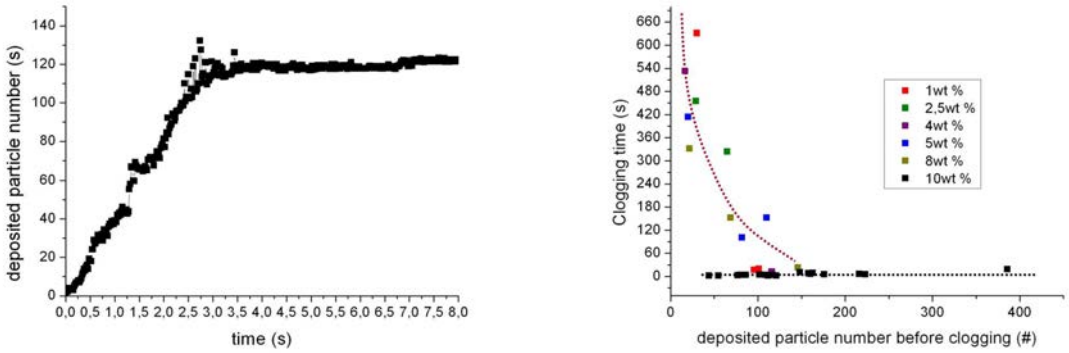

Figure A.6: Number of deposited particle vs. time (left), and clogging time vs. number of deposited particles before clogging (right) with different particle concentration.

clogging. Fig A.6 (left) shows increasing deposited particle number with time, the critical time when the curve reaches a plateau is defined as the time of clogging. Many of this measurement is done by using different concentration of particles suspension, and the relation between time of clogging with the number of deposited particles before clogging occurs is shown in Fig A.6 (right). It is reasonable that the more deposited particles in the channel, the shorter the clogging time is. $10\%wt$ is a critical concentration, above which the clogging arrives rapidly, and independent from number of deposited particle number before clogging.

A.3 Conclusion

Our experimental study allows us to draw the conclusion that the intrinsic clogging, which is caused by the particles deposition in the channel, takes place when the channel is confined enough, which means the height and width of channel is 3-4 times of the diameter

of particles, and when the particle concentration is relatively high (between $1 - 10\%wt$). Even under precaution of system cleaning during channel and sample preparation, dusts at low density still play a dominant role if the intrinsic clogging does not occur fast enough. The clogging is initiated by deposition of particles, when the deposition number exceeds a critical number locally, the confining effect makes the channel clogged. $10\%wt$ is a critical concentration, above which clogging time drops to the order of $1s$, fast enough to be independent from deposition number.

To the interest of petroleum companies, the channel dimension is of 1 μm and the particle size is less than 100 nm with concentration less than $1\%wt$. It is far away from the condition of intrinsic clogging. However, according to different purity of provided particles from AEC and their specific surface coating, deposition may be interesting, from which the information about retention of particles in porous media maybe extracted.

Bibliography

[1] A. Ajdari and L. Bocquet. Giant amplification of interfacially driven transport by hydrodynamic slip: Diffusio-osmosis and beyond. *physical review letters*, 96(18), May 12 2006.

[2] J.L. Anderson. Colloid transport by interfacial forces. *Annual review of fluid mechanics*, 21:61–99, 1989.

[3] S.L. Anna, N. Bontoux, and H.A. Stone. Formation of dispersions using "flow focusing" in microchannels. *Applied physics letters*, 82(3):364–366, Jan 20 2003.

[4] J.L. Barrat and L. Bocquet. Large slip effect at a nonwetting fluid-solid interface. *Physical review letters*, 82(23):4671–4674, Jun 7 1999.

[5] D. Bartolo, G. Degre, P. Nghe, and V. Studer. Microfluidic stickers. *Lab on a chip*, 8(2):274–279, 2008.

[6] J. Baudry, E. Charlaix, A. Tonck, and D. Mazuyer. Experimental evidence for a large slip effect at a nonwetting fluid-solid interface. *Langmuir*, 17(17):5232–5236, Aug 21 2001.

[7] H. Bayer and H. Engelhardt. Capillary electrophoresis in organic polymer capillaries. *Journal of microcolumn separations*, 8(7):479–484, 1996.

[8] M.A. Bevan and D.C. Prieve. Hindered diffusion of colloidal particles very near to a wall: revisited. *Journal of chemical physics*, 113:1228–1236, 2000.

[9] L. Bitsch, L.H. Olesen, C.H. Westergaard, H. Bruus, H. Klank, and J.P. Kutter. Micro particle-image velocimetry of bead suspensions and blood flows. *Experiments in fluids*, 39(3):505–511, Sep 2005.

[10] T.D. Blake. Slip between a liquid and a solid-Tolstoi, D.M. (1952) theory considered. *Colloids and surfaces*, 47:135–145, Jul 1990.

[11] L Bocquet and J.L. Barrat. Hydrodynamic boundary-conditions, correlation-functions, and Kubo relations for confined fluids. *Physical review E*, 49(4, A):3079–3092, Apr 1994.

[12] L. Bocquet and J.L. Barrat. Flow boundary conditions from nano- to micro-scales. *Soft matter*, 3(6):685–693, 2007.

[13] L. Bocquet and E. Charlaix. Nanofluidics, from bulk to interfaces. *Chemical society review*, 39(3):1073–1095, 2010.

[14] E Bonaccurso, H.J. Butt, and V.S.J. Craig. Surface roughness and hydrodynamic boundary slip of a newtonian fluid in a completely wetting system. *Physical review letters*, 90(14), Apr 11 2003.

[15] S. Bonneau, M. Dahan, and L.D. Cohen. Single quantum dot tracking based on perceptual grouping using minimal paths in a spatiotemporal volume. *IEEE transactions on image processing*, 14(9):1384–1395, Sep 2005.

[16] M. Born and E. Wolf. Principles of Optics: Electromagnetic Theory of Propagation, Interference and Diffraction of Light. *CUP Archive*, Oct 1999.

[17] C. I. Bouzigues, P. Tabeling, and L. Bocquet. Nanofluidics in the debye layer at hydrophilic and hydrophobic surfaces. *Physics review letters*, 101(11), Sep 12 2008.

[18] H. Brenner. The slow motion of a sphere through a viscous fluid towards a plane surface. *Chemical engineering science*, 16(3-4):242–251, 1961.

[19] A. Bright. Minimum drop volume in liquid jet breakup. *Chemical engineering research & design*, 63(1):59–66, 1985.

[20] F. Brochard and P.G. degennes. Shear-dependent slippage at a polymer solid interface. *Langmuir*, 8(12):3033–3037, Dec 1992.

[21] E. Brouzes, M. Medkova, N. Savenelli, D. Marran, M. Twardowski, J.B. Hutchison, J.M. Rothberg, D.R. Link, N. Perrimon, and M.L. Samuels. Droplet microfluidic technology for single-cell high-throughput screening. *Proceedings of he national academy of sciences of the United States of America*, 106(34):14195–14200, Aug 25 2009.

[22] J.B. Brzoska, I. Benazouz, and F. Rondelez. Silanization of solid substrates-a step toward reproducibility. *Langmuir*, 10(11):4367–4373, Nov 1994.

[23] C. Cheikh and G. Koper. Stick-slip transition at the nanometer scale. *Physical review letters*, 91(15), Oct 10 2003.

[24] J.T. Cheng and N. Giordano. Fluid flow through nanometer-scale channels. *Physical review E*, 65(3, 1), Mar 2002.

[25] J.H.J. Cho, B.M. Law, and F. Rieutord. Dipole-dependent slip of Newtonian liquids at smooth solid hydrophobic surfaces. *Physical review letters*, 92(16), Apr 23 2004.

[26] C.H. Choi, K.J.A. Westin, and K.S. Breuer. Apparent slip flows in hydrophilic and hydrophobic microchannels. *Physics of fluids*, 15(10):2897–2902, Oct 2003.

[27] N.V. Churaev, J. Ralston, I.P. Sergeeva, and V.D. Sobolev. Electrokinetic properties of methylated quartz capillaries. *Advances in colloid and interface science*, 96(1-3, SI):265–278, Feb 25 2002.

[28] C. Clanet and J.C. Lasheras. Transition from dripping to jetting. *Journal of fluid mechanics*, 383:307–326, Mar 25 1999.

[29] J. Clausell-Tormos, D. Lieber, J.C. Baret, A. El-Harrak, O.J. Miller, L. Frenz, J. Blouwolff, K.J. Humphry, S. Koster, H. Duan, C. Holtze, D.A. Weitz, A.D. Griffiths, and C.A. Merten. Droplet-based microfluidic platforms for the encapsulation

and screening of mammalian cells and multicellular organisms. *Chemistry & Technology*, 15(5):427–437, May 2008.

[30] Y. Cohen and A. B. Metzner. Adsorption effects in the flow of polymer solutions through capillaries. *Macromolecules*, 15(5), Sep 1982.

[31] C. Cottin-Bizonne, C. Barentin, E. Charlaix, L. Bocquet, and J.L. Barrat. Dynamics of simple liquids at heterogeneous surfaces: Molecular-dynamics simulations and hydrodynamic description. *European Physical Journal E*, 15(4):427–438, Dec 2004.

[32] C. Cottin-Bizonne, J.L. Barrat, L. Bocquet, and E. Charlaix. Low-friction flows of liquid at nanopatterned interfaces. *Nature Materials*, 2(4):237–240, Apr 2003.

[33] C. Cottin-Bizonne, B. Cross, A. Steinberger, and E. Charlaix. Boundary slip on smooth hydrophobic surfaces: Intrinsic effects and possible artifacts. *Physical review letters*, 94(5), Feb 11 2005.

[34] V.S.J. Craig, C. Neto, and D.R.M. Williams. Shear-dependent boundary slip in an aqueous Newtonian liquid. *Physical review letters*, 87(5), Jul 30 2001.

[35] R. Dangla, E. Fradet, Y. Lopez, and C.N. Baroud. The physical mechanisms of step emulsification. *Journal of physics D-applied physics*, 46(11), Mar 20 2013.

[36] A.R. de Boer, B. Bruyneel, J.G. Krabbe, H. Lingeman, W.M.A. Niessen, and H. Irth. A microfluidic-based enzymatic assay for bioactivity screening combined with capillary liquid chromatography and mass spectrometry. *Lab on a chip*, 5(11):1286–1292, 2005.

[37] P.G. de Gennes. Scaling Concepts in Polymer Physics. *Cornell University Press*, 1979.

[38] P.G. de Gennes. Polymer-solutions near an interface. 1. Adsorption and depletion layers. *Macromolecules*, 14(6):1637–1644, 1981.

[39] P.G. de Gennes. On fluid/wall slippage. *Langmuir*, 18(9):3413–3414, Apr 30 2002.

[40] P.G. de Gennes, F. Brochard-Wyart, and D. Quéré. Capillarity and Wetting phynomena:Drops, Bubbles, Pearls, Waves. *Springer*, 2004.

[41] A.J. deMello. Control and detection of chemical reactions in microfluidic systems. *Nature*, 442(7101):394–402, Jul 27 2006.

[42] B. Dollet, W. Van Hoeve, J.P. Raven, P. Marmottant, and M. Versluis. Role of the channel geometry on the bubble pinch-off in flow-focusing devices. *Physical review letters*, 100(3), Jan 25 2008.

[43] J. Duchet, B. Chabert, J.P. Chapel, J.F. Gerard, J.M. Chovelon, and N. JaffrezicRenault. Influence of the deposition process on the structure of grafted alkylsilane layers. *Langmuir*, 13(8):2271–2278, Apr 16 1997.

[44] L. Ducry and D.M. Roberge. Controlled autocatalytic nitration of phenol in a microreactor. *Angewandte chemie-international edition*, 44(48):7972–7975, 2005.

[45] E.P. Dupont, R. Luisier, and M.A.M. Gijs. NOA 63 as a UV-curable material for fabrication of microfluidic channels with native hydrophilicity. *Microelectronic engineering*, 87(5-8):1253–1255, May-Aug 2010. 35th International Conference on Micro-and Nano-Engineering, Ghent, Belgium, Sep 28-Oct 01, 2009.

[46] J. Eggers. Nonlinear dynamics and breakup of free-surface flows. *Reviews of modern physics*, 69(3):865–929, Jul 1997.

[47] D.L. Ermak and J.A. Mccammom. Brownian dynamics with hydrodynamic interactions. *Journal of chemical physics*, 69(4):1352–1360, 1978.

[48] P.J. Flory. Principles of Polymer Chemistry. *Cornell University Press*, 1953.

[49] S.M. Ford, J. Davies, B. Kar, S.D. Qi, S. McWhorter, S.A. Soper, and C.K. Malek. Micromachining in plastics using X-ray lithography for the fabrication of microelectrophoresis devices. *Journal of biomechanical engineering-transactions of the asme*, 121(1):13–21, Feb 1999.

[50] A. Franchi and C.R. O'Melia. Effects of natural organic matter and solution chemistry on the deposition and reentrainment of colloids in porous media. *Environmental science & Technology*, 37(6):1122–1129, Mar 15 2003.

[51] T.M. Galea and P. Attard. Molecular dynamics study of the effect of atomic roughness on the slip length at the fluid-solid boundary during shear flow. *Langmuir*, 20(8):3477–3482, Apr 13 2004.

[52] A.M. Ganan-Calvo and J.M. Gordillo. Perfectly monodisperse microbubbling by capillary flow focusing. *Physical review letters*, 87(27), Dec 31 2001.

[53] P. Garstecki, M.J. Fuerstman, H.A. Stone, and G.M. Whitesides. Formation of droplets and bubbles in a microfluidic T-junction - scaling and mechanism of break-up. *Lab on a chip*, 6(3):437–446, Mar 2006.

[54] A.J. Goldman, R.G. Cox, and H. Brenner. Slow viscous motion of a sphere parallel to a plane wall. 2. Coutte flow. *Chemical engineering science*, 22(4):653–&, 1967.

[55] A.J. Goldman, R.G. Cox, and H. Brenner. Slow viscous motion of a sphere parallel to a plane wall .I. Motion through a quiescent fluid. *Chemical engineering science*, 22(4):637–&, 1967.

[56] J.S. Guasto and K.S. Breuer. High-speed quantum dot tracking and velocimetry using evanescent wave illumination. *Experiments in fluids*, 47(6):1059–1066, Dec 2009.

[57] J.S. Guasto, P. Huang, and K.S. Breuer. Statistical particle tracking velocimetry using molecular and quantum dot tracer particles. *Experiments in fluids*, 41(6):869–880, Dec 2006.

[58] P.L. Hansen, J.A. Cohen, R. Podgornik, and V.A. Parsegian. Osmotic properties of poly(ethylene glycols): Quantitative features of brush and bulk scaling laws. *Biophysical Journal*, 84(1):350–355, Jan 2003.

[59] E. Hecht. Optics. *Pearson Education*, 2005.

[60] C.L. Henry, C. Neto, D.R. Evans, S. Biggs, and V.S.J. Craig. The effect of surfactant adsorption on liquid boundary slippage. *Physica A-statistical mechanics and its applications*, 339(1-2):60–65, Aug 1 2004. Conference on New Materials and Complexity, Canberra, Australia, Nov 03-07, 2003.

[61] H. Hervet and L. Leger. Flow with slip at the wall: from simple to complex fluids. *Comptes rendus physique*, 4(2):241–249, Mar 2003.

[62] P. Huang and K.S. Breuer. Direct measurement of anisotropic near-wall hindered diffusion using total internal reflection velocimetry. *Physical review E*, 76(4, 2), Oct 2007.

[63] P. Huang and K.S. Breuer. Direct measurement of slip length in electrolyte solutions. *Physics of fluids*, 19(2), Feb 2007.

[64] P. Huang, J. S. Guasto, and K.S. Breuer. Direct measurement of slip velocities using three-dimensional total internal reflection velocimetry. *Journal of fluid mechanics*, 566:447–464, Nov 10 2006.

[65] R.J. Hunter and L.R. White. Foundation of colloid science. *Clarendon Press (Oxford Oxfordshire and New York)*, 1987.

[66] K.M. Jansons. Determination of the macroscopic (partial) slip boundary-condition for a viscous-flow over a randomly rough-surface with a perfect slip microscopic boundary-condition. *Physics of fluids*, 31(1):15–17, Jan 1988.

[67] Y. Jiang, P.C. Wang, L.E. Locascio, and C.S. Lee. Integrated plastic microftuidic devices with ESI-MS for drug screening and residue analysis. *Analytical chemistry*, 73(9):2048–2053, May 1 2001.

[68] S. Jin, P. Huang, J. Park, J.Y. Yoo, and K.S. Breuer. Near-surface velocimetry using evanescent wave illumination. *Experiments in fluids*, 37(6):825–833, Dec 2004. 5th International Symposium on Particle Image Velocimetry, Busan, South Korea, Sep 22-24, 2003.

[69] L. Joly, C. Ybert, E. Trizac, and L. Bocquet. Hydrodynamics within the electric double layer on slipping surfaces. *Physical review letters*, 93(25), Dec 17 2004.

[70] P. Joseph and P. Tabeling. Direct measurement of the apparent slip length. *physical review E*, 71(3, 2), Mar 2005.

[71] D.S. Kalika, L. Nuel, and M.M. Denn. Gap-dependence of the viscosity of a thermotropic liquid-crystalline copolymer. *Journal of rheology*, 33(7):1059–1070, Oct 1989.

[72] T.M. Keenan and A. Folch. Biomolecular gradients in cell culture systems. *Lab on a chip*, 8(1):34–57, 2008.

[73] L. Kim, Y-C Toh, J. Voldman, and H. Yu. A practical guide to microfluidic perfusion culture of adherent mammalian cells. *Lab on a chip*, 7(6):681–694, Jun 2007.

[74] Y. Kitamura, H. Mishima, and T. Takahashi. Stability of jets in liquid-liquid systems. *Canadian journal of chemical engineering*, 60(6):723–731, 1982.

[75] I. Kobayashi, T. Takano, R. Maeda, Y. Wada, K. Uemura, and M. Nakajima. Straight-through microchannel devices for generating monodisperse emulsion droplets several microns in size. *Microfluidics and nanofluidics*, 4(3):167–177, Mar 2008.

[76] A.V. Krasnoslobodtsev and S.N. Smirnov. Effect of water on silanization of silica by trimethoxysilanes. *Langmuir*, 18(8):3181–3184, Apr 16 2002.

[77] C. Kunert and J. Harting. Roughness induced boundary slip in microchannel flows. *Physical review letters*, 99:176001, Oct 2007.

[78] E. Lauga, P. Brenner, and H.A. Stone. Microfluidics:The No-Slip Boundary Condition. *Handbook of Experimental Fluid Dynamics*, 2005.

[79] L. Leger, E. Raphael, and H. Hervet. Surface-anchored polymer chains: Their role in adhesion and friction. In *Polymers in confined environments*, volume 138 of *Advances in polymer science*, pages 185–225. 1999.

[80] D. Li. Electrokinetics in microfluidics. *Academic Press*, Aug 2004.

[81] H. Li and M. Yoda. An experimental study of slip considering the effects of non-uniform colloidal tracer distributions. *Journal of fluid mechanics*, 662:269–287, Nov 10 2010.

[82] H. F. Li and M. Yoda. Multilayer nano-particle image velocimetry (MnPIV) in microscale Poiseuille flows. *Measurement science & Technology*, 19(7), Jul 2008.

[83] H. F. Li and M. Yoda. Multilayer nano-particle image velocimetry (MnPIV) in microscale Poiseuille flows. *Measurement science & Technology*, 19(7), Jul 2008.

[84] J.R. Lister and H.A. Stone. Capillary breakup of a viscous thread surrounded by another viscous fluid. *Physics of fluids*, 10(11):2758–2764, Nov 1998.

[85] R.H. Liu, M.A. Stremler, K.V. Sharp, M.G. Olsen, J.G. Santiago, R.J. Adrian, H. Aref, and D.J. Beebe. Passive mixing in a three-dimensional serpentine microchannel. *Journal of microelectromechanical systems*, 9(2):190–197, Jun 2000.

[86] R.H. Liu, J.N. Yang, R. Lenigk, J. Bonanno, and P. Grodzinski. Self-contained, fully integrated biochip for sample preparation, polymerase chain reaction amplification, and DNA microarray detection. *Analytical chemistry*, 76(7):1824–1831, Apr 1 2004.

[87] F. Malloggi, N. Pannacci, R. Attia, F. Monti, P. Mary, H. Willaime, P. Tabeling, B. Cabane, and P. Poncet. Monodisperse Colloids Synthesized with Nanofluidic Technology. *Langmuir*, 26(4):2369–2373, Feb 16 2010.

[88] L. Martin-Banderas, M. Flores-Mosquera, P. Riesco-Chueca, A. Rodriguez-Gil, A. Cebolla, S. Chavez, and A.M. Ganan-Calvo. Flow focusing: A versatile technology to produce size-controlled and specific-morphology microparticles. *Small*, 1(7):688–692, Jul 2005.

[89] A.W. Martinez, S.T. Phillips, G.M. Whitesides, and E. Carrilho. Diagnostics for the Developing World: Microfluidic Paper-Based Analytical Devices. *Analytical chemistry*, 82(1):3–10, Jan 1 2010.

[90] J.C. McDonald, D.C. Duffy, J.R. Anderson, D.T. Chiu, H.K. Wu, O.J.A. Schueller, and G.M. Whitesides. Fabrication of microfluidic systems in poly(dimethylsiloxane). *Electrophoresis*, 21(1):27–40, Jan 2000.

[91] V. Mengeaud, J. Josserand, and H.H. Girault. Mixing processes in a zigzag microchannel: Finite element simulations and optical study. *Analytical chemistry*, 74(16):4279–4286, Aug 15 2002.

[92] V. Mhetar and L.A. Archer. Slip in entangled polymer melts. 1. General features. *Macromolecules*, 31(24):8607–8616, Dec 1 1998.

[93] D.H. Michael and Williams P.G. The Equilibrium and Stability of Axisymmetric Pendent Drops. *Proceedings of the royal society of London archives* , 351(1664):117–127, Oct 1976.

[94] M.J. Miksis and S.H. Davis. Slip over rough and cated surfaces. *Journal of fluid mechanics*, 273:125–139, Aug 25 1994.

[95] M.C. Mitchell, V. Spikmans, and A.J. de Mello. Microchip-based synthesis and analysis: Control of multicomponent reaction products and intermediates. *Analyst*, 126(1):24–27, 2001.

[96] C. Neto, V.S.J. Craig, and D.R.M. Williams. Evidence of shear-dependent boundary slip in newtonian liquids. *European physical journal E*, 12(1):S71–S74, Nov 2003.

[97] Z.H. Nie, S.Q. Xu, M. Seo, P.C. Lewis, and E. Kumacheva. Polymer particles with various shapes and morphologies produced in continuous microfluidic reactors. *Journal of the American chemical society*, 127(22):8058–8063, Jun 8 2005.

[98] T. Nisisako, T. Torii, and T. Higuchi. Droplet formation in a microchannel network. *Lab on a chip*, 2(1):24–26, 2002.

[99] M.R. Oberholzer, N.J. Wagner, and A.M. Lenhoff. Grand canonical Brownian dynamics simulation of colloidal adsorption. *Journal of chemical physics*, 107(21):9157–9167, Dec 1 1997.

[100] M.G. Olsen and R.J. Adrian. Out-of-focus effects on particle image visibility and correlation in microscopic particle image velocimetry. *Experiments in fluids*, 29(S):S166–S174, Dec 2000. 3rd International Workshop on Particle Image Velocimetry, Santa Barbara, California, Sep 16-18, 1999.

[101] A.L. Paguirigan and D.J. Beebe. Microfluidics meet cell biology: bridging the gap by validation and application of microscale techniques for cell biological assays. *Bioessays*, 30(9):811–821, Sep 2008.

[102] A.J. Pelley and N. Tufenkji. Effect of particle size and natural organic matter on the migration of nano- and microscale latex particles in saturated porous media. *Journal of colloid and inteface science*, 321(1):74–83, May 1 2008.

[103] A Pierres, AM Benoliel, C Zhu, and P Bongrand. Diffusion of microspheres in shear flow near a wall: Use to measure binding rates between attached molecules. *Biophysical Journal*, 81(1), jul.

[104] F. Pignon, A. Magnin, J.M. Piau, B. Cabane, P. Aimar, M. Meireles, and P. Lindner. Structural characterisation of deposits formed during frontal filtration. *Journal of membrane science*, 174(2):189–204, Jul 31 2000.

[105] R. Pit, H. Hervet, and L. Leger. Friction and slip of a simple liquid at a solid surface. *Tribology letters*, 7(2-3):147–152, 1999.

[106] R Pit, H Hervet, and L Leger. Direct experimental evidence of slip in hexadecane: Solid interfaces. *Physical review letters*, 85(5):980–983, July 2000.

[107] I.V. Ponomarev and A.E. Meyerovich. Surface roughness and effective stick-slip motion. *Physical Review E*, 67(2, 2), Feb 2003.

[108] C. Priest, S. Herminghaus, and R. Seemann. Generation of monodisperse gel emulsions in a microfluidic device. *Applied physics letters*, 88(2), Jan 9 2006.

[109] N.V. Priezjev. Effect of surface roughness on rate-dependent slip in simple fluids. *Journal of chemical physics*, 127(14), Oct 14 2007.

[110] J.R. Richard, A.N. Baris, and A.M. Lenhoff. Drop formation in liquid-liquid systems before nd after jetting. *Physics of fluids*, 7(11):2617–2630, Nov 1995.

[111] A.G. Richter, C.J. Yu, A. Datta, J. Kmetko, and P. Dutta. In situ and interrupted-growth studies of the self-assembly of octadecyltrichlorosilane monolayers. *physical review E*, 61(1):607–615, Jan 2000.

[112] M.A. Roberts, J.S. Rossier, P. Bercier, and H. Girault. UV laser machined polymer substrates for the development of microdiagnostic systems. *Analytical chemistry*, 69(11):2035–2042, Jun 1 1997.

[113] M.A. Roberts, J.S. Rossier, P. Bercier, and H. Girault. UV laser machined polymer substrates for the development of microdiagnostic systems. *Analytical chemistry*, 69(11):2035–2042, Jun 1 1997.

[114] R. Sadr, C. Hohenegger, H. Li, P.J. Mucha, and M. Yoda. Diffusion-induced bias in near-wall velocimetry. *Journal of fluid mechanics*, 577:443–456, Apr 25 2007.

[115] R. Sadr, H.F. Li, and M. Yoda. Impact of hindered Brownian diffusion on the accuracy of particle-image velocimetry using evanescent-wave illumination. *Experiments in fluids*, 38(1):90–98, Jan 2005.

[116] R. Sadr, M. Yoda, Z. Zheng, and A.T. Conlisk. An experimental study of electro-osmotic flow in rectangular microchannels. *Journal of fluid mechanics*, 506:357–367, May 10 2004.

[117] Y. Schaerli, R.C. Wootton, T. Robinson, V. Stein, C. Dunsby, M.A.A. Neil, P.M. W. French, A.J. deMello, C. Abell, and F. Hollfelder. Continuous-Flow Polymerase Chain Reaction of Single-Copy DNA in Microfluidic Microdroplets. *Analytical chemistry*, 81(1):302–306, Jan 1 2009.

[118] G.F. Scheele and B.J. Meister. Drop formation at low velocities in liquid-liquid systems .I. prediction of drop volume .2. prediction of jetting velocity. *Aiche journal*, 14(1):9–&, 1968.

[119] C. Sendner, D. Horinek, L. Bocquet, and R.R. Netz. Interfacial Water at Hydrophobic and Hydrophilic Surfaces: Slip, Viscosity, and Diffusion. *Langmuir*, 25(18):10768–10781, Sep 15 2009.

[120] X.D. Shi, M.P. Brenner, and S.R. Nagel. A cascade of structure in a drop falling from a faucet. *Science*, 265(5169):219–222, Jul 8 1994.

[121] L. Shui, A. van den Berg, and J.C.T. Eijkel. Scalable attoliter monodisperse droplet formation using multiphase nano-microfluidics. *Microfluidics and nanofluidics*, 11(1):87–92, Jul 2011.

[122] P. Silberzan, L. Leger, D. Ausserre, and J.J. Benattar. Silanation of silica surfaces - a new method of constructing pure or mixed monolayers. *Langmuir*, 7(8):1647–1651, Aug 1991.

[123] L.L. Song, E.J. Hennink, I.T. Young, and H.J. Tanke. Photobleaching kinetics of fluorescein in quantitative fluorescence microscopy. *Biophysical journal*, 68(6):2588–2600, Jun 1995.

[124] L.L. Song, R.P.M. vanGijlswijk, I.T. Young, and H.J. Tanke. Influence of fluorochrome labeling density on the photobleaching kinetics of fluorescein in microscopy. *Cytometry*, 27(3):213–223, Mar 1 1997.

[125] T.M. Squires and S.R. Quake. Microfluidics: Fluid physics at the nanoliter scale. *Review of modern physics*, 77(3):977–1026, Jul 2005.

[126] S. Sugiura, M. Nakajima, S. Iwamoto, and M. Seki. Interfacial tension driven monodispersed droplet formation from microfabricated channel array. *Langmuir*, 17(18):5562–5566, Sep 4 2001.

[127] P. Tabeling. Introduction to microfluidics. *Oxford*, 2003.

[128] S. Takeuchi, P. Garstecki, D.B. Weibel, and G.M. Whitesides. An axisymmetric flow-focusing microfluidic device. *Advanced materials*, 17(8):1067+, Apr 18 2005.

[129] Y.C. Tan, V. Cristini, and A.P. Lee. Monodispersed microfluidic droplet generation by shear focusing microfluidic device. *Sensors and actuators B-chemical*, 114(1):350–356, Mar 30 2006.

[130] S.Y. Teh, R. Lin, L.H. Hung, and A.P. Lee. Droplet microfluidics. *Lab on a chip*, 8(2):198–220, 2008.

[131] I. Teraoka. Polymer Solutions: An Introduction to Physical Properties. *John Wiley & Sons*, Mar 2002.

[132] T. Thorsen, R.W. Roberts, F.H. Arnold, and S.R. Quake. Dynamic pattern formation in a vesicle-generating microfluidic device. *Physical review letters*, 86(18):4163–4166, Apr 30 2001.

[133] D.M. Tolstoi. Molecular theory for slippage of liquids over solid surfaces (in Russian). *Doklady Akad. Nauk SSSR*, 85:1089, 1952.

[134] D.C. Tretheway and C.D. Meinhart. Apparent fluid slip at hydrophobic microchannel walls. *Physics of fluids*, 14(3):L9–L12, Mar 2002.

[135] E. Tyler. Instability of liquid jets. *Philosophical magazine*, 16(105, Aug, 7th series):504–518, Aug 1933.

[136] A.S. Utada, A. Fernandez-Nieves, H.A. Stone, and D.A. Weitz. Dripping to jetting transitions in coflowing liquid streams. *Physical review letters*, 99(9), Aug 31 2007.

[137] G.V. Vinogradov, V.P. Protasov, and V.E. Dreval. The theological behavior of flexible-chain polymers in the region of high shear rates and stresses, the critical process of spurting, and supercritical conditions of their movement at T greater than TG. *Rheologica acta*, 23(1):46–61, 1984.

[138] O.I. Vinogradova, Bunkinm N.F., N.V. Churaev, O.A. Kiseleva, A.V. Lobeyev, and B.W. Ninham. Submicrocavity submicrocavity structure of water between hydrophobic and hydrophilic walls as revealed by optical cavitation. *Journal of colloid and interface science*, 173(2):443–447, Aug 1995.

[139] S.Q. Wang and P.A. Drda. Superfluid-like stick-slip transition in capillary flow of linear polyethylene melts .1. General features. *Macromolecules*, 29(7):2627–2632, Mar 25 1996.

[140] W.H. Wang, Z.L. Zhang, Y.N. Xie, L. Wang, S. Yi, K. Liu, J. Liu, D.W. Pang, and X.Z. Zhao. Flow-focusing generation of monodisperse water droplets wrapped by ionic liquid on microfluidic chips: From plug to sphere. *Langmuir*, 23(23):11924–11931, Nov 6 2007.

[141] T. Ward, M. Faivre, M. Abkarian, and H.A. Stone. Microfluidic flow focusing: Drop size and scaling in pressure versus flow-rate-driven pumping. *Electrophoresis*, 26(19):3716–3724, Oct 2005.

[142] G.M. Whitesides. The origins and the future of microfluidics. *Nature*, 442(7101):368–373, Jul 27 2006.

[143] R.C.R. Wootton, R. Fortt, and A.J. de Mello. On-chip generation and reaction of unstable intermediates-monolithic nanoreactors for diazonium chemistry: Azo dyes. *Lab on a chip*, 2(1):5–7, 2002.

[144] H.M. Wyss, D.L. Blair, J.F. Morris, H.A. Stone, and D.A. Weitz. Mechanism for clogging of microchannels. *Physical review E*, 74(6, 1), Dec 2006.

[145] J. H. Xu, S. W. Li, J. Tan, Y. J. Wang, and G. S. Luo. Preparation of highly monodisperse droplet in a T-junction microfluidic device. *Aiche Journal*, 52(9):3005–3010, Sep 2006.

[146] J.H. Xu, S.W. Li, G.G. Chen, and G.S. Luo. Formation of monodisperse microbubbles in a microfluidic device. *Aiche Journal*, 52(6):2254–2259, Jun 2006.

[147] C. Ybert, C. Barentin, C. Cottin-Bizonne, P. Joseph, and L. Bocquet. Achieving large slip with superhydrophobic surfaces: Scaling laws for generic geometries. *Physics of fluids*, 19(12), Dec 2007.

[148] H. Yu, C.M. Alexander, and D.J. Beebe. A plate reader-compatible microchannel array for cell biology assays. *Lab on a chip*, 7(3):388–391, 2007.

[149] H. Yu, C.M. Alexander, and D.J. Beebe. Understanding microchannel culture: parameters involved in soluble factor signaling. *Lab on a chip*, 7(6):726–730, Jun 2007.

[150] C.M. Zettner and M. Yoda. Particle velocity field measurements in a near-wall flow using evanescent wave illumination. *Experiments in fluids*, 34(1):115–121, Jan 2003.

[151] W.W. Zhang and J.R. Lister. Similarity solutions for capillary pinch-off in fluids of differing viscosity. *Physicsl review letters*, 83(6):1151–1154, Aug 9 1999.

[152] B. Zheng, L.S. Roach, and R.F. Ismagilov. Screening of protein crystallization conditions on a microfluidic chip using nanoliter-size droplets. *Journal of the American chemical society*, 125(37):11170–11171, Sep 17 2003.

[153] Y.X. Zhu and S. Granick. Limits of the hydrodynamic no-slip boundary condition. *Physical review letters*, 88(10), Mar 11 2002.

abstract

In this work, we have addressed three projects with the application of Microfluidics:

1. With the technology of Total Internal Reflection Velocimetry, we realised the nano-PTV of fluid flow within 800 nm close to solid surface. We achieved unprecedented accuracy of measurement compared with the state of art, by determining precisely the wall position, and by Langevin simulation, which takes into account of the sources of biases, such as Brownian motion, shear stress, electrostatic repulsion between particles and the wall, effect of out of focus, etc. We achieved ± 5 nm and ± 10 nm accuracy on the slip length determination for sucrose solution and for water. The no-slip condition on hydrophilic surface is confirmed, and a positive slip length on hydrophobic surface is clearly illustrated. This result demonstrated that the nano-PTV by TIRF is a quantitative methodology for the study of fluid flow near solid surface. This technology is applied to study flow of semi diluted polymer solution close to hydrophilic solid surface, a negative slip length is observed, due to adsorption of polymer chain onto the surface.

2. We collaborated with A. Leshansky to study quantitatively the mechanism of step emulsification. The dispersed fluid and continuous fluid are co-flowing in a confined Hele-Shaw channel, before going into an unconfined pool. Drops are formed at the intersection between shallow channel and the pool. Two phases - step emulsification and large drops - are distinguished based on a well defined capillary number. The phase transition occurs at a critical capillary number, which is a function of the aspect ratio of the shallow channel. This discovery is confirmed by the theory, which is based on Hele-Shaw dynamics with the effect of capillary force. We found good agreement between experiments and theory, on the step emulsification droplet size, dispersed fluid pinching dynamics, and on the shape of free interface between dispersed fluid and continuous fluid prior to pinching. This work provides important theoretical support to the rising communities who utilise the step emulsification to make mono dispersed droplets for biological and chemical application.

3. We collaborated with a group of petroleum companies (AEC), to develop a technology which has potential application to the Enhanced Oil Recovery. Nano particles synthesized by the AEC is supposed to perform phase transition or deliver signals once in touch with oil. The principal idea consists in sending these nano particles into the porous media underground along with the injection fluids, and recollect them on the production well side. According to the information they deliver, the distribution oil may be mapped. We constructed a micro model based on microfluidic technology, which mimics the complex structure of porous media of rocks. The AEC synthesized nano particles are injected into the micro model, their motion and retention can be observed in real time. This work provides important information on the particle motion in porous media, which cannot be realised in conventional core experiments.

Key words

Microfluidic design, fabrication and control, fluid mechanics, complex fluids, petroleum recovery.